

# Energy Systems Research

---

Volume 4 • Number 2 • 2021

Published by  
Melentiev Energy Systems Institute  
Siberian Branch of Russian Academy of Sciences

Available online: [esrj.ru](http://esrj.ru)

ISSN 2618-9992

# Energy Systems Research

---

**Volume 4 • Number 2 • 2021**

International scientific peer-reviewed journal

Available online: <http://esj.ru>

## About the journal

*Energy Systems Research* is an international peer-reviewed journal addressing all the aspects of energy systems, including their sustainable development and effective use, smart and reliable operation, control and management, integration and interaction in a complex physical, technical, economic and social environment.

Energy systems research methodology is based on a systems approach considering energy objects as systems with complicated structure and external ties, and includes the methods and technologies of systems analysis.

Within this broad multi-disciplinary scope, topics of particular interest include strategic energy systems development at the international, regional, national and local levels; energy supply reliability and security; energy markets, regulations and policy; technological innovations with their impacts and future-oriented transformations of energy systems.

The journal welcomes papers on advances in heat and electric power industries, energy efficiency and energy saving, renewable energy and clean fossil fuel generation, and other energy technologies.

Energy Systems Research is also concerned with energy systems challenges related to the applications of information and communication technologies, including intelligent control and cyber security, modern approaches of systems analysis, modeling, forecasting, numerical computations and optimization.

The journal is published by Melentiev Energy Systems Institute of Siberian Branch of Russian Academy of Sciences. The journal's ISSN is 2618-9992. There are 4 issues per year (special issues are available). All articles are available online on English as Open access articles.

## Topics

- Energy production, conversion, transport and distribution systems
- Integrated energy systems
- Energy technologies
- International, regional, local energy systems
- Energy system protection, control and management
- Smart energy systems, smart grids
- Energy systems reliability and energy security
- Electricity, heating, cooling, gas and oil systems
- Energy system development and operation
- Demand-side management
- Energy economics and policy
- Renewable energy and clean fossil fuel based systems
- Distributed energy systems
- Sustainable energy transitions
- System problems of power and thermal engineering
- Artificial intelligence in energy systems
- Information and communication technologies in energy systems
- Energy systems analysis and modelling
- Computational methods and optimization in energy systems

### Editor-in-chief

Nikolai Voropai,  
Corresponding member of Russian Academy of Sciences,  
President of *Melentiev Energy Systems Institute SB RAS, Russia*

### Editorial board

- Valentin Barinov, *JSC ENIN, Russia*
- Sereeter Batmunkh, *Mongolia*
- Vitaly Bushuev, *Institute of Energy Strategy, Russia*
- Elena Bycova, *Institute of Power Engineering of Academy of Sciences of Moldova, Republic of Moldova*
- Gary Chang, *National Chung Cheng University, Taiwan*
- Pang Changwei, *China University of Petroleum, China*
- Cheng-I Chen, *National Central University, Taiwan*
- Gianfranco Chicco, *Politecnico di Torino, Italy*
- Van Binh Doan, *Institute of Energy Science of VAST, Vietnam*
- Petr Ekel, *Federal University of Minas Gerais, Pontifical Catholic University of Minas Gerais, Brasil*
- Ines Hauer, *Otto-von-Guericke-Universität, Magdeburg, Germany*
- Marija Ilic, *Massachusetts Institute of Technology, Cambridge, USA*
- James Kendell, *Asian Pacific Energy Research Center, Japan*
- Oleg Khamisov, *Melentiev Energy Systems Institute SB RAS, Russia*
- Alexander Kler, *Melentiev Energy Systems Institute SB RAS, Russia*
- Przemyslaw Komarnicki, *University of Applied Sciences Magdeburg-Stendal, Germany*
- Nadejda Komendantova, *International Institute for Applied Systems Analysis, Austria*
- Yuri Kononov, *Melentiev Energy Systems Institute SB RAS, Russia*
- Marcel Lamoureux, *Policy and Governance Research Institute, USA*
- Yong Li, *Hunan University, China*
- Faa-Jeng Lin, *National Central University, Taiwan*
- Alexey Makarov, *Energy Research Institute RAS, Russia*
- Lyudmila Massel, *Melentiev Energy Systems Institute SB RAS, Russia*
- Alexey Mastepanov, *Oil and Gas Research Institute RAS, Institute of Energy Strategy, Russia*
- Alexander Mikhalevich, *Institute of Energy, Belarus*
- Mikhael Negnevitsky, *Tasmania University, Australia*
- Takato Ojimi, *Asian Pacific Energy Research Center, Japan*
- Sergey Philippov, *Energy Research Institute RAS, Russia*
- Waldemar Rebizant, *Wroclaw University of Science and Technology, Poland*
- Christian Rehtanz, *Dortmund Technical University, Germany*
- Boris Saneev, *Melentiev Energy Systems Institute SB RAS, Russia*
- Sergey Senderov, *Melentiev Energy Systems Institute SB RAS, Russia*
- Valery Stennikov, *Melentiev Energy Systems Institute SB RAS, Russia*
- Zbigniew Styczynski, *Otto-von-Guericke University Magdeburg, Germany*
- Constantine Vournas, *National Technical University of Athens, Greece*
- Felix Wu, *Hong-Kong University, China*
- Ryuichi Yokoyama, *Energy and Environment Technology Research Institute, Waseda University, Tokyo, Japan*
- Jae-Young Yoon, *Korea Electrotechnology Research Institute, Republic of Korea*
- Xiao-Ping Zhang, *University of Birmingham, United Kingdom*

### Publishing board

Executive secretary:	Dmitry Zolotarev
Copyeditor:	Marina Ozerova
Math proofreading editor	Evgenia Markova

### Contacts

Scientific secretary:	Alexey Mikheev, Dr. of Eng.
E-mail:	<a href="mailto:info@estj.ru">info@estj.ru</a>
Tel:	+7 (3952) 950980 (English, Russian)
Fax:	+7 (3952) 426796
Address:	130, Lermontov str., Irkutsk, 664033, Russia

## Contents

<b>Review of Clustering Methods for Slow Coherency-Based Generator Grouping</b> Gianfranco Chicco	5
<b>Generation Structure, Prices, and Tariffs in the Russian Electric Power Industry in 2009-2018</b> M. Yu. Vasilyev	21
<b>A Numerical Study of the Influence of Process Parameters on the Efficiency of Staged Coal Gasification Using Mixtures of Oxygen and Carbon Dioxide</b> I. G. Donskoy	27
<b>Options for Modernization of Heat Supply to Consumers of Condensing Power Plant</b> D. Balzamor, I. Akhmetova, E. Balzamova	35
<b>Amplitude Sampled Reference-Based Space Vector Pulse Width Modulation for Control of Voltage Source Converters</b> Mohamed Khalid Ratib, Ahmed Rashwan	46
<b>A Methodological Approach to Assessing the Possible Effect of Distributed Generation Expansion on Regional Energy Supply Systems</b> E. V. Galperova	64
<b>Simulation of Electromagnetic Fields Generated by Overhead Power Lines and Railroad Traction Networks</b> Natalya V. Buyakova, Vasiliy P. Zakaryukin, Andrey V. Kryukov, Dmitriy A. Seredkin	70

# Review of Clustering Methods for Slow Coherency-Based Generator Grouping

Gianfranco Chicco\*

Dipartimento Energia “Galileo Ferraris”, Politecnico di Torino, Torino, Italy

**Abstract** — Slow coherency is one of the most relevant concepts used in power systems dynamics to group generators that exhibit similar response to disturbances. Among the approaches developed for generator grouping based on slow coherency, clustering algorithms play a significant role. This paper reviews the clustering algorithms applied in model-based and data-driven approaches, highlighting the metrics used, the feature selection, the types of algorithms and the comparison among the results obtained considering simulated or measured data.

**Index Terms:** clustering, contingency screening, data-driven, distance, feature selection, generator grouping, model-based, phasor measurement unit, power system dynamics, similarity metric, slow coherency, stability analysis.

## NOMENCLATURE

COA	Centre of Angle
COI	Centre of Inertia
COIFD	Centre of Inertia Frequency Deviation
DBI	Davies–Bouldin Index
DBSCAN	Density-Based Spatial Clustering of applications with Noise
DCD	Dynamic Coherency Determination
DFT	Discrete Fourier Transform
DMD	Dynamic Mode Decomposition
DTW	Dynamic Time Warping
FCM	Fuzzy c-Means
FCMdd	Fuzzy c-Medoids
ICA	Independent Component Analysis

KPCA	Kernel Principal Component Analysis
PCA	Principal Component Analysis
PMU	Phasor Measurement Unit
SOM	Self-Organising Maps
SVC	Support Vector Clustering
SVD	Singular Value Decomposition
WSSE	Weighted Sum Squared Error

## I. INTRODUCTION

The evolution of the computational frameworks for applying efficient data analytics through machine learning has a significant impact on the formulation and update of the computational codes used in many applications. The power system sector is heavily affected by this evolution, which is marking new differences between the two most used approaches:

1. The *model-based* approach, in which a suitable model is constructed by connecting a number of elements that represent the physical components with different degrees of approximation. Suitable parameters have to be associated to each element, and the solution is determined through simulations.
2. The *data-driven* approach (also indicated as *measurement-based* or *signal-based* approach), in which the computations are based on the available data gathered from the field in actual situations and are carried out by using machine learning approaches that do not need the construction of the system model nor the parameter setup, and do not depend on theoretical assumptions.

Advantages and drawbacks of these approaches are summarised in [1], together with the characterisation of different aspects that explain data consistency in terms of data characteristics, data quality, and information quality. The scientific community is contributing to the debate about the convenience of one approach or the other, by developing new computational procedures in both directions.

Concerning power system dynamics, both approaches share a major issue, given by the variability in time of the

\* Corresponding author.

E-mail: [gianfranco.chicco@polito.it](mailto:gianfranco.chicco@polito.it)

<http://dx.doi.org/10.38028/esr.2021.02.0001>

Received May 31 06, 2021. Revised June 21, 2021.

Accepted July 03, 2021. Available online July 23, 2021.

This is an open access article under a Creative Commons Attribution-NonCommercial 4.0 International License.

© 2021 ESI SB RAS and authors. All rights reserved.

data used in dynamic conditions. In particular:

- Methods based on the model-based approach are highly sensible on the accuracy of the model and parameters used to represent dynamics at different time scales. Dynamic models are available at different levels of detail, and dynamic reduction methods are available and are incorporated in the dynamic simulation tools. Modal analysis is applied, where the power system model is linearised around an equilibrium point, and the oscillation modes are extracted by calculating eigenvalues and eigenvectors from the small-signal analysis of the linearised power system model [2]. Further insights may come from the application of Koopman mode analysis, which is a nonlinear technique that requires no linearisation nor assumptions of scale separation [3, 4].
- Methods based on the data-driven approach require time series of data with appropriate resolution in time and data window length, to form a reasonable history, benchmark or comparative dataset. These methods are sensible to the consistency of the data gathered from the field. However, possible issues depend on accuracy of the measurements, sensitivity to disturbances, and in particular to the occurrence of major changes in the operational conditions of the network (e.g., changes in topology, loss of a generator, or large net power variations [5]). Following major disturbances, the dataset is typically partitioned into portions that represent the system operation before and after the change, by identifying the starting instant of the event and removing pre-event data. In particular, the methods based on similarities among time series can be adapted and used online, while the methods that carry out mode estimation or use information about the frequency spectrum (e.g., of inter-area oscillations) require longer computation time and are thus applied offline [6].

The determination of the dynamic equivalents of the generators connected to the power system power is a challenging and insightful line of research. Starting from dynamic models developed during the years, in the Seventies two main approaches emerged for the identification of similar behaviour of the generators in a multi-machine power system, especially during contingencies, and the formation of dynamic equivalents. One of these approaches is based on *modal analysis* [7] [8], while the other approach is based on the notion of *coherency* [9]. Two (or more) generators are considered to be coherent if their rotor angles follow the same evolution in time, both in normal conditions and after the occurrence of disturbances. The identification of coherency requires to set up appropriate criteria based on distance measures [10]. Many algorithms have been formulated for both modal analysis [11] and for coherency assessment, with various approaches [12, 13], among which clustering algorithms that exploit time-series similarity-based techniques. The creation of reduced dynamic equivalent models of

generators is a major asset to increase the computational speed and enable real-time applications. A discussion on methods for dynamic reduction can be found for example in [14]. Among these methods, the application of clustering techniques is an alternative to deal with this non-linear and large-scale problem in power system dynamics by using a suitable set of representative features (e.g., variables or indicators). Coherency-based generator grouping is the problem referring to power system dynamics for which most contributions that exploit clustering algorithms are available in the literature.

This paper addresses the application of clustering algorithms in the methods used to deal with the generator grouping based on coherency aspects. The application of clustering algorithms deals with the need of identifying groups inside the system that exhibit some similarity, and this similarity may be useful for specific purposes. Clustering algorithms have shown particularly promising results, and more refined variants are under continuous development.

In general terms, the main requirements of the clustering algorithms include:

- The choice of appropriate *features*.
- The incorporation of a suitable notion of *distance* for similarity assessment.
- The ability to operate with *high-dimensional* data set.
- The effectiveness of the clustering algorithm (assessed through *clustering validity* indices).
- The ability to discover possible *outliers* (when needed).
- The ability to estimate the *best number of clusters*.

In power system dynamic studies, clustering algorithms are applied to both model-based and data-driven approaches. In general, the challenging objective is to test and validate the proposed approaches as close as possible to real-time applications in actual systems. In model-based approaches, in addition to software simulation tools, examples oriented to practical validation have been explored with a hybrid analog-digital power system simulator [15], while solutions that incorporate the use of real-time data in power system models have recently emerged with the use of real-time simulators, which allow the implementation of hardware-in-the-loop solutions [6].

The aim of this paper is to illustrate and discuss why, in which phase of the analysis and how the clustering algorithms are used for solving the generator grouping on the basis of their dynamic behaviour. A selected set of references is considered, including recent references together with a number of historical references, without the intention to provide an exhaustive list of literature contributions.

The next sections of the paper are organised as follows. Section II discusses the notions of distance and metrics used in the clustering algorithms for analysing power system dynamics. Section III recalls the notion of slow coherency and its use for generator grouping. Section IV addresses in more details the feature selection stage. Section V deals

with the clustering algorithms used. Section 6 illustrates the comparisons carried out among the results obtained from literature contributions. The last section contains the concluding remarks.

## II. METRICS USED IN THE CLUSTERING ALGORITHMS

For the purpose of the contents presented in this paper, the input dataset is composed of  $M$  time series with  $T$  data points each, corresponding to a given feature. For  $m = 1, \dots, M$ , the time series of the individual feature  $\psi_m$  is represented as

$$\psi_m = \{\psi_{mt}, t = 1, \dots, T\}. \quad (1)$$

The metrics used are based on determining the distance between two time series. Since the dataset is discrete, discrete versions of the metrics are used. Without loss of generality, the distances are indicated in the sequel by considering two feature vectors. The same formulations are applicable to calculate the distance between a feature vector and a centroid, by replacing one of the feature vectors with the centroid.

In a clustering procedure, the choice of the metric to calculate the distances between time series is crucial [16]. In particular, four types of metrics can be identified:

- 1 Metrics based on the calculation of the distance for points located at the *same instant*: these metrics are relevant if it is important to maintain the identity of the individual time instants, calculating distances between time series on the vertical axis. The most classical metrics of this type are based on the Minkowski distances, defined for an integer parameter  $p > 0$ :

$$d_M^{(p)}(\Psi_i, \Psi_j) = \left( \sum_{t=1}^T |\psi_{it} - \psi_{jt}|^p \right)^{1/p}, \quad (2)$$

where in particular the distance for  $p = 2$  is the Euclidean distance:

$$d_M^{(2)}(\Psi_i, \Psi_j) = d_E(\Psi_i, \Psi_j) = \sqrt{\sum_{t=1}^T |\psi_{it} - \psi_{jt}|^2}. \quad (3)$$

When a weight factor  $w_{ijt}$  is introduced, which depends on the features, time, or combinations of them, the weighted versions of the Minkowski distances become:

$$d_{Mw}^{(p)}(\Psi_i, \Psi_j) = \left( \sum_{t=1}^T w_{ijt} |\psi_{it} - \psi_{jt}|^p \right)^{1/p}. \quad (4)$$

In particular,  $d_{Mw}^{(2)}(\Psi_i, \Psi_j)$  is the weighted sum squared error (WSSE).

- 2 Metrics based on the *proximity between points* in the time series. These distances are used if comparing the time series without the constraint of maintaining the correspondence between the instants of time is acceptable. The distance obtained is a single value that depends on the overall evolution of the trajectories. In this way, time series with similar shape but (slight) shift in time can be characterised by a small distance. Among these metrics, the *Hausdorff distance* is given

by the largest distance from a point belonging to the time series  $\psi_i$  to the closest point belonging to the other time series  $\psi_j$ . Let us first define the minimum distance between a point  $\psi_{it} \in \Psi_i$  for a given value of  $t$  and the points  $\psi_{jq} \in \Psi_j$ ,  $q = 1, \dots, T$ , as follows:

$$d(\psi_{it}, \Psi_j) = \min_{\psi_{jq} \in \Psi_j} \{d_E(\psi_{it}, \psi_{jq})\}. \quad (5)$$

Likewise,

$$d(\Psi_j, \psi_i) = \min_{\psi_{ij} \in \Psi_j} \{d_E(\psi_{ij}, \psi_{iq})\}. \quad (6)$$

The Hausdorff distance is then computed as:

$$d_H(\Psi_i, \Psi_j) = \max \left\{ \min_{\psi_{it} \in \Psi_i} \{d(\psi_{it}, \Psi_j)\}, \min_{\psi_{jt} \in \Psi_j} \{d(\psi_{jt}, \Psi_i)\} \right\}. \quad (7)$$

Moreover, the *Fréchet distance* is the maximum pairwise distance between the points located on the two time series [17]. It is also known as the person-dog metric, being based on the concept of considering a person who walks a dog on a leash. Both the person and the dog follow a separate trajectory but cannot move backwards (this is a conceptual difference with respect to the Hausdorff distance). The Fréchet distance is the length of the shortest leash needed to follow the entire trajectories.

The *Dynamic time warping* (DTW) distance is another possibility to determining the distance between two time series. In DTW, the differences between two time series are determined by changing the connections between the corresponding points in the time series. DTW creates a warping path of minimum local distances and computes the final distance as the mean distance along this path. The length of the warping path may be higher than the length of the time series.

The need for considering a distance notion that does not strictly refer to the same time instants is recognised as well in [18], where an *integrated weighted distance* is used. This distance is based on the definition of three distance functions: (i) ‘‘horizontal absolute value’’; (ii) weighted distance of ‘‘rate of change at adjacent time points’’; (iii) weighted distance of ‘‘coefficient of variation’’. The values obtained for each distance function are then subject to min-max normalisation. Finally, the weighted distance matrix is formed by weighting the matrices that contain the entries of the normalised distance functions, by using entropy-based weights.

- 3 Metrics that consider the *global behaviour* of the time series. These metrics are based on determining the similarity between the time series on the [0,1] scale, then defining the distances as the complement to unity of the similarity. The *correlation coefficient* is the most classical notion of similarity. Since the correlation coefficient  $\rho$  varies from  $-1$  to  $1$ , it is

needed to reconvert it to the  $[0,1]$  range by calculating  $(\rho + 1)/2$ . In addition, the *cosine similarity* derives from the definition of the Euclidean internal product and is the ratio between the internal product and the product of the magnitudes. The cosine distance is then calculated as:

$$d_C(\Psi_i, \Psi_j) = 1 - \frac{\sum_{t=1}^T \Psi_{it} \Psi_{jt}}{\sqrt{\sum_{t=1}^T \Psi_{it}^2} \sqrt{\sum_{t=1}^T \Psi_{jt}^2}}. \quad (8)$$

In the calculation of the cosine similarity, if the vectors are changed by subtracting the vector means, the resulting version is called *centred cosine similarity*, which corresponds to the Pearson correlation coefficient. Another way to calculate correlations by excluding the mean value is to take only non-zero  $F$  harmonic components of the spectrum computed from the Discrete Fourier Transform (DFT), in which the zero-order harmonic component, proportional to the mean value, is not considered [19]. In this case, the features  $\zeta_m$  for  $m = 1, \dots, M$  are expressed as a complex number, which can be written with the real part  $\zeta_m^{Re} = \{\zeta_{mv}^{Re}\}$  and the imaginary part  $\zeta_m^{Im} = \{\zeta_{mv}^{Im}\}$  for  $v = 1, \dots, F$ . The correlation coefficient between  $\zeta_i^{Re}$  and  $\zeta_j^{Re}$  is expressed as  $c_{ij}^{Re}$  (and with  $c_{ij}^{Im}$  considering the imaginary parts). The density function  $\delta_{Sm}$ , based on the dissimilarity between two entries expressed in an exponential form and depending on the user-defined parameter  $r$  that represents the neighbouring radius, is formulated as

$$\delta_{Sm} = \sum_{m=1}^M e^{-\left(\frac{(1-c_{im}^{Re})^2 + (1-c_{im}^{Im})^2}{(r/2)^2}\right)}. \quad (9)$$

The *Jaccard similarity* between two sets is generally defined as the ratio of the intersection over the union of the two sets. For two datasets formed by the same number of discrete points, the Jaccard distance is:

$$d_J(\Psi_i, \Psi_j) = 1 - \frac{\sum_{t=1}^T \min\{\Psi_{it}, \Psi_{jt}\}}{\sum_{t=1}^T \max\{\Psi_{it}, \Psi_{jt}\}}. \quad (10)$$

- 4) Metrics that exploit *global information* on the dataset. In general, when it is acceptable to compare two time series without taking into account the relationships between the instants of time, by observing only the global behaviour, it is possible to define metrics based on the probabilistic distribution of the data belonging to the time series. Both probability density functions and cumulative distribution functions can be constructed. In these cases, the connection with time is completely lost, and only the distribution of the amplitudes is relevant. This kind of metrics have not been used in the cases discussed in this paper.

### III. SLOW COHERENCY AND GENERATOR GROUPING

#### A. Slow coherency

In large power systems, a distinction is made between slow dynamics (due to low frequency oscillations between groups of coherent generators) and fast dynamics (with oscillations at higher frequencies that occur among the generators of the same group). *Slow coherency* is then considered when the oscillatory frequency varies in an indicative range from 0.1 to 0.8 Hz [6], while the transient dynamics of the system are not considered by the slow coherency theory. In [20] slow coherency is associated to the weak coupling among coherent areas, due to low connection or high impedance of the lines among coherent areas, or transmission lines with heavy load. Moreover, in the present systems with distributed generator and load dynamics, the causes of disturbances are increasing with respect to the classical power system supplied by large synchronous generators [21, 22]. Hence, the use of a model-based approach that incorporates all the variables needed becomes more and more challenging. This increases the interest towards exploiting measurement-based (data-driven) approaches.

The rotor angle gives a direct information on the machine dynamics [23]. The speed deviation of generators represents the energy absorbed or delivered by the generator [24]. Particularly relevant are the quantities that can be measured by using data taken from PMUs. A PMU installed at the generator terminals can provide positive sequence voltage measurements. However, the rotor angle cannot be measured directly nor estimated accurately with a PMU [6]. Hence, the rotor angles can be used in model-based approaches, in which they can be calculated by simulations, while for a data-driven approach it could be needed to find other variables.

The calculation of dynamic equivalents based on coherency by considering a model-based approach, in which the relevant variables are the voltage phase angles at the generator terminal nodes or at the generator internal nodes, is described in [25]. In this respect, two generator nodes are defined as coherent if the angular difference of their voltages does not exceed a certain tolerance over a given time interval. The corresponding automatic formation of dynamic equivalents is addressed in [26].

The identification of coherent generators enables the grouping of coherent terminal buses, which is at the basis of numerical procedures for power system model reduction in the model-based approach. In these procedures, after the determination of the coherent generator groups, the network is partitioned into an internal area (in which detailed modelling is desired) and in an external area (the rest of the network, where resorting to reduced modelling is of interest) [14, 27]. In the external area, each coherent generator group is aggregated by maintaining an equivalent generator, and the nodes in that area are reduced by using suitable techniques to form equivalent circuits [28].

### B. Slow coherency-based clustering algorithms for generator grouping

Following the above concepts, the application of clustering algorithms has become a viable way to form groups of generators characterised by slow coherency. In [25], a greedy clustering algorithm (i.e., an algorithm that makes direct choices at each step, following a predefined strategy) is applied to the terminal voltage angles (voltage swing curves). Starting from a reference generator, another generator is compared with it by calculating whether all terminal voltage angle variations in a given time interval do not differ more than a certain threshold from the terminal voltage angle variations at the reference generator. If this happens, the new generator is added to the same cluster of the reference generator, otherwise it becomes the reference generator of a new cluster. The process continues until all generators have been compared with the reference generators of the existing clusters. A successive check is made on the coherency of the generator internal bus voltages, looking for possible reallocations among the clusters. This contribution is based on the simulation of the power system by using a simplified linear model. With the evolution of the computational speed and resources, more contributions emerged to carry out calculations considering non-linear models or data-driven machine learning approaches.

Table I shows the features, the notions of distance, the clustering algorithms adopted, and additional notes on contributions presented in a number of selected publications. The main concepts that emerge from these applications are discussed in the next sections.

## IV. FEATURE SELECTION

The feature selection stage has the objective to form a matrix with dimensions  $(M, H)$ , where  $M$  is the number of generators, and  $H$  is the number of features. A plurality of features has been used in the literature. The various contributions have used the features directly coming from actual or simulated data or have created customised features by including specific knowledge about slow coherency.

The rotor angle and speed of the generators are the most used features, especially in the model-based approach in which all variables can be assumed to be available. In these approaches, the solution method for computing the variables of interest is based on simulations, assuming full observability by the measurements that could be provided by PMUs [29, 30]. In addition, the time window with which the data are available is long enough to represent the slow oscillations of the generators, and the data resolution inside the time window is appropriate. In general, PMUs cannot record the rotor angles and speeds of the synchronous generators. In some solutions the data on rotor angles and speeds are reconstructed from theoretical calculations based on electrical measurements [31, 32]. In [6] it is assumed that the generator terminal frequency is available from PMUs installed at each generator terminal

node. Higher frequency components are suppressed by using digital low-pass filtering with 0.8 Hz band. The time window is different in the case of normal operation and of the occurrence of transient phenomena due to topology variations or contingencies. In the presence of transient events, pre-event data are separated from post-event data. For the definition of the features to be used in the clustering algorithm, the distances among pairs of generators are calculated by using the cosine distance and the Minkowski distance. Then, the generator distance feature is formed by computing the weighted combination of the squared normalised distance matrices formed by the cosine and Minkowski metrics, taking user-defined weights.

Considering the variations of voltage angle  $\Delta\theta_{mt}$ , radian frequency  $\Delta\omega_{mt}$  and voltage magnitude with respect to equilibrium conditions of the power system [33], for the generator  $m = 1, \dots, M$  at discrete points in time  $t = 1, \dots, T$ , the root-mean square coherency criteria [34] can be written, concerning voltage angle and radian frequency, as:

$$\alpha_{ij} = \sqrt{\frac{1}{T} \sum_{t=1}^T \left( |\Delta\theta_{it} - \Delta\theta_{jt}|^2 + |\Delta\omega_{it} - \Delta\omega_{jt}|^2 \right)}. \quad (11)$$

and for voltage magnitudes, as:

$$\beta_{ij} = \sqrt{\frac{1}{T} \sum_{t=1}^T |\Delta V_{it} - \Delta V_{jt}|^2}. \quad (12)$$

On these bases, it is possible to form the coherency matrices  $\mathbf{A} = \{\alpha_{ij}\}$  for angles and  $\mathbf{B} = \{\beta_{ij}\}$  for voltages [35].

When the evolution in time of the rotor angles and speeds are available, a classical way to address dynamic problems is to convert the variables with respect to the Centre of Inertia (COI). In this case, the COI is conceptually considered as an infinite bus and is taken as the reference for rotor angle and speed variations. By considering the constant of inertia  $H_m$ , the rotor angle  $\delta_{mt}$  and the rotor speed  $\omega_{mt}$  for the generator  $m = 1, \dots, M$  at time  $t$ , the corresponding quantities reported to the COI are:

$$\delta_{mt}^{(COI)} = \delta_{mt} - \frac{\sum_{m=1}^M H_m \delta_{mt}}{\sum_{m=1}^M H_m}, \quad (13)$$

$$\omega_{mt}^{(COI)} = \omega_{mt} - \frac{\sum_{m=1}^M H_m \omega_{mt}}{\sum_{m=1}^M H_m}, \quad (14)$$

Since the evolution in time of the rotor angle and speed has a different starting point after the occurrence of an event, rotor angles and speeds have been further elaborated in [21] by calculating the differences with respect to the first instant of interest ( $t = 1$ ):

$$\hat{\delta}_{mt}^{(COI)} = \delta_{mt}^{(COI)} - \delta_{m1}^{(COI)}, \quad (15)$$

$$\hat{\omega}_{mt}^{(COI)} = \omega_{mt}^{(COI)} - \omega_{m1}^{(COI)}. \quad (16)$$

The evolution of these new variables starts from the same point and allow easier application of Jaccard similarity principles (10), based on the definition of areas calculated on the basis of the trajectories to be compared. This pre-processing step is rarely carried out. It seems promising for comparing the evolution of the time series that have different initial values, e.g., when the distances considered do not include explicit information about correlations. In addition, the initial difference has a negative impact on methods that use Euclidean distances between the time series [36]. However, if the initial difference is caused by far location of the generators, while the type of generator indicates similar behaviour, it has to be verified whether the connection point is relevant for establishing reduced dynamic models.

The centre of inertia frequency deviation (COIFD) is defined in [37] by considering the vector that contains the average frequency deviation for the group of  $M_g$  generators that belong to a coherent group  $g$ :

$$\Delta f_g^{(COIFD)} = \frac{\sum_{m=1}^{M_g} \Delta f_{gm}}{M_g}. \quad (17)$$

Considering voltages, a relevant quantity is the voltage angle  $\theta^{(COA)}$  of the Centre of Angle (COA), calculated by considering the constant of inertia  $H_m$  and the voltage angle  $\theta_m$  of the generator  $m = 1, \dots, M$ :

$$\theta^{(COA)} = \frac{\sum_{m=1}^M H_m \theta_m}{\sum_{m=1}^M H_m}. \quad (18)$$

Once defined, the COA is taken as the angle reference [15]. The difference between the voltage phase angle  $\theta_m$  of the  $m^{\text{th}}$  generator and the angle  $\theta^{(COA)}$  gives the angle variation at each individual generator  $m = 1, \dots, M$ , denoted as:

$$\delta_m = \theta_m - \theta^{(COA)}. \quad (19)$$

The principal component analysis (PCA) has been used in [38] to reduce the number of features from a dynamic model in which the rotor angles and speeds of the generators are taken as input variables. Results have been presented for simulations carried out on a system with 244 generators. The application of PCA to identify the first three principal components of generator speed and node voltage angles was suggested in [39], where some results were provided on a 16-machine 68-bus test system in the form of scattered data plots, without executing a clustering algorithm.

In [40] the extraction of the principal components of the rotor angles is enhanced by using the projection pursuit theory, with which optimal projection directions are identified and the signs of the entries of the projection direction vector are considered to assess the coherency of the generators. In particular, the generators for which the same combination of signs is found in all dominant

projection directions are grouped together.

A dynamic coupling-based criterion taken from [41] is used in [30] to define the following similarity function between generators:

$$\xi_{ij} = \left( \frac{1}{H_i} + \frac{1}{H_j} \right) E_i E_j B_{ij} \cos(\delta_{ij0}), \quad (20)$$

where, for the generators  $i$  and  $j$ ,  $H_i$  and  $H_j$  are the inertia constants,  $E_i$  and  $E_j$  are the internal node voltages,  $\delta_{ij0}$  is the relative voltage angle, and  $B_{ij}$  is the imaginary part of the bus admittance entry. The similarity values are then included in the matrix  $\Xi = \{\xi_{ij}\}$  and are used to form the diagonal

matrix  $\mathbf{G}_\xi$  with entries  $g_{im} = \sum_{m=1}^M \xi_{im}$ . A normalised Laplacian matrix is then formed as the positive semi-definite matrix

$$\mathbf{L}_\xi = \mathbf{G}_\xi^{-1/2} (\mathbf{\Xi} - \mathbf{G}_\xi) \mathbf{G}_\xi^{-1/2}. \quad (21)$$

and its entries are used to calculate a matrix of Euclidean distances. This matrix is then processed with a method based on Kernel Principal Component Analysis (KPCA), to obtain the features embedded into a Euclidean space, which are used in the clustering algorithm. The embedding strategy used has the advantage to allow the incorporation of non-Euclidean distance measures in the clustering procedure. KPCA is also used in [21] to create a similarity matrix by using the eight outcomes obtained from the calculation of four indices (based on Euclidean distance, Fréchet distance, cosine similarity and Jaccard similarity) on the variables (15) and (16), taking the correlations among these indices as weights. Spectral independent component analysis (ICA) is applied to form a set of features starting from the generator speeds and node voltage angles in the data-driven technique presented in [42], without following with a clustering algorithm. ICA has been used to overcome the drawbacks of PCA, which linear-type decomposition is considered to be insufficient for grouping the coherent generators on the basis of the measured data [42].

Ten similarity indices are calculated in [32], constructed on the basis of characteristic indicators defined for the angle trajectories in the COI coordinate, such as the dissimilarity of amplitude deviation, location deviation, corner deviation, swing direction, and correlation of the trajectories. Then, multicriteria decision-making principles are used to synthesise a single similarity matrix  $\Gamma$  to send to the clustering algorithm. For this purpose, starting from the entries of the  $q^{\text{th}}$  index normalised similarity matrix  $\Gamma_q$ , the similarity matrix  $\Gamma$  is obtained as

$$\Gamma = \sum_{q=1}^Q c_q \Gamma_q, \quad (22)$$

Where  $c_q$  is the normalised weight coefficient determined from the combination of two coefficients (the Gini coefficient and the Kendall rank correlation coefficient), such that  $\sum_{q=1}^Q c_q = 1$ . In particular, the Gini

coefficient measures the inequality among the indices, while the Kendall rank correlation coefficient measures the correlations. The exploitation of multiple indicators is also addressed in [18], where a multi-indicator panel data is constructed by considering, for each generator  $m = 1, \dots, M$ , the amplitude of the voltage at the generator terminal, the increment of the rotor kinetic energy (with respect to the initial instant  $t_0$ ), and the voltage phase angle variation  $\Delta\delta_{m_t}$  at time  $t$  with respect to the voltage phase angle  $\delta_{m_{t_0}}$  at the initial instant  $t_0$ :

$$\Delta\delta_{m_t} = \delta_{m_t} - \delta_{m_{t_0}}. \quad (23)$$

Another aspect included in [18] is the use of a monotonically decreasing function of time to weight the variables considered, in such a way that the importance of the variable decreases during time.

In some contributions, the Fourier coefficients of the generator speed deviations are determined through the Discrete Fourier transform (DFT) [15]. The rationale of using the DFT is that in normal operating conditions the rotor speed deviations of the generators are null, and after a disturbance there are oscillations that introduce non-zero frequency components (in amplitude and phase) of the rotor speed deviations with respect to the fundamental speed, from which it is possible to recognise the coherent behaviour of some groups of generators. In [15], the features constructed are the DFT coefficients (in amplitude and phase) of the angle variation at each individual generator with respect to the COA. Positive or negative variations of the phase spectrum components determined from the DFT are taken to identify possible generator groups, without explicitly indicating a clustering algorithm. Another use of the evolution of the voltage phase angle variations is to consider the correlations between the real parts and the imaginary parts of the frequencies, found from the DFT, of the velocity variation of the voltage phasors [19]. These correlations are calculated individually, and the cosine distances obtained from these correlations are then summed up in the Euclidean way.

The Discrete Cosine Stockwell Transform is used in [22] to transform the data taken from generator speed and frequency into data in the time-frequency domain. The features are prepared by defining a feature matrix with five indicators: cumulative energy of spectral difference, relative spectral flatness, relative spectral flux, relative spectral coherence, and relative linear correlation. The feature matrix is then subject to min-max normalisation before sending it to the clustering procedure. Wavelet-based coefficients have been used as features in [36], where the dominant frequency components of the generator rotor angles are identified, and the difference in their instantaneous phase is included in a phase difference matrix, which is used as input data for clustering. Features defined in the Taylor-Fourier subspace [43] are used in [44], with the possibility of constructing band-pass filters with different window lengths.

Simulated samples of the generator frequency, extracted with time window 0.25 s and sampling time 100 ms, are used in [45] to form the input data matrix. The data matrix dimension is then reduced by using the Singular Value Decomposition (SVD), and the reduced data are then sent to the clustering process.

The definition of the coherent generator groups could depend on the specific event considered, even though the identification of an overall coherency could be useful. For this purpose, in [34] multiple disturbances and weighted scenarios are considered, calculating the overall coherency matrix as the expected value of the coherency matrices formed with the coefficients  $\alpha_{ij}$  from Equation (11) or  $\beta_{ij}$  from Equation (12), determined by applying the same set of disturbances to randomly selected operating conditions. Likewise, in [46] an equivalent rotor speed deviation is determined by considering multiple events and calculating the weighted sum of the generator rotor speed deviations, assuming the active power of the generator as the weighting factor.

Further coherency indices have been defined by using specific data, such as:

- the average angular speed deviation of generators  $i$  and  $j$  [47]:

$$\chi_{\omega ij} = f_0 \max\{|\Delta\omega_i(t) - \Delta\omega_j(t)|\}; \quad (24)$$

- the similarity measure between generators  $i$  and  $j$  [29, 48]:

$$\chi_{Mij} = 1 - \frac{d_M^{(1)}(\Psi_i, \Psi_j)}{\max_{i,j} \left\{ \max_{i,j} \left\{ d_M^{(1)}(\Psi_i, \Psi_j) \right\} \right\}}. \quad (25)$$

A key point in the identification of the data to be used to form the features is the possible incorporation of information on the network topology. In principle, in the analysis of a network-based problem, a mere comparison among time series, without considering additional information referring to the network connections, could provide groupings in which some generators located into different portions of the network could be included in the same cluster. However, the nature itself of the power system dynamics tends to create groups in which similar types of generators located in a zone close to the large disturbance tend to have a coherent response, while the same type of generators located far from the area tend to have another response. These concepts are discussed in [49] with an algebraic characterisation of coherency, indicating that a generator with small inertia located far from a disturbance could be coherent with a generator with larger inertia but closer to the disturbance. This result also clarifies that using only the electrical distance for determining the coherency is not sufficient. These aspects are also discussed in [50], indicating that for each fault the coherent generators are not always electrically close. Hence, even though the role of the network can remain “hidden”, it is significant also when only the time series are analysed. This aspect may be helpful to justify the use of data-driven approaches for

Table 1. Characteristics of Selected Clustering Algorithms for Slow Coherency-based Generator Grouping.

Reference	Features	Distance	Algorithm	Notes
Agrawal & Thukaram (2013) [29]	Generator rotor measurement (angle or speed), simulated	Similarity measure $\chi_{Mij}$ between generators $i$ and $j$	SVC	Initial number of clusters not required. Specific clustering validity ratio for SVC and statistical assessment.
Alsafih & Dunn (2010) [46]	Equivalent rotor speed deviation, simulated	Euclidean	Hierarchical (average linkage)	Multiple events are weighted to define the equivalent rotor speed deviation.
Babaei <i>et al.</i> (2019) [30]	Components of a distance matrix calculated from the simulated generator rotor angles and voltages	Euclidean, based on an embedding strategy to incorporate non-Euclidean distance measures	SVC	Initial number of clusters not required. Total number of iterations reduced. Cluster validity measure defined based on the cluster compactness and separation between clusters.
Barocio <i>et al.</i> (2019) [45]	Generator frequency samples, simulated, reduced by SVD	Euclidean	kmeans	New concept based on clustering slopes. Simple global measure for stability condition.
Chen <i>et al.</i> (2019) [18]	Weighted distance matrix from a multi-indicator panel of simulated data (generator terminal voltage amplitude, increment of the rotor kinetic energy, and voltage phase angle variation with respect to the first instant, weighted with respect to time and indicators)	Weighted distance function with three indicators (horizontal absolute value, rate of change at adjacent time points, and coefficient of variation between two generators)	Hierarchical (Ward linkage criterion)	DBI for determining the number of clusters.
Joo <i>et al.</i> (2001) [52]	Modal responses of the generators from a linearised system model, simulated	Euclidean	kmeans	Calculation of centroids for each cluster.
Kamwa <i>et al.</i> (2007) [34]	Coherency matrix, calculated from simulated phase angle and radian frequency variation signals at the relevant nodes	Euclidean	Fuzzy c-medoids	Medoids are real time series.
Khalil & Irvani (2016) [37]	Simulated frequency deviations, with respect to the system rated frequency, at generator and non-generator nodes	Coherency coefficient (cosine similarity)	Threshold-based DCD	Initial number of clusters not required. Non-generator buses are associated with generator groups, forming electrical areas. Suitable for online applications.
Lin <i>et al.</i> (2018) [21]	Similarity matrix formed through KPCA, based on four indices defined from generator rotor angles and speeds, reported to the COI	Four indices: - Euclidean distance - Fréchet distance - Cosine similarity - Jaccard similarity Correlations among the indices are used as weights in KPCA	Affinity propagation	Initial number of clusters not required.
Lin <i>et al.</i> (2018) [32]	Generator rotor angles and speeds, recorded or simulated	Ten indices, integrated through a decision-making method based on the Gini and Kendall rank correlation coefficients	Spectral	Initial number of clusters not required. Average silhouette index used for determining the best number of clusters.

the creation of the generator groups, in which network data and modelling of generators and their control systems are not needed [51]. Refined versions of these methods will be useful for online applications.

## V. CLUSTERING ALGORITHMS

### A. Clustering algorithms for coherency-based generator or node grouping

In general, a clustering algorithm is applied starting

from the matrix of features with dimensions  $(M, H)$ , to form an output vector of dimensions  $(M, 1)$  in which each entry contains the number of the cluster to which the generator  $m = 1, \dots, M$  has been assigned.

Different clustering algorithms have been used in the literature. Most papers have implemented classical versions of known clustering algorithms, including new algorithms that have become available during time. In general, the authors have tried to get benefits from the advances of

Table 1 (continued). Characteristics of selected clustering algorithms for slow coherency-based generator grouping.

Reference	Features	Distance	Algorithm	Notes
Mei <i>et al.</i> (2008) [53]	Simulated generator rotor angle speeds	WSSE, considering the distance from each cluster element to the centroid, with inertia of the generator as the weight factor	Hierarchical (Ward linkage criterion)	
Nagic <i>et al.</i> (2020) [6]	Simulated frequency values at generator nodes, used to form a generator distance (weighted combination of the squared normalised distance matrices with cosine and Minkowski metrics, and user-defined weights)	Max-product algorithm	Affinity propagation	Initial number of clusters not required. Hardware in-the-loop implementation.
Rezaeian <i>et al.</i> (2018) [19]	Simulated frequency components existing in the angular velocity variation of voltage phasors, in the range of interarea and local oscillation modes	Euclidean sum of the correlations between the real parts and the imaginary parts of the features	Subtractive clustering	Initial number of clusters not required. Coherency assessed in two dimensions (real and imaginary parts).
Singh & Fozdar (2019) [36]	Rotor angles of the generators, used to form a phase difference matrix based on the outcomes of the complex wavelet transform	Euclidean	DBSCAN	Determines the instantaneous phase difference between rotor angles using the complex wavelet transform.
Tyuryukanov <i>et al.</i> (2021) [54]	Normalised eigenvectors of a matrix obtained from the second-order electromechanical model with neglected damping, simulated	Normalised graph cuts	Spectral clustering and classical coherency	Initial number of clusters not required. Model improvement for the second-order model of aggregated generators, to reduce the stiffening effect.
Wilfert <i>et al.</i> (2001) [38]	Simulated time responses of the rotor motions	Membership of the generators with their clusters, based on normalised principal components	Self-organising maps	
Yadav <i>et al.</i> (2019) [22]	Min-max normalised feature matrix with five indicators: cumulative energy of spectral difference, relative spectral flatness, relative spectral flux, relative spectral coherence, and relative linear correlation	Least mean	Mean shift spectral clustering	Useful for data-driven application, independent of changes in system structure and operating conditions.

the state of the art, trying to discover clustering algorithms most suitable for the structure of the problem with data available as time series. In a few cases (e.g., [37] and [54]), the proposed versions include some characteristics of the technical problem in the solution technique.

A classical distinguishing aspect among the clustering algorithms is the need for setting up the number of clusters as an input. In this respect, with reference to the selected contributions shown in Table I:

- The number of clusters has to be preliminarily defined in many classical methods, such as *kmeans* [55], hierarchical clustering [18, 46, 53], and fuzzy *c-medoids* [34].
- Methods that do not require the preliminary definition of the number of clusters include non-parametric clustering methods, such as support vector clustering [29, 30], the mean shift spectral clustering [22], the affinity propagation clustering versions [6, 21], the spectral clustering versions [32, 54], the threshold-based clustering [37], the subtractive clustering [19],

and the density-based spatial clustering of applications with noise (DBSCAN) [36].

Another typical distinction among clustering methods is based on their ability to isolate uncommon behaviours as *outliers*. The following cases can be identified, where the first two cases represent extreme situations:

- a) Methods that tend to isolate the outliers into small groups and to merge all the other cases into one or a few clusters. These methods have not been exploited for slow coherency studies.
- b) Methods that tend to create relatively uniform groups, in which the outliers are aggregated inside one of the groups.
- c) Methods in which the outliers are identified and singled out during the clustering process.

The situation b) may occur for clustering methods such as *kmeans*, *k-medoids* and their fuzzy logic-based versions, which tend to create a group that includes the

outliers. The classical kmeans clustering algorithm [56] is used in [52] to determine the groups of generators and calculate the centroids on the basis of an input vector that contains the modal responses of the generators taken from a linearised system model. Furthermore, kmeans is used in [45] in conjunction with the SVD, taking into account the acceleration and deceleration of the synchronous machines. The kmeans method is probabilistic and needs the initialisation of the centroids based on random numbers (or other specific criteria), so that multiple executions should be carried out to obtain a statistically significant analysis of the results. The *k-harmonic means* clustering used in [57] and [58] has been formulated to be non-sensitive to the initialisation of the centroids. The *fuzzy c-means* (FCM) algorithm [59] has been applied in [60]. The interest towards a fuzzy logic-based approach is the possibility of defining the degree of membership with which one generator belongs to different clusters. This is appropriate for interconnected power systems in which there are connections among the nodes that result in stronger or weaker coupling among the generators [34]. However, also FCM depends on some randomness in the initialisation. The subtractive clustering proposed in [19] on the basis of the method formulated in [61] to form the cluster centres can be used a pre-processing step to avoid the dependence on random initialisation. Medoid-based clustering algorithms (e.g., k-medoids and fuzzy c-medoids) are preferable to their centroid-based counterparts (kmeans and FCM), because the centroid is a fictitious output and does not represent any of the actual generators or nodes [34]. Conversely, the medoid gives by definition one of the actual generators or nodes per group, which can be taken as the representative element of the group. For this reason, the *fuzzy c-medoids* (FCMdd) algorithm developed in [62] has been used in [34], where the medoids are initialised by using the sequential PMU placement technique described in [35]. The concept of partitioning around medoids has also been used in [63], where the initial medoids are determined taking into account also information on the nodes to which the generators are connected and on the control systems of the generators.

Other clustering algorithms provide more balanced solutions, in which some outliers can be recognised, while the other generators are located into an appropriate number of clusters. Specific notes are indicated below.

*DBSCAN* [64] is a density-based method that defines the neighbourhood with a maximum radius and creates groups with a minimum number of points in the neighbourhood. DBSCAN is a deterministic algorithm, in which the number of groups is not fixed a priori. In [36], DBSCAN is applied by considering a phase difference matrix determined from the results of the complex wavelet transform (also considered in [65]). Because of these thresholds, some generators could not be included in any group and are considered as outliers.

*Self-organising maps* (SOM) [66] have been used in

[38] with the use of normalised principal components, and [67] with PCA-based features. The maximum number of clusters is given by the dimension of the map. For a two-dimensional SOM, the output has to be post-processed to identify the groups (e.g., with the kmeans algorithm). A one-dimensional self-organising map can be used if the number of clusters is relatively small (e.g., lower than 6 or 7) to avoid post-processing.

The *affinity propagation* clustering [68] requires in input a similarity matrix, and there is no need to specify the number of groups a priori. It has been used in [21] with a similarity matrix formed through KPCA, composed of four indices, whose correlations have been used as weights in KPCA. It has also been used in [6] to select the post-event measurements and identify groups of slow coherent generators after the occurrence of a disturbance, by using a max-product algorithm. Outliers are included into specific clusters.

In *subtractive* clustering [19], the cluster centres are selected on the basis of the density function  $\delta_{sm}$  from Equation (9), where the index  $m$  is extended to all the system nodes. The first cluster centre (centroid) is chosen on the basis of the highest density. The effect of the first centroid is then removed from the other nodes through a subtraction process. The procedure is continued to find the next centroids, until the stop criterion based on the ratio between the density at the current step and the density at the first step is satisfied.

*Hierarchical* clustering [69] is another typical algorithm, which can be used in the agglomerative or divisive version. In the agglomerative case, initially all nodes are taken as independent clusters, a distance metric is used, and the clusters with the lowest distance are progressively merged, until the user-defined number of clusters is reached. In the divisive version there is initially a single cluster, which is partitioned into two clusters by considering the relevant metric, then successive partitions are created until reaching the user-defined number of clusters. All contributions that use the hierarchical clustering have chosen the agglomerative version. The distances are defined by using the linkage criterion, with different solutions. The single linkage (based on the distance between the closest components of pairs of clusters) is used in [70], the average linkage (based on the average distances among the components of pairs of clusters) in [46], the complete linkage (based on the distance between the farthest components of pairs of clusters) in [71], which also considers unstable rotor angle trajectories, and the centroid linkage (based on the distances among the centroids) in [44]. The Ward linkage criterion [72] is used in [53], with the customised option of using the total inertia of the generators during the update of the dissimilarity matrix. In [73] the distance used to decide which pairs of clusters have to be merged is replaced by the dissimilarity coefficient constructed on the basis of ten normalised indicators.

*Support vector clustering* (SVC) [74] is a non-parametric clustering method that does not need to define the number of clusters a priori. It is able to find suitable clusters of arbitrary shape by determining boundaries of any type. The SVC procedure includes two steps, namely, (i) the mapping of the data points into a higher-dimensional vector space, with the identification of a number of support vectors that depend on a user-defined parameter, and (ii) the formation of the clusters by considering the support vectors to define the cluster boundaries. In [29] the SVC is applied by considering a non-Euclidean distance measure  $\chi_{Mij}$  between the generators  $i$  and  $j$ . The SVC is also applied in [55], where an embedding strategy is developed for making it possible to deal with non-Euclidean distance measures.

The *spectral clustering* algorithm [75] has gained interest in recent years in power system applications [76], also because it is possible to include user-defined similarities [77]. For this purpose, it is applied in [21] to a feature set that includes ten similarity indices. The spectral clustering is based on the definition of nodes in a connected graph, in which the branches are assigned suitable weights. For slow coherency studies, the generators are associated with the nodes, and the dissimilarity among the time series referring to appropriate variables referring to the dynamic behaviour (e.g., rotor angles and speeds) are considered as weights. The average silhouette index is used to assess the most appropriate number of clusters. The mean shift spectral clustering is used in [22] in a data-driven approach in which inertia is not used in the input dataset. Because of this, the method is suitable to deal with the intermittent variations in the renewable energy sources and is not affected by the changes of inertia due to the diffusion of converter-interfaced generators.

The threshold-based *dynamic coherency determination* (DCD) procedure presented in [37] includes two steps. In the first step the generators are partitioned into groups by imposing a minimum threshold on the cosine similarity, and the COIFD is calculated for each group. In the second step the threshold is relaxed to merge pairs of groups, recalculating the COIFD for the new groups as the weighted mean of the COIFD values of the two groups, using the number of generators as the weighting factor. Then, non-generator buses are associated to the groups formed on the basis of the cosine similarity between each bus and the groups formed, assuming full observability at the non-generator nodes. The DCD is extended in [78] by taking into account the impact of wind generators, highlighting how the coherent groups can change because of the presence of wind power plants.

#### B. New findings for enhancing model-based approaches

Close relations between the notion of slow coherency and the use of normalised graph cuts have been shown in [54]. Starting from the second-order electromechanical

model with neglected damping, the matrix that contains the synchronising torque coefficients between the generators is simplified by neglecting the components associated with the transfer conductances. In this way, the resulting matrix denoted as  $\mathbf{K}^B$  has the structure of a negated graph Laplacian matrix. Moreover, the scaled inertias of the generators are considered as weight factors and are included in a diagonal matrix called  $\mathbf{M}$ . By using these two matrices, it is shown that the solution of minimising the normalised graph cuts with relaxed constraints is equal to the negated sum of the  $K$  eigenvalues of  $\mathbf{M}^{-1}\mathbf{K}^B$  with smallest magnitude, where  $K$  is the number of groups formed, and the groups are determined on the basis of the corresponding eigenvectors. On these bases, a customised spectral clustering algorithm is developed, together with a refined algorithm for aggregating the generators belonging to the same group. The results shown indicate further improvements in the accuracy of model-based approaches based on the calculation of eigenvectors for dynamic model reduction, leading to renewing the interest towards these approaches.

Probabilistic clustering is a challenging perspective that is emerging to deal with the uncertain nature of the power output from wind generators. The identification of common characteristics for wind generators has been handled in [79] by using probabilistic clustering based on SVC, and in [80] by applying a practical four-machine wind turbine clustering method. In the presence of the sources of uncertainty in the power system operation, probabilistic methods associated with clustering techniques may provide more insights on the creation of the generator groups, also with the possible identification of critical generators [81]. The computational burden of the probabilistic power system dynamics analysis is still high, making the computations suitable for offline analysis. In addition, the power system models used have to be very detailed. The probabilistic assessment of multiple operational scenarios may provide more detailed information on the creation of the generator groups, in line with future developments towards probabilistic stability studies [82].

## VI. COMPARISONS AMONG CLUSTERING ALGORITHMS FOR GENERATOR GROUPING

Wide comparisons among the solution methods are not generally easy to be carried out. For clustering applications, the network to be used should be large enough and include enough generators to create a significant number of groups. Some IEEE test systems (e.g., the IEEE 68-bus 16-machine power system [83]) provide significant benchmarks, needed in model-based approaches to reproduce the results on the same network, using the same type of model of the synchronous machines, and with the testing carried out on the same contingency. In some cases, the authors have reimplemented the algorithms proposed in the selected reference methods. For data-driven approaches, the situation may become more complex because of data

property issues. Data management by large international organisations opens the possibility of carrying out extended applications to real cases [13].

Considering the selected methods reported in Table 1, different types of comparison have been carried out, as summarised below by considering the progressive year of publication of the related papers.

The earliest example considered here is the successful comparison reported in [34] for the use of FCMdd with respect to the FCM used in [60], also confirmed in [84] for a real system with 160 generators. For the hierarchical clustering described in [53] there is just a qualitative comparison with real data. Another hierarchical clustering algorithm proposed in [46] provides the same results of the calculation of eigenvalues and eigenvectors for the linearised model on a 16-machine system. The authors conclude that their proposed method has the advantage of its applicability to a wide-area measurement system, also considering the effects of the occurrence of different events on the clustering results. A more extended comparison is provided in [29], where the proposed SVC method is compared with kmeans [52], FCM [48], hierarchical (average and Ward linkages) [53, 70]. The comparison is carried out by using the cluster validity indicators Davies–Bouldin index (DBI) [85], silhouette coefficient [86] and Xie-Beni index [87], as well as the minimum average absolute angle difference over all the coherent groups. The results consistently show that the SVC method provides the best results, followed by the hierarchical method with average linkage criterion. The DCD method introduced in [37] exhibits a lower computation burden as compared to other measurements-based methods [42] by using the same system and disturbance.

The spectral clustering method presented in [32] is compared with three methods by using the average silhouette indicator [86], where the compared methods are executed with given parameters. Positive results are reported for the proposed method (with overall better results) and for the methods reported in [40] and [39]. Sensitivity analyses would be needed to perform more detailed verification. In [21] the affinity propagation method is compared with four methods, for three of which ([39, 42], and [40]) and for the proposed method the results are considered acceptable. The proposed method is then considered more appropriate by the authors because of the possibility of using it for online monitoring. The subtractive clustering proposed in [19] is compared with the re-implemented versions of kmeans and FCMdd from [34] on a 16-machine test system. The authors conclude that appropriate setting of the parameters of the subtractive clustering can provide better results.

The discussion in [36] is focused on indicating why DBSCAN is better than kmeans. The weighted clustering of multi-indicator panel data proposed in [18] is compared with other methods such as max-min, kmeans, coherence clustering based on feature extraction of wavelet transform and PCA, and provides better results by considering

the DBI indicator. In [30], the proposed SVC method is compared with FCM [60] and spectral clustering [77] by using the average silhouette indicator [86] and leads to better results, with the advantage that can identify in an automatic way the suitable number of clusters.

More extensive comparisons are carried out in some papers. The clustering algorithm presented in [55] is compared with PCA [39], the determination of Koopman modes [3] and the dynamic mode decomposition (DMD) introduced in [45]. The PCA is unable to provide information on damping, modes and participation factors as given by the Koopman mode and DMD. The proposed clustering method based on SVD and kmeans is able to reduce the dimension of the dataset and requires shorter time windows with respect to Koopman mode and DMD for capturing slow electromechanical modes (about 0.1 Hz). In addition, the proposed method gives information about the slope of the signal. The mean shift spectral clustering from [22] is compared with FCMdd [34], PCA [39], ICA [42], DCD [37], and COI-based affinity propagation [21]. The comparison is conducted with main reference to the behaviour of the methods in intermittency cases due to renewable energy sources. In this case, the information needed for PCA, ICA and COI-based methods are difficult to be obtained or updated in the presence of intermittency, while for FCMdd and DCD the authors indicate the presence of incorrect groupings.

In [6] the results of the proposed affinity propagation method are compared with the reimplemented DCD from [37], with tests carried out for a time interval of 86.6 s with multiple perturbations. The results are presented at different times, showing when the same coherent groups are found from the two methods, and discussing the higher adaptability of the proposed method. In [54] the comparison is conducted more on the modelling side, taking the slow coherency grouping algorithm [88] as the reference. Concerning the generator grouping into areas, some comparisons are carried out with the results shown in [20] and [89], providing some indications concerning the partitions in a small number of groups for a given disturbance.

## VII. CONCLUDING REMARKS

Slow coherency concepts and related applications implemented through clustering algorithms have been reviewed on the basis of historical contributions and recent developments. The topics addressed in this paper have been dedicated to the bulk power system, excluding distribution systems and microgrids, in which the context of dynamic analysis is evolving with the increasing presence of converter-interfaced generation, storage and participation of the demand-side. Different options have been followed by the authors concerning the choice of the features and the clustering algorithms.

In general, the comparisons shown are still too limited to conclude that any clustering method can be more

appropriate than others. Only extended applications to consolidated benchmarks could provide more hints. In any case, it is not expected to find that one clustering algorithm could be consistently superior to others across all test systems and for many sets of disturbances. The definition of specific benchmarks agreed among the scientific community and the definition of shared test procedures are important directions for carrying out further activity, with the possible development of more refined algorithms. The benchmarks themselves need to be upgraded to follow the current evolution of the power systems, where the integration of generation from renewable energy (mainly wind systems) with fluctuating behaviour and the increasing presence of converter-interfaced generation and storage introduce new challenges to the interpretation of the operating conditions. In this respect, also classical model-based approaches need to be revised to incorporate further details in line the evolving context of power systems operations. Some methodological trends include the development of methods based on constrained clustering, correlation-based clustering, and probabilistic clustering.

An insightful direction for future research is to extend data-driven approaches based on real-time measurements, in which the nature of the connections among the data can be constructed by the solver. The efficiency of these approaches will be satisfactory if sufficiently accurate results will be provided with a computational burden consistent with online applications.

## REFERENCES

- [1] G. Chicco, "Data Consistency for Data-Driven Smart Energy Assessment," *Frontiers in Big Data*, 4:683682, 2021, doi: 10.3389/fdata.2021.683682.
- [2] P. Kundur, *Power System Stability and Control*, McGraw-Hill, New York, NY, 1994.
- [3] Y. Susuki and I. Mezic, "Nonlinear Koopman Modes and Coherency Identification of Coupled Swing Dynamics," *IEEE Transactions on Power Systems*, vol. 26, no. 4, pp. 1894–1904, 2011.
- [4] F. Raak, Y. Susuki, and T. Hikihara, "Data-driven partitioning of power networks via Koopman mode analysis," *IEEE Transactions on Power Systems*, vol. 31, no. 4, pp. 2799–2808, Jul. 2016.
- [5] L. Ding, Y. Guo, P. Wall, K. Sun, and V. Terzija, "Identifying the timing of controlled islanding using a controlling UEP based method," *IEEE Transactions on Power Systems*, vol. 33, no. 6, pp. 5913–5922, 2018.
- [6] M. Naglic, M. Popov, M.A.M.M. van der Meijden, and V. Terzija, "Synchronized Measurement Technology Supported Online Generator Slow Coherency Identification and Adaptive Tracking," *IEEE Transactions on Smart Grid*, vol. 11, no. 4, pp. 3405–3417, July 2020.
- [7] J.M. Undrill and A.E. Turner, "Construction of power system electromechanical equivalents by modal analysis," *IEEE Transactions on Power Apparatus and Systems*, vol. PAS-90, no. 5, pp. 2049–2059, 1971.
- [8] J.M. Undrill, J.A. Cassaza, E.M. Gulachenski, and L.K. Kirchmayer, "Electromechanical equivalents for use in power system stability studies," *IEEE Transactions on Power Apparatus and Systems*, vol. PAS-90, no. 5, pp. 2060–2071, 1971.
- [9] A. Chang and M.M. Adibi, "Power System Dynamic Equivalents," *IEEE Transactions on Power Apparatus and Systems*, vol. PAS-89, no. 8, pp. 1737–1744, 1970.
- [10] S.T.Y. Lee and F.C. Schweppe, "Distance measures and coherency recognition for transient stability equivalents," *IEEE Transactions on Power Apparatus and Systems*, vol. PAS-82, pp. 1550–1557, 1973.
- [11] D.J. Trudnowski and J.W. Pierre, "Overview of algorithms for estimating swing modes from measured responses," Proc. IEEE Power Energy Soc. Gen. Meeting, Jul. 2009.
- [12] A. Vahidnia, G. Ledwich, E. Palmer, and A. Ghosh, "Generator coherency and area detection in large power systems," *IET Gener., Transmiss. Distrib.*, vol. 6, no. 9, pp. 874–883, 2012.
- [13] G. Giannuzzi, C. Pisani, and W. Sattinger, "Generator Coherency Analysis in ENTSO-E Continental System: Current Status and Ongoing Developments in Italian and Swiss Case," *IFAC-PapersOnLine*, vol. 49, no. 27, pp. 400–406, 2016.
- [14] R. Singh, M. Elizondo, and S. Lu, "A review of dynamic generator reduction methods for transient stability studies," Proc. IEEE Power & Energy Society General Meeting, 2011.
- [15] Y. Ota, H. Ukai, K. Nakamura, and H. Fujita, "PMU based midterm stability evaluation of wide-area power system," Proc. 2002 IEEE/PES Transmission and Distribution Conference and Exhibition: Asia Pacific, Yokohama, Japan, 6-10 Oct. 2002, vol. 3, pp. 1676–1680.
- [16] T.W. Liao, "Clustering of time series data—A survey," *Pattern Recognition*, vol. 38, pp. 1857–1874, 2005.
- [17] T. Heiter and H. Manilla, "**Computing Discrete Fréchet Distance**," Technical Report CD-TR 94/64, Christian Doppler Laboratory for Expert Systems, Technical University Vienna, Austria, 1994.
- [18] Y. Chen, Z. Zhang, X. Song, J. Liu, M. Hou, G. Li, W. Xu, and J. Ma, "Coherent Clustering Method Based on Weighted Clustering of Multi-Indicator Panel Data," *IEEE Access*, vol. 7, pp. 43462–43472, 2019.
- [19] M.H. Rezaeian, S. Esmaeili, and R. Fadaeinedjad, "Generator coherency and network partitioning for dynamic equivalencing using subtractive clustering algorithm," *IEEE Systems Journal*, vol. 12, no. 4, pp. 3085–3095, Dec. 2018.
- [20] J.H. Chow, "Slow Coherency and Aggregation," in J. Chow (ed.) *Power System Coherency and Model Reduction*, Power Electronics and Power Systems, vol. 94, Springer-Verlag, New York, NY, 2013.
- [21] Z. Lin, F. Wen, Y. Ding, Y. Xue, S. Liu, Y. Zhao, and S. Yi, "WAMS-based coherency detection for situational awareness in power systems with renewables," *IEEE*

- Transactions on Power Systems*, vol. 33, no. 5, pp. 5410–5426, Sep. 2018.
- [22] R. Yadav, A. K. Pradhan, and I. Kamwa, “A Spectrum Similarity Approach for Identifying Coherency Change Patterns in Power System Due to Variability in Renewable Generation,” *IEEE Transactions on Power Systems*, vol. 34, no. 5, pp. 3769–3779, 2019.
- [23] M. Klein, G. J. Rogers, and P. Kundur, “A fundamental study of interarea oscillations in power systems,” *IEEE Transactions on Power Systems*, vol. 6, no. 3, pp. 914–921, Aug. 1991.
- [24] M. Jonsson, M. Begovic, and J. Daalder, “A new method suitable for real-time generator coherency determination,” *IEEE Transactions on Power Systems*, vol. 19(3), pp. 1473–1482, Aug 2004.
- [25] R. Podmore, “Identification of coherent generators for dynamic equivalents,” *IEEE Transactions on Power Apparatus and Systems*, vol. PAS-97, no. 4, pp. 1344–1354, Jul. 1978.
- [26] A.J. Germond and R. Podmore, “Dynamic Aggregation of Generating Unit Models,” *IEEE Transactions on Power Apparatus and Systems*, vol. PAS-97, no. 4, pp. 1060–1069, July 1978.
- [27] J.H. Chow (ed.), *Power System Coherency and Model Reduction*, Power Electronics and Power Systems, vol. 94, Springer-Verlag, New York, NY, 2013.
- [28] J.B. Ward, “Equivalent circuits for power flow studies,” *AIEE Trans. Power Appl. Syst.*, vol. 68, no. 1, pp. 373–382, 1949.
- [29] R. Agrawal and D. Thukaram, “Support vector clustering-based direct coherency identification of generators in a multi-machine power system,” *IET Gener., Transm., Distrib.*, vol. 7, no. 12, p. 1357, 1366, Dec. 2013.
- [30] M. Babaei, S.M. Muyeen, and S. Islam, “Identification of Coherent Generators by Support Vector Clustering with an Embedding Strategy,” *IEEE Access*, vol. 7, pp. 105420–105431, 2019.
- [31] V. Venkatasubramanian and R.G. Kavasseri, “Direct computation of generator internal dynamic states from terminal measurements,” Proc. 37th Annu. Hawaii Int. Conf. System Sciences, January 2004.
- [32] Z. Lin, F. Wen, Y. Ding, and Y. Xue, “Data-driven coherency identification for generators based on spectral clustering,” *IEEE Transactions on Industrial Informatics*, vol. 14, no. 3, pp. 1275–1285, Mar. 2018.
- [33] S. Sastry and P. Varaiya, “Coherency for interconnected power systems,” *IEEE Transactions on Automatic Control*, vol. AC-26, no. 1, pp. 218–226, 1981.
- [34] I. Kamwa, A. K. Pradhan, and G. Joos, “Automatic segmentation of large power systems into fuzzy coherent areas for dynamic vulnerability Assessment,” *IEEE Transactions on Power Systems*, vol. 22, no. 4, pp. 1974–1985, Nov. 2007.
- [35] I. Kamwa and R. Grondin, “PMU configuration for system dynamic performance measurement in large, multiarea power systems,” *IEEE Transactions on Power Systems*, vol. 17, no. 2, pp. 385–394, May 2002.
- [36] A.K. Singh and M. Fozdar, “DBSCAN-based coherency identification of generators using complex wavelet transform,” *The Journal of Engineering*, vol. 2019, no. 18, pp. 4780–4784, 2019.
- [37] A.M. Khalil and R. Iravani, “A dynamic coherency identification method based on frequency deviation signals,” *IEEE Transactions on Power Systems*, vol. 31, no. 3, pp. 1779–1787, May 2016.
- [38] H.H. Wilfert, K. Voigtländer, I. Erlich, “Dynamic coherency identification of generators using self-organising feature maps,” *Control Engineering Practice*, vol. 9, pp. 769–775, 2001.
- [39] K. Anaparthi, B. Chaudhuri, N. Thornhill, and B. C. Pal, “Coherency identification in power systems through principal component analysis,” *IEEE Transactions on Power Systems*, vol. 20, no. 3, pp. 1658–1660, Aug. 2005.
- [40] T. Jiang, H. Jia, H. Yuan, N. Zhou, and F. Li, “Projection pursuit: A general methodology of wide-area coherency detection in bulk power grid,” *IEEE Transactions on Power Systems*, vol. 31, no. 4, pp. 2776–2786, Jul. 2016.
- [41] S.S. Lamba and R. Nath, “Coherency identification by the method of weak coupling,” *International Journal of Electrical Power & Energy Systems*, vol. 7, no. 4, pp. 233–242, 1985.
- [42] M.A.M. Ariff and B.C. Pal, “Coherency identification in interconnected power system—An independent component analysis approach,” *IEEE Transactions on Power Systems*, vol. 28, no. 2, pp. 1747–1755, May 2013.
- [43] J.A. de la O Serna, J.M. Ramirez, A. Zamora Mendez, and M.R.A. Paternina, “Identification of Electromechanical Modes Based on the Digital Taylor-Fourier Transform,” *IEEE Transactions on Power Systems*, vol. 31, no. 1, pp. 206–215, 2016.
- [44] M.R. Arrieta Paternina, A. Zamora-Mendez, J. Ortiz-Bejar, J.H. Chow, and J.M. Ramirez, “Identification of coherent trajectories by modal characteristics and hierarchical agglomerative clustering,” *Electric Power Systems Research*, vol. 158, pp. 170–183, 2018.
- [45] E. Barocio, B.C. Pal, N.F. Thornhill, and A.R. Messina, “A Dynamic Mode Decomposition Framework for Global Power System Oscillation Analysis,” *IEEE Transactions on Power Systems*, vol. 30, no. 6, pp. 2902–2912, 2015.
- [46] H.A. Alsafih and R. Dunn, “Determination of coherent clusters in a multi-machine power system based on wide-area signal measurements,” IEEE Power and Energy Society General Meeting, Minneapolis, MN, USA 2010.
- [47] D.E.T. Hiyama, “Identification of coherent generators using frequency response,” *IEE Proceedings C Generation, Transmission and Distribution*, vol. 128, no. 5, pp. 262 – 268, 1981.
- [48] S.C. Wang and P.H. Huang, “Direct coherency identification of synchronous generators in Taiwan

- power system based on fuzzy c-means clustering,” *IEICE Trans. Fundam. Electron. Commun. Comput. Sci.*, vol. E90A, no. 10, pp. 2223–2231, 2007.
- [49] F. Wu and N. Narasimhamurthi, “Coherency identification for power system dynamic equivalents,” *IEEE Transactions on Circuits and Systems*, vol. 30, no. 3, pp. 140–147, March 1983.
- [50] E.J.S. Pires de Souza, “Identification of coherent generators considering the electrical proximity for drastic dynamic equivalents,” *Electric Power Systems Research*, vol. 78, no. 7, pp. 1169–1174, 2008.
- [51] M.R. Aghamohammadi and S.M. Tabandeh, “A new approach for online coherency identification in power systems based on correlation characteristics of generators rotor oscillations,” *International Journal of Electrical Power & Energy Systems*, vol. 83, pp. 470–484, 2016.
- [52] S.K. Joo, C.C. Liu, and J.W. Choe, “Enhancement of coherency identification techniques for power system dynamic equivalents,” *IEEE Power Eng. Soc. Summer Meet.*, Vancouver, BC, Canada, 2001, 3, pp. 1811–1816.
- [53] K. Mei, S. M. Rovnyak, and C.M. Ong, “Clustering-Based Dynamic Event Location Using Wide-Area Phasor Measurements,” *IEEE Transactions on Power Systems*, vol. 23, no. 2, pp. 673–679, May 2008.
- [54] I. Tyuryukanov, M. Popov, M.A.M.M. Van Der Meijden, and V. Terzija, “Slow Coherency Identification and Power System Dynamic Model Reduction by using Orthogonal Structure of Electromechanical Eigenvectors,” *IEEE Transactions on Power Systems*, vol. 36, no. 2, pp. 1482–1492, 2021.
- [55] E. Barocio, P. Korba, W. Sattinger, and F.R. Segundo Sevilla, “Online coherency identification and stability condition for large interconnected power systems using an unsupervised data mining technique,” *IET Generation, Transmission & Distribution*, vol. 13, no. 15, pp. 3323–3333, 2019.
- [56] J.T. Tou and R.C. Gonzalez, *Pattern Recognition Principles*, Addison-Wesley, 1974.
- [57] K. Tang and G. K. Venayagamoorthy, “Online coherency analysis of synchronous generators in a power system,” *Proc. 2014 IEEE PES Innovative Smart Grid Technologies Conf. (ISGT)*, Feb. 19–22, 2014.
- [58] Y. Wei, P. Arunagirinathan, A. Arzani, and G.K. Venayagamoorthy, “Situational awareness of coherency behavior of synchronous generators in a power system with utility-scale photovoltaics,” *Electric Power Systems Research*, vol. 172, pp. 38–49, 2019.
- [59] J.C. Bezdek, *Pattern Recognition with Fuzzy Objective Function Algorithms*, Plenum Press, New York, 1981.
- [60] S.C. Wang and P.H. Huang, “Fuzzy c-means clustering for power system coherency,” *Proc. Int. Conf. Syst., Man, Cybern., Waikoloa, HI, Oct. 10–12, 2005*, vol. 3, pp. 2850–2855.
- [61] S.L. Chiu, “Fuzzy model identification based on cluster estimation,” *J. Intell. Fuzzy Syst.*, vol. 2, pp. 267–278, 1994.
- [62] R. Krishnapuram, A. Joshi, and O. Nasraoui, “Low-complexity fuzzy relational clustering algorithms for web mining,” *IEEE Transactions on Fuzzy Systems*, vol. 9, no. 4, pp. 595–607, Aug. 2001.
- [63] G. Pyo, J. Park, and S. Moon, “A new method for dynamic reduction of power system using PAM algorithm,” *Proc. IEEE PES General Meeting*, 2010, pp. 1–7.
- [64] M. Ester, H.P. Kriegel, J. Sander, and X. Xu, “A density-based algorithm for discovering clusters in large spatial databases with noise,” *Proc. of the Second International Conference on Knowledge Discovery and Data Mining (KDD-96)*. AAAI Press, pp. 226–231, 1996.
- [65] S. Avdaković, E. Becirović, A. Nuhanović, and M. Kusljugić, “Generator coherency using the wavelet phase difference approach,” *IEEE Transactions on Power Systems*, vol. 29, no. 1, pp. 271–278, Jan. 2014.
- [66] T. Kohonen, *Self-organisation and associative memory*, Springer Verlag, Heidelberg, Germany, 1989.
- [67] B.P. Padhy, S.C. Srivastava, and N.K. Verma, “A coherency-based approach for signal selection for wide area stabilizing control in power systems,” *IEEE Systems Journal*, vol. 7, no. 4, pp. 807–816, 2013.
- [68] B.J. Frey and D. Dueck, “Clustering by passing messages between data points,” *Science*, vol. 315, no. 5814, pp. 972–976, 2007.
- [69] M.R. Anderberg, *Cluster Analysis for Applications*, Academic Press, New York, 1973.
- [70] C. Juarez, A.R. Messina, R. Castellanos, and A.R. Espinosa-Pérez, “Characterization of multi-machine system behavior using a hierarchical trajectory cluster analysis,” *IEEE Transactions on Power Systems*, vol. 26, no. 3, pp. 972–981, 2011.
- [71] T. Guo and J.V. Milanović, “Online identification of power system dynamic signature using PMU measurements and data mining,” *IEEE Transactions on Power Systems*, vol. 31, no. 3, pp. 1760–1768, 2016.
- [72] J.H. Ward, “Hierarchical grouping to optimize an objective function,” *Journal of the American Statistical Association*, vol. 58, no. 301, pp. 235–244, 1963.
- [73] Z. Lin, F. Wen, Y. Ding, and Y. Xue, “Wide-area coherency identification of generators in interconnected power systems with renewables,” *IET Gener., Transmiss. Distrib.*, vol. 11, no. 18, pp. 4444–4455, 2017.
- [74] A. Ben-Hur, D. Horn, H.T. Siegelmann, and V. Vapnik, “Support vector clustering,” *J. Mach. Learning Res.*, vol. 2, pp. 125–137, 2001.
- [75] U. von Luxburg, “A tutorial on spectral clustering,” *Statist. Comput.*, vol. 17, no. 4, pp. 395–416, 2007.
- [76] R.J. Sánchez-García, M. Fennelly, S. Norris, N. Wright, G. Niblo, J. Brodzki, and J.W. Bialek, “Hierarchical Spectral Clustering of Power Grids,” *IEEE Transactions on Power Systems*, vol. 29, no. 5, pp. 2229–2237, 2014.
- [77] A. Thakallapelli, S. J. Hossain, and S. Kamalasan, “Coherency and online signal selection based wide area control of wind integrated power grid,” *IEEE*

*Transactions on Industry Applications*, vol. 54, no. 4, pp. 3712–3722, 2018.

- [78] A.M. Khalil and R. Iravani, “Power system coherency identification under high depth of penetration of wind power,” *IEEE Transactions on Power Systems*, vol. 33, no. 5, pp. 5401–5409, Sep. 2018.
- [79] M. Ali, I. Ilie, J.V. Milanović, and G. Chicco, “Wind Farm Model Aggregation Using Probabilistic Clustering,” *IEEE Transactions on Power Systems*, vol. 28, no. 1, pp. 309–316, 2013.
- [80] P. Wang, Z. Zhang, Q. Huang and W. Lee, “Wind Farm Dynamic Equivalent Modeling Method for Power System Probabilistic Stability Assessment,” *IEEE Transactions on Industry Applications*, vol. 56, no. 3, pp. 2273–2280, 2020.
- [81] P.N. Papadopoulos, T. Guo and J.V. Milanović, “Probabilistic framework for online identification of dynamic behavior of power systems with renewable generation,” *IEEE Transactions on Power Systems*, vol. 33, no. 1, pp. 45–54, Jan. 2018.
- [82] J.V. Milanović, “Probabilistic stability analysis: the way forward for stability analysis of sustainable power systems,” *Phil. Trans. R. Soc. A*, vl. 375, art. 20160296, 2017.
- [83] A.K. Singh and B.C. Pal, Report on the 68-bus, 16-machine, 5-area system. Technical Report. IEEE Power and Energy Society Task Force on Benchmark Systems for Stability Controls, 2013. [http://eioc.pnnl.gov/benchmark/ieeess/NETS68/New\\_England\\_New\\_York\\_68\\_Bus\\_System\\_study\\_report.pdf](http://eioc.pnnl.gov/benchmark/ieeess/NETS68/New_England_New_York_68_Bus_System_study_report.pdf)
- [84] I. Kamwa, A. K. Pradhan, G. Joos, and S.R. Samantaray, “Fuzzy partitioning of a real power system for dynamic vulnerability assessment,” *IEEE Transactions on Power Systems*, vol. 24, no. 3, pp. 1356–1365, Aug. 2009.
- [85] D.L. Davies and D.W. Bouldin, “A cluster separation measure,” *IEEE Trans. Pattern Anal. Mach. Intell.*, vol. PAM-1, no. 2, pp. 224–227, 1979.
- [86] P.J. Rousseeuw, “Silhouettes: A graphical aid to the interpretation and validation of cluster analysis,” *J. Comput. Appl. Math.*, vol. 20, no. 1, pp. 53–65, 1987.
- [87] X.L. Xie and G. Beni, “A validity measure for fuzzy clustering,” *IEEE Trans. Pattern Anal. Mach. Intell.*, 1991, 13, (8), pp. 841–847.
- [88] J.H. Chow, *Time-Scale Modeling of Dynamic Networks with Applications to Power Systems*, Lecture Notes in Control and Information Sciences, vol. 46. Berlin, Germany: Springer-Verlag, 1982.
- [89] J.H. Chow, R. Galarza, P. Accari, and W. W. Price, “Inertial and slow coherency aggregation algorithms for power system dynamic model reduction,” *IEEE Transactions on Power Systems*, vol. 10, no. 2, pp. 680–685, May 1995.



**Gianfranco Chicco** received the Ph.D. degree in Electrotechnics Engineering from Politecnico di Torino (POLITO), Turin, Italy. He is a Full Professor of Electrical Energy Systems at POLITO. His research interests include power system and distribution system analysis and optimization, multi-energy system optimization and planning, electrical load management, data analytics, and artificial intelligence applications to energy systems.

# Generation Structure, Prices, and Tariffs in the Russian Electric Power Industry in 2009-2018

M. Yu. Vasilyev\*

Melentiev Energy Systems Institute of Siberian Branch of Russian Academy of Sciences, Irkutsk, Russia

**Abstract** — The paper aims to summarize and analyze the statistical data on the generation structure and price behavior in the Russian electric power industry and, based on the analysis, make a statistical contribution to the discussion on the outcomes of the electricity reform in Russia. A brief review of this topic is provided. The study states that the electric power industry should be regarded as a combination of four sub-industries when regulation, market design, and industrial organization problems are discussed. These four sub-industries are generation, transmission, distribution, and sales because of different regulations applied to these businesses. The main trends in the retail price index and some other indexes in the four sub-industries are observed from 2009 to 2018. The trends in electricity consumption and generation structure are discussed as essential components of economic processes in the industry. The findings suggest that the four sub-industries make different contributions to the overall growth of the electricity supply costs for end consumers. Most growth was determined by regulated government-granted monopolies in network businesses (transmission and distribution companies). The sales business is represented in the research by suppliers of last resort.

**Index Terms:** electricity market, industrial organization, electric power industry reform, deregulation.

---

\* Corresponding author.

E-mail: [mikhail-vasilyev@yandex.ru](mailto:mikhail-vasilyev@yandex.ru)

<http://dx.doi.org/10.38028/esr.2021.02.0002>

Received June 27, 2021. Revised July 05, 2021.

Accepted July 15, 2021. Available online July 23, 2021.

This is an open access article under a Creative Commons Attribution-NonCommercial 4.0 International License.

© 2021 ESI SB RAS and authors. All rights reserved.

## I. INTRODUCTION

Nearly two decades have passed since the electric power industry reform in Russia started. However, until now, the process has not finished. The market models and rules, legal arrangements change regularly. Discussion about whether the reform is a success, what shortcomings of the new structure are, and how to improve the market, continues.

The changes in statutory regulation of the electric power industry in some countries (the process is referred to as «liberalization» or «deregulation») resulted in lower prices for the end consumers and higher competition in electricity production and sales. In 2000-2010, the electricity price index (EPI) in Russia was significantly higher than the retail price index (RPI). Later it was comparable or slightly higher than RPI. Thus, despite the long-term industry reform, there was no price decrease, which draws criticism of the reform (for example, [1]-[3]). Some authors note some positive results of the reform, including, in particular, a decline in the failure rate and an increase in the fuel utilization efficiency at thermal power plants. The reform led to significant investments in generation (primarily due to the mechanism of capacity supply agreement) and in electric networks [4]. Some researchers confirm that the electricity price growth sustainably exceeded the inflation rate [5]-[6]. This opinion, however, is not shared by all. Some authors believe that the electricity price growth in 2010-2017 was lower than the inflation rate [7].

In general, the researchers conclude that the Russian electricity reform was not successful, and further regulatory changes are necessary. The discussion on the industry problems, their possible solutions, and research methods continues ([8]-[14]).

Research and discussions of the electricity market can encounter the following issues. Some authors consider the electric power industry to be an integral whole and make conclusions based on the statistical

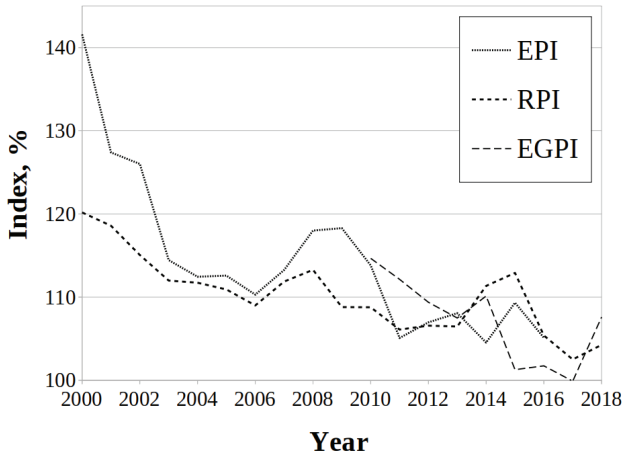


Fig. 1. Retail price index (RPI), electricity price index (EPI), and electricity generation price index (EGPI) in 2000-2018. Source: Federal State Statistics Service of the Russian Federation.

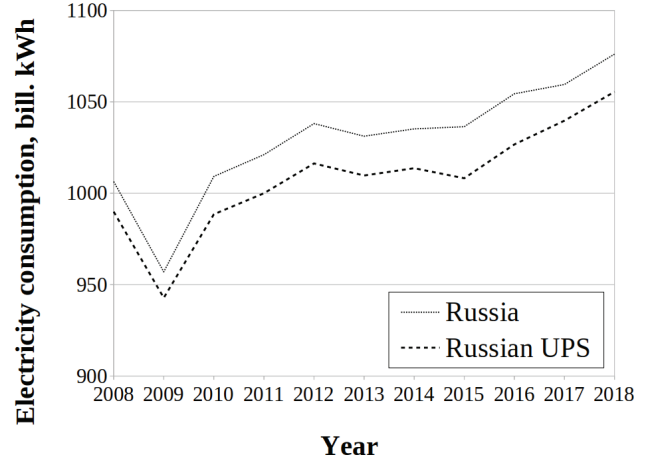


Fig. 2. Electricity consumption in the Russian Federation, including the consumption in the unified power system (UPS). Source — The System Operator of the Russian Federation.

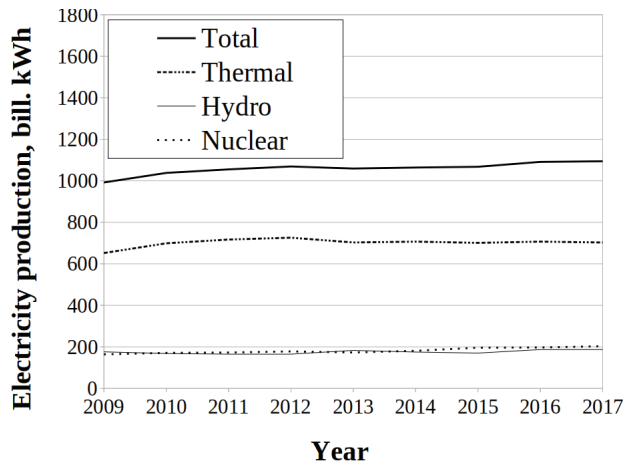


Fig. 3. Electricity production in 2009-2018 (bln. kWh per year). Source: Federal State Statistics Service of the Russian Federation.

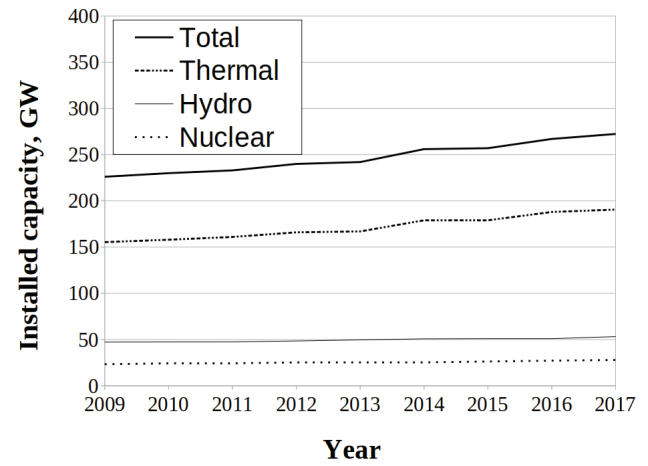


Fig. 4. Installed capacity of thermal, hydro, and nuclear power plants. Source: Federal State Statistics Service of the Russian Federation.

and econometric data of the entire industry. In this case, conclusions can hardly be applied to the organization and regulation issues since the electric power industry is a complex entity. Part of it (electricity generation and sales) functions under competition conditions, and the other part (electricity transmission and distribution) is, in general, a government-granted monopoly. Generalized statistical data summarize the contribution of the industry parts but do not allow detecting the regulatory mechanisms, which create problems or provoke destructive by-effects. To provide an efficient policy, the electric power industry should be viewed as a combination of interdependent components, i.e., sub-industries (generation, transmission, distribution, and sales). The analysis should be based on statistical data that describe each of the industries separately. In particular, monopolistic power in the generation is analyzed in [15].

This research focuses on the years 2009-2018. A similar analysis of the previous decade can be found in [16].

## II. INFLATION INDEXES AND ELECTRICITY CONSUMPTION

Before analyzing the electric power sub-industries, let us introduce the benchmarking data that characterize the economic conditions in general, i.e., inflation and total electricity consumption. Fig. 1 presents the retail price index (RPI), electricity price index (EPI), and electricity generation price index (EGPI). Further analysis will use RPI as the benchmark of the price growth. RPI will be reduced to the price value in the earliest year under consideration and will show how the price would change if it changed proportionally to RPI (shown by dotted lines in the diagrams).

The diagram shows that EPI was constantly higher than RPI in 2000-2010, i.e., for the end consumers, the electricity price increased more quickly than the price of other commodities and services. Since 2011, EPI has been similar or slightly lower than RPI.

The electricity consumption in 2008-2018 is shown in Fig. 2. The difference between the two lines reflects the electricity consumption outside of the Russian unified

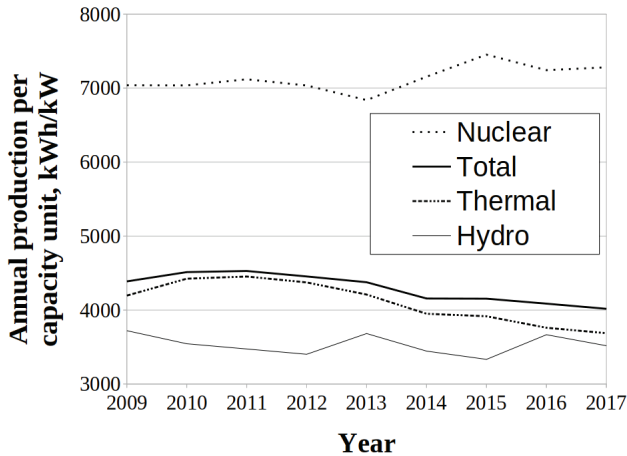


**Fig. 5. Production performance of 1 kW of installed capacity of thermal, hydro, and nuclear power plants. Source: Federal State Statistics Service of the Russian Federation, calculations by the author.**

power system. The total electricity consumption decrease in 2009 was followed by an intensive demand recovery in 2010, and, later, in 2011-2012, the growth was about 1.4% per year. After a stagnation of 2013-2014, the demand continued to rise with an average value of 1.5% per year, which implies that the economic situation of the considered period is characterized by rather stable growth of the total electricity consumption and by lower inflation than in the previous decade. This should be kept in mind in the analysis of electricity supply costs and tariffs.

The main components of the total electricity supply costs for the end consumers are the payments to the generators (for electricity and electric capacity) and the payments to the transmission and distribution networks. A noticeable part is a retail markup. The share of other payments, including those to the trading system administrator, system operator, and others, is less than 1% totally and is not considered in this paper.

### III. ELECTRICITY GENERATION

Understanding the price changes requires the consideration of trends in generation. These trends are partly influenced by economic conditions, for example, through investments into profitable projects. And vice versa, the trends in generation structure determine prices. Thus, price changes should not be considered separately from the generation structure.

The electricity generation in Russia increased in 2000-2008 by 2% annually on average. In 2009 it decreased by 4.6%. After recovery in 2010, the average annual growth was about 0.9% in 2011-2018 (Fig. 3). The generated volumes changed differently for various power plants. Thus, the nuclear plants increased production by 2.6% annually in 2000-2017.

Within the same period, 2000-2017, hydropower plant generation changed depending on weather conditions and grew on average by 0.4% annually. The output of thermal

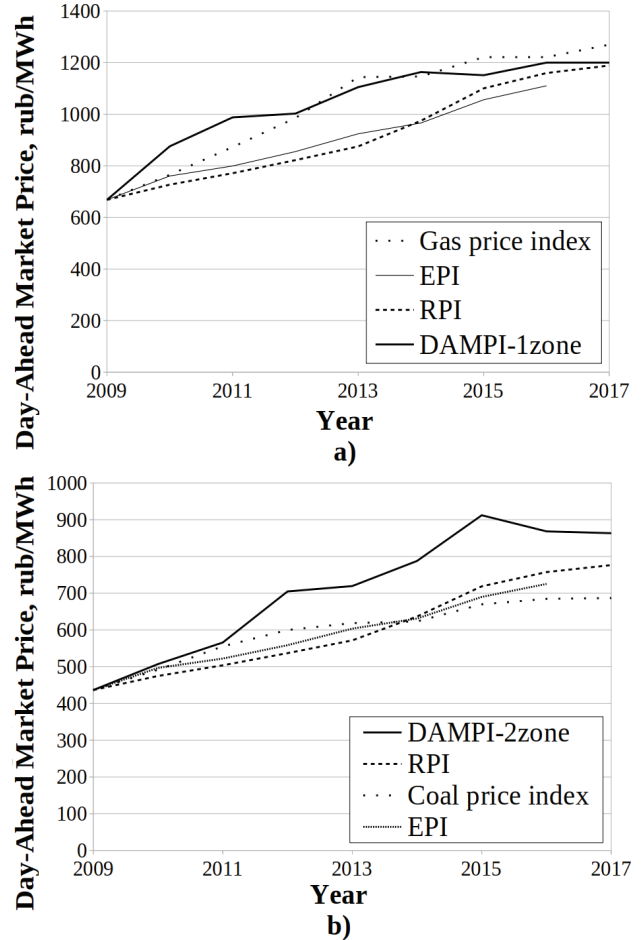


**Fig. 6. The day-ahead market prices in price zones I (a) and II (b) of the wholesale electricity market compared with the RPI, gas, and coal price indexes (reduced to the electricity price in 2009).**

power plants increased in 2000-2008 by 2.5% annually, and later, in 2009-2017, decreased by 0.1% annually.

The investments in new electricity generation, along with the low pace of withdrawal of old generators from service, resulted in a substantial surplus of generation capacity. The installed capacity of power plants increased from 212 GWh to 243 GWh in 2009-2018. At the same time, the maximum load rose from 150 GWh to 152 GWh, i.e., the regulatory mechanisms of the electric power industry development do not guarantee balanced construction and commissioning of new generation capacities in the context of the current electricity demand.

Therefore, the average annual electricity production per unit of installed capacity grew from 4126 kWh/kW to 4612 kWh/kW in 2000-2008. In 2009, electricity consumption decreased due to the economic crisis. In 2016, each kW of installed capacity produced only 4086 kWh per year, i.e., the production performance in 2016 was lower than that in 2000 (before the industry reform).

The installed capacity of all types of generation grows (Fig. 4), and the production performance differs for various generation types (Fig. 5). For nuclear generation, it increased from 6037 kWh/kW in 2000 to 7281 kWh/kW in

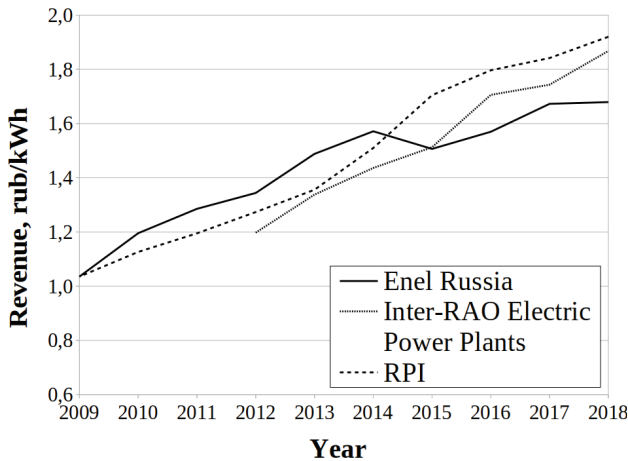


Fig. 7. The revenue from electricity and capacity sales divided by 1 kWh of generated electricity (compared to RPI).

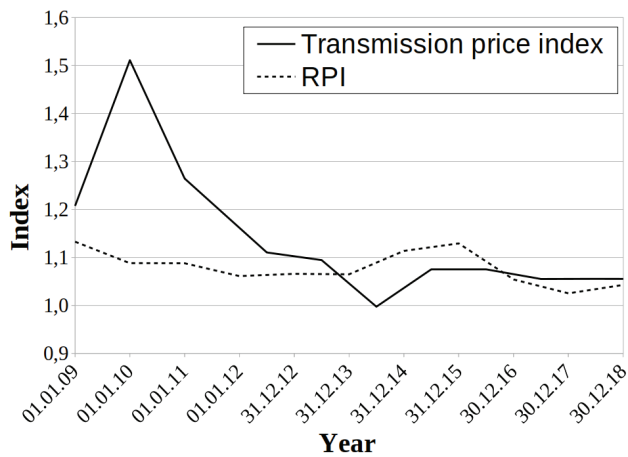


Fig. 9. Electricity transmission prices of the Unified Power System.

2017. At the same time, the same ratio decreased for hydro generation from 3725 kWh/kW to 3518 kWh/kW. The production performance of thermal power plants increased in 2000-2008. Later, in 2010-2017, it dropped from 4424 kWh/kW to 3687 kWh/kW, i.e., it became 16,7% lower. The power capacity factor of thermal power plants in 2017 was only 42.1%. It reveals discrimination of thermal generation in favor of nuclear one.

Such dynamics of the power capacity factor pose risks for the industry and provoke either growth in electricity prices or a decrease in the producers' profits. Less electricity generated by a power plant means smaller variable costs but the fixed costs remain the same. Thus, some producers need a higher market price to cover the fixed costs if they are not covered by the capacity payments. In this case, the wholesale electricity prices may grow more quickly than the prices of the fuel consumed by the plant.

Fig. 6 shows the prices in the day-ahead market in both price zones.

Prices in price zone I of the day-ahead market grew above the inflation rate in 2010, and later, the growth was equivalent to the RPI change. In 2009-2017, the price in

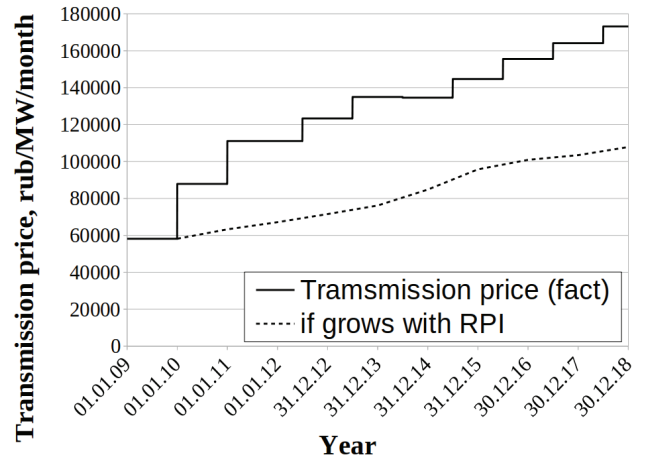


Fig. 8. Electricity transmission prices of the Unified Power System.

price zone I rose by 80%, RPI – by 77.9%, and gas price – by 90%, i.e., the total electricity price growth in the wholesale market was equivalent to the inflation rate and lower than the rise in the dominant fuel price in this price zone.

The dominant fuel of price zone II is coal. Coal price increased in 2009-2017 less than RPI. Within the considered period, the electricity price in the zone increased by 97.8%, coal price – by 57.3%, and RPI – by 77.9%.

To get a complete picture, let us look at the earnings of some generating companies. Fig. 7 indicates a normalized revenue of two wholesale market participants – Enel Russia and Inter-RAO Electric Power Plants (since 2012). The power plants of Enel Russia work in price zone I of the wholesale market. The Figure shows that the normalized revenue of the two companies (including the revenues from electricity and capacity sales) changed similarly to RPI. The normalized revenue of Enel Russia in 2009-2018 increased by 62%, while RPI increased by 85%.

Thus, within the period under review, there is an advanced growth of installed capacity in the sphere of electricity generation. In combination with moderate electricity consumption growth, it results in lower production performance of 1 kW of installed capacity. The prices in zone I of the day-ahead market changed similarly to gas prices, and the overall increase was equivalent to the retail price index change. The normalized revenue of the two considered producers also increased likewise, or less than RPI. The prices in price zone II increased more quickly than RPI and coal prices, but the difference had become smaller by 2017.

#### IV. ELECTRICITY TRANSMISSION

The major participants in electricity transmission are the Federal Grid Company (FGC) that operates the main transmission system and distribution companies. The FGC prices are shown in Figs. 8, 9.

The diagrams indicate that the grid transmission prices grew rapidly in 2010-2011, and later, they changed similarly to inflation. Nevertheless, due to the fast initial growth,

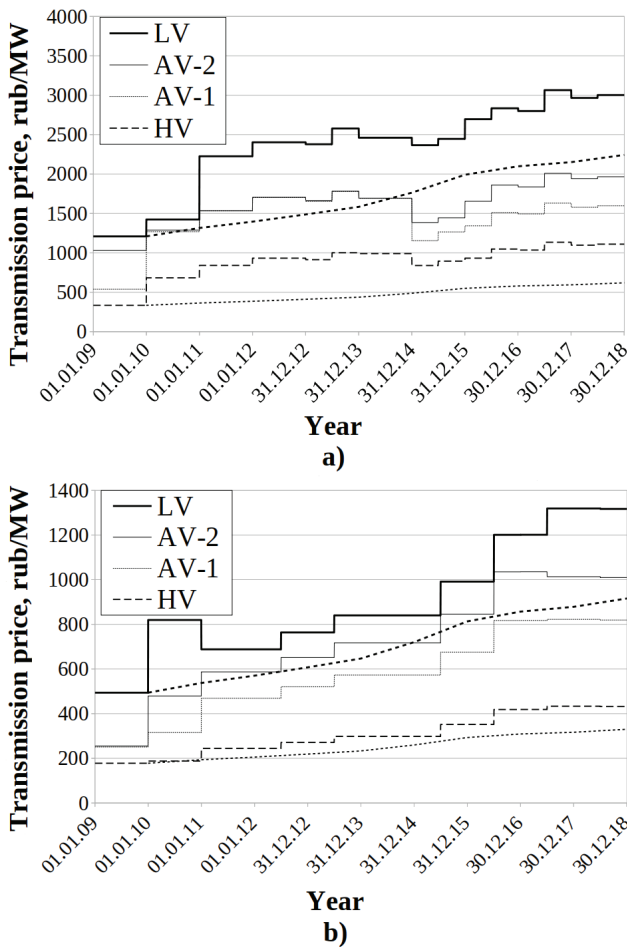


Fig. 10. One-part tariffs of MOESK (a) and IESK (b) for electricity distribution for different voltage levels.

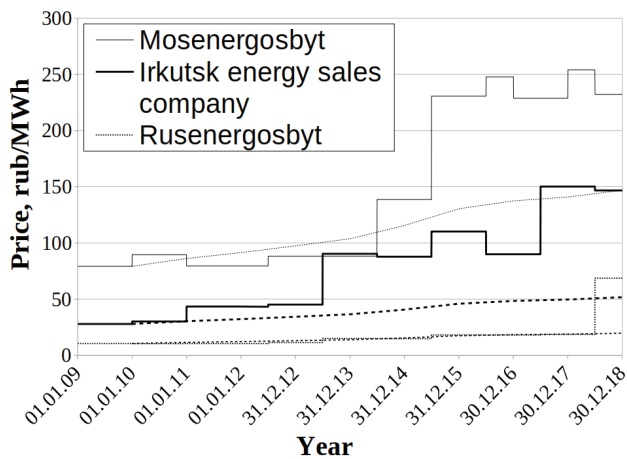


Fig. 11. The household tariffs of Mosenergosbyt, Irkutsk Energy Sales company, and Rusenergosbyt in 2009-2018.

the overall increase was 198% within the period under consideration. RPI, at the same time, increased by 85%.

To present the situation in distribution networks, let us consider two distribution companies (Rosseti Moscow Region (MOESK) and Irkutsk Network Company (IESK)) and one-part transmission tariffs for four voltage levels: high (HV), first average (AV-1), second average (AV-2)

and low voltage (LV). (Fig. 10). The Figures show that the distribution tariffs also increased more quickly than retail prices. For example, the one-part low-voltage tariff of MOESK increased by 148% within the period under consideration, the second medium-voltage tariff increased by 90%, the first medium-voltage tariff – by 197%, and the high-voltage tariff – by 232%. In the same period, RPI increased by 85% only. The dynamics of the IESK tariffs were similar.

Thus, the transmission and distribution tariffs rose more quickly than the inflation. Although the growth was distributed non-uniformly and most of the increase occurred in 2010-2011, the overall tariff increase exceeded RPI, in some cases, 1.5-2 times.

### V. SALES

The sphere of electricity sales is organized as a combination of suppliers of last resort and other suppliers that are not obliged to contract all the coming consumers. The prices of the suppliers of last resort are subject to regulation. The dynamics of the supply tariffs are represented by the suppliers of last resort in the city of Moscow (Mosenergosbyt) and the Irkutsk region (Irkutsk Energy Sales Company, and Rusenergosbyt). The household tariffs are shown in Fig. 11.

The diagram demonstrates that the pace of changes in tariffs under consideration was not steady. However, it is typical of the three suppliers that:

- in the early stage, the tariffs changed likewise the retail price index;
- an overall tariff growth exceeded the retail price index significantly.
- the tariff of Mosenergosbyt in 2018 was 58% higher than it should have been if it were indexed with RPI. The excessive growth for Irkutsk Energy Sales Company was 184% and for Rusenergosbyt – 249%.

### VI. CONCLUSIONS

The information and statistical data provided in the paper bring us to the following conclusions concerning the results of the electricity reform and the current regulatory conditions in the Russian electric power industry:

1. The economic situation in 2009-2018 was characterized by stable growth of the total electricity consumption and a lower inflation rate than in the previous decade.
2. The regulatory mechanisms of the electric power industry development do not guarantee balanced construction and commissioning of new generation capacities in the context of the current electricity demand. The provided data on production performance show discrimination of thermal generation in favor of nuclear one and excessive growth of generating capacities.
3. The data on the day-ahead market confirm a relative efficiency of the wholesale market regulatory framework, at least in the first price zone. In the second price zone, the electricity price grew excessively compared with the inflation rate and fuel price. The excessive growth,

however, is incomparable with the one in electricity transmission and distribution.

4. In electricity transmission and distribution, significant price growth was approved by the regulating authorities. The rise exceeded the retail price index, in some cases, by 200% and more.
5. In electricity sales, the uneven price growth exceeding inflation was also approved by the regulators. The sales prices do not influence the end consumer costs as much as the transmission prices. Their dynamics, however, require the attention of researchers.

The significant difference between price dynamics in various sub-industries also proves that generation, transmission, distribution, and sales should be considered separately when discussing electricity reform and regulation. Otherwise, the conclusions must be questioned.

#### ACKNOWLEDGEMENT

The research was carried out under State Assignment 17.4.4 (reg. number AAAA-A17-117030310449-7) of the Fundamental Research of Siberian Branch of the Russian Academy of Sciences and partly supported by the Russian Foundation for Basic Research, grant 19-010-00183.

#### REFERENCES

- [1] L.S. Belyaev, *Problems of the electricity market*. Novosibirsk, Russia: Nauka, 2009, 296 p. (in Russian)
- [2] G.P. Kutovoj, "Need for a new paradigm (or architectonics) of economic relations in the electric power industry," *Energetik*, vol. 2, pp. 8-13, Feb. 2016. (in Russian)
- [3] D.G. Kolesnikov, "The question of certain results of privatizing the electric power industry of Russia," *Science Vector of Togliatti State University. Series: Economics and Management*, vol.1 (32), pp. 25-30, Jan. 2018. DOI: 10.18323/2221-5689-2018-1-25-30. (in Russian)
- [4] A.B. Chubais, "Russian electric power industry reform: 10 years later," *Voprosy Ekonomiki*, vol. 8, pp. 39-56, Aug. 2018, DOI: 10.32609/0042-8736-2018-8-39-56. (in Russian)
- [5] I.S. Kozhukhovskii, "The key results of the electric power industry reform," *Regionalnaja energetika i energosberezhenije*, vol. 4, pp. 8-15, Apr. 2018. (in Russian)
- [6] A.N. Melnik, I.E. Naumova, R. Kurt, O.N. Mustafina, A.R. Sadriev, "Liberalization of the electricity market in Russia: achievements and problems," *Economic Revival of Russia*, vol. 3(37), pp. 133-143, Mar. 2013. (in Russian)
- [7] V.V. Rashevskii. (2018, Feb 6). On the modernization of the thermal power. Presented at Round table "Prospective of electric power industry development: long-term trends." Available at: <http://media.rspp.ru/document/1/4/0/40dd44874502cd043b6f60566821d25c.pdf>. (accessed: 15.01.2021). (in Russian)
- [8] V.A. Stennikov, S.I. Palamarchuk, B.O. Golovshikov, "Dimensions of improving the efficiency of the electric power industry," *Energosovet*, vol. 1(51), pp. 31-37, Jan. 2018. (in Russian)
- [9] S.I. Palamarchuk, "Improvement in Russian electricity and capacity markets," in *Improvement in the efficiency of energy production and utilization in Siberia*, Irkutsk, Russia, 2019, pp. 265-271. (in Russian)
- [10] S.I. Palamarchuk, "Efficiency of the electricity markets in Russia," *Journal of Engineering Science and Technology*, vol. 14, no. 6. pp. 3664-3678. Dec. 2019.
- [11] V.O. Golovshchikov, "Problems of electric power industry reform in Russia and their impact on market relations," *Energorynok*, vol. 5, pp. 30-35, May 2016. (in Russian)
- [12] E.V. Lyubimova, "Electric power industry: economic nuances of Russian trends," *ECO*, vol. 9, pp. 8-22, Sep. 2019. (in Russian)
- [13] V.V. Semikashev, "Heat supply in Russia: current state and problems of investment development," *ECO*, vol. 9, pp. 23-47, Sep. 2019. (in Russian)
- [14] M. Lamoureux, "Causality-based policy learning frameworks derived from Russian power sector liberalization," *Energy Systems Research*, vol. 3, no. 1, pp. 5-20, Jul. 2020. DOI: 10.38028/esr.2020.01.0001.
- [15] N. Aizenberg, S. Dzuba, "Market power evidence from electricity market of the Russian Federation," *ECO*, vol. 10, pp. 102-126, Oct. 2020, DOI: 10.30680/ECO0131-7652-2020-10-102-126. (in Russian)
- [16] M.Yu. Vasilyev, "The components of electricity price," in *Models of markets with imperfect competition: application to the electric power industry*, Irkutsk, Russia: Melentiev Energy Systems Institute, 2015, pp. 72-82. (in Russian)



**M. Yu. Vasilyev** was born in Irkutsk, Russia. He graduated from Irkutsk State Technical University in 1997, received a Ph.D. degree in 2002. Currently, he is a researcher at Melentiev Energy Systems Institute SB RAS, Irkutsk, Russia. His research interests include regulation and industrial organization of the electric power industry.

# A Numerical Study of the Influence of Process Parameters on the Efficiency of Staged Coal Gasification Using Mixtures of Oxygen and Carbon Dioxide

I. G. Donskoy\*

Melentiev Energy Systems Institute of Siberian Branch of Russian Academy of Sciences, Irkutsk, Russia

**Abstract** — The paper considers a staged conversion process of pulverized coal fuel in the MHPS-type gasifier, which uses mixtures of oxygen and carbon dioxide as a gasifying agent instead of air. Similar conversion processes can be applied in the process diagrams with the capture and disposal of carbon dioxide. The research tool is a reduced-order mathematical model of coal particles' conversion in a reacting gas flow. Replacement of nitrogen with carbon dioxide leads to significant changes in the gasification process characteristics: the average reaction temperature decreases, but this decrease is partially compensated by an increase in the concentration of gaseous reactants. Thus, the gasification process efficiency and the fuel conversion degree increase. Calculations make it possible to identify a range of parameters with the highest cold gas efficiency values. The influence of oxygen concentration is estimated, the dependence of the fuel conversion degree on the reaction temperature is analyzed.

**Index Terms:** coal gasification, staged process, mathematical modeling, oxy-fuel.

## I. INTRODUCTION

Coal is the first candidate for displacement in the process of decarbonization of the energy sector. Despite its prevalence, large reserves, and low cost compared to other fossil fuels, coal has the worst forecast indicators [1, 2]. This fact, among other things, is due to the growing environmental requirements for energy technologies.

Clean coal technologies, including gasification ones, are not yet widespread for various reasons, although their potential cannot be considered exhausted [3].

Gasification of coal dust and coal-water suspensions is widely used in industry, for example, in the production of chemicals [4]. According to [5], most of the large gasifiers operate for the needs of the chemical industry (mainly in China). There are some demonstration and commercial combined cycle power plants with integrated coal gasification (IGCC) [6]. Despite the better environmental characteristics and higher efficiency of such power plants, they are not widely used in the energy sector. This is due to both the progress of traditional coal-fired power plants operating with high steam parameters [7] and some unsolved problems (such as high capital costs [8] and insufficient reliability in comparison with other plants [9]). The IGCC efficiency largely depends on the efficiency and reliability of the gasification reactor and associated equipment (high-temperature heat exchangers, gas cleaning systems, and others). When the process conditions change, for example, fuel composition or power load, the reactor must maintain operation stability under existing technological constraints. The gasification agent composition and flow rate can be used as control parameters to this end.

Most of the existing high-power gasifiers use oxygen with a purity of up to 95% as a gasification agent [5]. In this case, the air separation costs should be compensated by an increase in the fuel conversion and the heating value of the produced gas. Other gasifier types use gasification agents with a low oxygen concentration (at the air level) [10]. In this case, the fuel conversion degree could be low. Consequently, additional systems are required for its combustion.

The flow diagrams of thermal power plants with carbon dioxide capture and storage (CCS) include the units designed to purify carbon dioxide from combustion products or intermediate products. The resulting carbon dioxide can be used, inter alia, to control the characteristics of combustion and gasification processes. For example, the recirculation of carbon dioxide and water vapor mixtures can be used in coal combustion to simplify the operation

\* Corresponding author.

E-mail: [donskoy.chem@mail.ru](mailto:donskoy.chem@mail.ru)

<http://dx.doi.org/10.38028/esr.2021.02.0003>

Received June 06, 2021. Revised June 21, 2021.

Accepted July 10, 2021. Available online July 23, 2021.

This is an open access article under a Creative Commons Attribution-NonCommercial 4.0 International License.

© 2021 ESI SB RAS and authors. All rights reserved.

of CCS systems [11]. Similar processes were proposed for coal gasification in [12, 13].

In [14], the authors used a mathematical model of a stationary gasification process to compare the efficiency of coal-water and coal-carbon dioxide suspensions. Calculations show that carbon dioxide additives make it possible to reduce the specific oxygen consumption at a given temperature (in comparison with the coal-water suspension). However, the average fuel conversion degree decreases. The authors of [15] experimentally investigated the properties of carbon dioxide suspensions: measurements indicate that the viscosity and surface tension of carbon dioxide suspensions are lower than those of coal-water suspensions, which is why their transport and spraying require lower mechanical costs. They obtained carbon dioxide suspensions with a solid phase fraction of up to 66% of the mass. The work with carbon dioxide suspensions requires higher pressures. Therefore, their economic efficiency is determined by the operating pressure and thermal power of the reactor.

The process of staged gasification with carbon dioxide added (up to 25 vol. %) was proposed in [12]. The experimental setup made it possible to achieve cold gas efficiency (CGE) of about 45-50% with a fuel conversion degree of 90-95%. The low efficiency of the process is associated with high heat losses (the reactor capacity was three t/d, and the oxygen concentration was close to air). A similar process was considered in the study [12], which indicates that the recirculation of carbon dioxide and its partial use in the gasification process can increase the power plant efficiency. The studies [13, 16] proposed the flow diagrams of power plants, in which carbon dioxide is used not only in the gasification process but also as a working medium in power generation: the authors believe that such power plants can have a gross efficiency up to 50%.

The fuel conversion patterns change slightly when using  $O_2/CO_2$  mixtures in contrast to  $O_2/N_2$  mixtures. Oxygen diffusivity changes significantly over the particle surface: it decreases in the carbon dioxide-rich region and increases in the carbon monoxide-rich region, which is formed during gasification [17]. The contribution of the fuel reaction with oxygen declines. Therefore, the average combustion rate of particles decreases: the oxidation completeness depends to a greater extent on burning combustible gases formed on the fuel surface in the gas volume [18, 19]. Due to the lower reactivity of carbon to  $CO_2$  and a decrease in the reaction temperature, the influence of the kinetic features of heterogeneous reactions and fuel porous structure increases [20]. The pyrolysis stage could be intensified due to an increase in the heat capacity of a high-temperature gas mixture [21]; however, with a decrease in the oxygen diffusivity, the ignition and combustion stages slow down [22]. The study [23] indicates that an increase in the heat capacity of a gas mixture due to carbon dioxide added could lead to flame extinction. In [24-26], the investigation indicates the effect of recirculation of combustion products

on the structure of a pulverized coal flame: when carbon dioxide and water vapor are added, the flame length and average temperature decrease, which leads to a significant redistribution of heat fluxes both in the combustion region and on the walls of the burner.

Thus, the effect of water vapor and carbon dioxide addition could influence the macrokinetics of solid fuel conversion in different directions. Thermodynamic calculations show that during coal gasification, there can be regions of parameters with high CGE corresponding to very low temperatures of gasification products (which can be achieved only with a huge reaction zone) [27]. Therefore, when optimizing the parameters of the gasification reactor, it is necessary to raise the process temperature by increasing oxygen consumption [28]. The achievable efficiency of gasification processes using  $O_2/CO_2$  mixtures will be determined by the competition between temperature and concentration factors.

There are some papers on modeling two-stage gasifiers, which address recirculation and consider the possibility of simultaneously varying both stoichiometric ratio and fuel distribution by stage [29, 30]. In this work, the model developed in [30, 31] is applied to the study of coal gasification under oxy-fuel conditions (i.e., gasification in mixtures of  $O_2/CO_2$ ). The use of reduced-order models makes it possible to carry out calculations for a wider range of conditions (compared with the previous works) and get enhanced estimations for optimal parameters.

## II. MATHEMATICAL MODEL

The two-stage gasifiers use chemical quenching. In the first stage, the fuel is burned to achieve the most complete conversion and high temperatures. The second stage suggests the supply of secondary fuel reacting with the decomposition products of primary fuel, which results in a decrease in the process temperature. The resulting coke ash residue is pneumatically transported back to the first stage for combustion. This diagram is currently used at Nakoso IGCC with Mitsubishi Hitachi Power Systems (MHPS) gasifier.

A mathematical model described in detail in [31, 32] is used to assess the characteristics of the gasification process. A feature of the model is the combination of computational approaches to chemical thermodynamics and kinetics of heterogeneous reactions, which can significantly reduce the computation efforts. Kinetics of heterogeneous reactions (drying, pyrolysis, gasification) is described using a system of differential equations, and the system composition is determined by the equilibrium conditions in the gas phase, i.e., by solving the extremum search problem [33]. Similar models were used to simulate coal gasification processes in [34-40].

The heat balance for fuel particles is written in the form of a differential equation:

$$U c_p \frac{d(m_p T_p)}{dz} = \alpha S_p (T_g - T_p) + \varepsilon \sigma S_p (T_w^4 - T_p^4) + \sum_{j=1}^5 Q_j r_j. \quad (1)$$

In equation (1)  $z$  is the spatial coordinate (length of the reaction zone), m;  $U$  is the particle velocity, m/s;  $m_p$  is the particle mass, kg;  $T_p$  is the particle temperature, K;  $c_p$  is the specific heat capacity of fuel, J/(kg·K);  $\alpha$  is the heat transfer coefficient, W/(m<sup>2</sup>·K);  $S_p$  is the outer surface of the particle, m<sup>2</sup>;  $\varepsilon$  is the emissivity of the particle surface;  $\sigma$  is Stefan-Boltzmann constant, W/(m<sup>2</sup>·K<sup>4</sup>);  $T_g$  is the gas temperature, K;  $T_w$  is the wall temperature, K;  $r_j$  is the rate of the physicochemical process associated with the particle, kg/s (drying, pyrolysis, reactions with gases);  $Q_j$  is the thermal effect, J/kg (it is estimated from thermochemical data).

The drying rate  $r_{dr}$  is calculated using two formulas depending on the temperature conditions:

$$r_{dr} = \begin{cases} \frac{\beta S_p M_{H_2O}}{R_g T_p} (P_{H_2O}^{eq} - P_{H_2O}), & T_p \leq T_b, \\ \frac{\alpha S_p (T_g - T_p) + \varepsilon \sigma S_p (T_w^4 - T_p^4)}{|Q_{dr}|}, & T_p > T_b. \end{cases} \quad (2)$$

Here  $T_b$  is the boiling point of water under the given conditions, K;  $\beta$  is the mass transfer coefficient, m/s;  $M_{H_2O}$  is water molar mass;  $P_{H_2O}$  and  $P_{H_2O}^{eq}$  are the partial pressure and saturated pressure of water vapor, Pa;  $R_g$  is the universal gas constant, J/(mol·K);  $Q_{dr}$  is water evaporation heat, J/kg.

The pyrolysis rate  $r_{pyr}$  depends on temperature according to the Arrhenius law:

$$r_{pyr} = k_{pyr} \exp\left(-\frac{E_{pyr}}{R_g T_p}\right) m_V. \quad (3)$$

Here  $k_{pyr}$  is the preexponential factor, 1/s;  $E_{pyr}$  is the activation energy, J/mol;  $m_V$  is the mass of volatile substances in the particle, kg. Heterogeneous reactions rate follows diffusion kinetics equation:

$$r_g = \frac{S_p C_g}{k_g e^{-\frac{E_g}{R_g T}} + \frac{d_p}{Nu_D D_g}}. \quad (4)$$

Here  $C_g$  is the concentration of gaseous oxidizer (O<sub>2</sub>, CO<sub>2</sub>, H<sub>2</sub>O),  $k_g$  is the preexponential factor of heterogeneous reaction, m/s;  $E_g$  is the activation energy, J/mol;  $Nu_D$  is the diffusion Nusselt number;  $D_g$  is the diffusivity of gaseous oxidizer, m<sup>2</sup>/s;  $d_p$  is particle size, m. The solution to the system of equations for individual stages is found as follows. Differential equations (2)–(4) related to the kinetics of heterogeneous chemical transformations are solved at a given temperature distribution, while the gas composition is determined from the partial thermodynamic equilibrium problem [33]. Then the stationary problem of heat transfer is solved given heat sources (1). These steps are repeated until the resulting solution stops changing with iterations.

The numerical method of solving the problem for both sequential stages also involves iterations; the shutdown condition is the achievement of the specified accuracy in terms of the consumption of the recirculated coke-ash residue (5% of the total mass flow of the fuel entering the first stage). A two-stage gasifier is a system with feedback. Therefore, the existence of a stationary solution, in this case, is not obvious: even simple systems can exhibit complex dynamic behavior [41]. Preliminary calculations indicate that consumption of the recycled residue converges to a constant value, and this convergence is achieved rather fast: the determination of the stationary state parameters requires fewer than ten iterations (in most cases, fewer than five iterations). Nevertheless, the question of the number and stability of stationary states, generally speaking, remains open and should be solved employing appropriate models [42].

Our previous research [43] investigated the effect of adding carbon dioxide and water vapor in the oxygen-blown one-stage coal gasification process. This work focuses on a staged process with an oxygen concentration of 21–30%. The initial gasification agent temperature is 500 K. The geometric parameters of reactors are constant for all calculations: the reaction zone length is 20 m (including the length of the first stage equal to 3 m), the diameter is 3 m. Fuel consumption is 1700 t/d, average particle size is 100  $\mu$ m. Fuel composition is as follows: moisture content is 9.2 wt%; ash content is 12.7 wt%; volatiles yield is 30.9 wt%; carbon content is 82.3 wt%; hydrogen content is 5.06 wt%; oxygen content is 9.47 wt%; nitrogen content is 1.91 wt%; sulfur content is 1.09 wt%. The blast is distributed between the stages as follows: 90% goes to the first stage, and 10% goes to the second stage. Solid particles do not pass from the first stage to the second: it is assumed that the fuel is either completely burned or escapes the reactor with slag as mechanical underburning. Recirculation of excess fuel mass leads to computational difficulties (the iterative process may be convergent due to this approximation). We assume that after the second stage the coke-ash residue is cooled to input temperature before returning to the first stage.

### III. MODELING RESULTS AND DISCUSSION

Calculated stationary profiles of temperature and gas composition during gasification of pulverized coal in O<sub>2</sub>/N<sub>2</sub> and O<sub>2</sub>/CO<sub>2</sub> mixtures are shown in Fig. 1 and 2 (the initial volume fraction of oxygen in both cases is equal to 21%). The reaction temperature decreases significantly in the case of the O<sub>2</sub>/CO<sub>2</sub> mixture (by 300–400 K in the first stage and by 100–200 K in the second stage). However, due to the high concentration of CO<sub>2</sub>, a more complete fuel conversion is observed, and the produced gas has a higher calorific value (similar results were obtained in [44] for one-stage processes). This implies that temperature declines not only due to an increase in the specific heat capacity of gas flow but also due to an intensification of endothermic reactions.

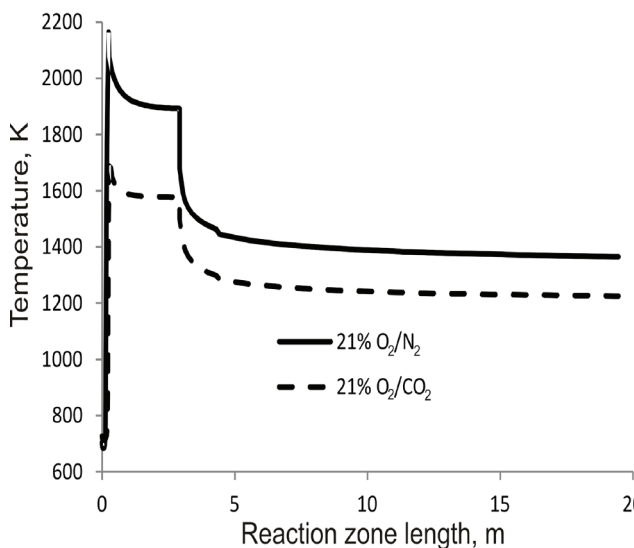


Fig. 1. Comparison of the calculated temperature profiles in the reaction zone of a two-stage gasification process with O<sub>2</sub>/N<sub>2</sub> and O<sub>2</sub>/CO<sub>2</sub> gasification agent.

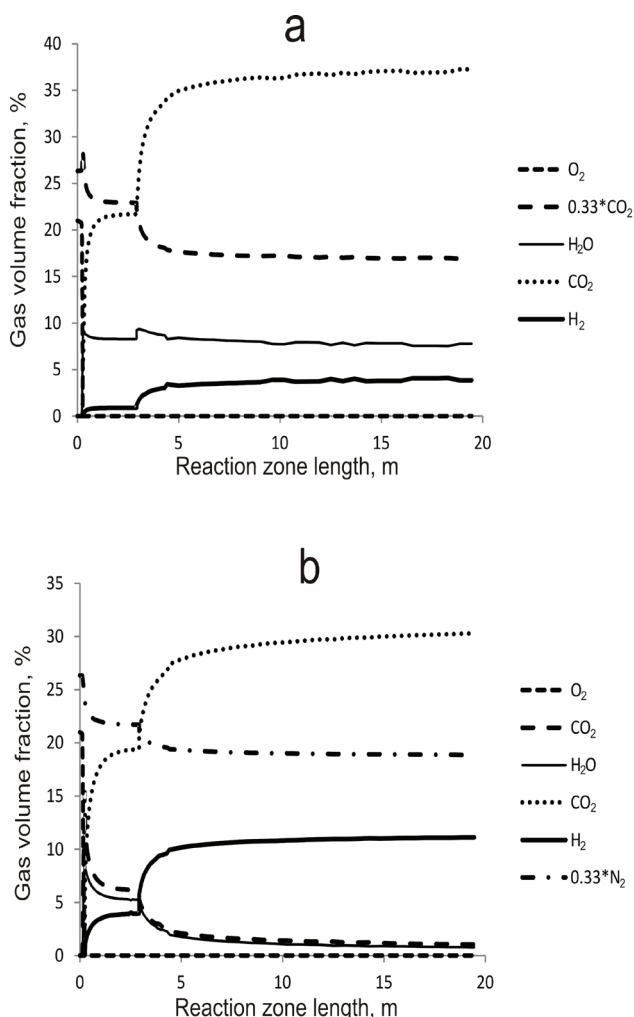


Fig. 2. Comparison of gas composition profiles in the reaction zone of a two-stage gasification process with O<sub>2</sub>/N<sub>2</sub> (a) and O<sub>2</sub>/CO<sub>2</sub> (b) gasification agent.

The CGE dependence on the fraction of primary fuel, when using the O<sub>2</sub>/N<sub>2</sub> mixture with an oxygen concentration of 21%, is shown in Fig. 3. The maximum CGE corresponds to a primary fuel fraction of about 60%. Earlier [30], the value of the optimal primary fuel fraction obtained for gasification in high-temperature air (initial temperature 1173 K) was about 30%. In present calculations, the maximum gas temperature at the first stage outlet is reached at a primary fuel fraction of 30-40%. With a primary fuel fraction of 60% and a stoichiometric ratio of 0.4, the gas temperature is about 1900 K, which is permissible under slagging conditions, and allows the process in the second stage with a sufficiently complete conversion of the secondary fuel. A further increase in the primary fuel fraction leads to a decrease in the temperature, and fuel conversion becomes low.

Switching from air blast to mixtures of oxygen and carbon dioxide, on the one hand, increases the concentration of oxidants, on the other hand, decreases the average reaction temperature. Therefore, the efficiency of fuel gasification under oxy-fuel conditions is determined by the ratio of these opposing factors.

The primary fuel dependence of CGE for O<sub>2</sub>/CO<sub>2</sub> mixtures with oxygen concentration equal to 21% is shown in Fig. 4. The optimal fraction of primary fuels is still about 60%. The form of the dependence does not change, optimal stoichiometric ratio value, however, shifts towards lower values. At a stoichiometric ratio equal to 0.45, a monotonic decrease in CGE is observed with an increase in the primary fuel fraction: such dependence [30] was observed for the high-temperature air gasification process. Under small proportions of primary fuel (up to 30%), the optimal value of the stoichiometric coefficient is 0.4, as for air gasification. With a further increase in the primary fuel fraction, the optimal value of the stoichiometric ratio goes down to 0.35. It can be assumed that this is due to a change in the dominant stage. With small proportions

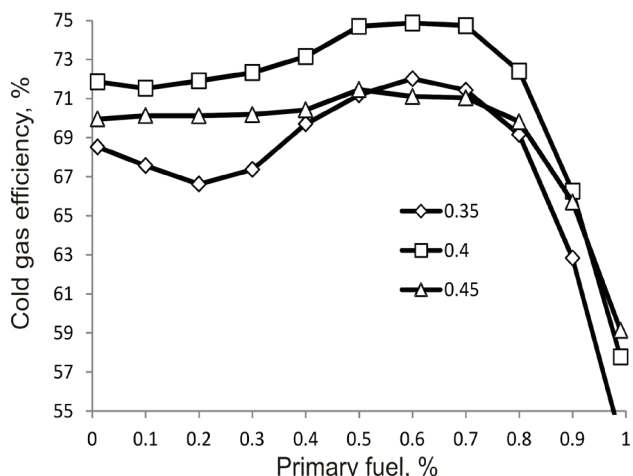


Fig. 3. Cold gas efficiency of two-stage gasification process with air: dependence on stoichiometric ratio and primary fuel fraction.

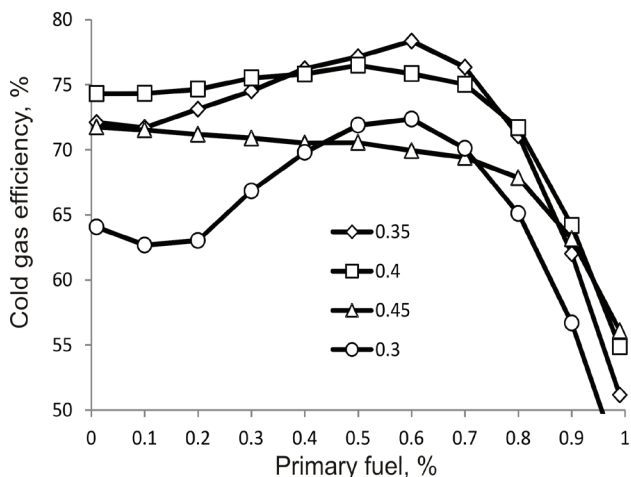


Fig. 4. Cold gas efficiency of two-stage gasification process with  $O_2/CO_2$  mixture (oxygen volume concentration is 21%): dependence on stoichiometric ratio and primary fuel fraction.

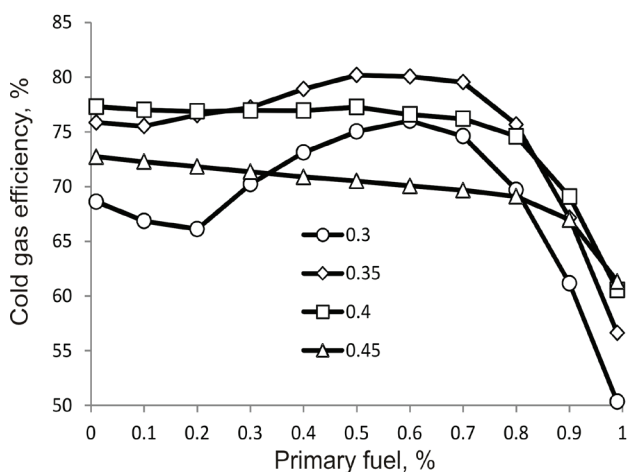


Fig. 5. Cold gas efficiency of two-stage gasification process with the  $O_2/CO_2$  mixture (oxygen volume concentration is 25%): dependence on stoichiometric ratio and primary fuel fraction.

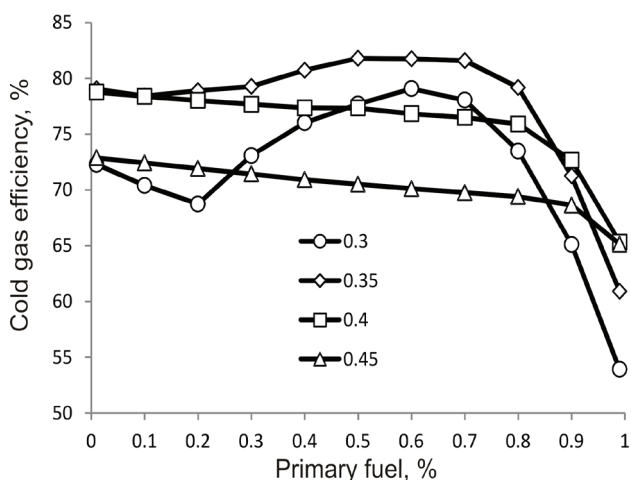


Fig. 6. Cold gas efficiency of two-stage gasification process with the  $O_2/CO_2$  mixture (oxygen volume concentration is 30%): dependence on stoichiometric ratio and primary fuel fraction.

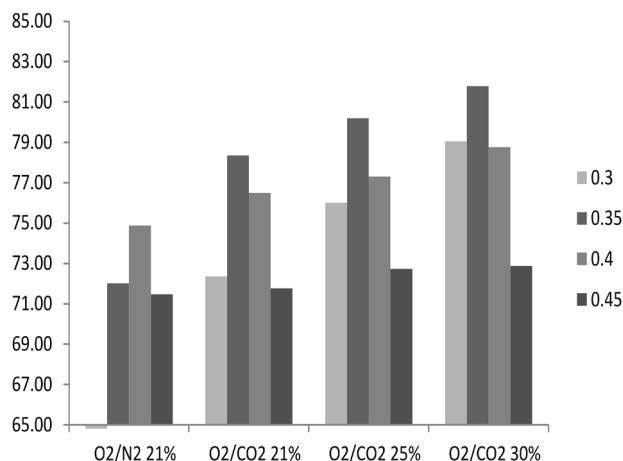


Fig. 7. Dependence of the maximum cold gas efficiency on the gasification agent composition and the stoichiometric ratio (numbers in legend).

of the primary fuel, gasification of the secondary fuel is of decisive importance; therefore, to increase the process efficiency, it is necessary to increase the temperature of hot gases before the second stage. With large proportions of secondary fuel, the completeness of the primary fuel conversion into combustible gas becomes more important; the secondary fuel is needed only for chemical quenching. Similar competition between the process stages was observed in the previous study [30] that examined the transition between one- and two-stage gasification conditions.

The same qualitative regularities are observed for the gasification process in mixtures with an oxygen volume concentration of 25 and 30% (Figs. 5 and 6). The CGE dependence on the primary fuel fraction flattens already at a stoichiometric ratio equal to 0.4. An oxygen concentration increase leads to a rise in the reaction temperature, therefore, at an oxygen volume concentration of 30%, the optimal value of the stoichiometric coefficient is 0.35 for all fuel distribution alternatives by stage. The temperature rise facilitates the endothermic reaction of fuel carbon with carbon dioxide; therefore, the average conversion rate and maximum chemical efficiency increase with the growing oxygen concentration.

The values of the maximum CGE are shown in Fig. 7. The higher the oxygen concentration, the higher the gasification process efficiency. The optimal stoichiometric ratio varies in a range of 0.3-0.4. With the air gasification of coal, one can reach a CGE of about 75%. With the  $O_2/CO_2$  mixtures, even at equal oxygen concentrations, the CGE can be increased up to 78%. The maximum CGE in all the considered options is about 82% (at an oxygen volume concentration of 30%, a stoichiometric ratio of 0.35, and a primary fuel fraction of 50%).

The temperature dependences of the fuel conversion degree for the first and second stages (based on the results of all calculations) are shown in Fig. 8. One can see that

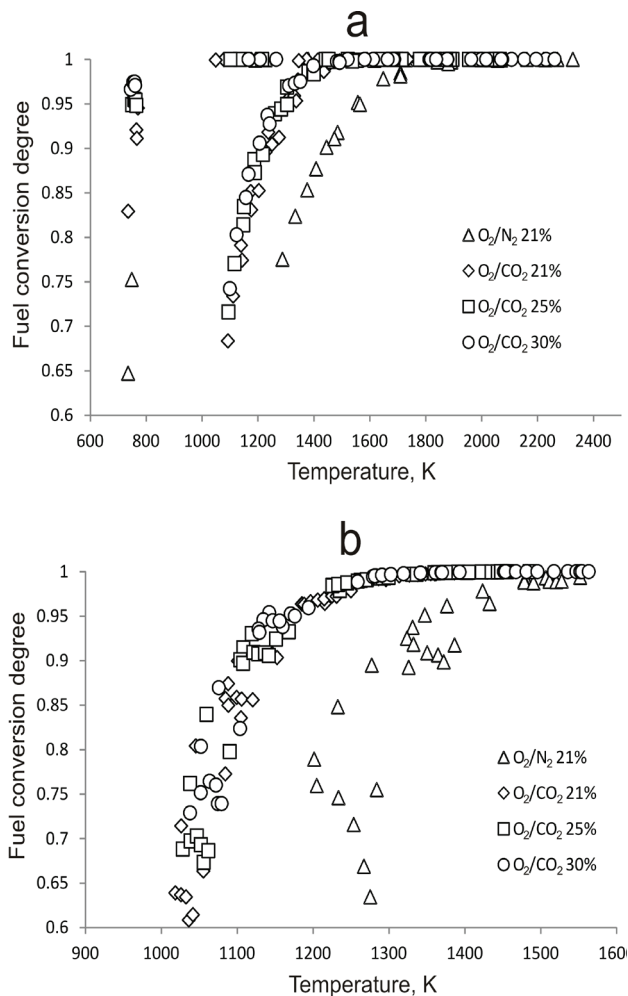


**Fig. 8. Temperature dependence of the fuel conversion degree: stage 1 (a) and stage 2 (b).**

for O<sub>2</sub>/CO<sub>2</sub> mixtures, the points are grouped around a common curve. Small scattering arises due to different conditions, mainly stoichiometric and kinetic factors (for example, the instability of combustion in the first reactor or a deficiency of primary fuel). Air gasification requires higher temperatures to achieve a complete fuel conversion: apparently, the concentration factor is prevailing.

#### IV. CONCLUSION

The calculations show that in the process of pulverized coal fuel staged gasification, the efficiency can be increased with the mixtures of oxygen and carbon dioxide used as a gasifying agent. The magnitude of the effect is determined by oxygen concentration and process temperature constraints. The optimal fraction of primary fuel is in a range of 50-60% for all cases, and the optimal value of the stoichiometric ratio is 0.35-0.4. The gasification process CGE rises from 75 to 82% with an increase in the oxygen volume concentration from 21 to 30%.

The results obtained can be used to assess the efficiency of gasification reactors and power plants with carbon dioxide capture and storage systems.

#### ACKNOWLEDGMENTS

The work was supported by the RF President grant for young Ph.D.s (MK-157.2020.8). The author is grateful to A.D. Nikitin for valuable discussions on some features of the mathematical model.

#### REFERENCES

- [1] *World Energy Outlook 2019*. International Energy Agency, 2019. 810 p.
- [2] L.S. Plakitkina, Yu.A. Plakitkin, and K.I. Dyachenko, "World trends of coal industry development," *Mining Industry Journal*, no. 1(143), p. 24, 2019. DOI: 10.30686/1609-9192-2019-1-143-24-29
- [3] S. P. Filippov and A. V. Keiko, "Coal Gasification: At the Crossroads. Technological Factors," *Thermal Engineering*, vol. 68, no. 3, pp. 209–220, 2021. DOI: 10.1134/S0040601521030046
- [4] T.S. Veras, T.S. Mozer, D.C.R.M. dos Santos, and A.S. Cesar, "Hydrogen: Trends, production, and characterization of the main process worldwide," *International Journal of Hydrogen Energy*, vol. 42, no. 4, pp. 2018–2033, 2017. DOI: 10.1016/j.ijhydene.2016.08.219
- [5] *Gasification technologies*. Thyssenkrupp Industrial Solutions AG. Germany, 2019. 24 p.
- [6] T. Wang and G. Stiegel (Eds.), *Integrated gasification combined cycle (IGCC) technologies*. Woodhead Publ., 2017. 929 p.
- [7] W. Feng, "China's national demonstration project achieves around 50% net efficiency with 600°C class materials," *Fuel*, vol. 223, pp. 344–353, 2018. DOI: 10.1016/j.fuel.2018.01.060
- [8] J.N. Phillips, G.S. Booras, and J. Marasigan, "The History of Integrated Gasification Combined-Cycle Power Plants," *Proceedings of ASME Turbo Expo 2017: Turbomachinery Technical Conference and Exposition GT 2017* (June 26-30, 2017, Charlotte, NC, USA), paper no. GT2017-64507, V003T03A007, 2017. DOI: 10.1115/GT2017-64507
- [9] A. Laugwitz, M. Grabner, and B. Meyer, "Availability analysis of integrated gasification combined cycle (IGCC) power plants," In *Power Plant Life Management and Performance Improvement*. Woodhead Publ., 2011. pp. 110–142. DOI: 10.1533/9780857093806.1.110
- [10] A. Ryzhkov, T. Bogatova, and S. Gordeev, "Technological solutions for an advanced IGCC plant," *Fuel*, vol. 214, pp. 63-72, 2018. DOI: 10.1016/j.fuel.2017.10.099
- [11] L. Chen, S.Z. Yong, and A.F. Ghoniem, "Oxy-fuel combustion of pulverized coal: Characterization, fundamentals, stabilization, and CFD-modeling," *Progress in Energy and Combustion Science*, vol. 38, pp. 156-214, 2012. DOI: 10.1016/j.peccs.2011.09.003

- [12] K. Kidoguchi, S. Hara, Y. Oki, S. Kajitani, S. Umemoto, and J. Inumaru, "Development of Oxy-Fuel IGCC System with CO<sub>2</sub> Recirculation for CO<sub>2</sub> Capture: Experimental Examination on Effect of Gasification Reaction Promotion by CO<sub>2</sub> Enriched Using Bench Scale Gasifier Facility," *Proceedings of the ASME 2011 Power Conference* (Denver, USA, July 12-14 2011), vol. 2, pp. 485-492, 2011. DOI: 10.1115/POWER2011-55458
- [13] R. Allam, S. Martin, B. Forrest, J. Fetvedt, X. Lu, D. Freed, G.W. Brown Jr., T. Sasaki, M. Itoh, and J. Manning, "Demonstration of the Allam Cycle: An Update on the Development Status of a High-Efficiency Supercritical Carbon Dioxide Power Process Employing Full Carbon Capture," *Energy Procedia*, vol. 114, pp. 5948-5966, 2017. DOI: 10.1016/j.egypro.2017.03.1731
- [14] C. Botero, R.P. Field, H.J. Herzog, and A.F. Ghoniem, "Impact of finite-rate kinetics on carbon conversion in a high-pressure, single-stage entrained flow gasifier with coal-CO<sub>2</sub> slurry feed," *Applied Energy*, 2013, vol. 104, pp. 408-417. DOI: 10.1016/j.apenergy.2012.11.028
- [15] S. Tupsakhare, J. Doohar, D. Modroukas, and M. Castaldi, "Improved gasification efficiency in IGCC plants & viscosity reduction of liquid fuels and solid fuel dispersion using liquid and gaseous CO<sub>2</sub>," *Fuel*, vol. 256, paper no. 115848, 2019. DOI: 10.1016/j.fuel.2019.115848
- [16] H. Ishi, T. Hayashi, H. Tada, K. Yokohama, R. Takashima, and J. Hayashi, "Critical assessment of oxy-fuel integrated coal gasification combined cycles," *Applied Energy*, vols. 233-234, pp. 156-169, 2019. DOI: 10.1016/j.apenergy.2018.10.021
- [17] J. Yu, W. Ou and K. Zhou, "Mass transfer coefficients considering boundary layer reaction in oxy-fuel combustion of coal char," *Fuel*, vol. 124, pp. 173-182, 2014. DOI: 10.1016/j.fuel.2014.01.101
- [18] B. Roy and S. Bhattacharya, "Combustion of single char particles from Victorian brown coal under oxy-fuel fluidized bed conditions," *Fuel*, vol. 165, pp. 477-483, 2016. DOI: 10.1016/j.fuel.2015.10.099
- [19] Z. Zhang, B. Lu, Z. Zhao, L. Zhang, Y. Chen, S. Li, C. Luo, and C. Zheng, "CFD modeling on char surface reaction behavior of pulverized coal MILD-oxy combustion: Effects of oxygen and steam," *Fuel Processing Technology*, vol. 204, paper no. 106405, 2020. DOI: 10.1016/j.fuproc.2020.106405
- [20] Z. Xue, Q. Guo, Y. Gong, J. Xu, and G. Yu, "Numerical study of a reacting single coal char particle with different pore structures moving in a hot O<sub>2</sub>/CO<sub>2</sub> atmosphere," *Fuel*, vol. 206, pp. 381-389, 2017. DOI: 10.1016/j.fuel.2017.06.035
- [21] T. Li, P. Farmand, C. Geschwinder, M. Greifenstein, J. Koser, C. Schumann, A. Attili, H. Pitsch, A. Dreizler, and B. Bohm, "Homogeneous ignition and volatile combustion of single solid fuel particles in air and oxy-fuel conditions," *Fuel*, vol. 291, paper no. 120101, 2021. DOI: 10.1016/j.fuel.2020.120101
- [22] L. Duan, L. Li, D. Liu, and C. Zhao, "Fundamental study on fuel-staged oxy-fuel fluidized bed combustion," *Combustion and Flame*, vol. 206, pp. 227-238, 2019. DOI: 10.1016/j.combustflame.2019.05.008
- [23] Z. Zhang, B. Lu, Z. Zhao, L. Zhang, Y. Chen, C. Luo, and C. Zheng, "Heterogeneous reactions behaviors of pulverized coal MILD combustion under different injection conditions," *Fuel*, vol. 275, paper no. 117925, 2020. DOI: 10.1016/j.fuel.2020.117925
- [24] Z. Zhang, X. Li, L. Zhang, C. Luo, B. Lu, Y. Xu, J. Liu, A. Chen, and C. Zheng, "Effect of H<sub>2</sub>O/CO<sub>2</sub> mixture on heat transfer characteristics of pulverized coal MILD-oxy combustion," *Fuel Processing Technology*, vol. 184, pp. 27-35, 2019. DOI: 10.1016/j.fuproc.2018.11.011
- [25] S.-S. Hou, C.-Y. Chiang, and T.-H. Lin, "Oxy-Fuel Combustion Characteristics of Pulverized Coal under O<sub>2</sub>/Recirculated Flue Gas Atmospheres," *Applied Sciences*, vol. 10, paper no. 1362, 2020. DOI: 10.3390/app10041362
- [26] Z. Zhao, Z. Zhang, F. Wu, Y. Chen, C. Luo, X. Li, G. Gao, L. Zhang, and C. Zheng, "Effect of steam addition on turbulence-chemistry interaction behaviors of pulverized coal MILD-oxy combustion," *Fuel*, vol. 294, paper no. 120496, 2021. DOI: 10.1016/j.fuel.2021.120496
- [27] D. Svishchev, A. Keiko, I. Donskoy, A. Kozlov, V. Shamansky, and A. Ryzhkov, "Thermodynamic efficiency of IGCC plant with overheated cycle air and two-stage gasification," *Sustainable Energy for a Resilient Future: Proceedings of the 14th International Conference on Sustainable Energy Technologies* (25-27 August 2015, Nottingham, UK), vol. 1, pp. 112-117, 2016.
- [28] I.G. Donskoy, "Influence of coal-biomass fuel composition on the efficiency of its conversion in entrained-flow gasifiers," *Solid Fuel Chemistry*, vol. 53, no. 2, pp. 113-119, 2019. DOI: 10.3103/S0361521919020046
- [29] L. Wang, Y. Jia, S. Kumar, R. Li, R.B. Mahar, M. Ali, I.N. Unar, U. Sultan, and K. Memon, "Numerical analysis on the influential factors of coal gasification performance in two-stage entrained flow gasifier," *Applied Thermal Engineering*, vol. 112, pp. 1601-1611, 2017. DOI: 10.1016/j.applthermaleng.2016.10.122
- [30] I.G. Donskoy, D.A. Svishchev, and A.F. Ryzhkov, "Reduced-Order Modelling of Pulverized Coal Staged Gasification: Influence of Primary and Secondary Fuel Ratio," *Energy Systems Research*, vol. 1, no. 4, pp. 27-35, 2018. DOI: 10.25729/esr.2018.04.0003
- [31] I.G. Donskoy, V.A. Shamansky, A.N. Kozlov, and D.A. Svishchev, "Coal gasification process simulations using combined kinetic-thermodynamic models in one-dimensional approximation," *Combustion*

- Theory and Modelling*, vol. 21, no. 3, pp. 529–559, 2017. DOI: 10.1080/13647830.2016.1259505
- [32] I.G. Donskoy, “Influence of gasification agent parameters on the efficiency of the high-temperature staged pulverized coal gasification process,” *Bulletin of the South Ural State University. Ser. Power Engineering*, vol. 20, no. 1, pp. 12–21, 2020. DOI: 10.14529/power200102 (in Russian)
- [33] B.M. Kaganovich, A.V. Keiko, and V.A. Shamansky, “Equilibrium thermodynamic modeling of dissipative macroscopic systems,” *Advances in Chemical Engineering*, vol. 39, pp. 1–74, 2010. DOI: 10.1016/S0065-2377(10)39001-6
- [34] A. Valero and S. Uson, “Oxy-co-gasification of coal and biomass in an integrated gasification combined cycle (IGCC) power plant,” *Energy*, vol. 31, pp. 1643–1655, 2006. DOI: 10.1016/j.energy.2006.01.005
- [35] M. Perez-Fortes, A.D. Bojarski, E. Velo, J.M. Nougues, and L. Puigjaner, “Conceptual model and evaluation of generated power and emissions in an IGCC plant,” *Energy*, vol. 34, no. 10, pp. 1721–1732, 2009. DOI: 10.1016/j.energy.2009.05.012
- [36] A.V. Messerle, V.E. Messerle, and A.B. Ustimenko, “Plasma thermochemical preparation for combustion of pulverized coal,” *High Temperature*, vol. 55, no. 3, pp. 352–360, 2017. DOI: 10.1134/S0018151X17030142
- [37] R. Gao, B. Huang, J. Huang, J. Xu, Z. Dai, and F. Wang, “Process modeling of two-stage entrained-bed gasification composed of rapid pyrolysis and gasification processes,” *Fuel*, vol. 262, paper no. 116531, 2020. DOI: 10.1016/j.fuel.2019.116531
- [38] M. Hwang, E. Song, and J. Song, “One-dimensional modeling of an entrained coal gasification process using kinetic parameters,” *Energies*, vol. 9, paper no. 99, 2016. DOI: 10.3390/en9020099
- [39] R. Rodrigues, *Modelagem Cinetics e de Equilibrio Combunadas para Simulacao de Processos de Gaseificacao*, Tese de Doutorado, Porto Alegre: Universidade Federal do Rio Grande do Sul, Escola de Engenharia, Departamento de Engenharia Quimica, 2015. 135 p.
- [40] K.V. Slyusarskiy, A.G. Korotkikh, and I.V. Sorokin, “Physical-mathematical model for fixed-bed solid fuel gasification process simulation,” *MATEC Web of Conferences*, vol. 91, paper no. 01011, 2017. DOI: 10.1051/mateconf/20179101011
- [41] V. Hlavacek, M. Kubicek, and J. Jelinek, “Modeling of chemical reactors-XVIII stability and oscillatory behavior of the CSTR,” *Chemical Engineering Science*, vol. 25, pp. 1441–1461, 1970. DOI: 10.1016/0009-2509(70)85067-9
- [42] H.-H. Lee, J.-C. Lee, Y.-J. Joo, M. Oh, and C.-H. Lee, “Dynamic modeling of Shell entrained flow gasifier in an integrated gasification combined cycle process,” *Applied Energy*, vol. 131, pp. 425–440, 2014. DOI: 10.1016/j.apenergy.2014.06.044
- [43] I.G. Donskoy, “How water vapor and carbon dioxide additives affect oxygen gasification of pulverized coal fuel,” *Bulletin of the South Ural State University. Ser. Power Engineering*, vol. 21, no. 1, pp. 21–28, 2021. DOI: 10.14529/power210102 (in Russian)
- [44] I. Donskoy, “Mathematical modeling of the oxy-fuel gasification of pulverized coal fuel,” *E3S Web of Conferences*, vol. 209, paper no. 03011, 2020. DOI: 10.1051/e3sconf/202020903011



**Igor G. Donskoy** received the Ph.D. degree in 2014. Currently he is a Senior researcher in the Laboratory of Thermodynamics at Melentiev Energy Systems Institute SB RAS (Irkutsk). His main research interests include mathematical modelling in fuel processing and thermal engineering.

# Options for Modernization of Heat Supply to Consumers of Condensing Power Plant

D. Balzamov\*, I. Akhmetova, E. Balzamova

Kazan State Power Engineering University, Kazan, Russia.

**Abstract** — High competition and strict requirements of the wholesale electricity and capacity market make optimization of heat supply schemes an urgent issue for generating companies. Replacement of life-expired generation equipment with new capacities based on advanced technologies is a priority goal for the energy industry development. This work focuses on condensing power plant (CPP), which is the only source in the city that supplies heat to all consumer categories. The plant carries out quantitative and qualitative heat supply regulation according to the temperature profile of 135/70°C with a cutoff of 110/70°C. The study examines the possibility of CPP modernization based on three options: building a pressure-reducing cooling unit 140/12, commissioning an auxiliary boiler house, and building a 110 MW combined-cycle gas plant. This paper presents technical solutions for the considered options and preliminary technical and economic calculations of their efficiency.

**Index Terms:** – auxiliary boiler house; boiler unit; combined-cycle gas plant; pressure-reducing cooling unit; water heater.

## I. INTRODUCTION

This paper considers optimization solutions of a scheme of heat supply to consumers from a condensing power plant (CPP), which is the only source in the city. For reliable and uninterrupted heat supply during the heating period, part of the CPP power units operate at minimum loads of 110 MW, which leads to losses from electricity sales in the wholesale electricity and capacity market (WECM), since the cost of electricity generated at some points of time (night, weekends, holidays) exceeds market

electricity prices. According to the data provided by the Production and Technical Department of the CPP, its loss in the year under consideration was RUR 50 million.

Thus, this study aims to:

1. Develop technical solutions to optimize the scheme of heat supply to urban consumers.
2. Evaluate the effectiveness of the solutions developed.

The accomplishment of the set goals involved the analysis of:

1. The plant operating conditions.
2. The heat network operation.
3. The technical condition of the CPP equipment.
4. Heat and electricity generation, specific fuel consumption rates, and the development of the heat balance for the CPP.

## II. MATERIALS AND METHODS

The following options are considered to optimize heat supply to consumers:

1. Construction of a pressure-reducing cooling unit (RCU) 140/12 with a steam capacity of 50 t/h, and reconstruction of RCU 12/6.
2. Commissioning of an auxiliary boiler house (ABH).
3. Construction of a combined-cycle gas plant (CCGP) with a capacity of 110 MW.

*A. Construction of RCU 140/12 with a steam capacity of 50 t/h and reconstruction of RCU 12/6*

To optimize heat supply with no additional units employed, one can construct RCU 140/12 with a steam capacity of 50 t/h (Fig. 1), which entails a reduced steam flow in the steam header of 12 atm, then to the network water heater PSV-500-I (33.64 t/h of steam from RCU 140/12 and 24.49 t/h of steam from two turbines using RCU 25/12) located in the turbine hall of stage 1 of the main building and through RCU 12/6 and a steam header of 7 atm to PSV-500-II (16.36 t/h from RCU 140/12 via RCU 12/6 and 16.1 t/h from two turbine extractions via RCU 25/6) located in the turbine compartment. With a nominal steam capacity of 640 t/h and nominal steam consumption of 575.5 t/h per turbine, the backup steam capacity of power boilers of each power unit is 64.5 t/h [1, 2].

At the same time, the steam consumption through the 12 atm header will be:

\* Corresponding author.

E-mail: [dbalzamov@mail.ru](mailto:dbalzamov@mail.ru)

<http://dx.doi.org/10.38028/esr.2021.02.0004>

Received June 09, 2021. Revised June 25, 2021.

Accepted July 08, 2021. Available online July 23, 2021.

This is an open access article under a Creative Commons Attribution-NonCommercial 4.0 International License.

© 2021 ESI SB RAS and authors. All rights reserved.

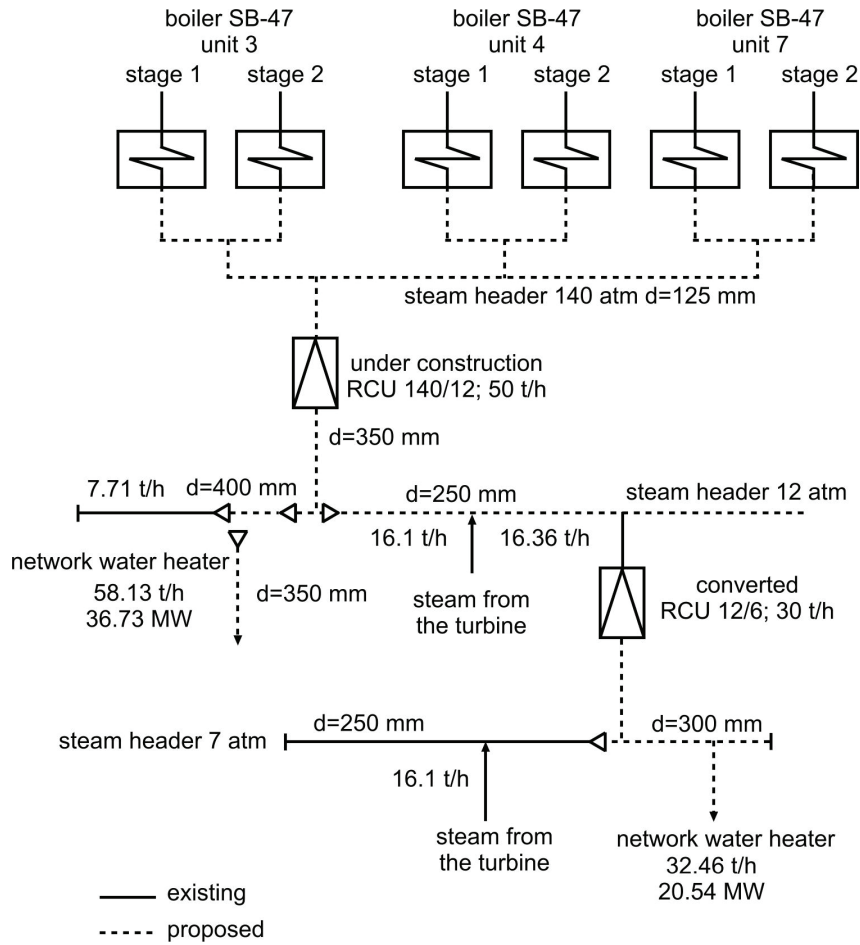


Fig. 1. Schematic diagram of RCU 140/12 connection.

TABLE 1. Distribution of heat output under current conditions.

Source	Current conditions of heat output			
	Stage 1 Quantity of power units	$Q$ , MW (G, t/h)	Stage 2 Quantity of power units	$Q$ , MW (G, t/h)
From RCU 140/12		-		-
From extraction 2 of turbines	3	-	1	-
From extractions 4 and 5 of turbines		31.65 (63.24)		16.08 (25.94)

TABLE 2. Distribution of heat output with RCU 140/12 in operation.

Source	Proposed heat supply scheme			
	Stage 1 Quantity of power units	$Q$ , MW (G, t/h)	Stage 2 Quantity of power units	$Q$ , MW (G, t/h)
From RCU 140/12		21.26 (33.64)		10.35 (16.36)
From extraction 2 of turbines	1	10.29 (16.1)	1	10.29 (16.1)
From extractions 4 and 5 of turbines		20.53 (27.7)		20.53 (27.7)

TABLE 3. Distribution of heat output under current conditions.

Source	Current conditions of heat output			
	Stage 1		Stage 2	
	Quantity of power units	$\underline{Q}$ , MW (G, t/h)	Quantity of power units	$\underline{Q}$ , MW (G, t/h)
From RCU 140/12		-		-
From extraction 2 of turbines	2	3.04 (4.8)	1	7.19 (11.35)
From extractions 4 and 5 of turbines		45.59 (63.24)		22.80 (31.62)

TABLE 4. Distribution of heat output with RCU 140/12 in operation.

Source	Proposed heat output scheme			
	Stage 1		Stage 2	
	Quantity of power units	$\underline{Q}$ , MW (G, t/h)	Quantity of power units	$\underline{Q}$ , MW (G, t/h)
From RCU 140/12		21.26 (33.64)		10.35 (16.36)
From extraction 2 of turbines	1	10.79 (16.1)	1	10.29 (16.1)
From extractions 4 and 5 of turbines		20.53 (27.7)		20.53 (27.7)

TABLE 5. Heat output distribution under current conditions.

Source	Current conditions of heat output			
	Stage 1		Stage 2	
	Quantity of power units	$\underline{Q}$ , MW (G, t/h)	Quantity of power units	$\underline{Q}$ , MW (G, t/h)
From RCU 140/12		-		-
From extraction 2 of turbines	5	7.76	3	4.95
From extractions 4 and 5 of turbines		113.97 (158.1)		68.38 (94.86)

- 50 t/h with RCU 140/12;
  - 32.2 t/h from the second extraction of turbine units (2 power units);
  - 58.13 t/h at PSV-500 of the first stage;
  - 7.71 t/h for fuel oil production;
  - 16.36 t/h with RCU 12/6.
- The steam consumption through the 7 atm steam header at the same time will be:
- 16.36 t/h with RCU 12/6;
  - 16.1 t/h from the second extraction of turbine units;
  - 32.46 t/h for the PSV-500 network water heater of the second stage.

Distribution of heat output (at an outdoor temperature of  $-5.2^{\circ}\text{C}$ ) under current conditions and the conditions with RCU 140/12 in operation is presented in Tables 1 and 2.

In Table 1–6,  $\underline{Q}$  is heat output, MW;  $G$  is steam consumption, t/h.

Tables 1 and 2 indicate that commissioning of RCU 140/12 at an outdoor temperature of  $-5.2^{\circ}\text{C}$  will allow the decommissioning of two power units and reduce the load on the remaining power units to 110 MW.

Distribution of heat output (at an outdoor temperature of  $-22$  to  $-24^{\circ}\text{C}$ ) under current conditions and the conditions with RCU 140/12 in operation is presented in Tables 3 and 4.

TABLE 6. Heat output distribution with RCU 140/12 in operation.

Source	Proposed heat output scheme			
	Stage 1 Quantity of power units	Q, MW (G, t/h)	Stage 2 Quantity of power units	Q, MW (G, t/h)
From RCU 140/12		21.26 (33.64)		10.35 (16.36)
From extraction 2 of turbines	4	15.48 (24.49)	3	10.79 (16.1)
From extractions 4 and 5 of turbines		91.18 (126.48)		68.38 (94.86)

Tables 3 and 4 indicate that the commissioning of RCU 140/12 at an outdoor temperature of  $-22$  to  $-24^{\circ}\text{C}$  will allow decommissioning of one power unit and reducing a load of remaining power units to 110 MW.

Heat output distribution (at an outdoor temperature of  $-34^{\circ}\text{C}$ ) under current conditions and the conditions with RCU 140/12 in operation is presented in Tables 5 and 6.

Tables 5 and 6 show that commissioning of RCU 140/12 at an outdoor temperature of  $-34^{\circ}\text{C}$  will allow decommissioning of one power unit.

To increase the flexibility of the heating plant when commissioning the new RCU 140/12, it is necessary to provide a cross-connection between the live steam boilers so that when one of the power units is stopped, RCU 140/12 remains in operation [3, 4]. Estimation of

the power unit operation duration and equipment layout characteristics should take into account that cross-connection for live steam should be arranged between power units 3, 4, and 7, as the most loaded ones [5, 6]. The hot steam header diameter will be 125 mm to ensure the required performance of RCU 140/12.

The existing thermal capacity of the network water heater PSV-500 of the first stage with the parameters of heating steam  $P = 8$  atm and  $t = 250^{\circ}\text{C}$  is 15.58 MW, which corresponds to the consumption of 24.69 t/h of heating steam by PSV-500 of the first stage and 7.71 t/h by the fuel oil industry.

To increase steam consumption by PSV-500 of the first stage to 58.13 t/h (36.73 MW), it is necessary to relay the existing steam pipeline of 12 atm with a diameter of 250 mm:

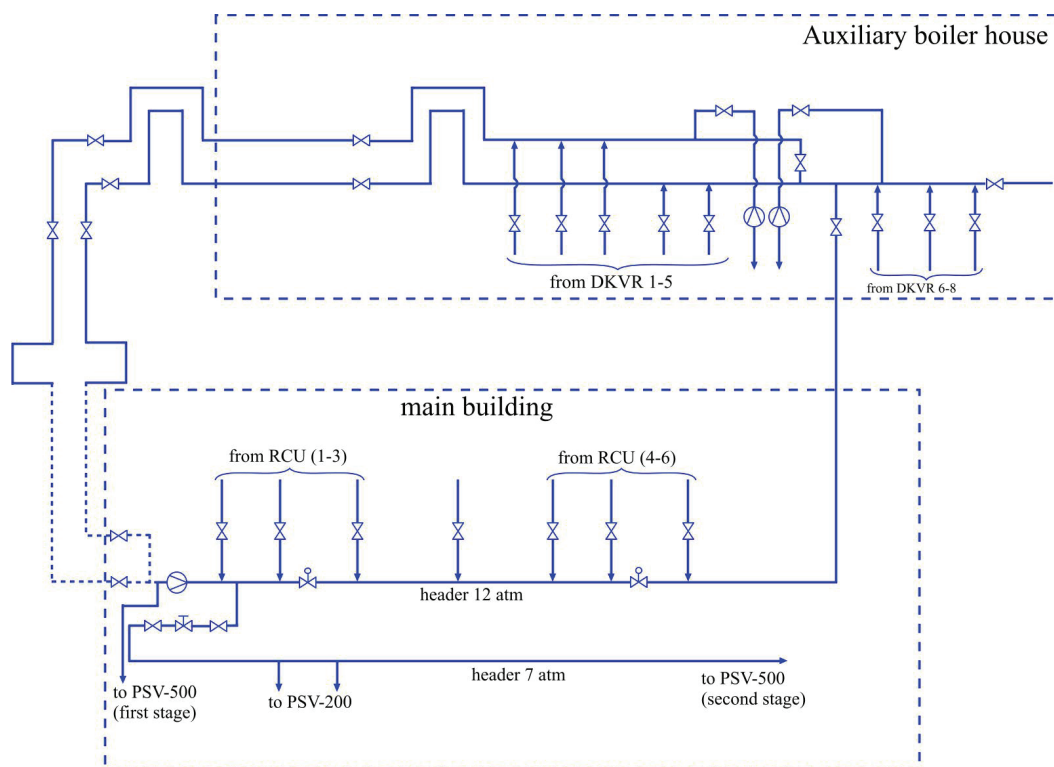


Fig. 2. The diagram of steam supply from ABH to the water heater PSV-500.

- on the section from RCU 140/12 to the tie-in to the 12 atm steam header of the first stage with a diameter of 350 mm;
- on the section from the header with RCU 140/12 to the header to PSV-500 of the first stage with a diameter of 400 mm;
- on the section from PSV-500 of the first stage to the tie-in to the 12 atm steam header with a diameter of 350 mm.

*B. Commissioning of ABH*

The option of upgrading the existing heat supply scheme by commissioning the ABH [7-9] is suggested to optimize the heat supply from CPP without involving additional power units.

The diagram of the steam supply from ABH to the water heater PSV-500 of the first and second stages is presented in Fig. 2.

Commissioning of ABH implies the steam supply from the existing boiler house to the steam header of 12 atm [10, 11].

There are seven steam boilers in the ABH. Technical parameters of the produced steam are  $P_o = 23$  atm,  $T_o = 370^\circ\text{C}$ .

The boiler house is connected to the steam headers of 12 and 7 atm, which are located in the CPP main building.

According to the calculations, the actual steam production with parameters  $P_o = 8$  atm and  $T_o = 210^\circ\text{C}$  is 34.8 t/h by boilers DKVR-10-23 (5.8 t/h  $\times$  6 pcs. = 34.8 t/h) and 11.0 t/h by boiler DKVR-20-23. The total steam production by the boiler house is 45.8 t/h or 29.16 MW, which is slightly less than the total capacity of the boiler group, and the second extraction of one power unit at a load of 110 MW (30.82 MW). The average weighted specific consumption of reference fuel (hereinafter fuel, in

tonnes of oil equivalent, t.o.e.) for heat production for the boiler house will be  $b_{t.o.e.-abh} = 136.8$  kg/MW [12-14].

Currently, boiler DKVR-10-23 is in operation. The service life of other boilers has expired.

Years of commissioning and service life extension of boilers are presented in Fig. 3.

As seen from Fig. 3, most boilers were put in service in 1967-1968, and service life for most of them has expired.

To increase the steam flow to the network water heater (PSV-500) of the first stage up to 70.49 t/h (44.54 MW), it is required to transfer the existing steam pipeline of 12 atm with a diameter of 250 mm from the condensate pump to PSV-500 of the first stage to the pipeline with a diameter of 400 mm [15].

Thus, the commissioning of ABH will allow removing no more than one power unit from the “forced” operation in the heating period [16,17].

The annual hot water supply was  $Q_{ta} = 323\ 618.7$  MW with an average annual specific fuel consumption for heat supply of 147.2 kg/MW.

Consumption of fuel for heat production at CPP [18] is as follows:

$$G_{t.o.e.} = (Q_{ta} \cdot b_{t.o.e.-h.y.}) / 1\ 000 = (323\ 618.7 \cdot 147.2) / 1\ 000 \approx 47\ 636.7, \tag{1}$$

where  $b_{t.o.e.-h.y.}$  is specific fuel consumption for heat production from thermal power plant.

The planned heat supply from ABH for three months (December, January, February) of the heating period is as follows:

$$Q_{abh} = 29.16 \cdot 90 \cdot 24 = 62\ 985.6, \tag{2}$$

where:

- 29.16 is heat production by ABH, MW/hour;
- 90 is the duration of boiler operation, day;
- 24 is the number of hours per day, an hour.

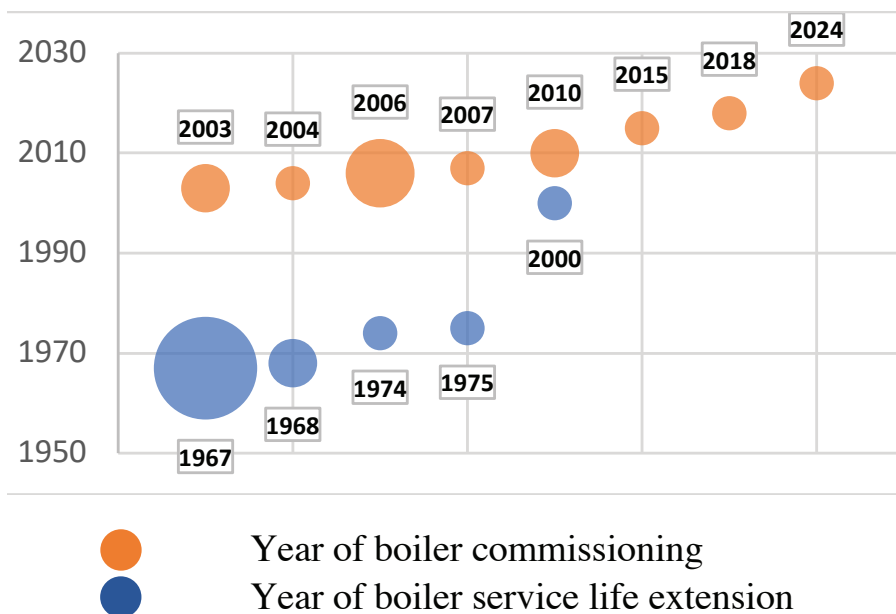


Fig. 3. Data on boiler commissioning and service life extension.

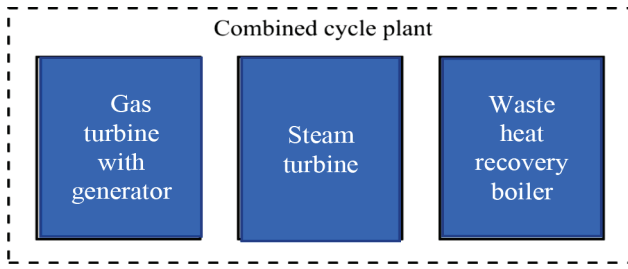


Fig. 4. The CCGP configuration.

TABLE 7. The preliminary cost of the project for 110 MW CCGP construction at CPP.

No.	Type of work, equipment, and costs	Price, RUR million (without VAT)
1	Equipment, including gas turbine plants, waste heat recovery boilers, steam turbine plants, electrical equipment, auxiliary equipment.	3 000
2	Construction and installation	900
3	Commissioning	100
4	Design and survey	200
5	Unforeseen expenses	300
6	Dismantling of the existing power unit	500
	Total	5 000

TABLE 8. Specific parameters of the 110 MW CCGP for heat and electricity supply.

No.	Type of work, equipment, and costs	Price, RUR million (without VAT)
1	Equipment, including gas turbine plants, waste heat recovery boilers, steam turbine plants, electrical equipment, auxiliary equipment.	3 000
2	Construction and installation	900
3	Commissioning	100
4	Design and survey	200
5	Unforeseen expenses	300
6	Dismantling of the existing power unit	500
	Total	5 000

TABLE 9. Costs of the solution.

No.	Item	Estimated cost, RUR thousand
1	Equipment	19 000
2	Revision of the existing project	250
3	Replacement of RCU 12/6	2 000
4	Replacement of the 12 atm steam header with a diameter of 400 mm and replacement of the 12 atm steam header with the PSV-500	3 000
5	Installation of gate valves	1 500
	Total	25 750

Consumption of fuel for heat supply from ABH:

$$G_{abh} = (Q_{abh} \cdot b_{t.o.e.-abh}) / 1\,000 = (62\,985.6 \cdot 136.8) / 1\,000 \approx 8\,616.4. \tag{3}$$

Heat supply from power units when involved in the ABH operation is:

$$Q_{h,y} = Q_{ta} - Q_{abh} = 323\,618.7 - 62\,985.6 = 260\,633.1. \tag{4}$$

Fuel consumption for heat supply from power units when involved in the ABH operation is:

$$G_{h,y} = (Q_{h,y} \cdot b_{t.o.e.-h,y}) / 1\,000 = (260\,633.1 \cdot 147.2) / 1\,000 \approx 38\,365.2. \tag{5}$$

Fuel saving for hot water heat supply during the ABH operation (December, January, February) is as follows:

$$E_{abh} = G_{t.o.e.} - (G_{abh} + G_{h,y}) = 47\,636.7 - (8\,616.4 + 38\,365.2) = 655.1, \tag{6}$$

which corresponds to RUR 1.966 million.

*C Construction of 110 MW combined-cycle gas plant (CCGP)*

Nowadays, one of the most common and successful solutions for replacing obsolete capacities is the construction of combined-cycle power units. In the Republic of Tatarstan, natural gas combined-cycle plants were put into operation at the Kazan CHPP-1 and CHPP-2, the Yelabuga CHPP, and the Nizhnekamsk industrial zone, where they proved to be an effective solution for the combined electricity and heat generation.

The possibility of upgrading the CPP by constructing a 110 MW CCGP to deliver electricity to an outdoor 110 kV switchgear and supply heat for heating needs is considered.

The CCGP configuration is shown in Fig. 4.

The heat output of a steam turbine with adjustable extractions used as part of a CCGP is 87.23 MW. An increase in the efficiency of gas turbine exhaust gases can be achieved by installing gas network water heaters in the waste heat recovery boiler, which allow an additional production of about 5.82–6.98 MW. Thus, the total heat output of the combined-cycle plant will be 93.04–94.20

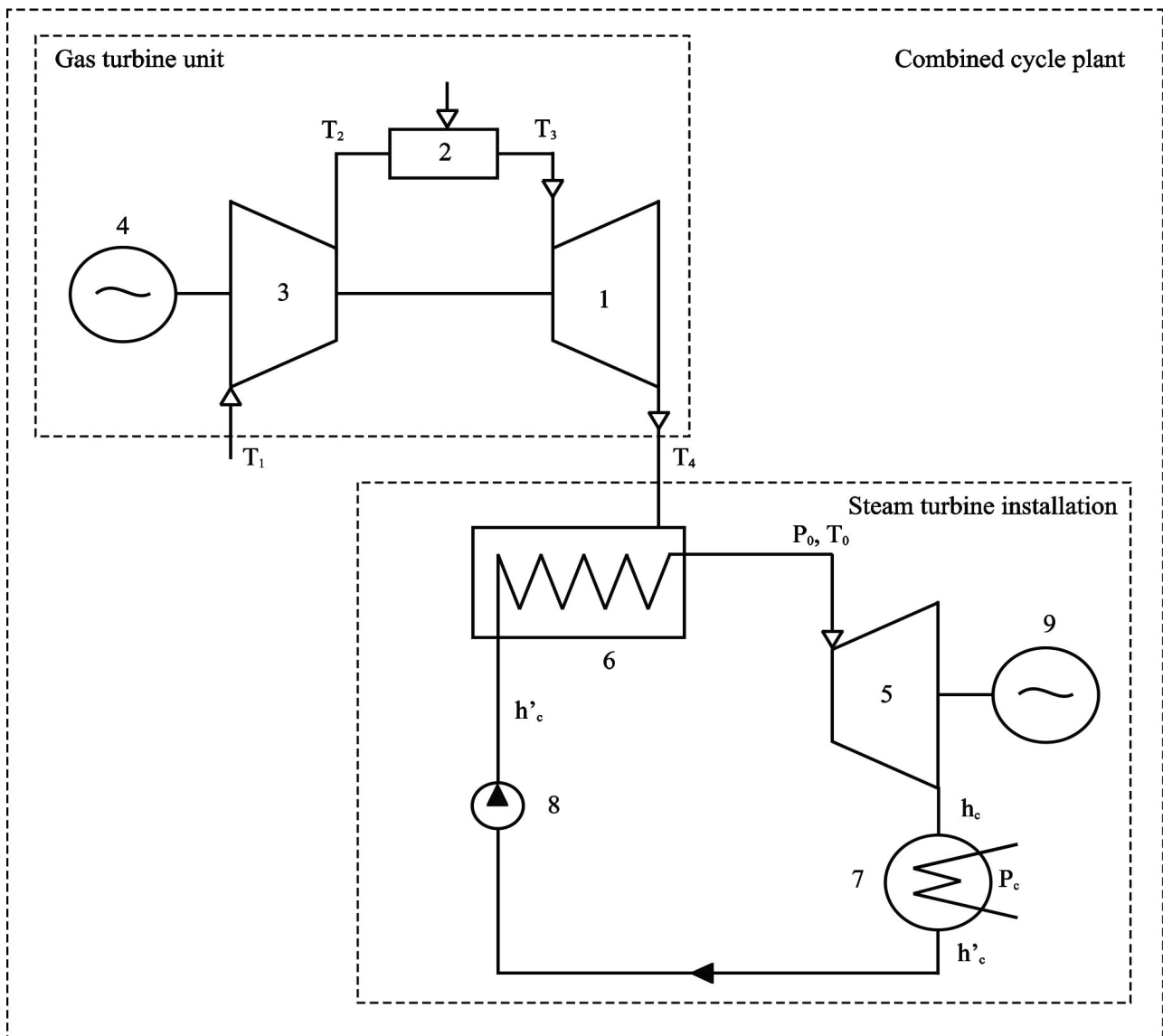


Fig. 5. The CCGP heat network diagram.

MW, which partially covers the heat demand of the residential area, the main building, and the industrial site of CPP (the heat load at a rated outdoor temperature of  $-34^{\circ}\text{C}$  is 195.38 MW).

The CPP heat flow diagram, including 100 MW CCGP, will provide heat supply to consumers as efficiently as possible [19].

An estimated cost of the project for 110 MW CCGP construction at CPP is presented in Table 7.

The cost of building the 110 MW combined-cycle plant, according to the calculations performed in the pre-feasibility study for the construction of the unit, is RUR 4.5 billion. The cost of equipment indicated in Table 7 is based on technical and commercial quotes of manufacturers. The cost of items 2–6 in Table 7 is determined factoring in the implemented projects for the construction of combined-cycle power units in the Republic of Tatarstan. Given the cost for dismantling of one CPP power unit, which is

RUR 0.5 billion, the total cost of this technical solution will be RUR 5.0 billion. According to expert estimates, the implementation period of this option will be three years. The heat network diagram of the CCGP is shown in Fig. 5. Table 8 indicates specific parameters of the 110 MW CCGP.

The designations used in Fig.5 are 1 – gas turbine; 2 – combustion chamber; 3 – compressor; 4 – compressor electric motor; 5 – steam turbine; 6 - heat recovery boiler; 7 – condenser; 8 – condensate pump; 9 – generator.

### III. RESULTS

The results of the feasibility studies of the proposed technical solutions are presented below.

#### A. Construction of RCU 140/12 with a steam capacity of 50 t/h and reconstruction of RCU 12/6

The existing heating capacity of the network water heater PSV-500 of the second stage under the heating steam

parameters  $P = 7 \text{ atm}$  and  $t = 250^\circ\text{C}$  is 17.60 MW, which corresponds to the consumption of 27.8 t/h of heating steam of PSV-500 of the second stage (actual throughput of the pipeline is 27.8 t/h).

To increase steam consumption at PSV-500 of the second stage to 32.46 t/h (20.64 MW), it is necessary to relay the existing steam pipeline with a pressure of 7 atm and diameter of 250 mm in the section from RCU 12/6 to PSV-500 of the second stage with a diameter of 300 mm to replace RCU 25/6 due to its unsatisfactory technical condition.

The specific fuel consumption for heat production with the commissioning of RCU 140/12 will remain at the level of the existing actual values and amount to 146.17–147.9 kg.o.e./MW.

The costs of the option are summarized in Table 9.

The simple payback period is determined by the formula:

$$C = S_{cost} / (S_{econ} - S_{cost,year}), \quad (7)$$

where  $S_{cost}$  is project costs, RUR thousand;

$S_{cost,year}$  is annual project costs, RUR thousand ( $S_{cost,year} = 0$ );

$S_{econ}$  is the total economic effect of the project for the heating period determined by the financial results of the source activity in the wholesale electricity and capacity market in the months with losses ( $S_{econ} = \text{RUR } 50\,000$  thousand). Information provided by the station's technical department.

The simple payback period will be:

$$C = 25\,750 / 50\,000 \approx 0.5$$

of the heating period.

At the same time, the specific capital investment per 1 Gcal is determined by the formula:

$$K = S_{cost} / W_{power} \quad (8)$$

where  $W_{power}$  is heat output of the commissioned equipment, MW (30.18 MW).

The specific capital investment (RUR million) per 1 MW will be:

$$K = 25.750 / 30.18 \approx 0.853.$$

### B. Commissioning of ABH

The annual cost of maintaining the ABH performance:

- Maintenance and repair of instrumentation, material, and equipment are RUR 1.3 million.
- Operating costs, maintenance of boilers and additional equipment are RUR 0.68 million.

The payback period is calculated by the formula:

$$C = S_{cost} / (S_{econ} - S_{an.cost}), \quad (9)$$

where:

$S_{cost}$  is the costs of the project, RUR 39 250 thousand;

$S_{an.cost}$  is the annual costs of the project, RUR 1 980 thousand;

$S_{econ}$  is the project economic effect during the heating period (49 899 + 1 966, RUR thousand), where 49 899 is the plant's loss according to the Finance Department; 1 966 is fuel saving for the period of the ABH operation.

The payback period is:

$$C = 39\,250 / (49\,899 + 1\,966 - 1\,980) \approx 0.79 \quad (10)$$

of heating period.

The formula determines specific capital investment (RUR million) per 1 MW:

$$K = S_{cost} / W_{power} \quad (11)$$

where  $W_{power}$  is the heat capacity of the new equipment, Gcal/h (29.16 MW).

Specific capital investment (RUR million) per 1 Gcal is:

$$K = 39.25 / 29.16 \approx 1.35. \quad (12)$$

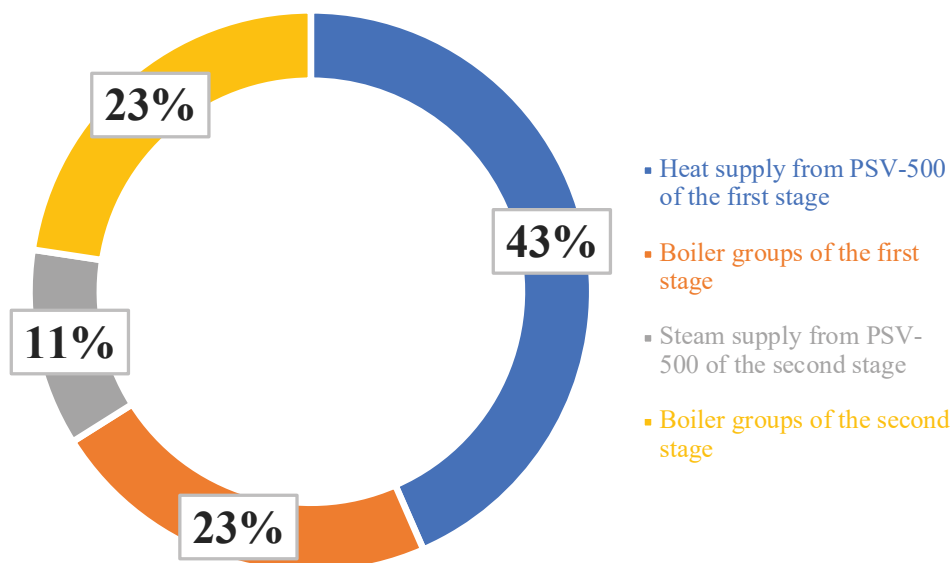


Fig. 6. Unit commitment required to meet heat load at an air temperature of -24°C.

Figure 6 presents the unit commitment necessary to ensure the heating load of consumers. Thus, the most significant heat supply is from PSV-500 of the first stage.

### C. Construction of 110 MW CCGP

Annual fuel saving in hot water heat generation at 110 MW CCGP was calculated according to the following algorithm [20].

Fuel consumption for hot water heat supply under the existing scheme will be:

$$G_{t.o.e.} = (Q_{tg} \cdot b_{t.o.e.-h.y.}) / 1000 = (278\,262 \cdot 147.2) / 1000 \approx 40\,960.2, \quad (13)$$

where  $Q_{tg}$  is heat output for hot water according to the Technical Department.

Fuel consumption for heat production with the 110 MW CCGP in operation will be:

$$G_{ccp} = (Q_{tg} \cdot b_{h/p-ccp-110}) / 1000 = (278\,262 \cdot 126.91) / 1000 \approx 35\,314.23, \quad (14)$$

where  $b_{h/p-ccp-110}$  is specific fuel consumption for heat production at a combined cycle gas plant.

Annual fuel saving for heat supply from the CPP will be:

$$E_{year\ h/p} = G_{t.o.e.} - G_{ccp} = 40\,960.2 - 35\,314.23 = 5\,645.97. \quad (15)$$

The saving was calculated for the following initial conditions:

- the number of utilization hours of 110 MW CCGP is 8 300 h./y.;
- the combined cycle gas plant operates for a base-load power generation of 110 MW.

According to the reported data, the actual electricity output of CPP is 8 662 876 thousand kWh ( $E_{aao}$ ).

The average annual specific consumption of fuel for electricity generation is 349 g/kWh.

Fuel consumption for electricity generation at the whole plant is:

$$G_{t.o.e.} = (8\,662\,876\,000 \cdot 349) / 10^6 \approx 3\,023\,343.7. \quad (16)$$

Power generation at 110 MW CCGP, MWh, is:

$$E_{ccp} = (110\,000 \cdot 8\,300) / 10^3 = 913\,000. \quad (17)$$

Power output from 110 MW CCGP, MWh, is:

$$E_{ccp\ vac.} = (110\,000 \cdot 8\,300) / 10^3 \cdot 0.9404 = 858\,585.2. \quad (18)$$

According to the reported data, the auxiliary power consumption is 5.96%.

Fuel consumption for electricity supply from 110 MW CCGP is:

$$G_{ccp} = (858\,585\,200 \cdot 252.4) / 10^6 \approx 216\,706.9, \quad (19)$$

where 252.4 is specific fuel consumption for electricity supply (Table 8).

Electricity supply by power units of the plant without electricity supply from 110 MW CCGP, MWh, is:

$$E_{eb} = E_{aao} - E_{ccp\ vac.} = 8\,662\,876 - 858\,585.2 = 7\,804\,290.8. \quad (20)$$

Fuel consumption for electricity supply by power units of the plant, excluding 110 MW CCGP, is:

$$G_{t.o.e.-eb} = (E_{eb} \cdot b_{eb}) / 10^6 = (7\,804\,290\,800 \cdot 348.8) / 10^6 \approx 2\,722\,136.6, \quad (21)$$

where  $b_{eb}$  is average specific fuel consumption for electricity generation.

Annual fuel saving for CPP is:

$$E_{year\ e/p} = G_{t.o.e.} - G_{ccp} - G_{t.o.e.-eb} = 3\,023\,343.7 - 216\,706.9 - 2\,722\,136.6 = 84\,500.2. \quad (22)$$

The total annual fuel saving due to the commissioning of 110 MW CCGP will be:

$$E_{year} = E_{year\ h/p} + E_{year\ e/p} = 5\,645.97 + 84\,500.2 = 90\,146.17. \quad (23)$$

The expected economic effect of the project (RUR million) will be:

$$S_{sav.} = E_{year} \cdot Z_f / 10^6 = 90\,146.17 \cdot 4\,700 / 10^6 \approx 423.69, \quad (24)$$

where  $Z_f = 4\,700$  RUR/t.o.e. is the fuel cost.

The formula for calculating the payback period is:

$$PP = S_{cost} / S_{sav.} \quad (25)$$

The simple payback period will be:

$$PP = 5\,000 / 423.69 \approx 11.80.$$

In this case, the specific CapEx per 1 Gcal are determined by the formula:

$$SCI = S_{cost} / W_{power} \quad (26)$$

where  $W_{power}$  is the heat output of the newly introduced equipment, Gcal/h (94.2 MW).

The specific capital investment (RUR million) per 1 MW will be:

$$SCI = 5\,000 / 94.2 \approx 53.08.$$

## IV. CONCLUSION

The optimization option of the heat supply scheme based on the construction of RCU 140/12 with a steam capacity of 50 t/h will partially cover the district heating load of 29.08 MW and 110.45 MW. The remaining power units can operate at a 110 MW load.

The commissioning of ABH with lower parameters partially reduces the plant heating load of 29.16 MW, which provides a heat output of one CPP power unit under "forced" heat generation. The remaining power units can operate at a 110 MW load.

The main criterion for the option of 110 MW CCGP is the replacement of obsolete generating equipment with new capacities.

At the same time, the option of building the 110 MW CCGP with a heat output of 94.2 MW with a calculated

heating load of 195.38 MW does not fully solve the problem of upgrading the heat supply scheme.

With the project period of about 4.5-5 years, there can be considerable losses due to power units operating under the conditions of “forced” heat generation. Nevertheless, it is worth noting that CCGPs are a promising option for the energy industry due to their high efficiency and acceptable payback periods within the framework of power supply contract programs designed to provide the investment in the construction of new generating capacities.

#### ACKNOWLEDGMENTS

The study was carried out within the framework of the scientific project of the Russian Science Foundation (RSF) No 18-79-10136.

#### REFERENCES

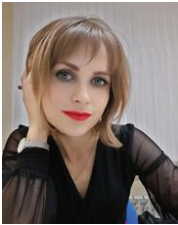
- [1] Tongjun Zhang, “Methods of Improving the Efficiency of Thermal Power Plants,” *Journal of Physics: Conf. Ser.*, vol. 1449, 012001, 2020.
- [2] O.S. Kharitonova, V.V. Bronskaya, T.V. Ignashina, A. Al-Muntaser, and L.E. Khairullina, “Modeling of absorption process using neural networks,” *IOP Conference Series: Earth and Environmental Science*, vol. 315, 032025, 2019.
- [3] Yu.N. Zatsarinnaya, N.A. Staroverova, M.M. Volkova, S.I. Galymullina, and R.K. Khakimzyanov, “Heat supply system computer laboratory stand development,” *IOP Conf. Ser.: Earth Environ. Sci.*, vol. 288, 012131, 2019.
- [4] Soloveva O.V., Solovev S.A., Yafizov R.R. “Determination of the particle deposition efficiency value in a granular and open-cell foam filter,” *IOP Conf. Ser.: Mater. Sci. and Eng.*, vol. 709(3), 033064, 2020.
- [5] D.S. Balzamov, E.Yu. Balzamova, V.V. Bronskaya, T.V. Ignashina, and O.S. Kharitonova, “Analysis of the possibility of modernization of the state district power station by building the combined cycle plant,” *Journal of Physics: Conf. Ser.*, vol. 1515, 042100, 2020.
- [6] G.A. Aminova, G.V. Manuiko, T.V. Ignashina, V.V. Bronskaya, N.E. Kharitonova, G.S. D'yakonov, and V.P. Arkhireev, “Optimal parameters of butadiene polymerization in the synthesis of rubber on a neodymium-containing catalytic system,” *Theoretical Foundations of Chemical Engineering*, vol. 40, pp. 59-67, 2006.
- [7] E.Yu. Balzamova, D.S. Balzamov, V.V. Bronskaya, and O.S. Kharitonova, “Modernization of the scheme for the delivery of thermal power from the state district power station,” *IOP Conf. Ser.: Mater. Sci. Eng.*, vol. 734, 012194, 2020.
- [8] O.V. Soloveva, “Comparison of granular and open-cell foam filter models by numerical simulation,” *IOP Conf. Ser.: Earth and Env. Sci.*, vol. 421(6), 062038, 2020.
- [9] A. Zhigurs, Y. Golunovs, D. Tourlayss, and S. Pliskachev, “Flue gas heat recovery in Riga heat sources,” *Heat Supply News*, vol. 5, pp. 19-24, 2010.
- [10] J.N. Zatsarinnaya, A.G. Logacheva and A.A. Solovyova, “Analysis of thermodynamic efficiency of the fuel preparation systems with an intermediate hopper at thermal power plants,” *IOP Conf. Ser.: Earth Environ. Sci.*, vol. 288, 012130, 2019.
- [11] I.A. Konakhina, A.M. Konakhin, and O.P. Shinkevich, “Thermodynamic analysis of the system for collection and re-use of condensate,” *Bulletin of Ivanovo State Energy University*, vol. 2, pp. 11-14, 2011.
- [12] S.A. Solovev, O.V. Soloveva, B.Sh. Gilmurahmanov and A. Lamberov, “Numerical simulation of a flow mixer for a radial-type chemical reactor,” *IOP Conf. Ser.: Earth Environ. Sci.*, vol. 421, 072017, 2020.
- [13] US 2010/0077722 A1 Peak load management by combined cycle power augmentation using peaking cycle exhaust heat recovery 30.09.2008, General Electric Company, Ajit Singh Sengar, Saravanan Venkataraman Nattanmai, Shivaprasad Lokanath.
- [14] Michael McManus David Boyce Raymond Baumgartner, Integrated Technologies that Enhance Power Plant Operating Flexibility POWER-GEN International 2007 New Orleans, LA Dec 11-13, 2007, © Siemens AG 2007
- [15] H. Emberger, E. Schmid and E. Gobrecht, Fast Cycling Capability for New Plants and Upgrade Opportunities Siemens Power Generation (PG), Germany © Siemens AG 2005.
- [16] V.I. Sharapov and M.E. Orlov, *Technologies for ensuring peak load of heat supply systems*. Moscow: Publishing house “News of Heat Supply,” 2006, 208 p.
- [17] O. Soloveva, S. Solovev, R. Khusainov, R. Yafizov, “Mathematical modeling of heat transfer in open-cell foam of different porosities,” *Advances in Intelligent Systems and Computing*, vol. 1259 AISC, pp. 371-382, 2021.
- [18] A.I. Andryushchenko “Modern problems of heat supply to cities and rational ways to solve them,” *Vestnik SSTU*, No 3, pp. 110-115, 2005.
- [19] V.M. Kravchenko, “Current state of the heat supply industry,” *Report of the Ministry of Energy of Russia*, March 2016, Moscow.
- [20] D.S. Balzamov, I.G. Akhmetova, E.Yu. Balzamova, G.I. Oykina, and V.V. Bronskaya, “Options for organizing own sources of energy supply at the facilities of generating companies based on steam screw machines,” *Journal of Physics: Conference Series*, vol. 1399(5), 055018, 2019.
- [21] E.K. Arakelyan, V.A. Starshinov, *Improving the efficiency and maneuverability of thermal power plants equipment*. Moscow: Publishing house of MEI, 1993, 326 p.



**Denis Balzamor**, Ph.D. in Industrial Heat Power Engineering, Associate Professor of the Department “Power Supply to Enterprises and Energy Saving Technologies” of Kazan State Power Engineering University, Kazan, Russia. Research interests are energy saving at the enterprises of the fuel and energy complex, energy technology combination.



**Irina Akhmetova**, D.Sc. in Industrial Heat Power Engineering, Vice-Rector for Research, Kazan State Power Engineering University, Kazan, Russia. Research interests are optimization of heat supply systems to increase the energy efficiency of heat supply sources.



**Elena Balzamova**, Master of Engineering and Technology in Heat Power Engineering, assistant of the Department of Economics and Organization of Production, Kazan State Power Engineering University, Kazan, Russia. Research interests are feasibility studies of investment projects aimed at increasing energy efficiency.

# Amplitude Sampled Reference-Based Space Vector Pulse Width Modulation for Control of Voltage Source Converters

Mohamed Khalid Ratib\*, Ahmed Rashwan

Department of Electrical Engineering, Faculty of Energy Engineering, Aswan University, Aswan, Egypt

**Abstract** — Memory, speed, reliability, and efficiency are the main characteristics of concern in new contemporary control techniques of electric power converters. Space vector pulse width modulation (SVPWM) is a widespread digital compute-intensive control technique used in the control of power converters. This study aims to overcome the large number of calculations needed by the SVPWM algorithm, which limits its implementation in many advanced industrial applications. This paper presents a low-cost software implemented simplified SVPWM technique. The proposed strategy generates the inverter switching times in a straightforward manner with no need for complicated and time-consuming sector identification and look-up switching tables. A simulation study has been done using MATLAB/SIMULINK environment for the three-phase voltage source converter (VSC). The results in terms of total harmonic distortion (THD) in the converter line voltage are compared for the proposed technique, conventional SVPWM, and space pulse width modulation (SPWM). The execution time is reduced considerably with a slight increase in the value of THD and about 14.4 percent DC-link voltage utilization over the SPWM.

**Index Terms:** Offset voltage, sinusoidal pulse width modulation, space vector pulse width modulation and voltage source converter.

\* Corresponding author.

E-mail: [mohammedkhalid@energy.aswu.edu.eg](mailto:mohammedkhalid@energy.aswu.edu.eg)

<http://dx.doi.org/10.38028/esr.2021.02.0005>

Received July 26, 2021. Revised July 01, 2021.

Accepted July 11, 2021. Available online July 23, 2021.

This is an open access article under a Creative Commons Attribution-NonCommercial 4.0 International License.

© 2021 ESI SB RAS and authors. All rights reserved.

## I. INTRODUCTION

Electrical energy conversion is a common term nowadays [1]. Electrical energy conversion devices are ordinarily named converters. Electrical power converters have become extensively used with various types and ratings ranging from low voltage to high voltage in many industrial applications [2], [3]. Optimum voltage vectors can be exerted to the power grid or attached loads by various electrical power converters such as two-level voltage source converter (2L-VSC), matrix converter, AC / AC voltage converter, and multilevel inverters. In the midst of all these, the three-phase 2L-VSC is an interesting topology used in almost all drive applications because it covers both medium and high-power range applications.

Besides, these converters can be controlled by many control techniques, which all aim to improve the converter efficiency by reducing the switching power loss and the ratio of total harmonic distortion (THD) in the converter output voltage [4], [5]. Among these control approaches, pulse width modulation (PWM) is the most common control method used in industrial applications these days. PWM has many different techniques [6], [7]. Sinusoidal and space vector pulse width modulations (SPWM, SVPWM) are the most well-known techniques among the PWM methodologies. The PWM technique is reliable when the current or voltage required for driving a typical load are to be obtained. Due to the lower harmonic current and the maximum output voltage conducted to load, the PWM procedure is generally used for AC drives [8], [9]. The vital objective in all PWM methods is to generate the necessary amplitude and frequency of the fundamental frequency component along with a reduction in the THD value [10], [11].

Carrier-based sinusoidal PWM generates gating signals for switches by comparing a modulating signal with a triangular carrier signal [4]. These modulating signals are usually three-phase sinusoidal reference waveforms. SPWM has a relatively high current harmonic content and THD

Table 1: Switching states and space vectors of the three-phase 2L-VSC.

Switching state			Switches			$V_n$	States	$V_0$	$\alpha_0$
$S_A$	$S_B$	$S_C$							
1	0	0	$S_1$	$S_4$	$S_6$	$V_1 = \frac{2}{3}V_{dc}$	+1	$\frac{2}{3}V_{dc}$	0
1	1	0	$S_1$	$S_3$	$S_6$	$V_2 = \frac{1}{3}V_{dc} + j\frac{\sqrt{3}}{2}V_{dc}$	+2	$\frac{2}{3}V_{dc}$	$\frac{\pi}{3}$
0	1	0	$S_2$	$S_3$	$S_6$	$V_3 = -\frac{1}{3}V_{dc} + j\frac{\sqrt{3}}{2}V_{dc}$	+3	$\frac{2}{3}V_{dc}$	$\frac{2\pi}{3}$
0	1	1	$S_2$	$S_3$	$S_5$	$V_4 = -\frac{2}{3}V_{dc}$	-1	$-\frac{2}{3}V_{dc}$	0
0	0	1	$S_2$	$S_4$	$S_5$	$V_5 = -\frac{1}{3}V_{dc} - j\frac{\sqrt{3}}{2}V_{dc}$	-2	$-\frac{2}{3}V_{dc}$	$\frac{\pi}{3}$
1	0	1	$S_1$	$S_4$	$S_5$	$V_6 = \frac{1}{3}V_{dc} - j\frac{\sqrt{3}}{2}V_{dc}$	-3	$-\frac{2}{3}V_{dc}$	$\frac{2\pi}{3}$
0	0	0	$S_2$	$S_4$	$S_6$	$V_0 = 0$	$0_0$	0	—
1	1	1	$S_1$	$S_3$	$S_5$	$V_7 = 0$	$0_7$	0	—

value compared with more sophisticated PWM methods; and, SVPWM is one of these methods [12]. SVPWM relies on the space vector distribution of a typical converter, and a specific reference voltage vector is synthesized by two active voltage vectors and one zero vector. The time values related to these three vectors are calculated and distributed according to some preferred time sequencing diagrams [13], [14]. Considering these time values for six sectors, a modified modulating signal is obtained and compared with a triangular carrier signal to get the switching pulses for all switches in a converter.

SVPWM is a superior digital PWM technique with many admirable advantages. It is a sophisticated, compute-intensive, and possibly the best of all PWM methods for variable frequency drive applications [15]. However, a large number of calculations and incredible computational effort are essentially the main drawbacks of space vector modulation (SVM) [16]. A new simplified approach based on the principle of adding an offset voltage to the original sinusoidal phase reference signal to obtain a re-shaped signal to be used as a modulating signal has been developed in recent years [17]. This approach can be used with all PWM procedures.

Following this procedure, SVM could be interestingly simplified and the modulating wave of SVPWM be generated directly from the three sinusoidal phase reference voltages [18]. Without any computational effort or time-consuming calculations, SVM is introduced here in this work with MATLAB simulation to support and reinforce the use of VSCs controlled with this method for AC drives and industrial applications.

The main contribution of this paper is a software-coded and implemented method for SVPWM simplification. This work also presents a comparative analysis of software implemented techniques (SPWM, conventional SVPWM, and the simplified SVPWM). Furthermore, the application of the offset voltage procedure to simplify SVM in a programmable code implementation is an intrinsic aim in this paper. Section II of this paper briefly considers VSCs and a basic power circuit for the three-phase 2L-VSC. Section III briefly presents and explains the pulse duration modulation techniques. Section IV contains the parameters and results of MATLAB simulation and related discussion. Section V concludes the results expected from the proposed method, and, finally, the references used are listed at the end of this paper.

## II. POWER CIRCUIT FOR THE THREE-PHASE 2L-VSC

A VSC generates AC voltage from a DC voltage, and it can transfer power in either direction. The DC voltage always has one polarity, and the power reversal occurs through the current polarity reversal. With a voltage source converter, output voltage magnitude and frequency can be controlled independently. VSCs have many different configurations and topologies for single and three-phase systems [19], [20]. The two-level neutral-point-clamped converter, modular multilevel converter (MMC), variant MMC, and alternate-arm converter (AAC) are all types of voltage source converters. There are also hybrid VSC systems, which aim to achieve low losses and high harmonic performance of MMC with a more compact design and greater controllability, but these concepts are still under research [21], [22].

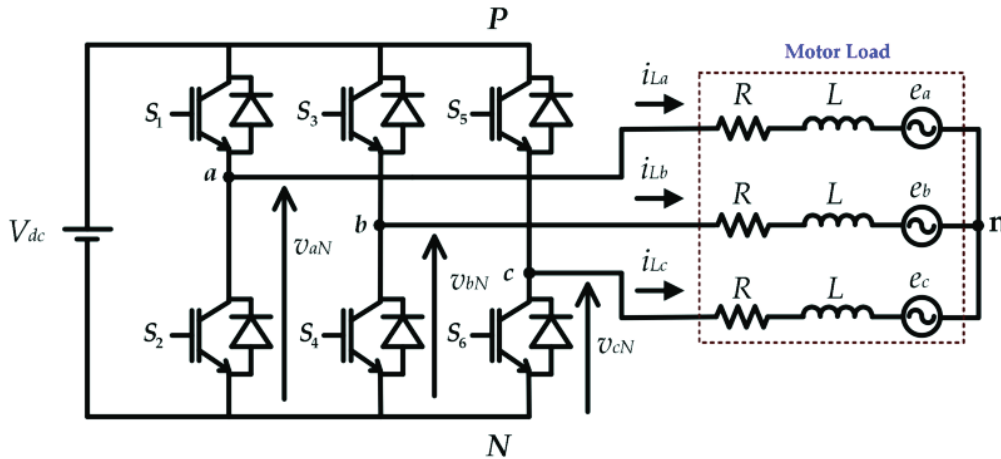


Fig. 1. 2L-VSC with an RL load [23]

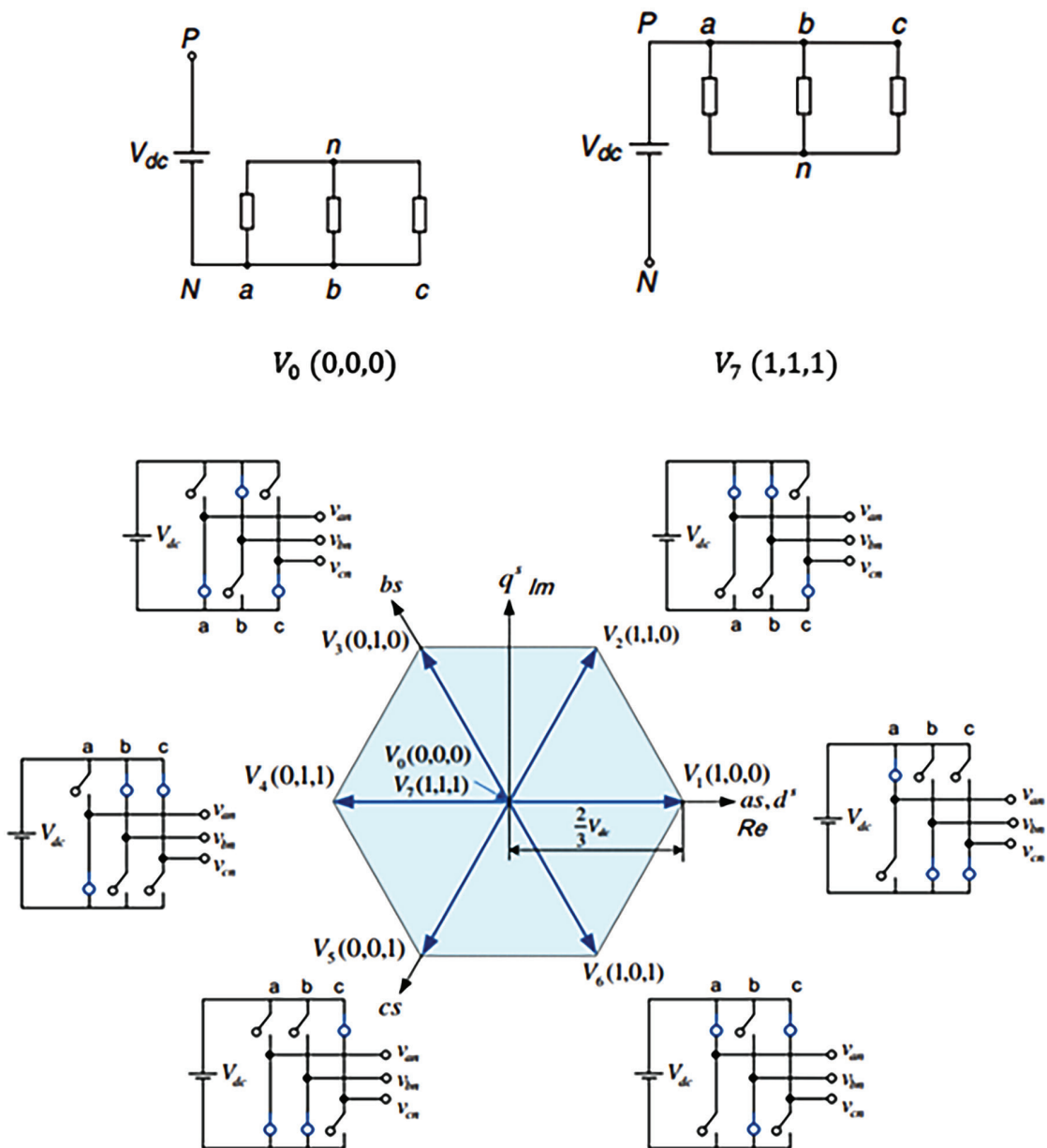


Fig. 2. Output voltage vectors of the three-phase inverter with associated switching states in the complex  $\alpha$ - $\beta$  plane.

This paper focuses on 2L-VSC since it is the simplest one for implementation in most of the electrical power conversion systems found today. The electric circuit studied here consists of a constant DC voltage source and a three-phase 2L-VSC connected with an RL load.

### 1. Power Circuit of 2L-VSC

The three-phase 2L-VSC has six power switches ( $s_1 - s_6$ ) in its power circuit, as shown in Fig.1 [23]. These switches should operate in a complementary mode to avoid the DC source short-circuit. The switching state of each of the power switches  $S_x$  with  $x = 1 \dots 6$ , can be declared with switching signals  $S_a$ ,  $S_b$ , and  $S_c$  corresponding to three phases as follows:

$$S_a = \begin{cases} 1 & \text{when } S_1 \text{ ON and } S_4 \text{ OFF,} \\ 0 & \text{when } S_1 \text{ OFF and } S_4 \text{ ON,} \end{cases} \quad (1)$$

$$S_b = \begin{cases} 1 & \text{when } S_2 \text{ ON and } S_5 \text{ OFF,} \\ 0 & \text{when } S_2 \text{ OFF and } S_5 \text{ ON,} \end{cases} \quad (2)$$

$$S_c = \begin{cases} 1 & \text{when } S_3 \text{ ON and } S_6 \text{ OFF,} \\ 0 & \text{when } S_3 \text{ OFF and } S_6 \text{ ON.} \end{cases} \quad (3)$$

The inverter output voltages can be defined with these switching signals as:

$$v_{aN} = S_a V_{dc}, \quad (4)$$

$$v_{bN} = S_b V_{dc}, \quad (5)$$

$$v_{cN} = S_c V_{dc}, \quad (6)$$

where  $V_{dc}$  is the DC voltage connected to the inverter.

Considering the unit vector  $\mathbf{a} = e^{j2\pi/3} = -\frac{1}{2} + \frac{j\sqrt{3}}{2}$  which represents the 120° phase displacement between the phases, the output voltage vector can be defined as:

$$V_0 = \frac{2}{3} (v_{aN} + \mathbf{a}v_{bN} + \mathbf{a}^2v_{cN}) = V_{max} \cdot e^{j\alpha}, \quad (7)$$

Where  $v_{aN}$ ,  $v_{bN}$ , and  $v_{cN}$  are the phase-to-neutral ( $N$ ) voltages of the inverter. Various voltage vectors can be produced when the available switching states are applied to the inverter power circuit due to different configurations of the three-phase load connection to the DC source. The three-phase inverter has eight possible switching states that result in eight inverter output voltage vectors. These voltage vectors are listed in Table. 1, and shown in Fig. 2, as six active vectors distributed in space and two zero vectors located at the origin of the complex  $\alpha$ - $\beta$  plane. All the six voltage vectors have the same magnitude of  $\frac{2}{3}V_{dc}$  but are displaced from each other by 60 degrees in space. As shown in Fig.2, the zero vectors  $V_0$  and  $V_7$  are equal to zero and located at the origin in the complex  $\alpha$ - $\beta$  plane.

### 2. Pulse-duration modulation techniques for inverters

Pulse-duration modulation (PDM) or pulse-width modulation (PWM), is a method of controlling the average

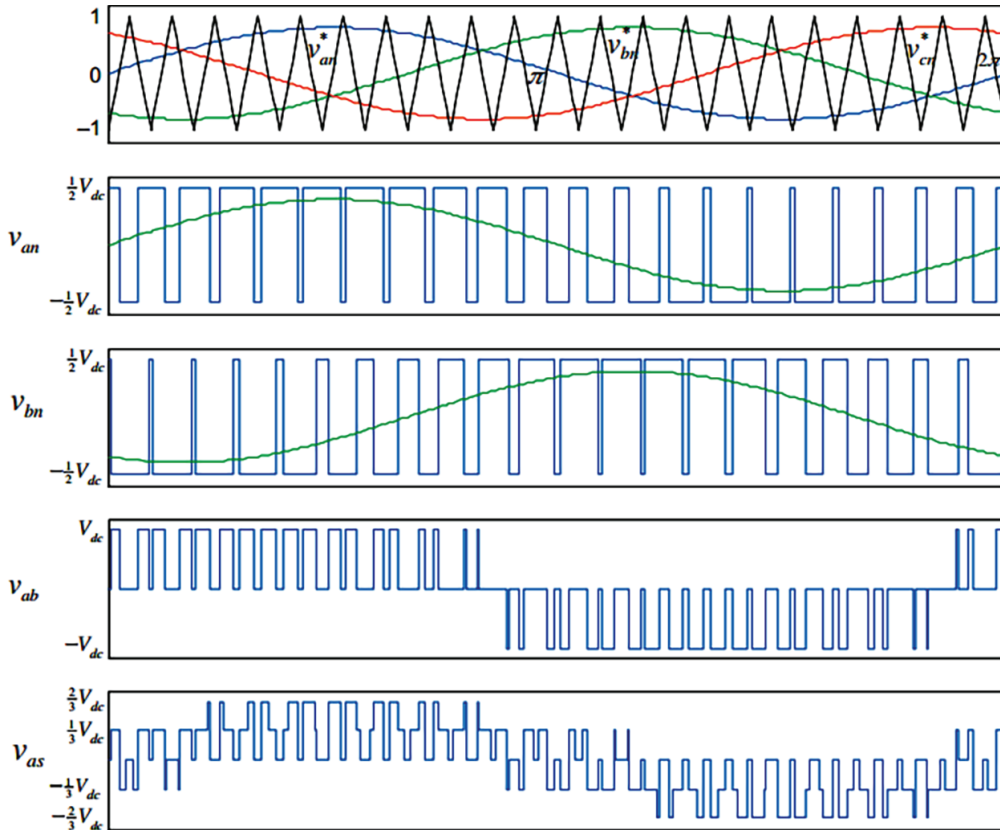


Fig. 3. SPWM technique for the three-phase two-level inverter [18]

power delivered by an electrical signal by effectively chopping it up into discrete parts. The average value of voltage (and current) fed to the load is controlled by quickly turning the switch on and off. The longer the switch is on compared to the off periods, the higher the total power supplied to the load. PWM is particularly suited for inertial loads such as motors, which are not easily affected by this discrete switching because they have inertia to react slowly [24]. The PWM switching frequency has to be high enough not to affect the load, and the waveform perceived by load should be as smooth as possible. The main advantage of PWM is that power loss in the switching devices is very low. When a switch is off, there is practically no current, and when it is on and power is transferred to load, there is almost no voltage drop across the switch. Power loss, i.e., the product of voltage and current, is thus in both cases close to zero. PWM also works well with digital controls, which, because of their on/off nature, can easily set the needed duty cycle.

PDM can be used effectively in the control of VSCs, and it usually has various techniques. These control techniques are classified and depicted in [18]. This paper is dedicated to the study and analysis of output waveforms and performance of 2L-VSC with two of these main techniques plus a modified version of one of them:

- a. Carrier-based SPWM;
- b. SVPWM or SVM (Continuous - Symmetrical PWM);
- c. SVPWM with a reduced computational burden.

It is worth noting that the switching frequency of high-power converters is constricted to some low values of 350 Hz to 1 kHz to reduce/minimize the switching losses. This results in low values of  $m_f$  that can be defined as the ratio of switching frequency to fundamental component frequency, where  $f_{sw} = f_{cr}$  for 2L-VSC, which, in turn, makes the inverter output voltage rich in harmonics. For this reason,  $m_f$  should be a multiple of three to achieve symmetry, and the output voltage should be synchronized with its fundamental component to eliminate subharmonics.

### 3. The SPWM technique for three-phase 2L-VSC

The basis of the sinusoidal PWM technique for the three-phase 2L-VSC is shown in Fig. 3, where  $v_{an}^*$ ,  $v_{bn}^*$ , and  $v_{cn}^*$  are the three-phase modulating signals and  $v_{cr}$  is the triangular carrier signal.

The amplitude and frequency of the fundamental frequency component of the inverter output voltage can be controlled independently by the amplitude modulation index and frequency of the modulating waves, respectively.

The amplitude and frequency modulation indexes are defined by:

$$m_a = \frac{V_m}{V_{cr}}, \quad m_f = \frac{f_{cr}}{f_m},$$

where  $V_m$ ,  $f_m$ , and  $V_{cr}$ ,  $f_{cr}$  are the modulating and carrier maximum voltage and frequency, respectively.

For linear modulation, the modulation index should be in a range of  $0 \leq m_a \leq 1$  for the inverter output voltage to

be directly proportional to the reference voltage. When  $m_a \geq 1$ ,  $V_m \geq V_{cr}$  and the case called overmodulation occurs, where the inverter output voltage is no longer linearly proportional to the reference voltage. The maximum output line-to-line voltage that could be obtained with the SPWM technique used is about  $0.612V_{dc}$ .

### 4. The SVPWM technique for three-phase 2L-VSC with the conventional algorithm

PWM has many different techniques with various bases; Unlike the SPWM where the three-phase reference voltages are modulated individually, the SVPWM uses a different approach of transforming the rotating three-phase reference voltages to two voltages in the stationary reference frame, where they are expressed as a space vector  $V_{abc}$  in the complex  $\alpha$ - $\beta$  plane.

The SVPWM method is an advanced compute-intensive PWM technique, and it is one of the best techniques for real-time modulation, which is why it is widespread in the digital control of VSCs and variable-frequency drive applications [25],[26].

The three-phase 2L-VSC has six active vectors ( $V_1$  to  $V_6$ ) that divide the plane into six sectors in space (each one spans 60 degrees in space) and two zero vectors ( $V_0$ ,  $V_7$ ). With SVM technique, the reference voltage  $V_{ref}$  is synthesized in various sectors by two adjacent non-zero vectors and one zero vector to produce a voltage that has the same fundamental volt-second average as the given reference voltage vector  $V_{ref}$  over the modulation period  $T_s$ .

If the voltage reference vector is located in sector ①, as shown in Fig. 4, the inverter cannot generate this reference voltage vector directly because the inverter has no output voltage vector that has the same magnitude and phase angle as this reference voltage vector. Instead, and according to Table 2, this reference vector can be synthesized from the inverter output voltage vectors based on the average Volt-Second Principle using two adjacent active vectors  $V_1$  and  $V_2$ , and zero vector  $V_{0/7}$  as follows: firstly, the voltage vector  $V_1$  is applied with a duty time  $T_a$ , which results in an output voltage of magnitude  $V_1 \cdot (T_a / T_b)$  and the same direction as  $V_1$ ; secondly, another vector  $V_2$  is applied to time  $T_b$  to meet the magnitude and phase of the reference voltage vector  $V_{ref}$ . An output voltage, the same as the reference voltage, can be obtained using these two steps over the modulation period  $T_s$ . Lastly, if the sum of  $T_a$  and  $T_b$  is less than the modulation period  $T_s$ , one zero vector  $V_{0/7}$  is applied for the rest of the time, where  $T_0 = T_s - T_a - T_b$ . These three steps are presented in Fig. 5.

The dwell time durations  $T_0, T_a, T_b$  can be determined by the Volt-Second Principle that can be expressed mathematically as:

$$\int_0^{T_s} \vec{V}_{ref} \cdot dt = \int_0^{T_a} \vec{V}_1 \cdot dt + \int_{T_a}^{T_a+T_b} \vec{V}_2 \cdot dt + \int_{T_a+T_b}^{T_s} \vec{V}_{0/7} \cdot dt \quad (8)$$

Assuming a constant DC-link voltage, we can write equation (8) in sector ① as:

$$\vec{V}_{ref} \cdot T_s = \vec{V}_1 \cdot T_a + \vec{V}_2 \cdot T_b + \vec{V}_{0/7} \cdot T_0, \quad (9)$$

$$T_s = T_a + T_b + T_0. \quad (10)$$

The space vectors in (9) are expressed in polar form:

$$\vec{V}_{ref} = V_{ref} e^{j\theta}, \quad \vec{V}_1 = \frac{2}{3} V_{dc}, \quad \vec{V}_2 = \frac{2}{3} V_{dc} e^{j(\pi/3)}. \quad (11)$$

Decompose equation (9) into its real and imaginary components:

$$\begin{cases} Re: & V_{ref} (\cos \theta) T_s = \frac{2}{3} V_{dc} T_a + \frac{1}{3} V_{dc} T_b, \\ Im: & V_{ref} (\sin \theta) T_s = \frac{1}{\sqrt{3}} V_{dc} T_b. \end{cases} \quad (12)$$

Solve two parts of equation (12) together with  $T_s = T_a + T_b + T_0$ :

$$T_a = T_s m_a \sin(\pi/3 - \theta), \quad (13)$$

$$T_b = T_s m_a \sin(\theta), \quad (14)$$

$$T_0 = T_s - T_a - T_b. \quad (15)$$

Note that  $m_a$  is the Modulation Index, and  $m_a = \frac{\sqrt{3} V_{ref}}{V_{dc}}$  for SVM.

Similar calculations can be made for the duration times for the reference voltage vector in the remaining sectors ② – ⑥.

The sequence, in which these dwell times calculated with (13), (14), and (15) are placed, is characteristic; the SVPWM scheme where the effective voltage vectors are placed in the middle of the modulation time interval is called symmetrical SVPWM, and this placement technique shows superior harmonic characteristics.

Table 2: The voltage vectors available in each sector for reference voltage vector formation.

Angle $ \theta_{sector} $	$\frac{\pi}{3}$	$\frac{2\pi}{3}$	$\pi$	$\frac{4\pi}{3}$	$\frac{5\pi}{3}$	$2\pi$
Included Vectors	$V_1, V_2$	$V_2, V_3$	$V_3, V_4$	$V_4, V_5$	$V_5, V_6$	$V_6, V_1$
Sector Number ( $S_N$ )	1	2	3	4	5	6

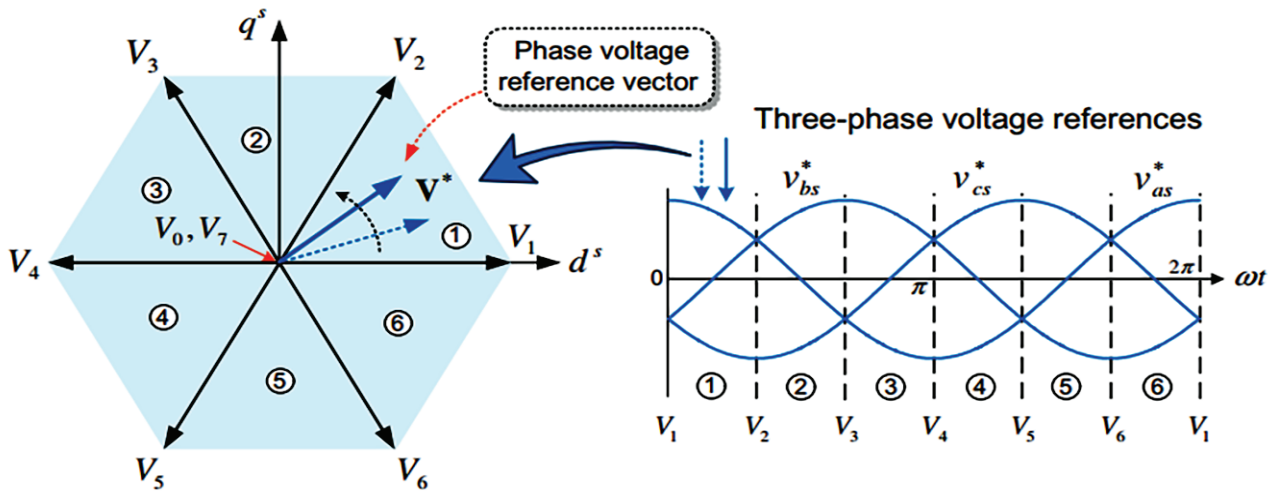


Fig.4. Reference vector rotation in the complex plane [18]

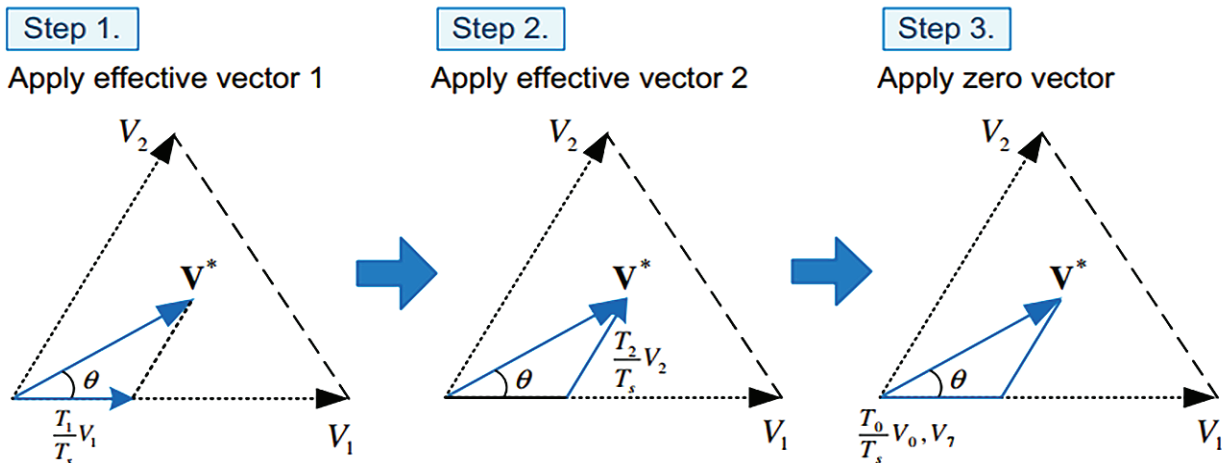


Fig. 5. Reference voltage vector generation process using two inverter-active voltage vectors [18].

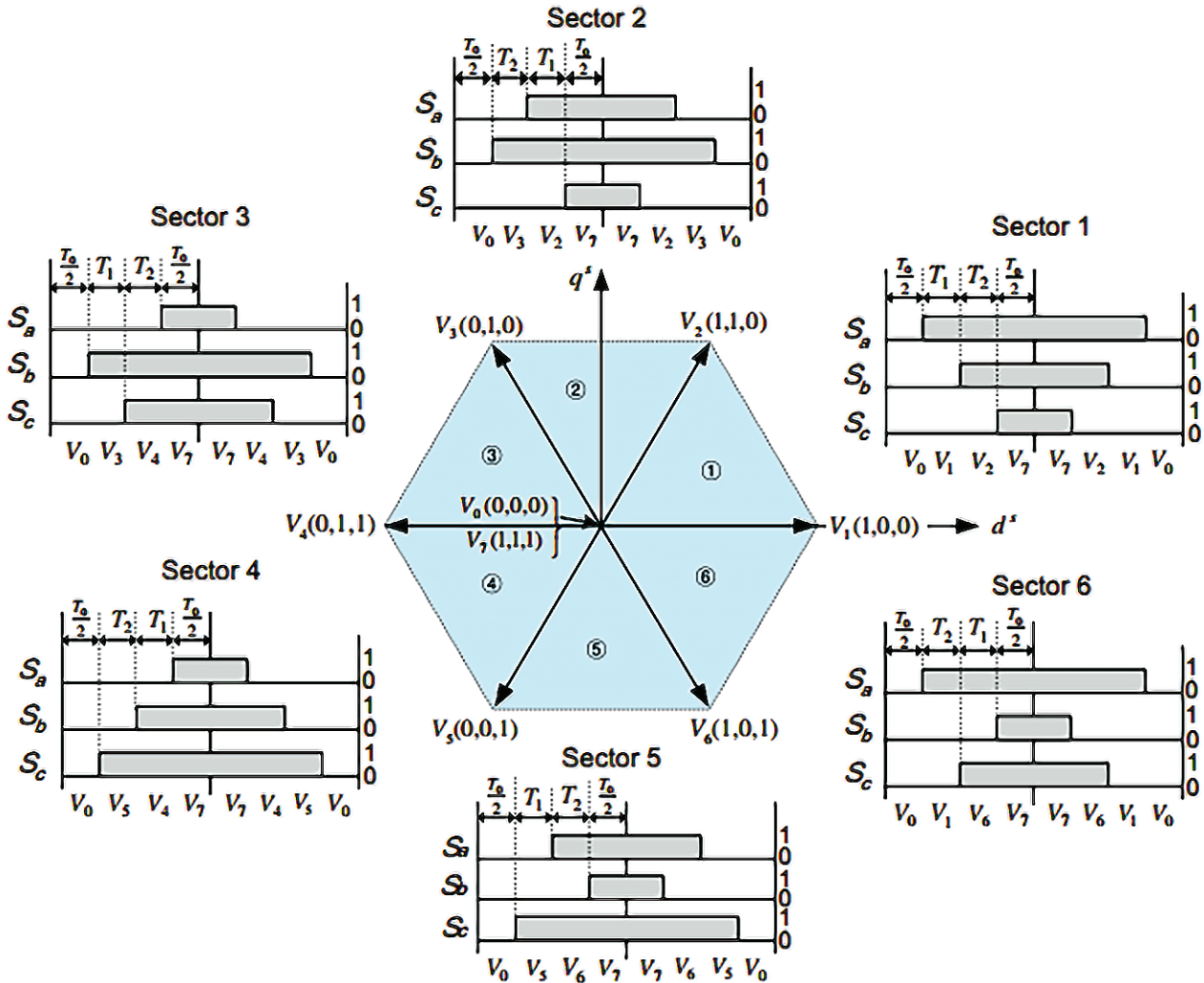


Fig. 6. Switching sequences in six sectors [18].

In this technique, time  $T_0$  of the two zero vectors  $V_{0/7}$  is equally divided and distributed at the beginning and end of the modulation time interval  $T_s$ . This will result in a minimum switching frequency since every switch in the inverter is switched only once from an on state to an off state or vice versa in one sampling time interval.

The switching sequences in all six sectors for the symmetrical SVPWM technique are shown in Fig.6. The maximum magnitude of the reference voltage vector  $V_{ref,max}$  corresponds to the radius of the largest circle inscribed in the hexagon, as explained in [18]. This radius equals  $V_{dc} / \sqrt{3}$ , which is the maximum fundamental phase voltage achieved with the SVPWM technique. This value is about 15.5% larger than that of the SPWM technique. Substituting this value in  $m_a$ , we can find the maximum modulation index for SVM as:

$$m_{a,max} = \frac{\sqrt{3} (V_{dc} / \sqrt{3})}{V_{dc}} = 1,$$

from which the modulation index for the SVM scheme is in the range of

$$0 \leq m_a \leq 1. \tag{16}$$

### 5. SVPWM technique for three-phase 2L-VSI with a reduced computational burden method

The conventional SVPWM has superior advantages and is preferable in many applications, but it also has its disadvantages. The conventional SVPWM scheme requires a whole host of calculations and a trigonometric computational effort to calculate the switching times of active voltage vectors. Nowadays, however, with the continuous technological advancement and development of more intelligent microprocessors and faster switching devices, nothing remains as it was before, and new techniques and methodologies are proposed, including the one presented in this study.

The presented method can considerably reduce the number of calculations and computational burden and make the concept of SVPWM more simple and more intuitive. The proposed SVPWM method is easily implemented by the carrier-based PWM technique based on the offset voltage procedure [18].

In the two-level sinusoidal PWM inverter, each reference phase voltage is compared with the triangular

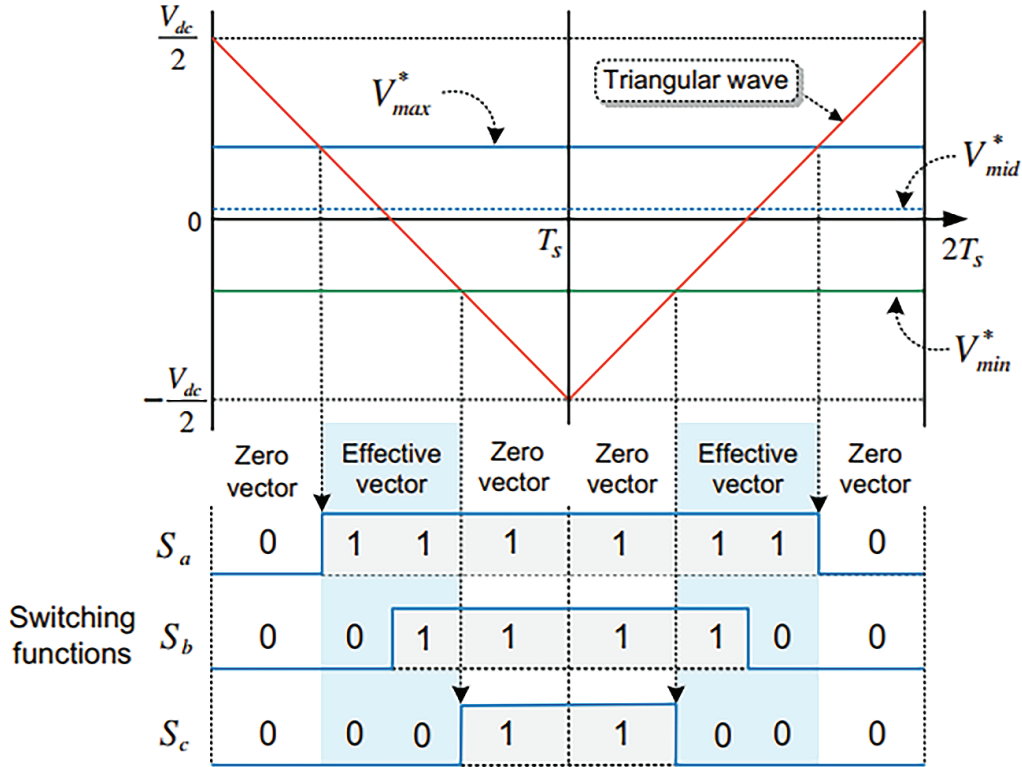


Fig.7. Centering the effective voltage vectors for symmetrical SVPWM [18].

carrier signal, and separate pole voltages are produced independently of one another. In the presented technique, a common-mode voltage is applied to the reference phase voltages to achieve the maximum possible peak amplitude of the fundamental phase voltage in linear modulation [27], where the magnitude of this common-mode voltage is determined from:

$$V_{CM} = -\frac{V_{max} + V_{min}}{2}. \quad (17)$$

In equation (17),  $V_{max}$  is the maximum magnitude of the sequenced three-phase voltages, while  $V_{min}$  is the minimum magnitude of the three sequenced reference phase voltages. The introduction of this common-mode voltage in a sampling time interval results in centering the inverter-active vectors in the time interval as presented in Fig.7, making the SVPWM equivalent to the linear SPWM. To determine the reference pole voltages directly from the reference phase voltages, we first need to read the sampled instantaneous reference phase voltages  $V_{as}$ ,  $V_{bs}$ ,  $V_{cs}$ , and then calculate the time equivalent of these voltages termed as  $T_{as}$ ,  $T_{bs}$ , and  $T_{cs}$ , respectively.

$$T_{as} = \frac{V_{as}}{V_{dc}} T_s, \quad (18)$$

$$T_{bs} = \frac{V_{bs}}{V_{dc}} T_s, \quad (19)$$

$$T_{cs} = \frac{V_{cs}}{V_{dc}} T_s. \quad (20)$$

Sort these times to find  $T_{max}$  and  $T_{min}$ , then the time corresponding to the common-mode offset voltage can be found from

$$T_{offset} = (1/2)[T_s - (T_{max} + T_{min})] \quad (21)$$

and the pole voltage times are found from

$$\begin{aligned} T_{ga} &= T_{as} + T_{offset} \\ T_{gb} &= T_{bs} + T_{offset} \\ T_{gc} &= T_{cs} + T_{offset} \end{aligned} \quad (22)$$

where  $V_{dc}$  is the DC-link voltage,  $T_s$  is the sampling time, and  $T_{ga}$ ,  $T_{gb}$ ,  $T_{gc}$  are the reference pole voltage-time equivalents. When these time signals are compared with the carrier-based triangular wave, the outputs are the gating signals for the upper switches in each inverter leg to be turned on. With the procedure of the aforementioned equations (18)–(22), the reference pole voltages are directly determined from the reference phase voltages without any heavy calculations or computational effort mentioned. A schematic diagram for this operation is introduced in Fig.8.

Since the offset voltage can be freely determined within specific limitations, in this way, many PWM techniques can be directly incorporated by using a convenient offset voltage depending on the reshaped pole voltage reference, and this alteration leads to a shift in the zero-vector time distribution. Thus, without any change in its duty cycle, the position of the effective voltage can be relocated in the sampling interval, as the three-pole voltage references are changed with the offset voltage.

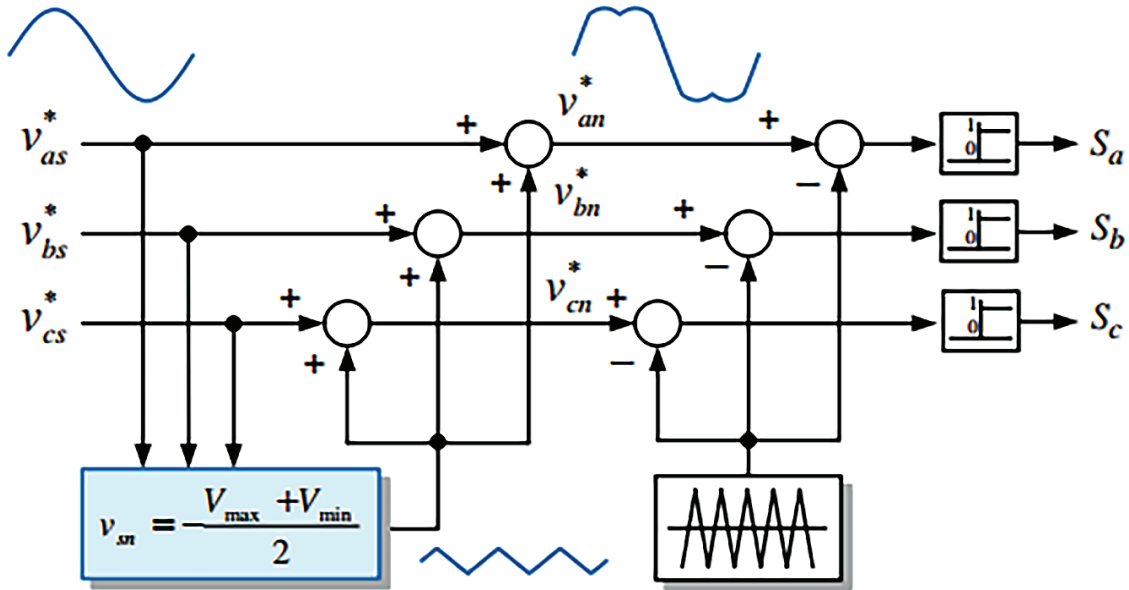


Fig.8. Equivalent SVPWM technique using the offset voltage [18].

6. The overall control procedure

The proposed simplified SVPWM for the three-phase 2L-VSC -fed RL load can be summarized as follows:

- Step 1: Sample the three-phase sinusoidal reference voltages, determine the associated time equivalents by equations (18) to (20).
- Step 2: Sort these times to find  $T_{max}$  and  $T_{min}$ .
- Step 3: Calculate the offset voltage-time equivalent  $T_{offset}$  using (21).
- Step 4: Add the time offset calculated in step 3 and the equivalent time references to find the pole voltage times from (22).
- Step 5: Compare the waveforms that result from step 4 with the triangular carrier signal to find switching pulses of the upper switch in each inverter leg.

III. SIMULATION RESULTS AND DISCUSSION

To assess the performance of the proposed simplified SVPWM method based on the offset voltage, the output characteristics were compared with the conventional SVPWM and the SPWM procedures using MATLAB/SIMULINK software. The simulation results and expected performance of the three techniques, including SPWM, conventional SVPWM, and the proposed reduced SVPWM with an offset signal, are shown ordered in each Figure with (a), (b), and (c), respectively.

The simulation conditions are constant DC-link voltage  $V_{dc} = 400$  V, modulating signal frequency  $f_m = 50$  Hz, frequency modulation index  $m_f = 9, 15$ , and variable amplitude modulation index  $m_a = 0.1, 0.9$ , and  $1.15$ , with the inverter output connected to an RL load with  $R = 10 \Omega$ ,  $L = 100$  mH. Simulation is performed for  $f_{cr} = 450$  Hz and  $750$  Hz corresponding to  $m_f = 9, 15$  to achieve synchronization and waveform symmetry [28]. The system

steady-state is investigated with the three algorithms. The results for modulation indexes  $0.1, 0.9$ , and  $1.15$  are presented in Fig. 9, Fig. 10, and Fig. 11 for  $m_f = 9$ , and in Fig. 12, Fig. 13, and Fig. 14 for  $m_f = 15$ , respectively. The sampling time for all three algorithms is  $T_s = (1/f_{cr})$  s, given that  $f_{cr} = m_f \times f_m$ .

It is worth mentioning that the execution time for the proposed method is shorter than that of the conventional SVM since the number of sector-time calculations is reduced considerably in the former. Close inspection shows that the output voltage produced by the presented technique is closer to the result from the SPWM than that of the conventional SVPWM, although its harmonic content is less than that of SPWM but higher than that of the conventional SVPWM. The fast Fourier transform (FFT) analysis of the inverter line voltage with the three techniques is shown in Fig. 15.

The data shown in the Figure indicate that the conventional SVM has the fundamental output voltage of  $363.7$  V, which is  $0.167$  times more than that of the SPWM ( $311.6$  V), while the fundamental output voltage of the simplified SVM ( $357$  V) is  $0.144$  times greater than the fundamental line voltage of the SPWM. The THD values are  $79.28\%$ ,  $62.27\%$ , and  $65.38\%$  for the three methods (SPWM, conventional SVPWM, and simplified SVPWM), respectively. Such results assure that the technique proposed can be implemented instead of the conventional SVM control method with the benefit of getting a shorter execution time and similar performance parameters like peak output voltage and THD value. Shorter execution time opens the way for a lower-cost microprocessor to be used for implementing such a control circuit, in addition to fast response and lower memory usage characteristics, which will be achieved with the simplified SVM control method.

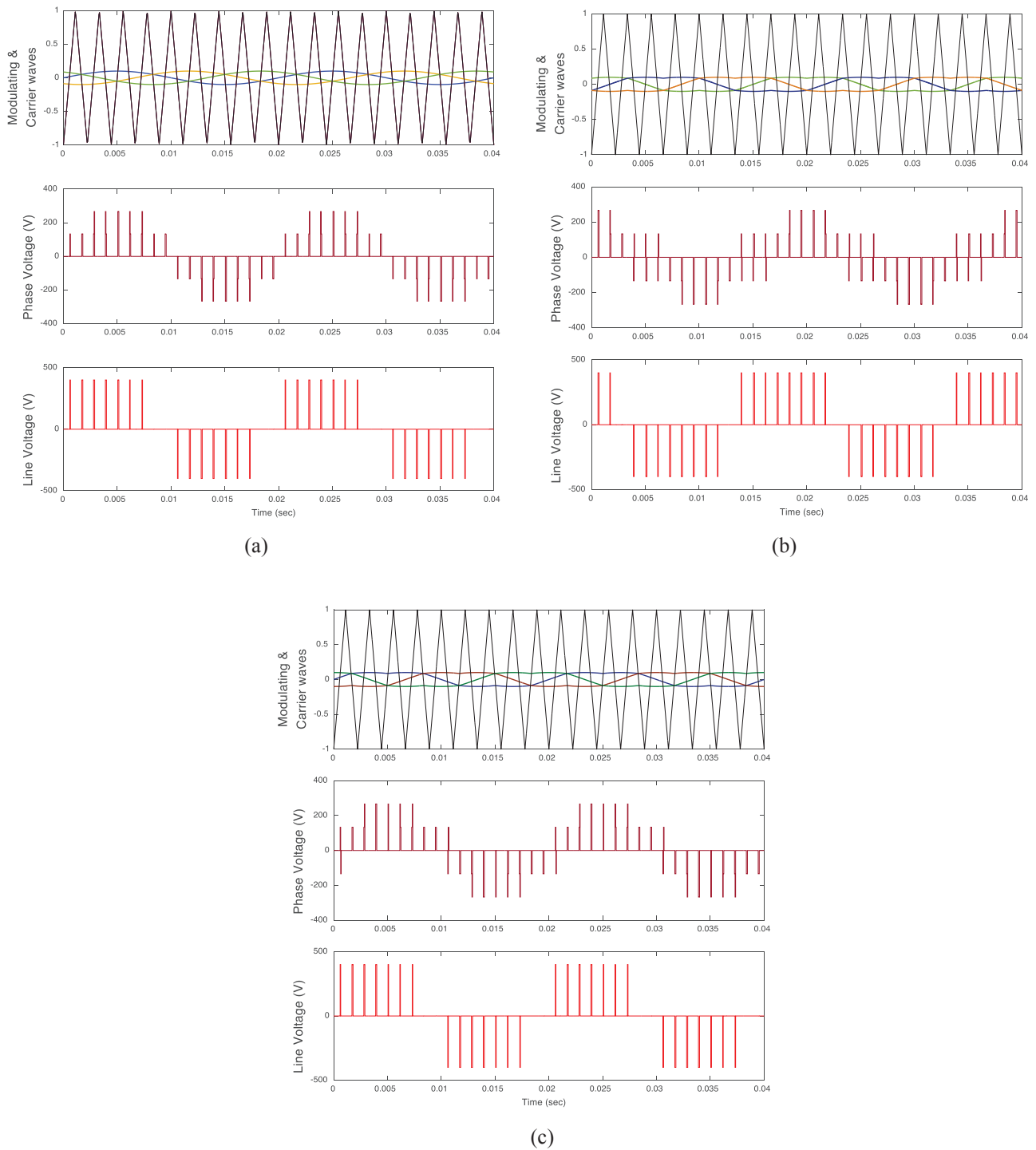
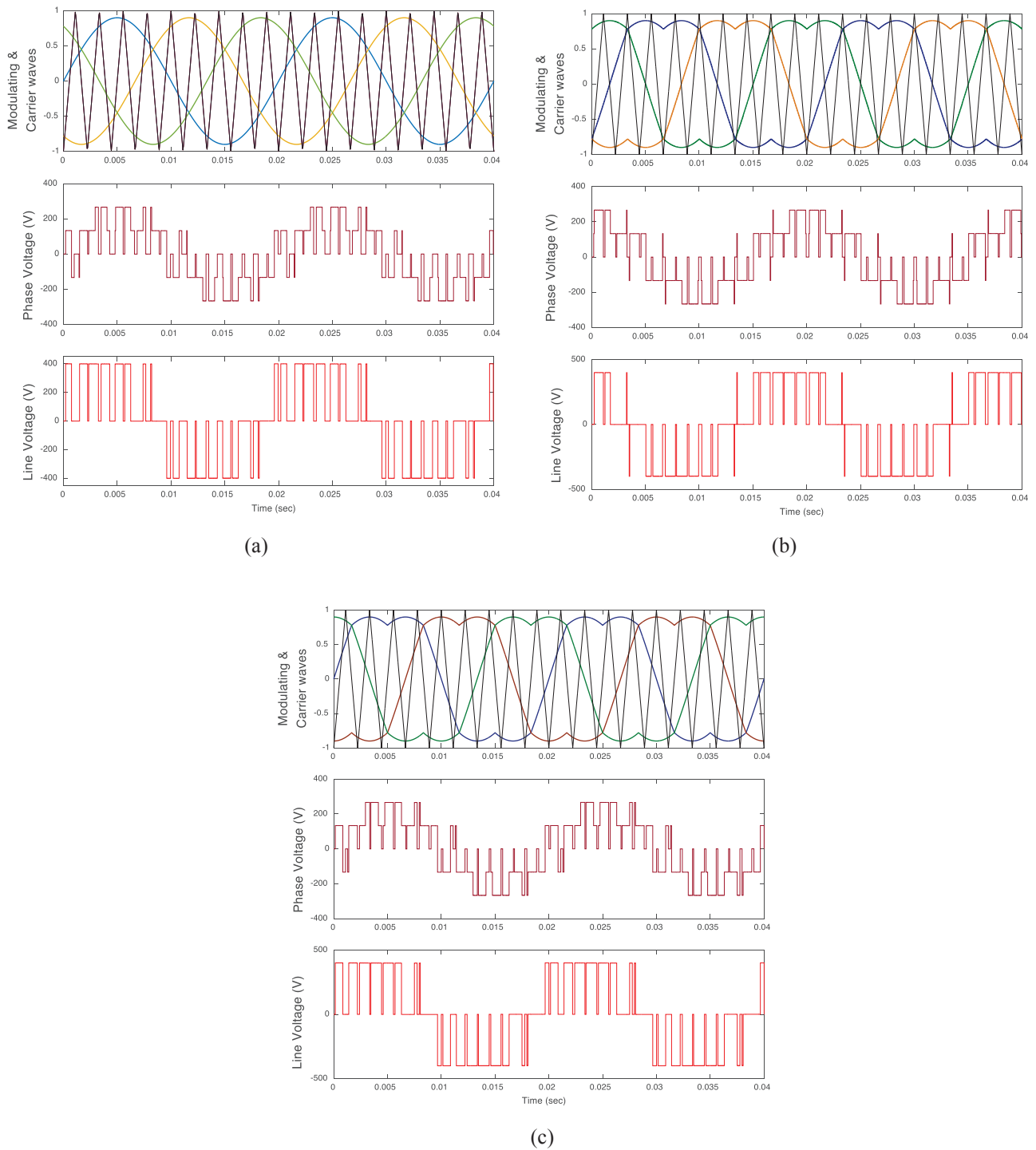
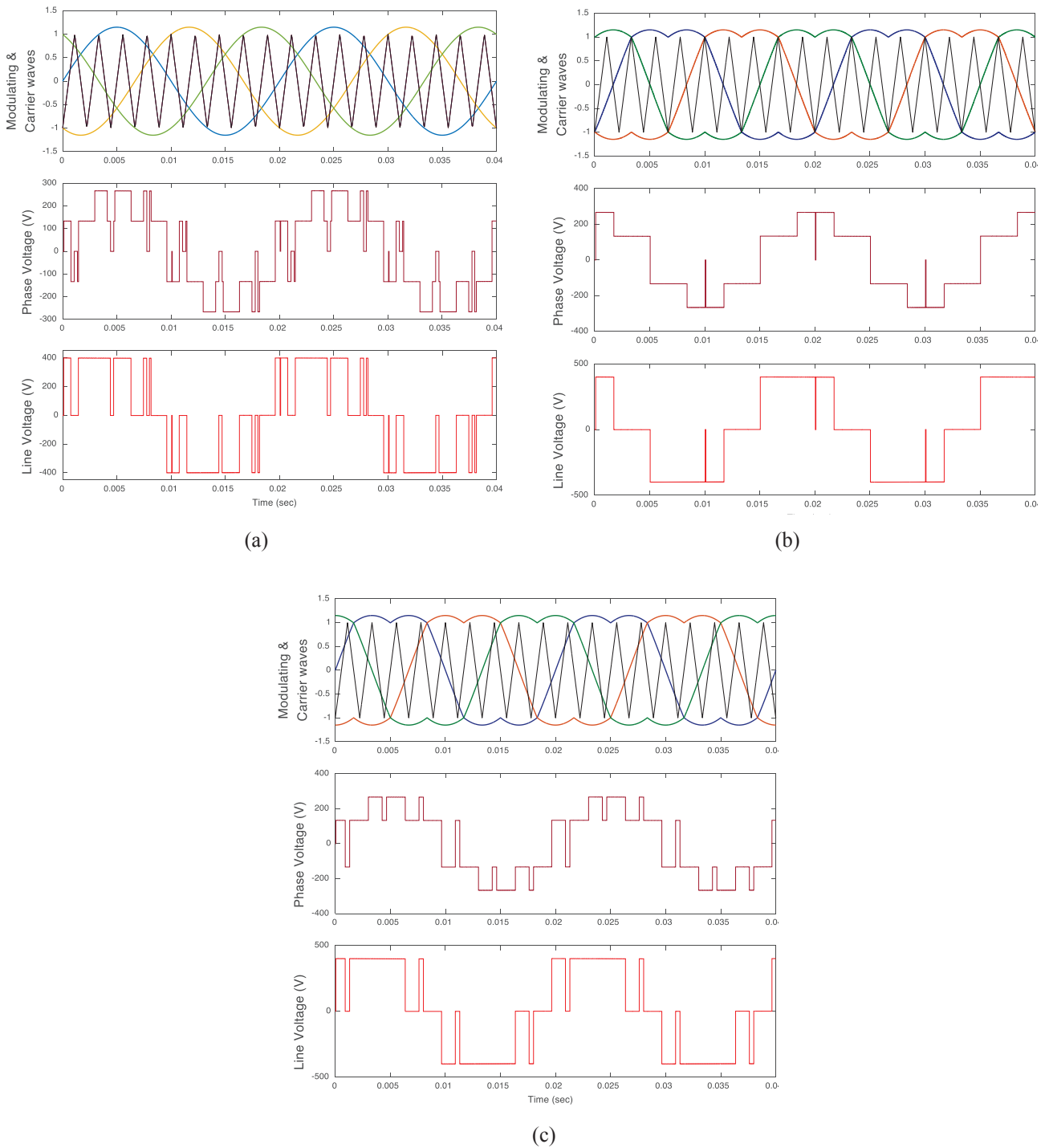


Fig. 9. Simulation results with  $ma = 0.1$  and  $mf = 9$  ( $fsw = 450$  Hz) for (a) SPWM, (b) conventional SVPWM, and (c) SVPWM with offset signal.



**Fig. 10. Simulation results with  $m_a = 0.9$  and  $m_f = 9$  ( $f_{sw} = 450$  Hz) for (a) SPWM, (b) conventional SVPWM, and (c) SVPWM with offset signal.**



**Fig. 11. Simulation results with  $ma = 1.15$  and  $mf = 9$  ( $f_{sw} = 450$  Hz) for (a) SPWM, (b) conventional SVPWM, and (c) SVPWM with offset signal.**

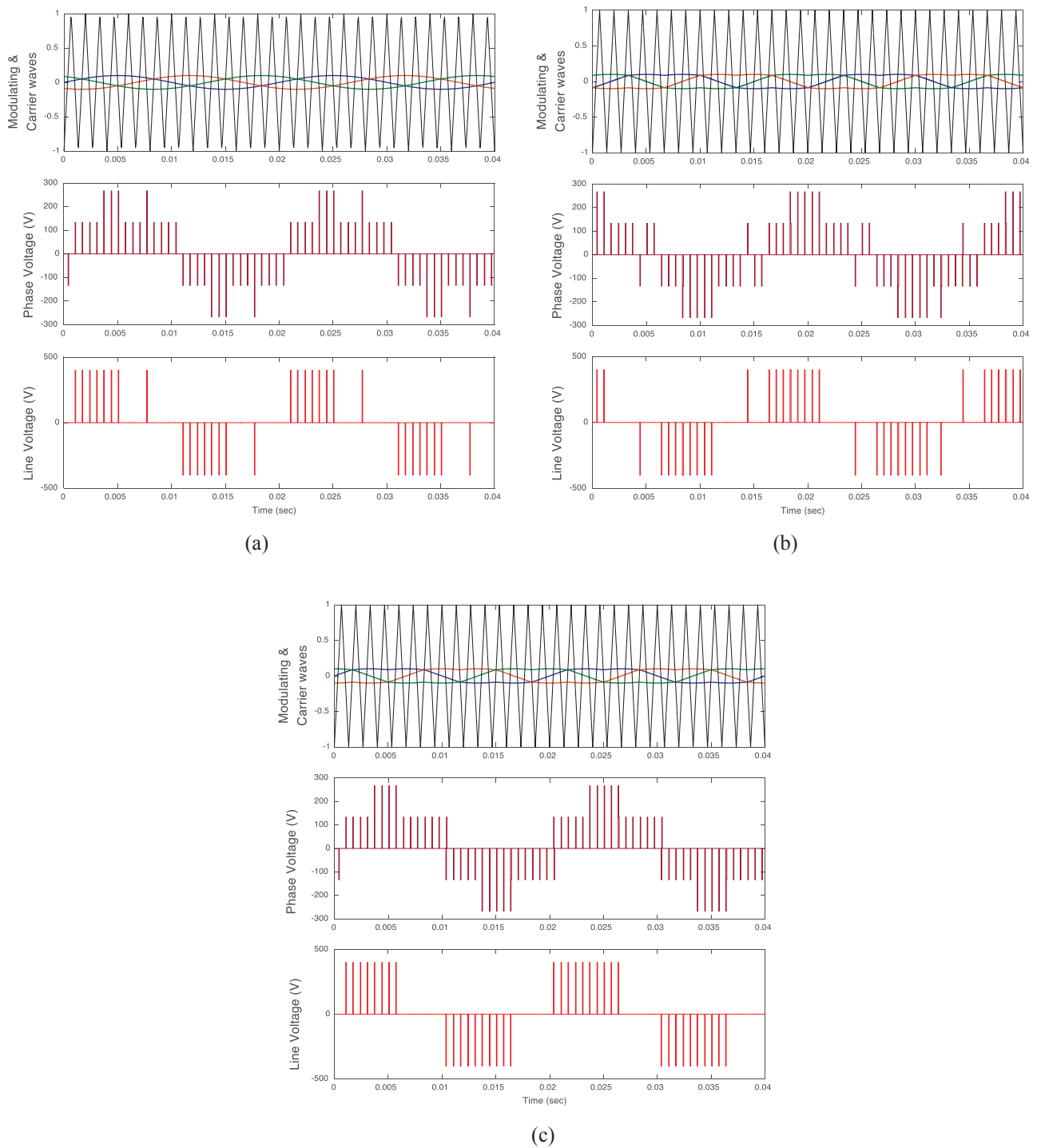


**Fig. 12. Simulation results with  $ma = 0.1$  and  $mf = 15$  ( $f_{sw} = 750$  Hz) for (a) SPWM, (b) conventional SVPWM, and (c) SVPWM with offset signal.**

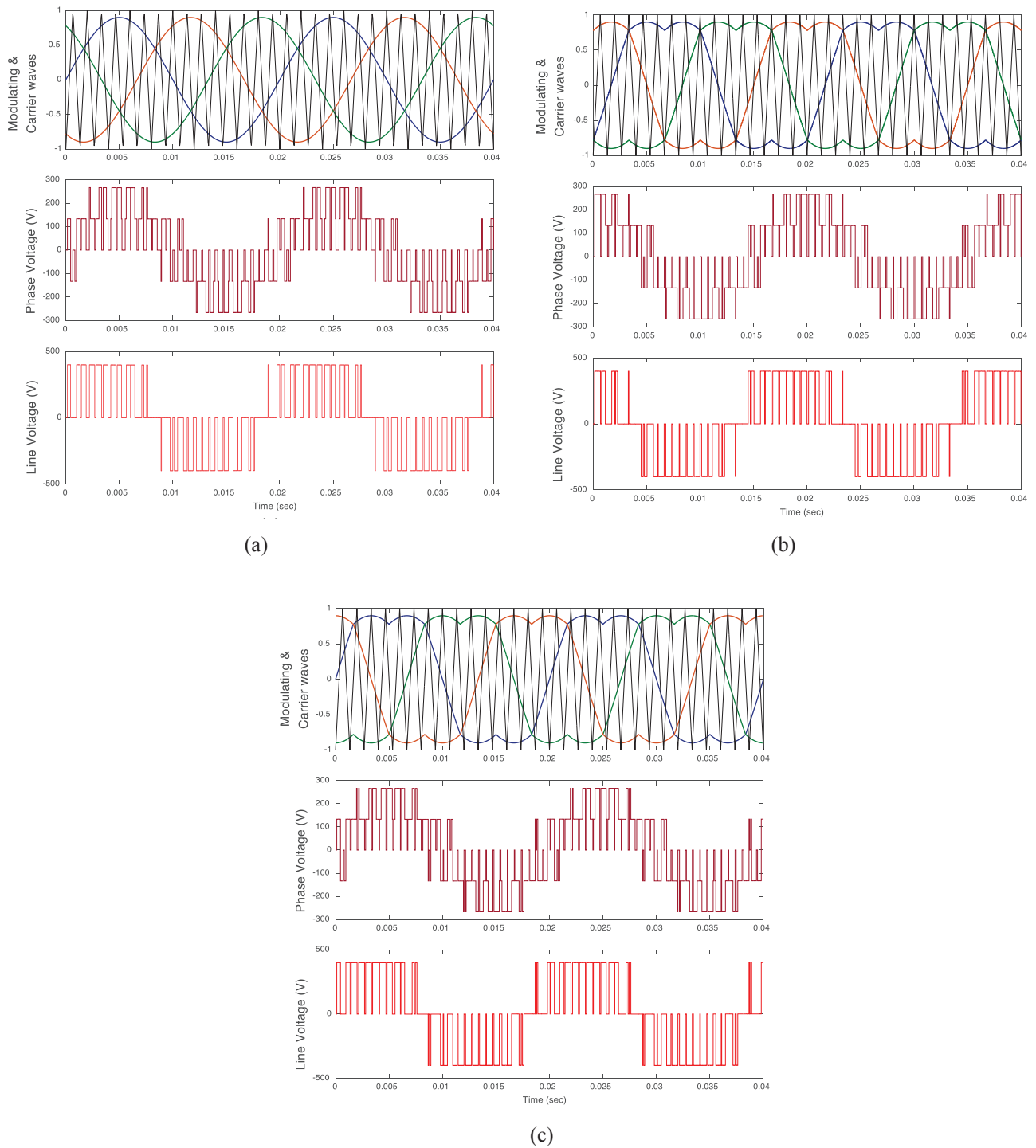


**Fig. 13. Simulation results with  $ma = 0.9$  and  $mf = 15$  ( $f_{sw} = 750$  Hz) for (a) SPWM, (b) conventional SVPWM, and (c) SVPWM with offset signal.**

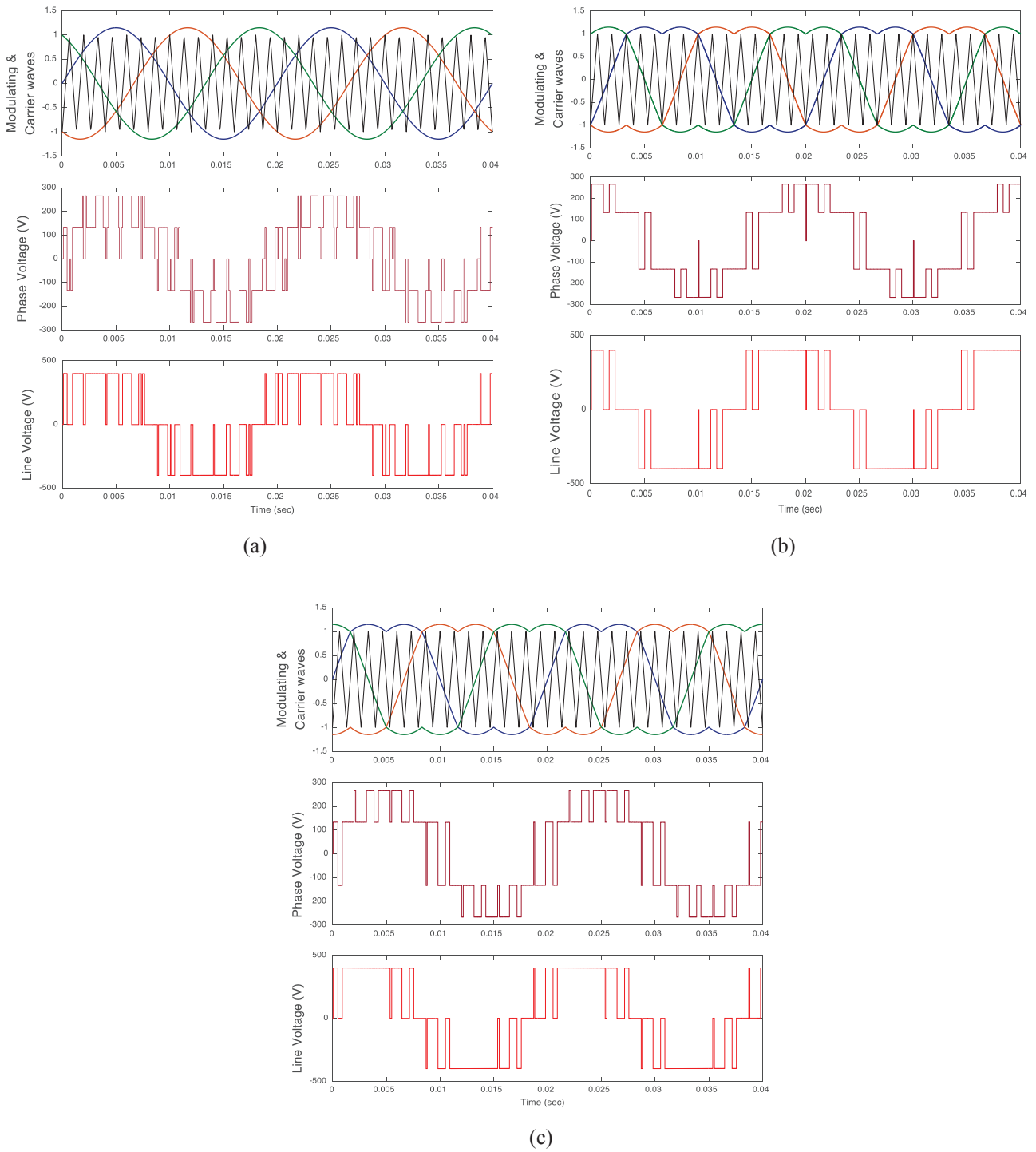
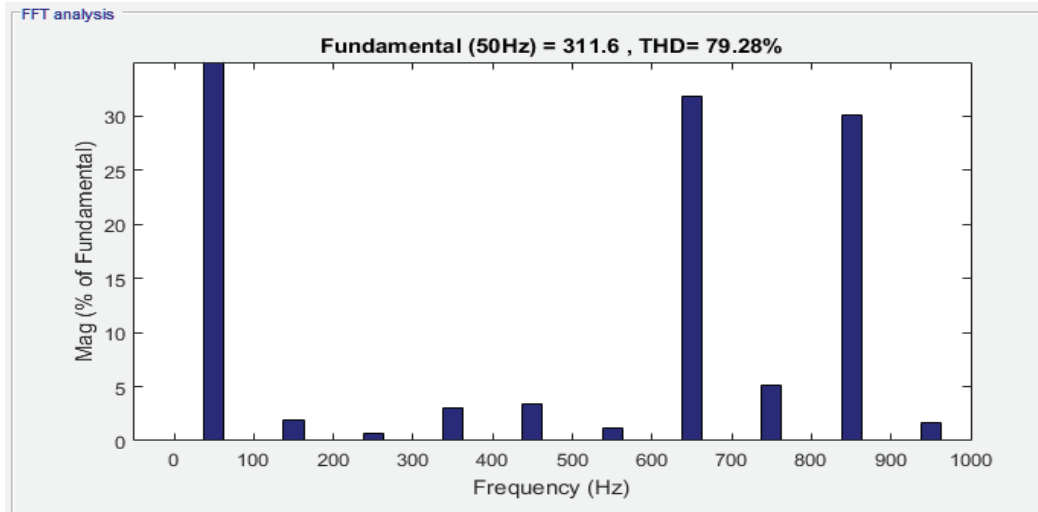
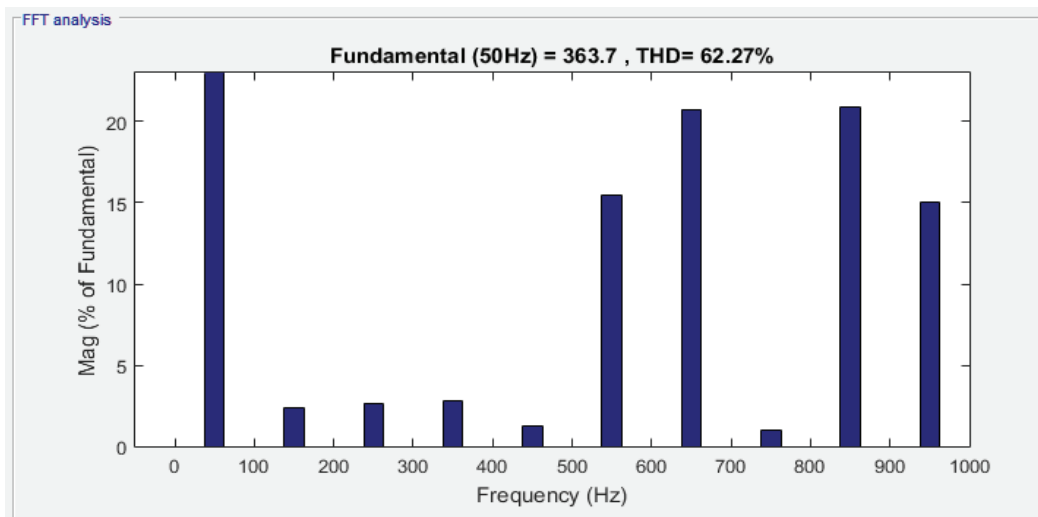


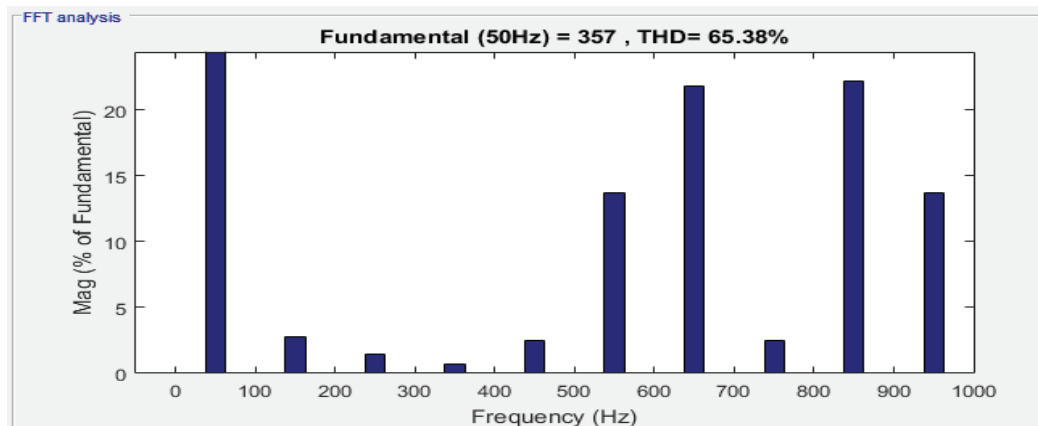
**Fig. 14. Simulation results with  $ma = 1.15$  and  $mf = 15$  ( $f_{sw} = 750$  Hz) for (a) SPWM, (b) conventional SVPWM, and (c) SVPWM with offset signal.**



(a)



(b)



(c)

Fig. 15. FFT analysis of the output line voltage expressed as a % of fundamental line voltage with  $m_a = 0.9$  and  $m_f = 15$  ( $f_{sw} = 750$  Hz) for (a) SPWM, (b) conventional SVPWM, and (c) SVPWM with offset signal.

## IV. CONCLUSION

Several PWM techniques can be used to control three-phase Voltage Source Converters for industrial and variable frequency AC drive applications. This paper proposes a software preprogrammed code for SVPWM implementation with a reduced computational time strategy. The simplified SVPWM method relies on the offset voltage principle and factors in the symmetry and synchronization achieved between the output voltage and its fundamental component to remove any possible subharmonics. SVM utilizes the DC voltage more efficiently than the SPWM since its output voltage is about 15.5% greater than that of SPWM. Conventional SVM is a superior modulation technique but its enormous number of calculations needed to determine the switches gating signals struggles and diminishes its application in relatively small real-time implementations. The proposed simplified SVM method avoids the conventional time-sector calculations and reproduces approximately the same modulating signal as the conventional way, directly from the sampled sinusoidal three-phase reference voltages without any appreciably mentioned calculations.

The simulation results indicate that the performance achieved is very similar to that of the conventional SVM but with a decreased algorithm execution time, which allows using lower-cost microcontrollers for the same components and circuit utilization. The proposed method waveforms have an appearance similar to that of the SPWM and performance parameters roughly like the original SVPWM.

## REFERENCES

- [1] S. Toledo, M. Rivera, and J. L. Elizondo, "Overview of wind energy conversion systems development, technologies and power electronics research trends," *2016 IEEE Int. Conf. Autom. ICA-ACCA 2016*, 2016, DOI: 10.1109/ICA-ACCA.2016.7778454.
- [2] F. Blaabjerg, T. Dragicevic, and P. Davari, "Applications of power electronics," *Electron.*, vol. 8, no. 4, 2019, DOI: 10.3390/electronics8040465.
- [3] M. M. Mahmoud, M. M. Aly, and A.-M. M. Abdel-Rahim, "Enhancing the dynamic performance of a wind-driven PMSG implementing different optimization techniques," *SN Appl. Sci.*, 2020, DOI: 10.1007/s42452-020-2439-3.
- [4] J. Sabarad and G. H. Kulkarni, "Comparative analysis of SVPWM and SPWM techniques for multilevel inverter," 2015, DOI: 10.1109/ICPACE.2015.7274949.
- [5] T. Brückner and D. G. Holmes, "Optimal pulse-width modulation for three-level inverters," *IEEE Trans. Power Electron.*, vol. 20, no. 1, pp. 82–89, 2005, DOI: 10.1109/TPEL.2004.839831.
- [6] S. Vazquez, J. Rodriguez, M. Rivera, L. G. Franquelo, and M. Norambuena, "Model Predictive Control for Power Converters and Drives: Advances and Trends," *IEEE Trans. Ind. Electron.*, 2017, DOI: 10.1109/TIE.2016.2625238.
- [7] P. Falkowski and A. Sikorski, "Comparative Analysis of Finite Control Set Model Predictive Control Methods for Grid-Connected AC-DC Converters with LCL Filter," *IEEE Int. Symp. Ind. Electron.*, vol. 2018–June, pp. 193–200, 2018, DOI: 10.1109/ISIE.2018.8433673.
- [8] B. Chokkalingham, S. Padmanaban, and F. Blaabjerg, "Investigation and Comparative Analysis of Advanced PWM Techniques for Three-Phase Three-Level NPC-MLI Drives," *Electr. Power Components Syst.*, vol. 46, no. 3, pp. 258–269, 2018, DOI: 10.1080/15325008.2018.1445142.
- [9] M. M. Mahmoud, M. M. Aly, H. S. Salama, and A. M. M. Abdel-Rahim, "Dynamic evaluation of optimization techniques-based proportional-integral controller for wind-driven permanent magnet synchronous generator," *Wind Eng.*, 2020, DOI: 10.1177/0309524X20930421.
- [10] N. Prakash, J. Jacob, and V. Reshmi, "Comparison of DVR performance with Sinusoidal and Space Vector PWM techniques," *2014 Annu. Int. Conf. Emerg. Res. Areas Magn. Mach. Drives, AICERA/iCMMMD 2014 - Proc.*, 2014, DOI: 10.1109/AICERA.2014.6908196.
- [11] C. Hari Krishna, J. Amarnath, and S. Kamakshiah, "Simplified SVPWM algorithm for neutral point clamped 3-level inverter fed DTC-IM drive," *2012 Int. Conf. Adv. Power Convers. Energy Technol. AP CET 2012*, 2012, DOI: 10.1109/APCET.2012.6302002.
- [12] R. V. Thomas, E. Rakesh, J. Jacob, and A. Chitra, "Identification of optimal SVPWM technique for diode clamped multilevel inverter based induction motor drive," *Proc. 2015 IEEE Int. Conf. Electr. Comput. Commun. Technol. ICECCT 2015*, 2015, DOI: 10.1109/ICECCT.2015.7225926.
- [13] A. R. Beig, M. Poshtan, and S. Kanukollu, "Novel SVPWM based switching sequences for modular multilevel DC to AC converter," *Conf. Proc. - IEEE Appl. Power Electron. Conf. Expo. - APEC*, vol. 2019–March, pp. 1858–1864, 2019, DOI: 10.1109/APEC.2019.8721773.
- [14] M. M. Mahmoud, A. Mohamed Hemeida, and A. M. M. Abdel-Rahim, "Behavior of PMSG Wind Turbines with Active Crowbar Protection under Faults," 2019, DOI: 10.1109/i-PACT44901.2019.8960004.
- [15] K. V. Kumar, P. A. Michael, J. P. John, and S. S. Kumar, "Simulation and Comparison of Spwm and Svpwm Control for Three Phase Inverter," *ARPN J. Eng. Appl. Sci.*, 2010.
- [16] A. R. Beig, G. Narayanan, and V. T. Ranganathan, "Modified SVPWM algorithm for three-level VSI with synchronized and symmetrical waveforms," *IEEE Trans. Ind. Electron.*, vol. 54, no. 1, pp. 486–494, 2007, DOI: 10.1109/TIE.2006.888801.
- [17] J. S. Lee, K. B. Lee, and F. Blaabjerg, "Predictive Control with Discrete Space-Vector Modulation of Vienna Rectifier for Driving PMSG of Wind Turbine Systems," *IEEE Trans. Power Electron.*, vol. 34, no. 12, pp. 12368–12383, 2019, DOI: 10.1109/TPEL.2019.2905843.

- [18] S. H. Kim, *Electric Motor Control: DC, AC, and BLDC Motors*, 1st edition. Elsevier Science, 2017.
- [19] G. Chen, A. Bahrami, S. Member, M. Narimani, and S. Member, "A New Seven-Level Topology for High-Power Medium-Voltage Application," vol. 0046, no. c, 2019, DOI: 10.1109/TIE.2019.2962456.
- [20] M. M. Mahmoud, A. M. Hemeida, T. Senjy, and A. M. Eweis, "Fault Ride-Through Capability Enhancement For Grid-Connected Permanent Magnet Synchronous Generator Driven by Wind Turbines," in *2019 IEEE Conference on Power Electronics and Renewable Energy (CPERE)*, 2019, pp. 567–572.
- [21] M. Metwally Mahmoud, H. S. Salama, M. M. Aly, and A. M. M. Abdel-Rahim, "Design and implementation of FLC system for fault ride-through capability enhancement in PMSG-wind systems," *Wind Eng.*, 2020, DOI: 10.1177/0309524X20981773.
- [22] D. R. Trainer, C. C. Davidson, C. D. M. Oates, N. M. Macleod, and D. R. Critchley, «CIGRE 2010 A New Hybrid Voltage-Sourced Converter for HVDC Power Transmission AREVA T & D HVDC & FACTS Stafford, UK R . W . CROOKES AREVA T & D Technology Centre,» *Converter*, 2010.
- [23] V. K. Singh, R. N. Tripathi, and T. Hanamoto, "HIL co-simulation of finite set-model predictive control using FPGA for a three-phase VSI system," *Energies*, 2018, DOI: 10.3390/en11040909.
- [24] "Pulse-width modulation - WikiMili, The Free Encyclopedia."
- [25] D. G. Holmes and T. A. Lipo, "Pulse Width Modulation for Power Converters," *Pulse Width Modul. Power Convert.*, 2010, DOI: 10.1109/9780470546284.
- [26] M. H. Rashid, *Power Electronics Handbook*, 4th ed. Elsevier Inc, 2018.
- [27] M. Gaballah, M. El-Bardini, S. Sharaf, and M. Mabrouk, "Implementation of Space Vector-PWM for Driving Two Level Voltage Source Inverters," *J. Eng. Sci.*, vol. 39, no. 4, pp. 871–884, 2011.
- [28] Q. Ge, X. Wang, S. Zhang, L. I. Yaohua, and L. Kong, "A high power NPC three-level inverter equipped with IGCTs," 2004.



**Mohamed Khalid Ratib** was born in Sohag, Egypt, in 1993. He received his B.Sc. and M.Sc. degrees in Electrical Engineering from Aswan University, Aswan, Egypt, in 2016 and 2020, respectively. Since, 2017 he has been with the Department of Electrical Engineering, Aswan University, as a Teaching Assistant. His research interests include wind generators, solid-state transformers, power converters, MPC techniques, PWM techniques, and renewable energy conversion systems.



**Ahmed Rashwan** was born in Sohag, Egypt, in 1984. He received his B.Sc. and M.Sc. degrees from Aswan University, Aswan, Egypt, in 2006 and 2012, respectively. In 2007, he joined the Department of Electrical Engineering, Faculty of Energy Engineering, Aswan University, Aswan, Egypt, as an Administrator, and became a Research Assistant in 2008. In 2015-2016, he joined the Power Energy System Control Laboratory, University of the Ryukyus, Japan, as a Researcher. His research interests include predictive control modulation of power converters in addition to renewable energy applications.

# A Methodological Approach to Assessing the Possible Effect of Distributed Generation Expansion on Regional Energy Supply Systems

E. V. Galperova\*

Melentiev Energy Systems Institute of Siberian Branch of Russian Academy of Sciences, Irkutsk, Russia

**Abstract** — One of the new challenges arising from the transition of the energy industry to the path of intelligent development is to assess the effect of distributed generation (DG) on the prospects for the development of regional energy supply systems. Such an assessment requires that the factors characterized by high uncertainty be taken into account. In this case, it is expedient to employ a combination of the optimization method with the Monte Carlo method. Such an approach has already been adopted in a model (computer program) developed at the Melentiev Energy Systems Institute, Siberian Branch of the Russian Academy of Sciences. This model is designed to determine the rational mix of new power plants (with investment risks assessed and factored in) and the likely cost of electricity generation in a given aggregated region. We propose using this model as a source of projected data for an approximate assessment of the DG expansion, given the projected conditions for the energy sector and electric power industry development. It may also provide the basis for an array of research tools for relevant studies. The new toolkit requires a more detailed representation of the administrative division and the inclusion of consumers with their sources of electric power generation in the generating capacity. Although such an estimate is approximate, it can give an overall idea of the extent to which the cost and demand for electricity may vary under different options for the DG expansion in a region.

**Index Terms:** projections, distributed generation, consumers, energy carriers, demand, energy sector, electric power industry, optimization, uncertainty.

\* Corresponding author.  
E-mail: galper@isem.irk.ru

<http://dx.doi.org/10.38028/esr.2021.02.0006>  
Received June 16, 2021. Revised June 21, 2021.  
Accepted July 03, 2021. Available online July 23, 2021.

This is an open access article under a Creative Commons Attribution-NonCommercial 4.0 International License.

© 2021 ESI SB RAS and authors. All rights reserved.

## I. INTRODUCTION

The well-established practice of making projections for Russia's energy sector [1-3] focuses primarily on determining the structure of energy carriers production and the volume of fuel and energy consumption in the sector itself, so as to meet a given demand of the economy for energy carriers, such demand being exogenous to the sector. Such studies fail to consider the possible adjustment effect of consumption on the energy development options, for example, due to the emergence of the consumer's ability to change their energy consumption when prices of different types of energy change or to have self-generation and/or storage facilities. These new opportunities may entail changes in the structure or volume of the initially assumed energy demand and affect the optimization of the energy sector.

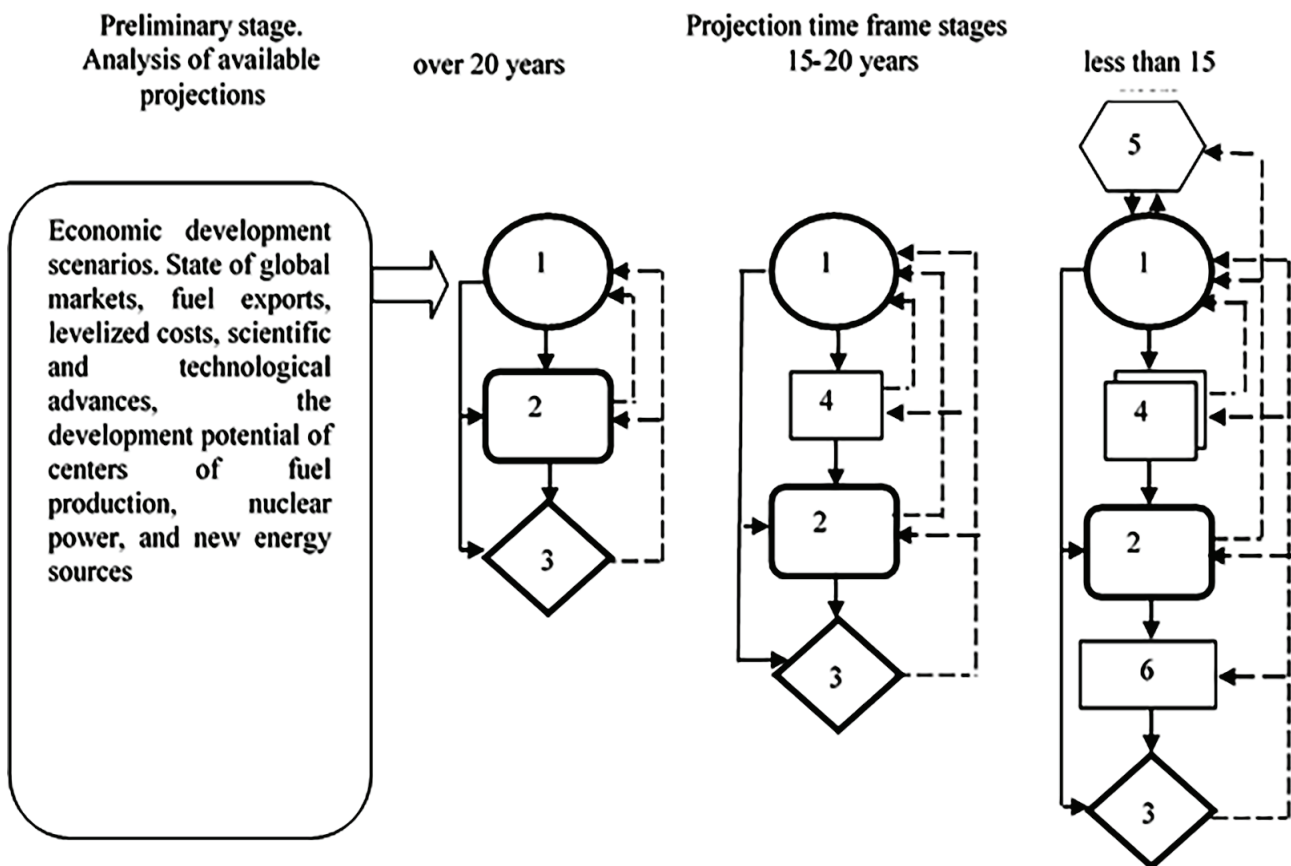
At present, the global energy system is rapidly transitioning from an electric power system built on conventional centralized generation with a unidirectional flow to an integrated and hybridized grid containing elements of both centralized generation and distributed energy resources [4]. According to [5], the technologies of distributed energy (distributed energy resources (DER)) are understood internationally as covering the following:

- distributed generation;
- demand response;
- energy efficiency management;
- microgrids;
- distributed energy storage systems;
- electric cars.

The basic property of all these technologies is proximity to the energy consumer.

As stated in [6 p. 272], «distributed generation is the generation of electricity/heat at the place of its consumption. Having no grid eliminates the losses (costs) of electricity/heat transmission, which implies the presence of many consumers that generate heat/electricity for their own needs and transfer its surplus to a common grid.»

Small-scale distributed energy has been a leading trend in the world for several decades now. Experts estimate that this trend will continue in the coming decade. Navigant Research predicts that by 2026, the amount of distributed



1 - prospects for the energy sector; 2 - a study of the state of regional energy markets (demand and prices); 3 - an assessment of barriers and threats to energy security; 4 - development of individual industries of the energy sector; 5 - the interaction with the macroeconomic system; 6 - investment policy of energy companies.

*Fig. 1. The structure and relationships of problems to be solved at different time stages of the study of the long-term energy development options. Source: [1].*

generation capacity commissioned worldwide will exceed the amount of centralized generation by a factor of three. According to the data published by the SCC Research company, the size of the global market for distributed generation technologies in 2015 was \$65.8 billion. [7]. The International Energy Agency estimates that distributed energy can provide up to 75% of new connections in the course of global electrification by 2030 [5].

There is virtually no accurate data on the share of distributed generation and its dynamics in the energy industry of Russia. In [5], the total capacity of distributed generation facilities in Russia as of 2017 was estimated at 23-24 GW or 9-9.5%. The studies presented in [5] demonstrate that given the full utilization of the distributed energy potential it is possible to meet the entire projected demand for generating capacity of 54-66 GW in the Unified Energy System of Russia by 2035.

## II. LITERATURE REVIEW

Research into various aspects of distributed generation development has become a relevant topic in recent years. In [8-13], the authors consider the main advantages,

system-wide effects, and issues related to the connection of distributed energy sources to distribution networks. Studies [14-16] cover the operation of power grids with DG, including power system protection, hourly load, and electric power quality of distributed generation devices [17-20]. In [21-23], the authors investigate the security of electric power systems with distributed generation in terms of cascading failures and present the models for determining the limit operating conditions in power grids and methods for assessing the operating parameters of energy service areas with distributed generation facilities. Some studies address the reliability of energy supply systems [24, 25] and examine the possibility of ensuring reliable electric power supply to consumers through the construction of distributed generation facilities [26-29]. Furthermore, distributed energy generation is viewed as a factor of energy security improvement and sustainable development of regions [30-32]. Despite the significant body of published research covering various issues of distributed generation expansion, it proved impossible to find the studies on its effect on electricity demand, its price, and generation structure.

III. PROPOSED METHODOLOGICAL APPROACH

The Melentiev Energy Systems Institute, SB RAS (ESI SB RAS), has developed and has been continuously improving a multi-stage methodological approach to enhance the validity of long-term projections of the national energy sector development. This approach assumes the existence of problems varying in their importance and complexity and ways to solve them at different time stages of the projection time frame (Figure 1).

We have built a methodological toolkit (a pool (set) of various types of models) for projection studies [33, 34]. The models are not linked to each other by automatic procedures, which allows solving individual problems, for which the models were originally developed, and employing them as building blocks of systems to be used for calculations. In this case, the results of solving some models are used as input data for others. As new problems arise, the pool is supplemented with new models or modifications of existing ones.

One of the new problems arising with the transition of the energy industry to the path of intelligent development is a projection of the possible effect of distributed generation (DG) on the projected structure and cost of electricity generation and the demand for it in a region. A prerequisite for solving it lies in considering the region-specific energy and economic development conditions and the quality of the information used. Earlier studies [35] attested to a significant disparity in the cost of electricity generation by region and its dependence on the type of probability distribution within the ranges of the assumed values of input data (Table 1).

Methodological approaches to assessing the energy development options depend on the given time frame and the objectives of the projection studies. The uncertainty increases as the projection time frame extends further into

the future. Hence, the decision on strategic directions of energy industry development looking ahead 20 years or more will have less stringent requirements for the accuracy of the results, the degree of detail with respect to the administrative divisions, and the factors to be considered.

The assessment of the possible effect of distributed generation on the projected structure, production cost, and demand for electricity in a region is most important when the projections extend up to 15 years into the future because it is this period that predetermines the conditions for the modernization of regional energy supply systems.

A specific feature of the assessment is the need to consider the diversity of behaviors and ways of self-generation in different groups of consumers, which requires a more detailed treatment of the administrative division given the conditions for the development of individual regional power systems, the characteristics of consumers, electrical load curves, and others. All these parameters are highly uncertain, which is why the Monte Carlo method along with the optimization method may prove appropriate for the assessment. This approach is used in the MISS-EL model developed at the ESI SB RAS [35]. The model designed determines a rational mix of new power plants (with investment risks assessed and factored in) and the likely cost of electricity generation in aggregated regions (Federal districts and/or interconnected power systems) for a time horizon of up to 15 years.

The methodological principles and results of the studies based on the MISS-EL model are proposed as a framework to be used for the approximate assessment of the DG effect on the development of regional energy supply systems. It is supposed to use model (1) as a source of projected data on the conditions for the electric power supply systems expansion and (2) as a basis for the new toolkit development. The toolkit should factor in the projection

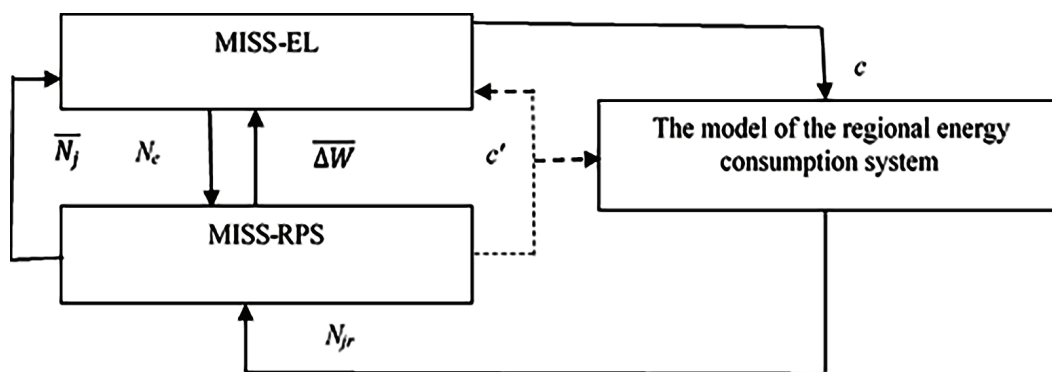


Fig. 2. The overall flow diagram of the proposed approach to assessing the effect of the DG expansion on regional energy supply systems. Source: developed by the author.

TABLE 1. Effect of regional differences and the nature of uncertainty in the input data on the cost of electricity generation in the interconnected power systems (IPSS) of European Russia as compared to the Ural IPS, %

The nature of information uncertainty	IPS				
	Northwestern	Central	Middle Volga	Southern	Ural
Normal distribution	105	103	111	105	100
Uniform distribution	110	110	118	114	100

time frame, the required level of detail with respect to the administrative division, the characteristics of consumers, and the conditions and opportunities for the DG expansion. In essence, the MISS-EL model should serve as a basis for a new model of the regional power system (MISS-RPS). The flow diagram of the proposed approach to assessing the effect of the DG expansion on regional energy supply systems and the main relationships between the models are shown in Figure 2.

In the MISS-RPS model, DG is represented as an additional source of electric power generation. The functional of such a model for the given region consists of the following: costs of electricity generated by centralized sources (data obtained from the MISS-EL model) detailed for individual administrative divisions  $r$  (by Federal entity, by district, by city, etc.) of a region, costs of electricity generated by DG units (data from the regional energy consumption model), and the tariff for electricity transmission from centralized and distributed sources:

$$F = \sum_r \sum_e c_{er} N_{er} h_{er} + \sum_r \sum_j c_{jr} N_{jr} h_{jr} + \sum_{e,j} T_{ej} W_{ej} \rightarrow \min,$$

where  $c_{er}$  – discounted costs of electricity generation at a power plant of type  $e$  (cent/kWh) in territory  $r$ ,  $N_{er}$  – the installed capacity of a power plant of type  $e$  (kW) in the administrative division  $r$ ,  $h_{er}$  – the number of hours of the installed capacity utilization at a power plant of type  $e$  (hour) in territory  $r$ ,  $c_{jr}$  – discounted costs of electricity generation by a DG unit of type  $j$  (cent/kWh) in the administrative division  $r$ ,  $N_{jr}$  – the installed capacity of a DG unit of type  $j$  (kW) in the administrative division  $r$ ,  $h_{jr}$  – the number of hours of the installed capacity utilization of a DG unit of type  $j$  (hour),  $T_{ej}$  – the tariff for electricity transmission from a power plant of type  $e$  and a DG unit of type  $j$  (cent/kWh),  $W_{ej}$  – the amount of electricity transmitted from a power plant of type  $e$  and DG unit of type  $j$  (kWh).

The main constraints in the MISS-RPS model are as follows:

available potential for the expansion of DG units of type  $j$

$$0 \leq N_j \leq \bar{N}_j;$$

possible commissioning of new power plants of type  $e$

$$\underline{N}_e \leq N_e \leq \bar{N}_e;$$

the projected level of electricity consumption

$$\underline{W} \leq W \leq \bar{W};$$

where

$$W = \sum_e N_e h_e + \sum_j N_j h_j.$$

The calculation of the values of economic performance indicators of DG in the model of regional energy consumption involves the analysis of the following: what are the sectors of the economy (residential, commercial, industrial) that have (are planned to have) the DG units, what is their possible generation capacity, what is the cost of electricity generation at these facilities, and which part of the electrical load curve they can help to handle. Specific capital and operating costs are determined for

each sector separately, given their dependence on the scale of DG expansion.

Values of fuel prices, technical and economic performance parameters of plants and constraints are represented as ranges of their prospective values with the possibility of setting the type of probability distribution within these ranges (normal, uniform, exponential, etc.). The Monte Carlo method allows determining a set of well-balanced solutions under different combinations of characteristics of future conditions. This set is used to form an option of the electricity generation structure at its minimum cost under the assumed conditions.

The study presupposes the following sequence:

1. The MISS-EL model is calibrated to match the given scenario of economic and energy development. Calculations based on the model determine the likely mix of new capacity additions ( $N_e$ ) and the cost of electricity generation ( $c$ ) in the included IPSs. The results thus obtained serve as the input data for the MISS-RPS model.
2. In the MISS-RPS model, the capacity added is detailed for administrative divisions of the region in question and is supplemented by the DG capacity of different consumer categories ( $N_{jr}$ ). The latter is determined in the model of the regional energy consumption system in terms of the electricity production cost obtained by MISS-EL ( $c$ ).
3. Calculations based on the MISS-RPS model clarify the cost of electricity generation  $c'$  in the considered region, given its distinctive features. Furthermore, they allow one to determine the potential of substituting centrally commissioned capacity ( $N_e$ ) for DG capacity ( $\bar{N}_j$  – the upper limit of DG capacity) and the volume of electricity generation ( $\Delta \bar{W}$ ) by the DG capacity.
4. Based on contingency calculations (different scenarios of DG expansion), we arrive at the dependencies of prices and demand for electricity on the scale of the DG expansion in a region.

Results of calculations based on the MISS-RPS model in the form of a decrease in demand for electricity ( $\Delta \bar{W}$ ) in the region under consideration can be used to clarify and assess possible changes in the structure and cost of electricity generation in the studies performed based on the MISS-EL model.

#### IV. CONCLUSION

The development of distributed energy is a leading global trend, contributing to the transition from the conventional unidirectional arrangement of energy systems to their new integrated and hybridized types that combine large-scale centralized energy sources with distributed ones. In this context, one of the challenges arising in long-term studies of feasible options for the electric power industry and the energy sector is to assess the effect of the DG adoption scale on the structure of electricity generation, its cost, and

demand for electricity in a region.

The methodological approach and toolkit proposed for solving this problem rely on a combination of the methods of optimization and Monte Carlo simulation and enable contingency calculations in terms of the quality of available information and assessment of changes in the cost of electricity and its demand for different options of the DG expansion in a region.

Such an estimate is approximate, but it can provide an overall idea of the extent of the DG impact on the development of regional energy supply systems, which will be instrumental in improving the validity of projections of the electric power industry and the energy sector development.

#### ACKNOWLEDGMENT

The research was conducted under State Assignment Project (no. FWEU-2021-0003) of the Fundamental Research Program of the Russian Federation 2021-2030 (reg. number AAAA-A21-121012090014-5). Some results were obtained with partial support by RFBR project number 20-010-00204.

#### REFERENCES

- [1] Yu. D. Kononov, *Approaches to improve the validity of long-term projections of the energy sector*. Novosibirsk: Nauka, 2015. 147 p. (in Russian)
- [2] *Energy systems analysis: methodology and research findings*, A.A. Makarov and N.I. Voropai, Eds. Moscow: Energy Research Institute RAS, 2018, 309 p. (In Russian)
- [3] A.A. Makarov. "Half a century of the systems analysis of the energy industry development in the USSR and Russia - and what is next? (review)," *Thermal Engineering*, no. 12, pp. 5-14, 2020. (in Russian)
- [4] N.I. Voropai, "Distributed generation in electric power systems," *International Scientific and Practical Conference «Small-scale generation-2005»*, Available at: <http://www.combienergy.ru/stat/983-Raspredelennaya-generaciya-v-elektroenergeticheskikh-sistemah> (accessed 03.02. 2021). (in Russian)
- [5] *Distributed energy in Russia: Potential for development*. Energy Centre of the SKOLKOVO Moscow Business School, 89 p. Available at: [https://energy.skolkovo.ru/downloads/documents/SEneC/Research/SKOLKOVO\\_EneC\\_DER-3.0\\_2018.02.01.pdf](https://energy.skolkovo.ru/downloads/documents/SEneC/Research/SKOLKOVO_EneC_DER-3.0_2018.02.01.pdf) (accessed 03.02. 2021). (in Russian)
- [6] *The innovation-driven electric power sector-21*, V.M. Batenin, V.V. Bushuev, and N.I. Voropai, Eds. Moscow: Energiya Publishing Center, 2017, 584 p. (in Russian)
- [7] A. Khokhlov, F. Veselov, "Internet of Energy: how distributed energy will influence safety, electricity prices, and the environment." Available at: <http://www.forbes.ru/biznes/351485-internet-energy-kak-raspredelennaya-energetika-povliyaet-na-bezopasnost-ceny-na>. (accessed 03.02. 2021). (in Russian)
- [8] Yu.E. Gurevich, P.V. Ilyushin, *Special aspects of calculations of operation modes in the energy service area with distributed generation: a research monograph*. Nizhny Novgorod: Nizhny Novgorod Branch of the Russian Presidential Academy of National Economy and Public Administration, 2018, 280 p. (in Russian)
- [9] P.V. Ilyushin, *Prospects for application and outstanding issues of integration of distributed energy sources into power grids: a research monograph*. Moscow: NTF «Energoprogress», 2020, 116 p. DOI: 10.34831/EP.2020.260.8.001 (in Russian)
- [10] L. Mehigan, J.P. Deane, B.P.O. Gallachoir, V. Bertsch, "A review of the role of distributed generation in future electricity systems," *Energy*, vol. 163, pp. 822-836, 2018.
- [11] C. Mateo, P. Frias, K. Tapia-Ahumada, "A comprehensive techno-economic assessment of the impact of natural gas-fueled distributed generation in European electricity distribution networks," *Energy*, vol. 192, pp. 116523, 2020.
- [12] S.P.S. Matosa, M.C. Vargas, L.G.V. Fracalossi, L.F. Encarnaç ao, O.E. Batista, "Protection philosophy for distribution grids with high penetration of distributed generation," *Electric Power Systems Research*, vol. 196, pp. 107203, 2021.
- [13] Ali Ehsan, Qiang Yang, "Optimal integration and planning of renewable distributed generation in the power distribution networks: A review of analytical techniques," *Applied Energy*, vol. 210, pp. 44-59, 2018.
- [14] B.A. Kosarev, G.A. Koshchuk, V.K. Fedorov, O.A. Lysenko, "Optimization of the operation of the electrical engineering system with distributed generation," *Actual Issues of Energy*, no. 1, pp. 99-103, 2019. (in Russian)
- [15] N.A. Gorshkova, Yu.E. Gurevich, P.V. Ilyushin, "Promising directions in the automation of distributed generation facilities during their integration into distribution networks," *Relejnaya zashchita i avtomatizatsiya*, no. 1 (10), pp. 48-55, 2013. (in Russian)
- [16] Chenjie Maa, Johannes Dasenbrocka, J.-Christian Töbermann, Martin Braun, "A novel indicator for evaluation of the impact of distributed generations on the energy losses of low voltage distribution grids," *Applied Energy*, vol. 242, pp. 674-683, 2019.
- [17] M.V. Sharygin, A.L. Kulikov, V.Yu. Vukolov, A.A. Petrov, "Adaptive power system protection for power grids with distributed generation sources," *Proceedings of the Russian Academy of Sciences. Power Engineering*, no. 3, pp. 60-68, 2020. DOI: 10.31857/S000233102003005X (in Russian)
- [18] A.V. Kirpikov, I.L. Kirpikova, V.P. Oboskalov, "Loading strategies for distributed generation devices

- during the day,” *Industrial Power Engineering*, no. 4, pp. 12-15, 2014. (in Russian)
- [19] E.B. Solntsev, A.M. Mamonov, A.N. Fitasov, S.A. Petritskij, A.A. Sevostyanov, “Analysis of electric power quality (voltage fluctuations) in distributed generation,” *Energobezopasnost’ i Energobezopasnost’*, no. 3, pp. 37-40, 2019. (in Russian)
- [20] G.B. Guliev, N.R. Rakhmanov, “Fuzzy logic controller for reactive power and voltage control in distributed generation networks,” *Elektro. Elektrotehnika, elektroenergetika, elektrotehnicheskaya promyshlennost’*, no. 2, pp. 47-52, 2014. (in Russian)
- [21] Ch. Sh. Fam, N.I. Voropai, “The study of the security of electric power supply systems with distributed generation and cascading failures factored in,” *Elektrichestvo*, no. 12, pp. 14-20, 2013. (in Russian)
- [22] Yu.N. Bulatov, A.V. Kryukov, A.V. Cherepanov, “Mathematical models for determining the limit operating conditions in power grids with distributed generation installations,” *Science Bulletin of Novosibirsk State Technical University*, no. 4 (80), pp. 17-36, 2020. (in Russian)
- [23] A.L. Kulikov, P.V. Ilyushin, P.S. Pelevin, “Application of discriminatory methods for estimation of operating parameters of energy service areas with distributed generation facilities,” *Elektrichestvo*, no. 7, pp. 22-35, 2019. (in Russian)
- [24] B.V. Papkov, V.L. Osokin, “Special aspects of the assessment of structural reliability of systems with distributed generation facilities,” *Proceedings of the Russian Academy of Sciences. Power Engineering*, no. 2, pp. 75-84, 2020. DOI: 10.31857/S0002331020020090. (in Russian)
- [25] S.A. Nekrasov, “Improving the reliability and availability of power supply of Russian cities based on distributed generation,” *NRE*, no. 9, pp.15-25, 2012. (in Russian)
- [26] P.V. Ilyushin, Yu.N. Kucherov, “Approaches to assessment of the possibility of ensuring reliable electric power supply to consumers by means of construction of distributed generation facilities,” *Elektro. Elektrotehnika, elektroenergetika, elektrotehnicheskaya promyshlennost’*, no. 5, pp. 2-7, 2014. (in Russian)
- [27] D.A. Chechushkov, T.Yu. Panikovskaya, E.A. Bun’kova, “Method of optimal placement of distributed generation sources to improve the reliability of electricity supply,” *Industrial Power Engineering*, no. 9, pp. 17-21, 2014. (in Russian)
- [28] A.V. Varganova, Yu.M. Bajramgulova, I.N. Goncharova, O.A. Krotkova, “Feasibility study of the installation site of distributed generation sources,” *Electrotechnical Systems and Complexes*, no. 3 (44), pp. 68-72, 2019. (in Russian)
- [29] Surender Singh Tanwara, D.K. Khatod, “Techno-economic and environmental approach for optimal placement and sizing of renewable DGs in the distribution system,” *Applied Energy*, vol. 127, pp. 52-67, 2017.
- [30] L.L. Moiseev, V.N. Slivnoy, “Distributed energy generation: a factor in increasing energy security of a region,” *Polzunovskiy Vestnik*, no. 1, pp. 226-229, 2004. (in Russian)
- [31] S. Mayorov, “Distributed stand-alone generation as a basis for energy security,” *Energonadzor*, no. 5 (81), pp. 8, 2016. (in Russian)
- [32] S.P. Filippov, M.D. Dil’man, P.V. Ilyushin, “Distributed generation and sustainable development of regions,” *Thermal Engineering*, no. 12, pp. 4-17, 2019. (in Russian)
- [33] E.V. Galperova, “Employing a model pool for long-term projections of market demand for energy carriers,” *Informatsionnye i Matematicheskie Tekhnologii v Nauke i Upravlenii*, no. 4-2, pp. 17-27, 2016. (in Russian)
- [34] Yu.D. Kononov, E.V. Galperova, D.Yu. Kononov, A.V. Lagerev, O.V. Mazurova, V.N. Tyrtysny. *Methods and models for projections of energy-economy interactions*. Novosibirsk: Nauka, 2009, 178 p. (in Russian)
- [35] Yu.D. Kononov, D.Yu. Kononov, “The economic component of energy security and methodological approaches to its assessment,” *National Interests: Priority and Security*, vol. 5, no. 6, pp. 1086-1096, 2019. (in Russian)



**E. V. Galperova** – Ph. D., Associate Professor, Senior researcher of Melentiev Energy Systems Institute of Siberian Branch of the Russian Academy of Sciences, Russia, Irkutsk. Her main research interests are long-term forecasting of regional energy markets and energy consumption patterns, projections of energy demand in terms of technological patterns, standards of living, price indicators.

# Simulation of Electromagnetic Fields Generated by Overhead Power Lines and Railroad Traction Networks

Natalya V. Buyakova<sup>1</sup>, Vasiliy P. Zakaryukin<sup>2</sup>, Andrey V. Kryukov<sup>\*3,4</sup>, Dmitriy A. Seredkin<sup>3</sup>

<sup>1</sup> Angarsk State Technical University, Angarsk, Russia

<sup>2</sup> Smart Grid LLC, Irkutsk, Russia

<sup>3</sup> Irkutsk State Transport University, Irkutsk, Russia

<sup>4</sup> Irkutsk National Research Technical University, Irkutsk, Russia

**Abstract** — The establishment of smart grids requires special attention to the safety of power industry facilities and the reduction in their negative impact on personnel and the environment. A significant factor of such an impact is the considerable intensities of electromagnetic field (EMF) generated by such facilities. In the context of power industry digitalization, the development of methods and tools for EMF digital simulation is needed to ensure the electromagnetic safety of the service personnel. Computer models designed to adequately determine the EMF generated by overhead power lines (OPL) can be implemented based on the methods and tools created to determine operating parameters of electric power systems in phase coordinates developed at Irkutsk State Transport University. The technique of electromagnetic safety analysis is implemented based on the proposed approach and has the following features: a systems approach, which is the possibility of simulating electromagnetic fields in terms of properties and characteristics of a complex electric power system; versatility, which allows simulating power lines and traction networks of various designs; appropriateness to the environment achieved by considering the profile of the underlying surface, underground utilities, and artificial structures of rail transport, such as galleries, bridges, and tunnels; comprehensiveness, which is provided by combining the computation of operating parameters and the determination of EMF intensities. The paper describes methods and algorithms developed to determine the intensities of electromagnetic

fields generated by multi-conductor power lines at fundamental and higher harmonics frequencies. A technique for the EMF determination at the points of OPL orthogonal crossing is also presented.

**Index Terms:** modeling, electromagnetic field, power transmission line, traction network.

## I. INTRODUCTION

Electric power facilities generate electromagnetic fields (EMFs) of fundamental and higher harmonic frequencies [1, 2], which are among the main factors that determine the electromagnetic safety conditions [3-17]. High-intensity electromagnetic fields can generate interference causing malfunctioning of electrical and electronic devices and result in serious accidents when one operates at tripped power lines due to the impact of induced voltage on personnel.

Methods and tools for simulation of operating conditions in phase coordinates developed at Irkutsk State Transport University (ISTrU) [18] allow simultaneous computations of EMF for multi-conductor power lines [4] and determination of operating conditions of the electric power system (EPS) or traction power supply system (TPSS), being its part. In this case, the line at issue is considered inseparably with a complex EPS or TPSS. Simultaneous computation of operating conditions and generated EMFs enables the systems approach to the electromagnetic environment analysis. Its distinct feature is the possibility of EMF simulation with proper consideration of all properties and characteristics of the complex TPSS and EPS. Advantages of the method proposed are, first of all, the possibility for simulation modeling [4, 18] of trains operation in the TPSS under study and determination of EMF intensity dynamics, and secondly, due consideration of factors that affect the EMF intensity levels, including [4]:

- unevenness of the underlying surface caused by embankments, depressions, slopes, and passenger platforms;
- metal railroad cars and cisterns on tracks that

\* Corresponding author.

E-mail: [and\\_kryukov@mail.ru](mailto:and_kryukov@mail.ru)

<http://dx.doi.org/10.38028/esr.2021.02.0007>

Received June 26, 2021. Revised July 01, 2021.

Accepted July 13, 2021. Available online July 23, 2021.

This is an open access article under a Creative Commons Attribution-NonCommercial 4.0 International License.

© 2021 ESI SB RAS and authors. All rights reserved.

significantly affect spatial distribution patterns of EMF intensities;

- earthed extended metal objects (pipelines, cable lines with earthed coatings, and earthed ropes) that also change the EMF distribution pattern.

The methods and tools developed at ISTRU for modeling the TPSS operation and the Fazonord software implemented on their basis allow using several hundred wires in the models [18]. This makes it possible to simulate the embankments, depressions, railroad cars, and cisterns with a set of wires earthed at one end and located so as to make the distance between the wires significantly shorter than the distance to the observation point. This technology also allows calculation of EMF in artificial railroad transport structures, i.e., tunnels, galleries, bridges.

The proposed approach underlies the technique of electromagnetic safety analysis that has the following characteristics:

- systems approach, which manifests itself through the possibility of modeling electromagnetic fields by factoring in the properties and characteristics of a complex TPSS and a supply EPS;
- universality, which ensures modeling of power transmission lines and traction networks of various designs;
- consideration of the environment via a thorough analysis of underlying surface, underground utilities, and track structures, including galleries, bridges, and tunnels;
- integrity ensured by combining the computation of operating conditions and the determination of EMF intensities.

## II MODELING OF OPERATING CONDITIONS IN PHASE COORDINATES

In a more generalized option, the modeling of electrical network operation can be represented as the following functional relationship:

$$\mathbf{A} : \mathbf{D} \Rightarrow \mathbf{X} \tag{1}$$

where  $\mathbf{A}$  – the nonlinear operator;  $\mathbf{D} = \mathbf{S} \mathbf{U} \mathbf{Y}$  – the vector of source data;  $\mathbf{X}$  – the vector of operating parameters;  $\mathbf{S}$  – the set of data describing the structure and parameters of EPS (TPSS) components;  $\mathbf{Y}$  – parameters characterizing generators and loads.

The system of steady-state equations (nonlinear in a general case) is generated by transformation of (1):

$$\mathbf{F}(\mathbf{X}, \mathbf{Y}) = 0,$$

where  $\mathbf{X}$  – the vector formed from node voltage components in Cartesian  $(U'_k, U''_k)$  or polar  $(U_k, \delta_k)$  coordinates;  $\mathbf{Y}$  – the vector that includes active and reactive power of generators and loads.

Technology of simulating the EPS operating conditions in phase coordinates [18] serves as the basis for models and methods proposed in this work. The EPS (TPSS) modeling methods rely on lattice-type equivalent circuits (LEC)

with fully connected topology. The following formalized definition can be written for LEC:

$$TEC : hub \cup con, \forall i, j \in hub \rightarrow con_{i,j} \subset con,$$

where  $TEC$  – stands for lattice-type equivalent circuit;  $hub$  – a set of LEC nodes;  $con$  – a set of LEC branches.

The basic elements that constitute the EPS three-phase – one-phase network supplying traction power systems can be subdivided into two groups:

- electricity transport elements, i.e., overhead power lines and cable lines, conductors, traction networks;
- conversion elements, i.e., transformers of various designs.

The above devices can be generally considered as static multi-wire elements, which can be represented as a set of wires or windings with inductive couplings (Fig. 1). Simulation of power sources, electrical loads and elements employed to control EPS operating conditions are analyzed in detail in [18, 19]. Adequate assessment of electromagnetic safety conditions requires, apart from EMF to be determined for particular operation situations, the construction of time relationships between the intensities of electric  $\dot{E} = \dot{E}(t)$  and magnetic  $\dot{H} = \dot{H}(t)$  fields. These tasks can be accomplished based on simulation modeling. In this case, the concept of instantaneous diagrams is used and dynamic model is reduced to a set of static diagrams. The simulation procedure involves dividing the interval under study into smaller intervals, within which the operating parameters are assumed to be invariable. The analysis of experimental measurements of operating parameters in real TPSSs, and computer simulation results indicate that such an assumption is acceptable and does not introduce a significant error to computation results.

The development of a simulation model of the mainline railroad power system requires the construction of models of the EPS and TPSS elements with an algorithm of their interaction and includes the following stages:

- modeling of train operation schedule;
- generation of instantaneous diagrams and calculation of operating parameters for each of them;

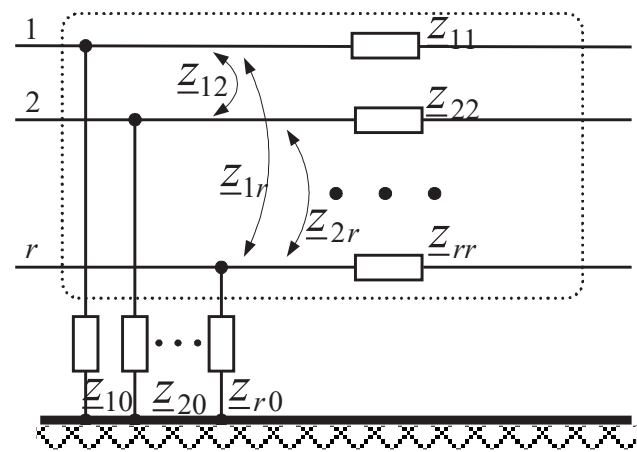


Fig. 1. The diagram of static multi-wire element.

- determination of integral values of simulation modeling.

At each modeling interval  $\Delta t$ , the following system of non-linear equations that define steady-state of the respective instantaneous diagram is solved:

$$\mathbf{F}(\mathbf{X}_k, \mathbf{Y}_k) = 0, \quad (2)$$

where  $\mathbf{X}_k, \mathbf{Y}_k$  – values of vectors  $\mathbf{X}, \mathbf{Y}$  for the  $k$ -th instantaneous diagram.

Modeling of moving traction loads is based on traffic schedule, which relates train location coordinate with time. Traction load values are determined based on traction computations or experiments. Traction loads are normally set by values of currents, although such an approach insufficiently adequately defines the physics of running processes. The train driver shall follow the specified traffic schedule. Thus, a change in voltage at current collecting equipment causes the need to adjust the electric locomotive current to maintain the necessary traction effort. Consequently, setting traction load with power consumed is a more appropriate approach that reflects energy conservation law. Software tools developed to determine traction loads obtain traction currents under rated voltage of the current collecting equipment, consequently, there is no problem in their translation to consumed power.

Railroad AC power system can be divided into the following segments:

- three-phase EPS that performs the external power supply function;
- one-phase traction power supply system;
- power supply areas of non-traction and non-transport consumers, including transmission lines of particular design following the pattern “wire – rail” and “two wires – rail.”

The railroad power supply systems (RPSS) have longitudinal and transversal asymmetry of parameters due to the single-phase traction networks and devices of transverse and series capacitive compensation. This asymmetry affects the operation of the external power supply system and power supply areas.

The operating conditions for integrated systems of traction and external power supply are calculated by successively determining the operating conditions for some instantaneous diagrams of train operation. The instantaneous diagram requires the following data:

- a connection diagram of stationary elements with data on their parameters, as well as loads and generation of the RPSS stationary part; the location of electrical traction loads at the considered time instant, which is determined by train operation schedule; location of trains determines parameters of the system’s changing part that includes the traction network sections;
- loads created by trains at the time instant at issue; these loads are determined based on traction loads or experimental rides.

The train schedule is used to determine the train location. The train location determines the lengths of the current sections of the traction network between its

discontinuities, i.e., between neighboring trains or between trains and stationary nodes that include connection points of traction network feeders, sectioning points, parallel connection points, neutral sections, switching to another number of tracks or another suspension type.

### III. EMF SIMULATION IN PHASE COORDINATES

After determining the instantaneous diagram operation by solving the set of equations (2), we can calculate the intensities of electromagnetic fields generated by any of the multi-wire systems, which are part of the simulated system. With the vertically upward direction of the Y-axis of the Cartesian coordinate system and the X-axis perpendicular to the railroad or power line axis so that the Z-axis is oriented in a negative direction of the wire current, the components of the electric field intensity of the system of N wires at the point with coordinates (x, y) are determined using the following formulas:

$$\begin{aligned} \dot{E}_Y &= -\frac{1}{\pi \varepsilon_0} \sum_{i=1}^N \dot{\tau}_i \frac{y_i [(x-x_i)^2 - y^2 + y_i^2]}{\xi_i}, \\ \dot{E}_X &= \frac{2}{\pi \varepsilon_0} \sum_{i=1}^N \dot{\tau}_i \frac{(x-x_i) y y_i}{\xi_i}, \end{aligned} \quad (3)$$

where  $\xi_i = [(x-x_i)^2 + (y+y_i)^2][(x-x_i)^2 + (y-y_i)^2]$ ;  $\dot{\tau}_i$  – charge of wire  $i$  per length unit, which is determined from the first group of Maxwell’s formulas  $\dot{\mathbf{T}} = \mathbf{A}^{-1} \cdot \dot{\mathbf{U}}$ .

Here  $\dot{\mathbf{U}} = [\dot{U}_1 \dots \dot{U}_N]^T$  – column-vector of wire voltages relative to earth;  $\dot{\mathbf{T}} = [\dot{\tau}_1 \dots \dot{\tau}_N]^T$  – column-vector of wire charges,  $\mathbf{A}$  – symmetric matrix of potential coefficients, in which

$$\begin{aligned} \alpha_{ii} &= \frac{1}{2\pi \varepsilon_0} \ln \frac{2y_i}{r_i}, \\ \alpha_{ij} &= \frac{1}{2\pi \varepsilon_0} \ln \frac{\sqrt{(x_i-x_j)^2 + (y_i+y_j)^2}}{\sqrt{(x_i-x_j)^2 + (y_i-y_j)^2}}, \end{aligned}$$

where  $x_i, y_i$  – the coordinates of wire  $i$  above the ground ( $y = 0$  corresponds to the flat earth surface),  $r_i$  – radius of wire  $i$ ;  $\varepsilon_0$  – electrical constant.

After transition from complex effective values of components  $\dot{E}_X$  and  $\dot{E}_Y$  to time dependences, one can obtain parametric equations for locus of the electrical field intensity vector:

$$\begin{aligned} E_x(t) &= \sqrt{2} E_X \sin(\omega t + \varphi_X); \\ E_y(t) &= \sqrt{2} E_Y \sin(\omega t + \varphi_Y), \end{aligned}$$

where the factor  $\sqrt{2}$  is required because computations are based on effective values;  $\omega = 314$  rad/s.

The field intensity reaches its maximum value  $E_{\max}$  at time instants defined by the following equation:

$$t_{\max} = \frac{1}{2\omega} \text{Arctg} \left( \frac{E_X^2 \sin 2\varphi_X + E_Y^2 \sin 2\varphi_Y}{E_X^2 \cos 2\varphi_X + E_Y^2 \cos 2\varphi_Y} \right).$$

One of arctangent values is chosen when the second derivative has a negative value:

$$E_X^2 \cos 2(\omega t_{\max} + \varphi_X) + E_Y^2 \cos 2(\omega t_{\max} + \varphi_Y) < 0 .$$

The effective value of field intensity for some direction  $\psi$ , measured from the  $X$ -axis positive direction is equal to

$$E_{\psi} = \sqrt{E_X^2 \cos^2 \psi + E_Y^2 \sin^2 \psi + D_E} ;$$

$$D_E = 2E_X E_Y \sin \psi \cos \psi \cos(\varphi_X - \varphi_Y) .$$

Intensity extreme value is calculated using the following formula:

$$E_{\psi E} = \left[ \frac{(E_X^2 + E_Y^2)^2 \pm \sqrt{D_{\psi E}}}{2} \right]^{\frac{1}{2}} ;$$

$$D_{\psi E} = (E_X^2 + E_Y^2)^2 - 4E_X^2 E_Y^2 \sin^2(\varphi_X - \varphi_Y) .$$

In this case, plus sign corresponds to the maximum, and the minus sign corresponds to the minimum.

This formula is given in [21], where the authors point out that in the calculation of field near the ground surface, the error of simple quadratic summation

$$E = \sqrt{E_X^2 + E_Y^2}$$

usually does not exceed 10% towards increase above the effective value maximum.

The horizontal and vertical components of the intensity of the magnetic field generated by all conductors are calculated using the following formulas:

$$\dot{H}_X = \frac{1}{2\pi} \sum_{i=1}^N \dot{I}_i \frac{y - y_i}{(x_i - x)^2 + (y_i - y)^2} ;$$

$$\dot{H}_Y = -\frac{1}{2\pi} \sum_{i=1}^N \dot{I}_i \frac{x - x_i}{(x_i - x)^2 + (y_i - y)^2} .$$

The determination of the electric and magnetic field intensities involves the calculation of the RPSS operating conditions, the determination of charges and currents of wires, including earthed ones, and the components  $\dot{E}_X, \dot{E}_Y, \dot{H}_X, \dot{H}_Y$ . The described technique is implemented in the Fazonord software [18]. In this case, electromagnetic field intensities can be determined both for an individual instantaneous diagram and for their set, which determines the change in EMF intensities over time.

Such a problem statement significantly simplifies the computation of EMF intensities. Indeed, the traditional formulation of this problem requires solving differential equations in partial derivatives. Traditional methods considerably complicate the problem-solving procedure, especially when there is a need to factor in the underlying surface inhomogeneities (embankments, slopes, depressions) and the extended conductive facilities (artificial structures of railroad transport, metal cars and cisterns, underground pipelines, and others). The use of sets of grounded wires as part of the corresponding multi-wire element for simulation of roadbed inhomogeneity

and conductive facilities allows the use of the proposed technique to determine EMF without additional complications and modifications, given the external environment [4].

Computations of electric and magnetic field intensities under the proposed technique can be referred to as integral computation methods with a distribution of charges on fictitious earthed conductors located on the surface of nonplanar (but parallel to the plane) ground or the surface of the conductive boundary of an artificial structure. In contrast to the integral methods used, in this technique, the charges on the earthed conductors are found through the calculations of operating conditions in phase coordinates. After the operating conditions of a system that includes a multi-wire element are calculated, it is possible to determine the wire charges per unit of length.

Since the resistances of multi-wire power lines are calculated using the height of the equivalent wire, which is below the point of the wire suspension on the pole by two-thirds of the slack, the computation will give some averaged electric field intensity value throughout span length. At a small (about two or three meters) height of the observation point location, the actual intensity in the middle of the span will be somewhat higher than the calculated one, while at the pole, it will be less than the calculated one.

These differences, however, are relatively small and are usually overarched by the idealization of the considered facility and errors of source data.

The EMF active power flux density can be determined using the formula [4]

$$\Pi_0 = \frac{1}{2} [\Pi_{01} - \Pi_{02}] ;$$

$$\Pi_{01} = E_{mx} H_{my} \cos(\psi_{Ex} - \psi_{Hy}) ;$$

$$\Pi_{02} = E_{my} H_{mx} \cos(\psi_{Ey} - \psi_{Hx}) .$$

Thus, after computing the components  $E_X, \dot{E}_Y, \dot{H}_X, \dot{H}_Y$ , electromagnetic energy flux density determined by the Poynting vector can be calculated.

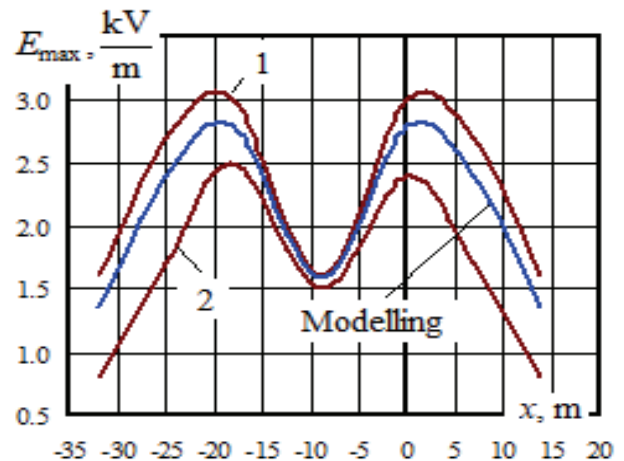


Fig. 2. Comparison of experimental and calculated data: 1, 2 – boundaries of the experimental data scatter area.

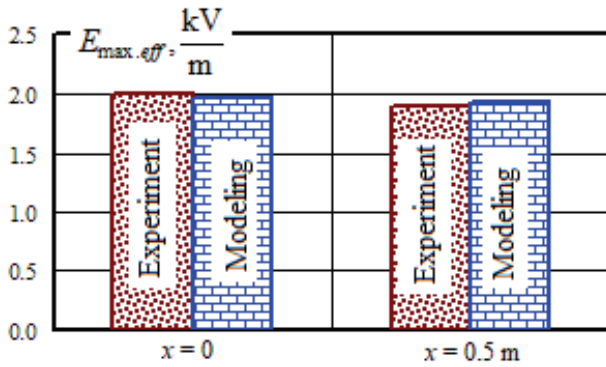


Fig. 3. Calculated and experimental values of the electric field intensity of the overhead system.

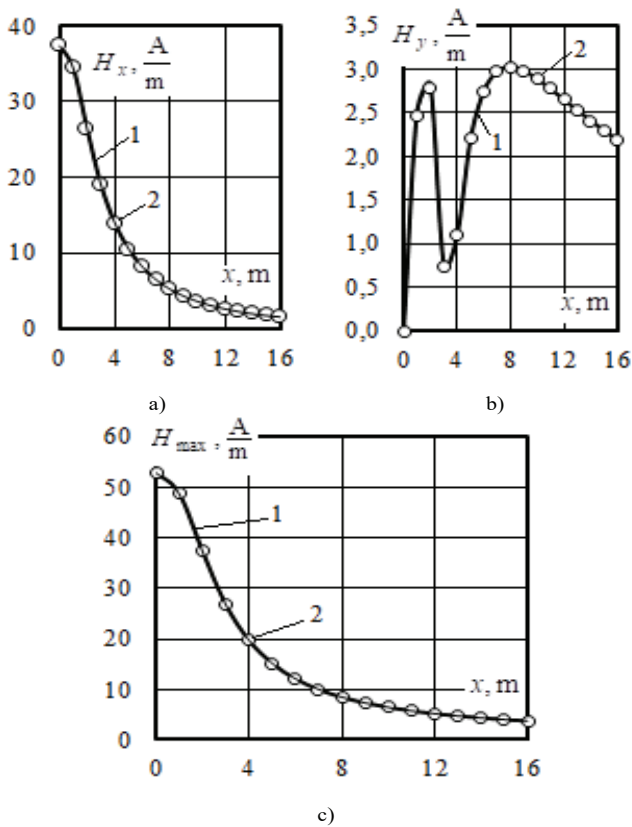


Fig. 4. Comparison results.

IV. VERIFICATION OF THE SIMULATION ADEQUACY

Experimental verification of the technique was carried out by comparing the calculation results for the intensity of electric field generated by 220 kV transmission line with the experimental data obtained in [20]. The results of measurements and computations indicating the acceptable accuracy are shown in Fig. 2.

Fig. 3 shows the results of calculations and experimental studies on the electric field of the overhead system [3]. The results obtained indicate that the discrepancy between the experimental and calculated data does not exceed 2%.

Experimental verification of the adequacy of calculation of the overhead system magnetic field is problematic because it is difficult to obtain source data for simulation

of the RPSS operating conditions. Such information can be obtained only in the future, when the satellite system is employed to locate the trains in space. It is also difficult to restore the overhead power line conditions as there are no means for measuring magnitudes and phases of currents flowing through its wires.

Such measurements will also become possible only when electric power systems are equipped with devices for synchronized measurements of phasors (PMU-WAMS) on a large scale.

Therefore, the verification of adequacy of the magnetic field intensity calculations relied on the comparison with the results of analytical calculations (Fig. 4). The findings show a good agreement between the data of analytical computations and simulation based on the proposed technique.

To additionally verify the simulation adequacy, 50 Hz EMF intensities were measured, and comparative calculations for a 110 kV double-circuit line with a lightning protection cable located within the city were performed. These measurements were made between two towers. The heights of the wire suspension above the measurement site were 19 m (ground wire), 16 m, 13 m, and 10 m (phase wires). A 110 kV single-circuit dead-end tap is connected to a line at the closest tower to the measurement site. At a distance of 10 m from the power transmission line with a slight decrease in the earth surface, there is a metal fence of the garage cooperative, which can have a significant effect on the electric field.

According to the data of measurements of operating parameters of a double-circuit overhead power line (OPL) located close to the branch line, the power flow of the first circuit was about  $9 - j12 \text{ MV}\cdot\text{A}$  (the minus sign corresponds to the accepted positive direction of the power flow of the branch line); the power flow on the second circuit was  $6 - j9 \text{ MV}\cdot\text{A}$ ; the branch line consumes  $6 + j3 \text{ MV}\cdot\text{A}$ . To correctly factor in the multi-wire system with the facilities affecting EMF (metallic fence), its model, including 19 wires, was implemented in the Fazonord software.

Phase voltages were assumed symmetrical, equal to 65 kV for a more loaded circuit and 66 kV for a less loaded one. In the calculation of operating conditions, the above loads symmetrically distributed among phases resulted in 77 A currents for the left-hand circuit wires, 54 A for the right-hand circuit wires, and 34 A for the branch line.

According to the calculation of operating conditions, the value of the ground wire current was of the order of 0.1 A. Thus, while significantly changing the electric field, the ground wire has almost no effect on the magnetic field.

Experimental measurements of electromagnetic field intensities, performed with the P3-50 device, are represented by three groups of values obtained at different times; the directions of coordinate axes were assumed the same as in the computation technique. The origin of coordinates is under the OPL center in the middle of the span on the ground surface.

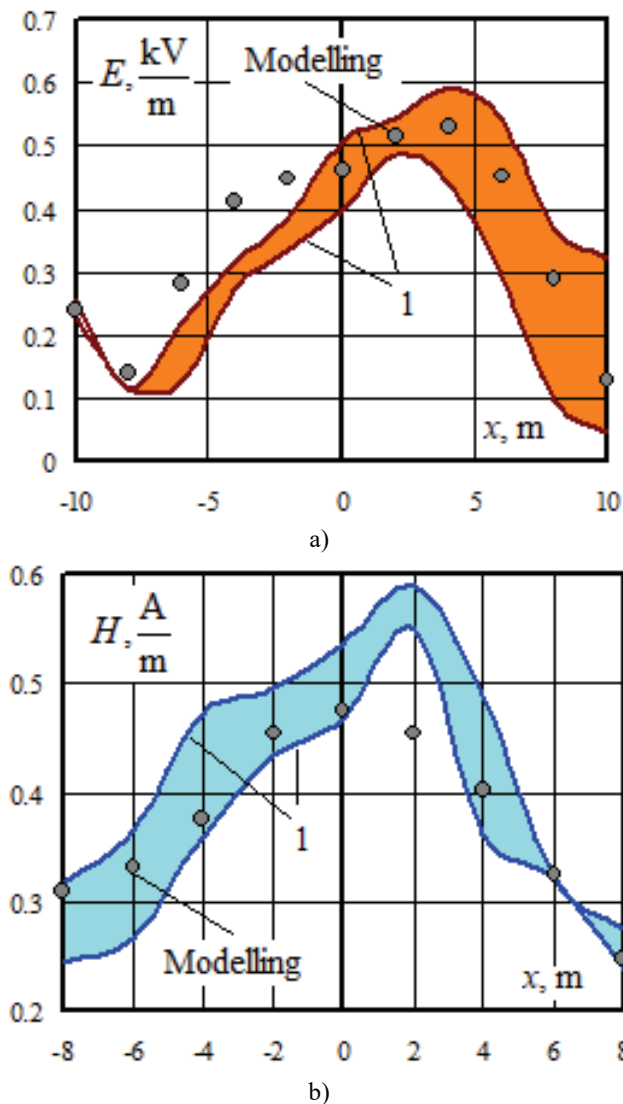


Fig. 5. Interval representation of the EMF intensity measurement results: a – electric field; b – magnetic field; 1 boundaries of scatter area of the experimental data.

Measurements were carried out with a P3-50 field intensity meter using projections of intensities on corresponding coordinate axes at a height of 1.5 m from the ground surface.

The results of measurements and computations are presented in Fig. 5.

In general, the nature of the relationship between the electric field intensity and the x coordinate, obtained by computation, corresponds to similar relationships constructed based on experiments. In the first experiment, the maximum intensity values are virtually equal to the calculated values.

The calculated values for the OPL right-hand circuit lie within the boundaries of the scatter area of the experimental values.

Adequacy of modeling is confirmed by high values of correlation coefficients between experimental and calculated data.

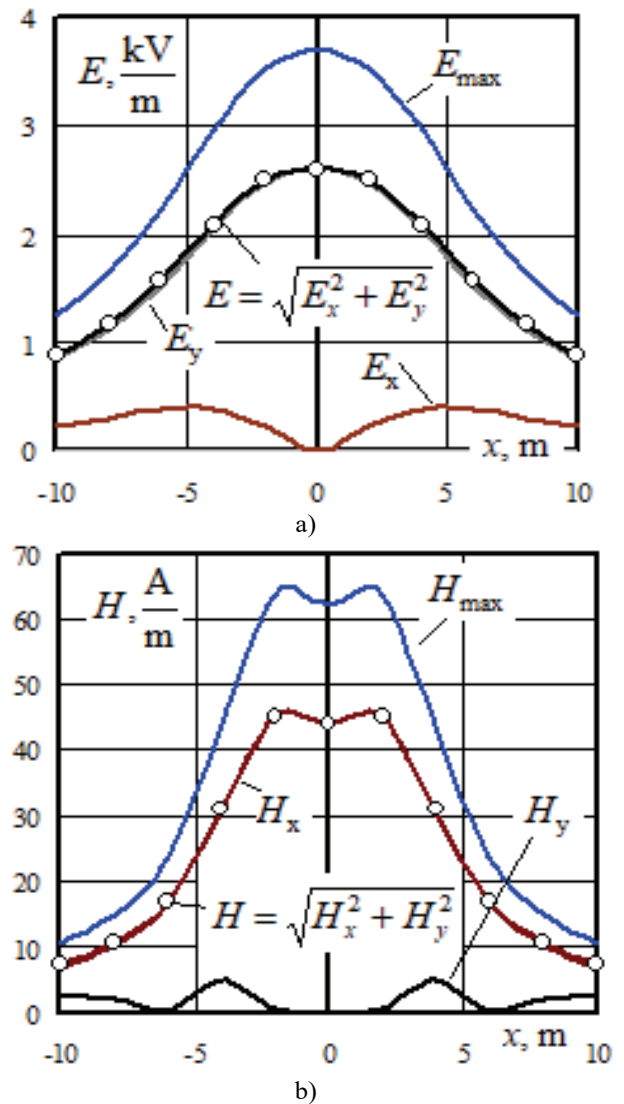


Fig. 6. Amplitudes, effective values and components of EMF intensities at the height of 1.8m: a – electric field; b – magnetic field.

#### V. CASE STUDIES TO DETERMINE THE EMF INTENSITIES

Figures 6–8 present the simulation results of EMF intensities at the height of 1.8 m for a typical 25 kV TPSS of the double-track road section with a current of 414 A and voltage of 25 kV of overhead catenaries.

The dependences obtained indicate the following:

- the low voltage of the traction network results in the maximum level of electric field intensity below the standard value of 5 kV/m;
- the level of magnetic field intensity is quite close to the maximum permissible value but with the current of overhead catenaries equal to 414 A, EMF does not exceed it;
- electromagnetic energy density reaches 80 kV-A/m<sup>2</sup> near the center of the traction network. These data may serve as a basis for specifying electromagnetic safety standards in AC traction networks.

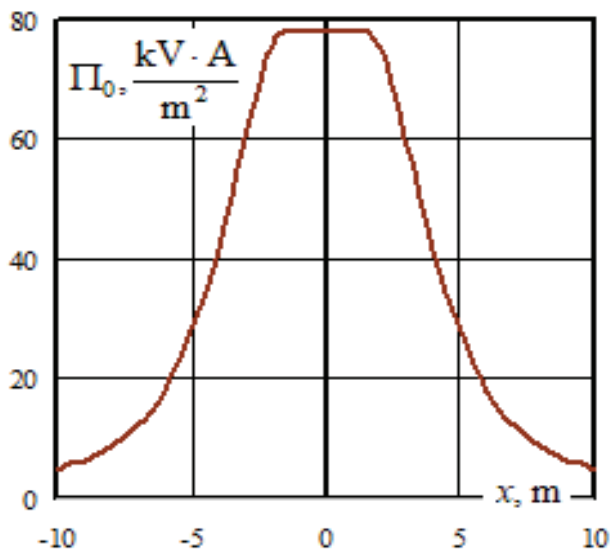
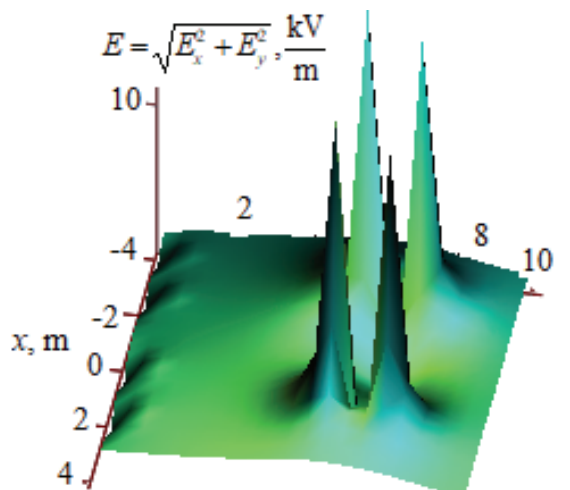
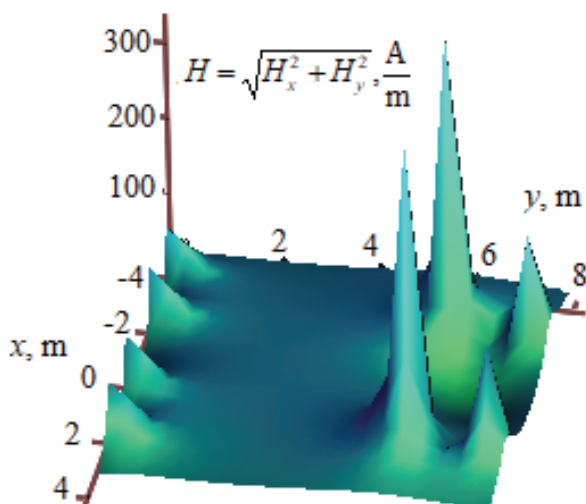


Fig. 7. Density of electromagnetic energy flux at the height of 1.8 m.

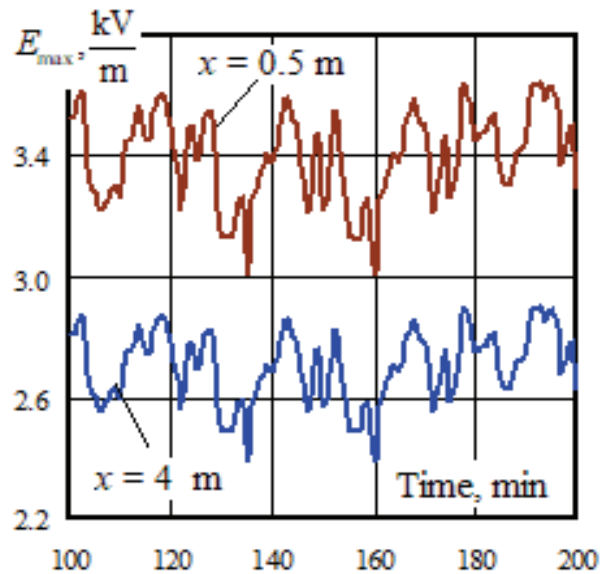


a)

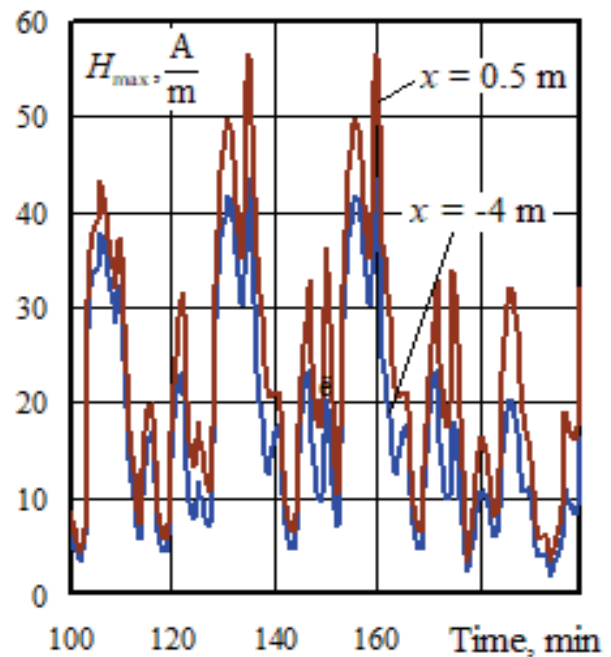


b)

Fig. 8. Cross-section of EMF intensity surfaces: a – electric field; b – magnetic field.



a)



b)

Fig. 9. Time dependences of the intensity amplitude values: a – electric field; b – magnetic field

Results of simulation of the EMF intensity changing over time at the height of 1.8 m are presented in Fig. 9.

Figure 10 shows the simulation results for the electromagnetic fields generated by a double-circuit 220 kV line with a current of 300 A.

The presented results confirm the applicability of the considered technique for determining EMF when assessing the conditions of electromagnetic safety in traction networks and on the routes of high-voltage OPL. It is worth noting that this technique can be used in the EMF calculations for overhead power lines, cable power lines, and conductors of various designs.

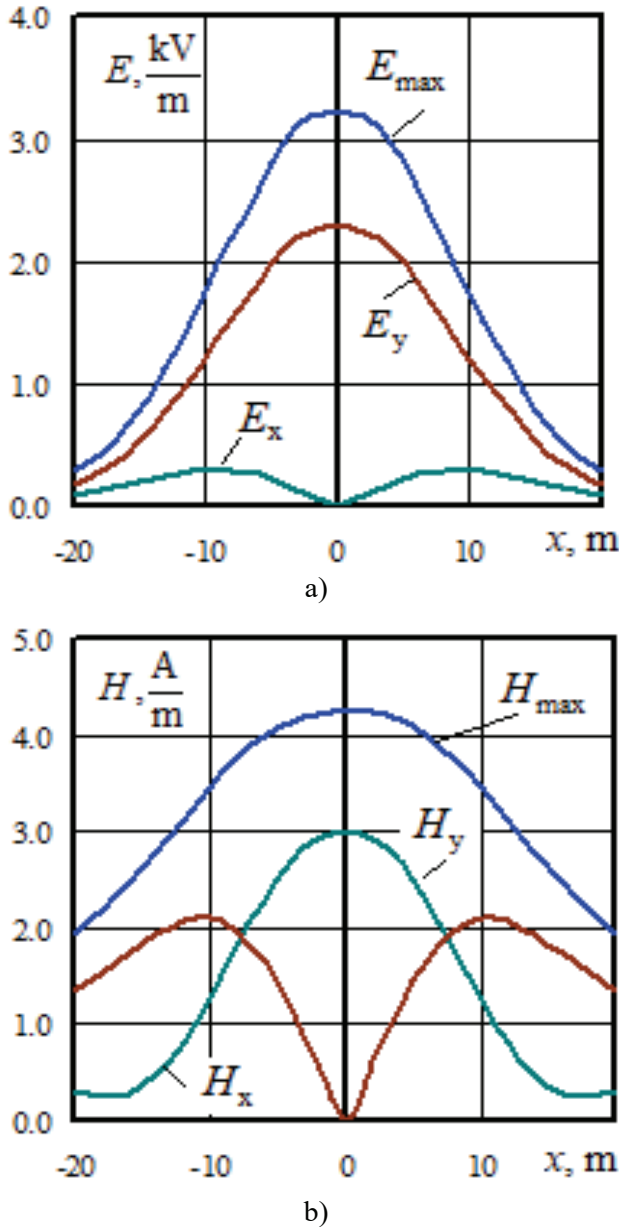


Fig. 10. The intensity components versus the x-coordinate: a – electric field; b – magnetic field

VI. EMF AT THE INTERSECTIONS OF TRACTION NETWORKS AND HIGH-VOLTAGE POWER LINES

The above-described technique was extended to the detailed analysis of the electromagnetic field structure at points of power lines crossing the railroad.

Assuming mutual perpendicularity of the overhead power line and railroad wires, we can calculate components of EMF vectors and determine the resultant field, which is complicated by the following factors:

- overhead power line can be either single-circuit or double-circuit;
- mutual voltage phasing of TPSS and OPL, the spatial location of the OPL wires of different phases, and the number of electrified railroad tracks are to be factored in.

The problem statement at issue takes into account both these factors. Fig. 11 shows a frequently encountered situation where a 220 kV line is crossing a double-track road section. In this Figure, the overhead catenary wires and rails of the odd track are given in black, while those of the even track are in gray. The dotted line shows OPL wires. Different systems of coordinates are chosen for railroad and OPL, which simplifies the calculation of fields. The coordinates are determined for the conditions where the  $Z$ -axis is directed along the railroad and the  $Z_T$  axis goes along the OPL wires. Currents have opposite directions to  $Z$  and  $Z_T$  axes directions. The origins of coordinates are located on the railroad axis. In this case, electromagnetic fields can be calculated with the Fazonord software separately for traction network and overhead power line with the subsequent addition of respective field vector components.

In the  $XYZ$  coordinate system of railroad, the intensities of traction network electromagnetic field are calculated using formulas (3). In the  $X_T Y_T Z_T$  coordinate system of overhead power line, similar relations are written as follows:

$$\begin{aligned} \dot{E}_{TX} &= \frac{2}{\pi \epsilon_0} \sum_{i=1}^{N_T} \dot{\tau}_i \frac{(x_T - x_{Ti}) y_T y_{Ti}}{\lambda_{Ti}}; \\ \dot{E}_{TY} &= -\frac{1}{\pi \epsilon_0} \sum_{i=1}^{N_T} \dot{\tau}_i \frac{y_{Ti} [(x_T - x_{Ti})^2 - y_T^2 + y_{Ti}^2]}{\lambda_{Ti}}; \\ \dot{H}_{TX} &= \frac{1}{2\pi} \sum_{i=1}^{N_T} \dot{I}_i \frac{y_T - y_{Ti}}{\xi_{Ti}}; \quad \dot{H}_{TY} = -\frac{1}{2\pi} \sum_{i=1}^{N_T} \dot{I}_i \frac{x_T - x_{Ti}}{\xi_{Ti}}; \\ \dot{E}_{TZ} &= 0; \quad \dot{H}_{TZ} = 0, \end{aligned}$$

where

$$\begin{aligned} \xi_{Ti} &= [(x_T - x_{Ti})^2 + [(y_T + y_{Ti})^2 C] [(x_T - x_{Ti})^2 + [(y_T - y_{Ti})^2]]; \\ \lambda_{Ti} &= (x_{Ti} - x_T)^2 + [(y_{Ti} - y_T)^2]. \end{aligned}$$

In the formulas,  $N$  is the number of traction network wires,  $N_T$  is the number of OPL wires;  $\dot{\tau}_i$  is charge per unit of length of wire  $i$ ,  $\dot{I}_i$  is current of wire  $i$  in the direction opposite to the direction of  $Z$  or  $Z_T$  axis;  $(x_i, y_i)$ ,  $(x_{Ti}, y_{Ti})$  are wire coordinates in respective cross-sections.

Observation point coordinates in the  $X_T Y_T Z_T$  system are related to the  $XYZ$  coordinates with following relationships on an assumption that origins of coordinates concur at one point:

$$x = z_T, y = y_T, z = -x_T.$$

The components of OPL field vectors are similarly transformed from the  $X_T Y_T Z_T$  coordinate system to the  $XYZ$  system:

$$\begin{aligned} \dot{E}'_X &= \dot{E}'_{TZ}; \quad \dot{E}'_Y = \dot{E}'_{TY}; \quad \dot{E}'_Z = -\dot{E}'_{TX}; \\ \dot{H}'_X &= \dot{H}'_{TZ}; \quad \dot{H}'_Y = \dot{H}'_{TY}; \quad \dot{H}'_Z = -\dot{H}'_{TX}. \end{aligned} \tag{4}$$

The operations necessary to calculate field intensities at a specified point with coordinates  $(x, y, z)$  are as follows:

1. Determine the components of intensities of the field created by railroad traction network by the given coordinates  $(x, y, z)$  with the aid of Fazonord software in

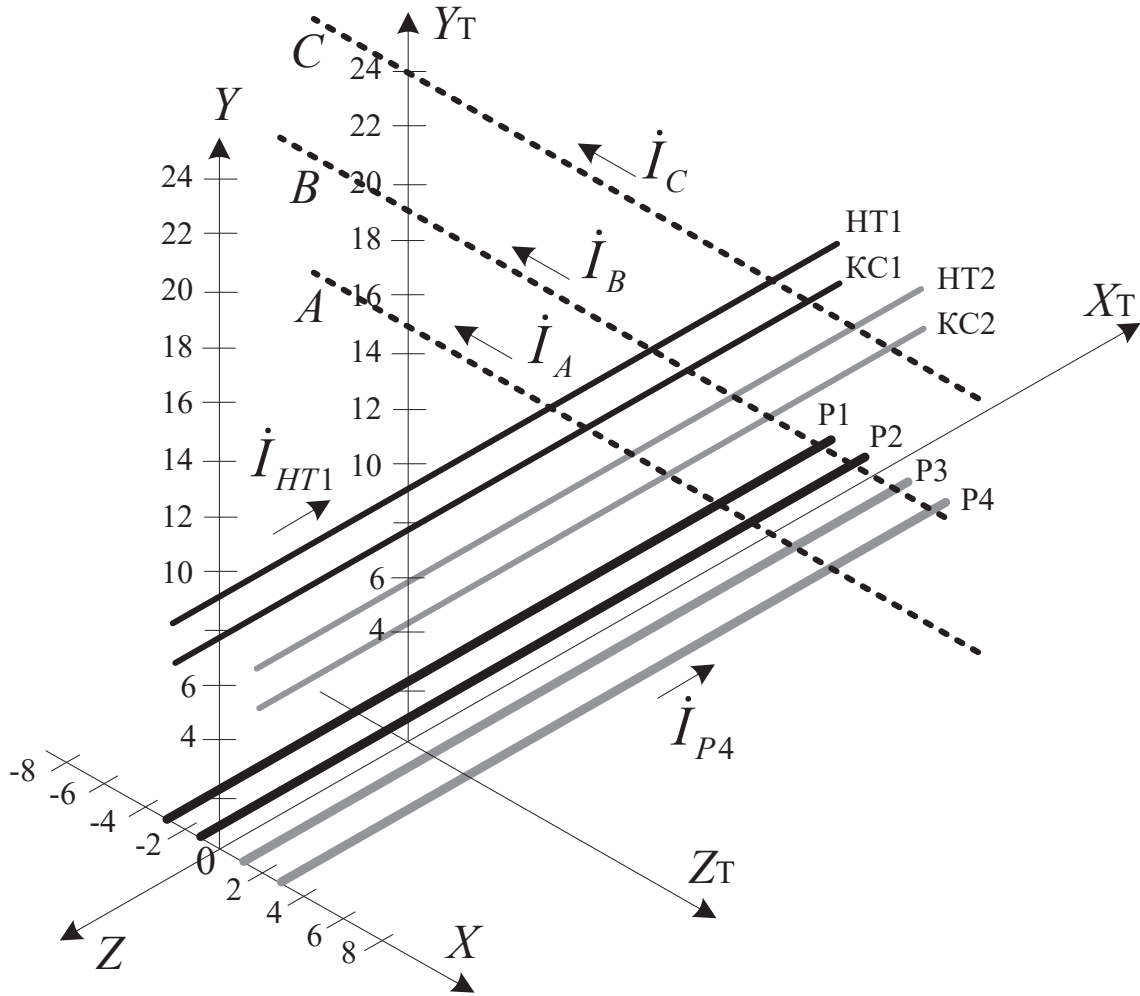


Fig. 11. The diagram of mutual location of OPL and traction network.

- which the electromagnetic field intensity is determined after the operating conditions are calculated.
- Determine the components of intensities of the field generated by overhead power line by the specified coordinates  $z_T = x; y_T = y; x_T = -z$  using the Fazonord software.
  - Calculate the total components of intensities at a specified point according to the expressions (4):

$$\begin{aligned} \dot{E}_{\Sigma X} &= \dot{E}_X + \dot{E}_{TZ} = \dot{E}_X; \quad \dot{E}_{\Sigma Y} = \dot{E}_Y + \dot{E}_{TY}; \\ \dot{E}_{\Sigma Z} &= \dot{E}_Z - \dot{E}_{TX} = -\dot{E}_{TX}; \\ \dot{H}_{\Sigma X} &= \dot{H}_X + \dot{H}_{TZ} = \dot{H}_X; \quad \dot{H}_{\Sigma Y} = \dot{H}_Y + \dot{H}_{TY}; \\ \dot{H}_{\Sigma Z} &= \dot{H}_Z - \dot{H}_{TX} = -\dot{H}_{TX}. \end{aligned}$$

Thus, we determine all three components of the intensity vectors of electric and magnetic fields:

$$\begin{aligned} \dot{E}_{\Sigma i} &= E_{\Sigma i} e^{j\omega t}; \quad E_{\Sigma i}(t) = \sqrt{2} E_{\Sigma i} \sin(\omega t + \varphi_i); \\ \dot{H}_{\Sigma i} &= H_{\Sigma i} e^{j\omega t}; \quad H_{\Sigma i}(t) = \sqrt{2} H_{\Sigma i} \sin(\omega t + \psi_i); \\ & i = x, y, z. \end{aligned}$$

Ends of vectors of electric and magnetic field intensities calculated at some point trace out ellipses lying in the plane

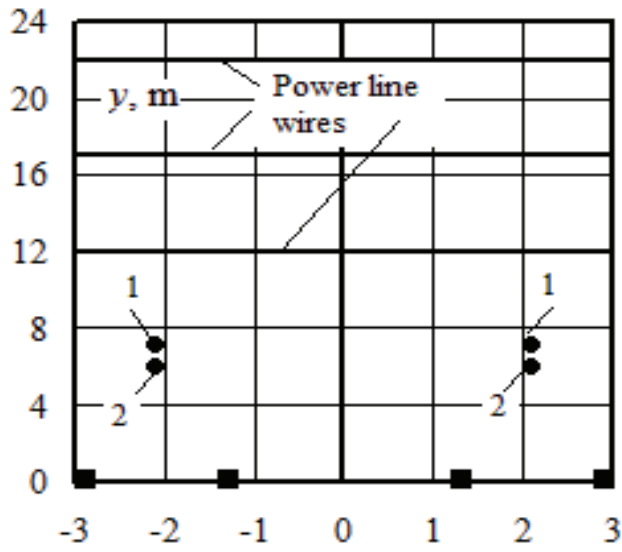
determined by components of these vectors [21]. Whether the vector belongs to a specific plane can be shown by the product of two vectors of the field at different time instants. Vector of this product is perpendicular to the direction of the plane in which the terms lie. In particular, one can analyze two vectors at time  $t = 0$  and at current time  $t$ . The components of vector product  $\vec{E}_0 \times \vec{E}_t$  are determined as follows:

$$\begin{aligned} (\vec{E}_0 \times \vec{E}_t)_X &= 2 E_{\Sigma Y} E_{\Sigma Z} \sin(\varphi_Y - \varphi_Z) \sin(\omega t); \\ (\vec{E}_0 \times \vec{E}_t)_Y &= 2 E_{\Sigma X} E_{\Sigma Z} \sin(\varphi_Z - \varphi_X) \sin(\omega t); \\ (\vec{E}_0 \times \vec{E}_t)_Z &= 2 E_{\Sigma X} E_{\Sigma Y} \sin(\varphi_X - \varphi_Y) \sin(\omega t). \end{aligned}$$

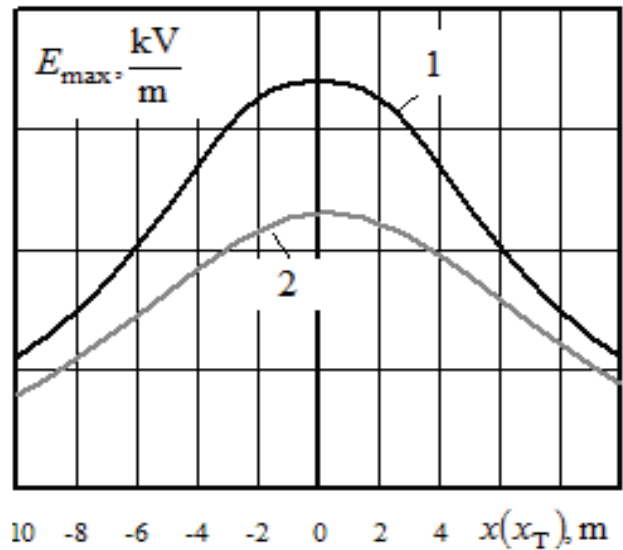
Squared absolute value of the vector product equals

$$|(\vec{E}_0 \times \vec{E}_t)|^2 = (\vec{E}_0 \times \vec{E}_t)_X^2 + (\vec{E}_0 \times \vec{E}_t)_Y^2 + (\vec{E}_0 \times \vec{E}_t)_Z^2.$$

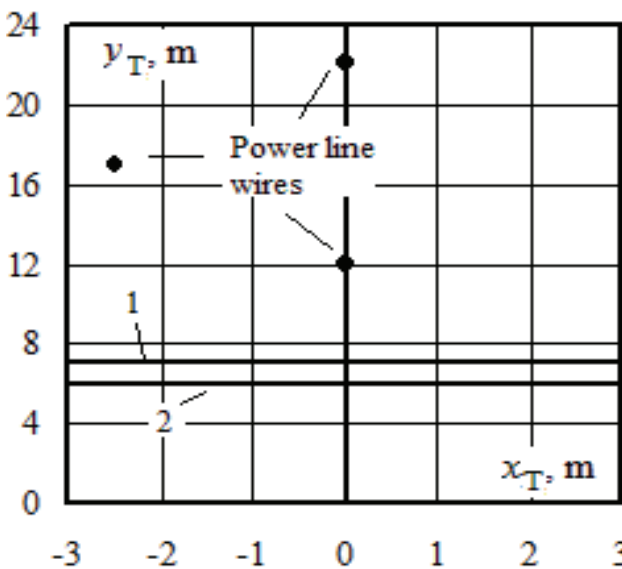
These data show that ratios of the vector product components to the vector absolute value (vector direction cosines) do not depend on time, which indicates that intensity vector is located at any time instant in the same plane. Normal line to this plane is determined by a single vector with components equal to



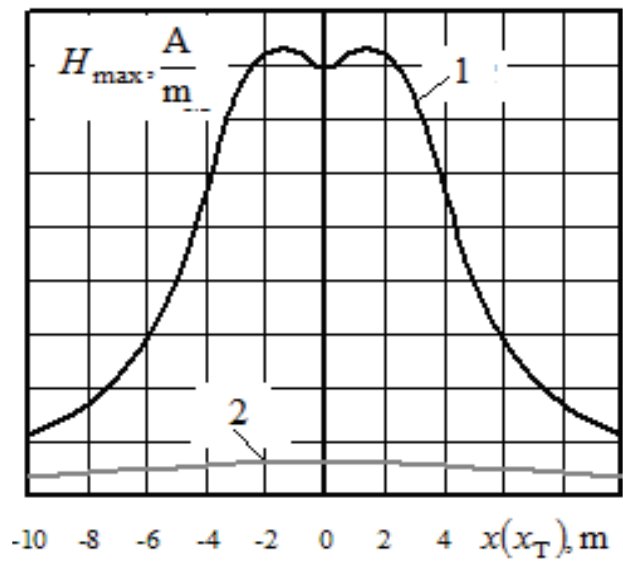
a)



a)



b)



b)

Fig. 12. Location of traction network (a) and OPL (b) wires: 1 – contact wire; 2 – catenary messenger.

Fig. 13. The amplitudes of electric (a) and magnetic (b) field intensities versus the x coordinate: 1 – traction network; 2 – OPL.

$$\frac{(\vec{E}_0 \times \vec{E}_t)_x}{|\vec{E}_0 \times \vec{E}_t|} ; \frac{(\vec{E}_0 \times \vec{E}_t)_y}{|\vec{E}_0 \times \vec{E}_t|} ; \frac{(\vec{E}_0 \times \vec{E}_t)_z}{|\vec{E}_0 \times \vec{E}_t|}$$

Extreme values of the intensity vector can be calculated by differentiating the squared vector length:

$$E_s = [E_{\Sigma i}(t)]^2 = 2 \sum_{i=1}^3 E_{\Sigma i}^2 \sin^2(\omega t + \varphi_i) = \sum_{i=1}^3 E_{\Sigma i}^2 - \sum_{i=1}^3 E_{\Sigma i}^2 \cos(2\omega t + 2\varphi_i)$$

Extreme values are determined by zero value of the derivative:

$$\frac{d E_s}{d t} = 2\omega \sum_{i=1}^3 E_{\Sigma i}^2 \sin(2\omega t + 2\varphi_i) = 0,$$

from which

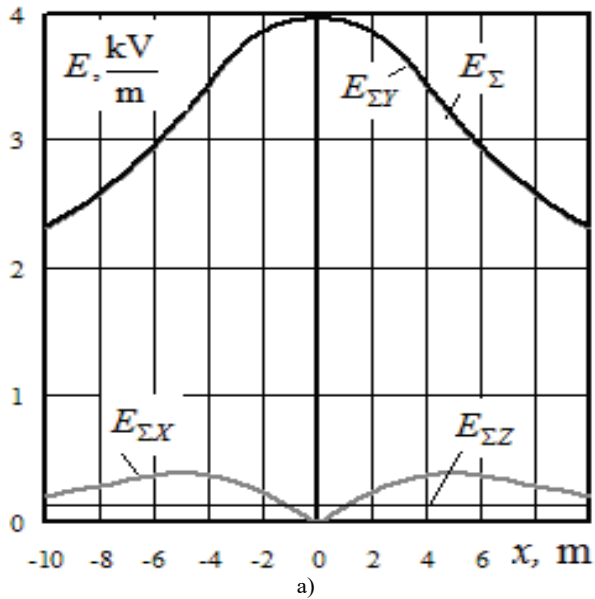
$$t_{\max, \min} = -\frac{1}{2\omega} \text{Arctg} \frac{\sum_{i=1}^3 E_{\Sigma i}^2 \sin(2\varphi_i)}{\sum_{i=1}^3 E_{\Sigma i}^2 \cos(2\varphi_i)},$$

where the maximum is determined by negative value of the second derivative:

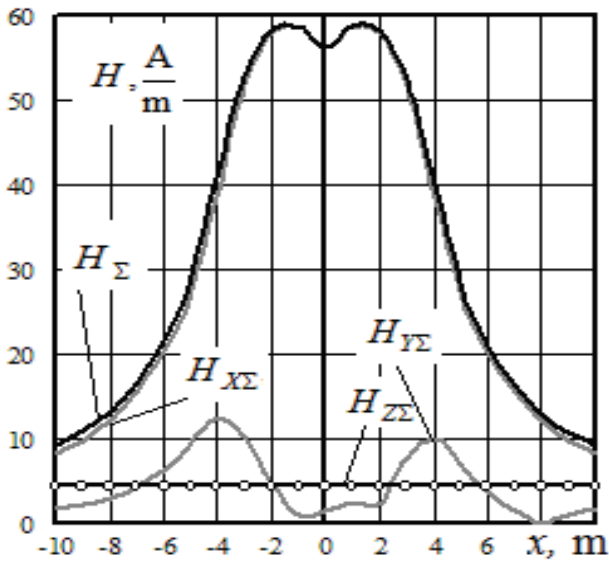
$$\sin(2\omega t_{\max}) \sum_{i=1}^3 E_{\Sigma i}^2 \sin(2\varphi_i) > \cos(2\omega t_{\max}) \sum_{i=1}^3 E_{\Sigma i}^2 \cos(2\varphi_i),$$

while the minimum is determined by positive value:

$$\sin(2\omega t_{\min}) \sum_{i=1}^3 E_{\Sigma i}^2 \sin(2\varphi_i) < \cos(2\omega t_{\min}) \sum_{i=1}^3 E_{\Sigma i}^2 \cos(2\varphi_i).$$

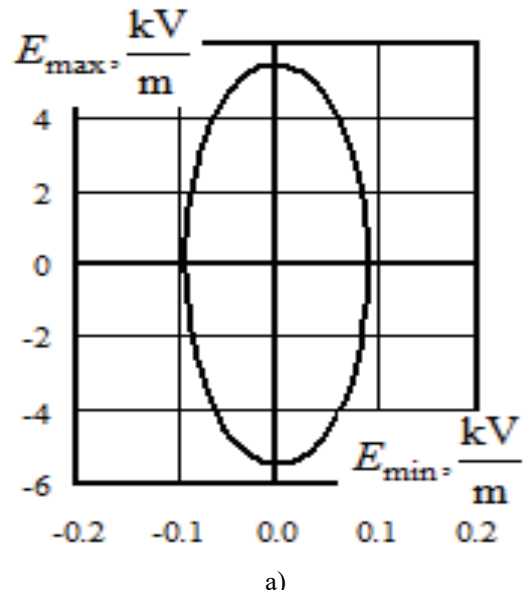


a)

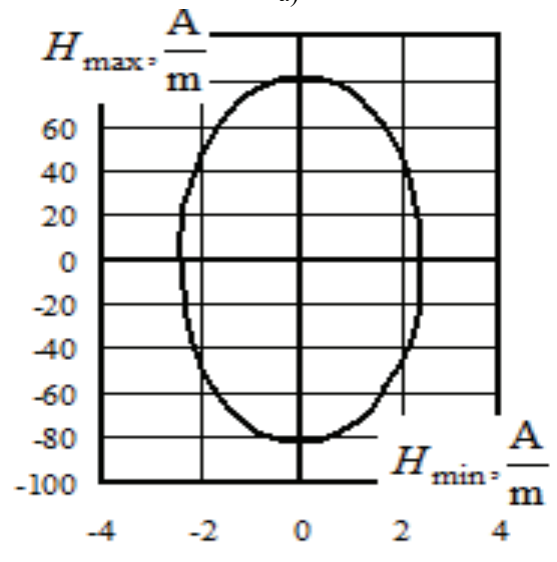


b)

Fig. 14. The total components of intensities for electric (a) and magnetic (b) fields (effective values) versus x coordinate.



a)



b)

Fig. 15. Loci of resultant intensity vectors of electric (a) and magnetic (b) fields in coordinate axes of polarization ellipse for the point with coordinates  $x = 2$  m;  $y = 1.8$  m.

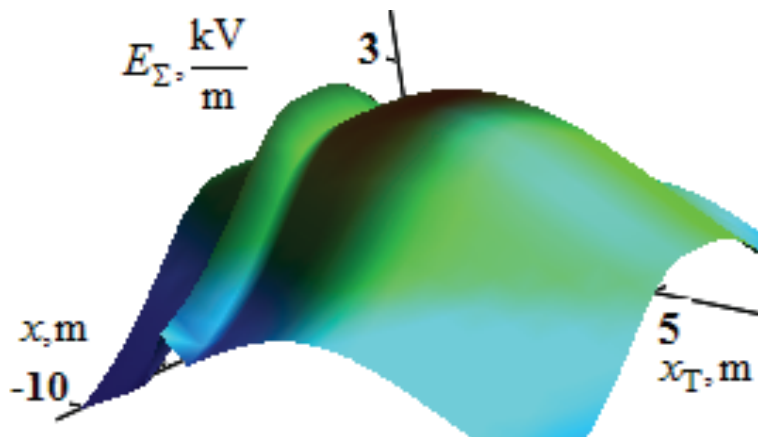


Fig. 16. The graph of the surface of electric field total intensity in  $x, x_T$  coordinates.

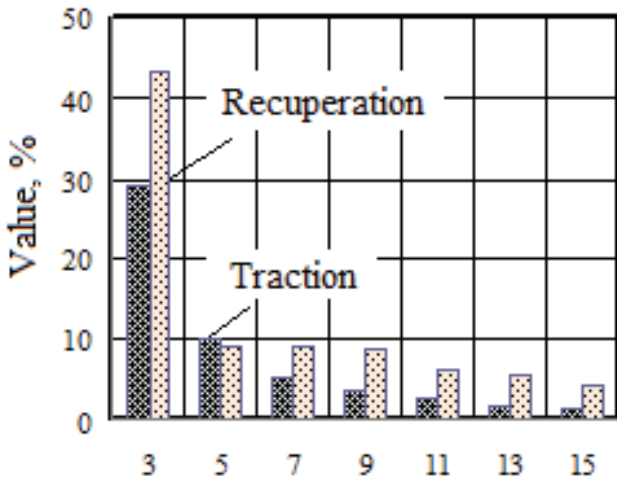


Fig. 17. Typical levels of electric locomotive current harmonics as a percentage of the fundamental frequency current.

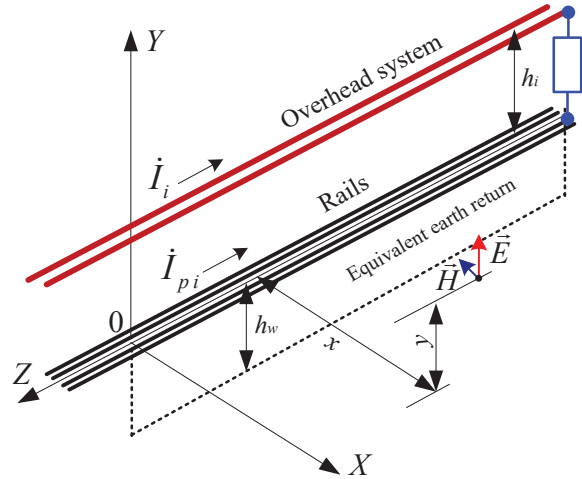


Fig. 18. Coordinate system exemplified by a traction network.

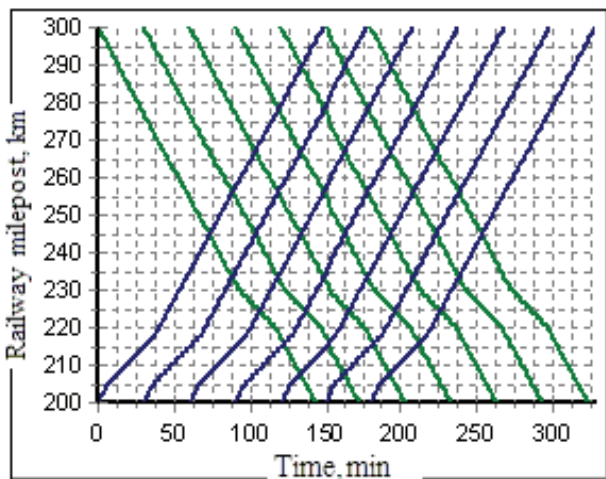
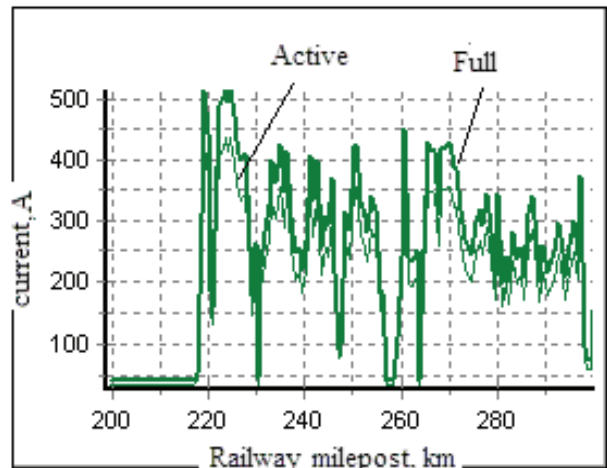
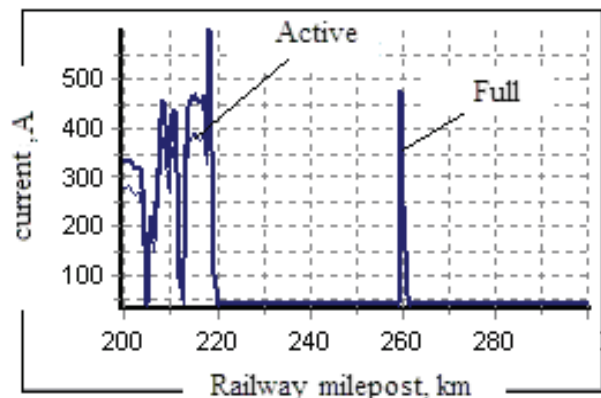


Fig. 19. Train schedule.



a)



b)

Fig. 20. Train current profiles: a – odd direction; b – even direction.

Different field points are characterized by different polarizations and field component relationships. Locus of the intensity vector located in the plane of polarization can be determined using the procedure from [4]. The simulation results of EMF of the wire systems according to Fig. 12 for the height of the observation point of 1.8 m are shown in Figs. 13–16.

Coordinate  $z$  was measured from the point of intersection of the overhead power line (AC-300 wires) with the traction network. The overhead line was assumed to transit the power of  $5 + j40 \text{ MV} \cdot \text{A}$  by each phase with a linear voltage of 230 kV and current of 648 A, which are close to maximum permissible values for the AC-300 wires. Voltages at OPL starting end were equal to 132.8 kV with angles  $0^\circ, -120^\circ, 120^\circ$ , currents flowing into these nodes were  $648e^{-j28.6^\circ} \text{ A}, 647e^{-j148.6^\circ} \text{ A},$  and  $647e^{j91.3^\circ} \text{ A}$ . The power of  $8 + j8 \text{ MB} \cdot \text{A}$  was transmitted by catenaries of each railway track. The calculated voltage of the overhead system was  $25.6e^{-j5.6^\circ} \text{ kV}$ , and overhead catenaries currents were equal to  $450e^{-j51.1^\circ} \text{ A}$ .

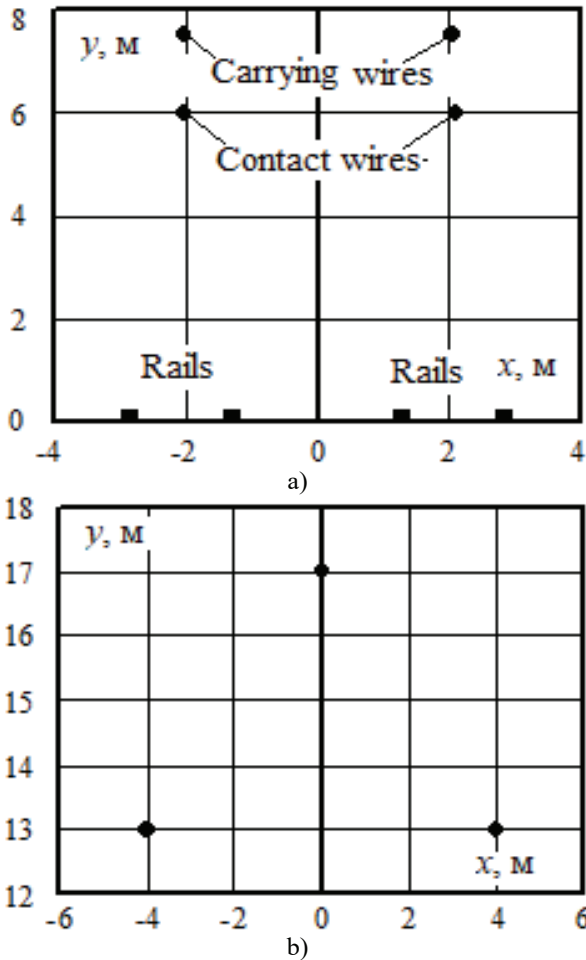


Fig. 21. Coordinates of conductive parts: a – traction network; b – OPL.

The findings suggest the following.

1. The total intensities of magnetic fields of traction network and OPL differ from the intensity of magnetic field generated by traction network by  $-2...+13\%$ . At the point with coordinates  $x = 2$  m;  $y = 1.8$  m, the magnetic field intensity amplitude in the calculated option was equal to 82 A/m.
2. The increase in the maximum value of the electric field intensity amplitude at the intersection point of the OPL and traction network reaches 66%; at the point indicated in the previous paragraph, the value of this parameter is 5.4 kV/m.

The developed technique can be used to resolve practical issues associated with the improvement in electromagnetic safety for personnel engaged in the operation of high voltage power grids and AC railroad power supply systems.

VII. CONSIDERATION OF HIGHER HARMONICS IN EMF SIMULATION

AC traction networks are the sources of higher harmonics, as their voltage often exceeds the standards. Russian rectifier electric locomotives with a rated voltage of 25 kV not only consume the current from overhead catenary but also generate considerable higher

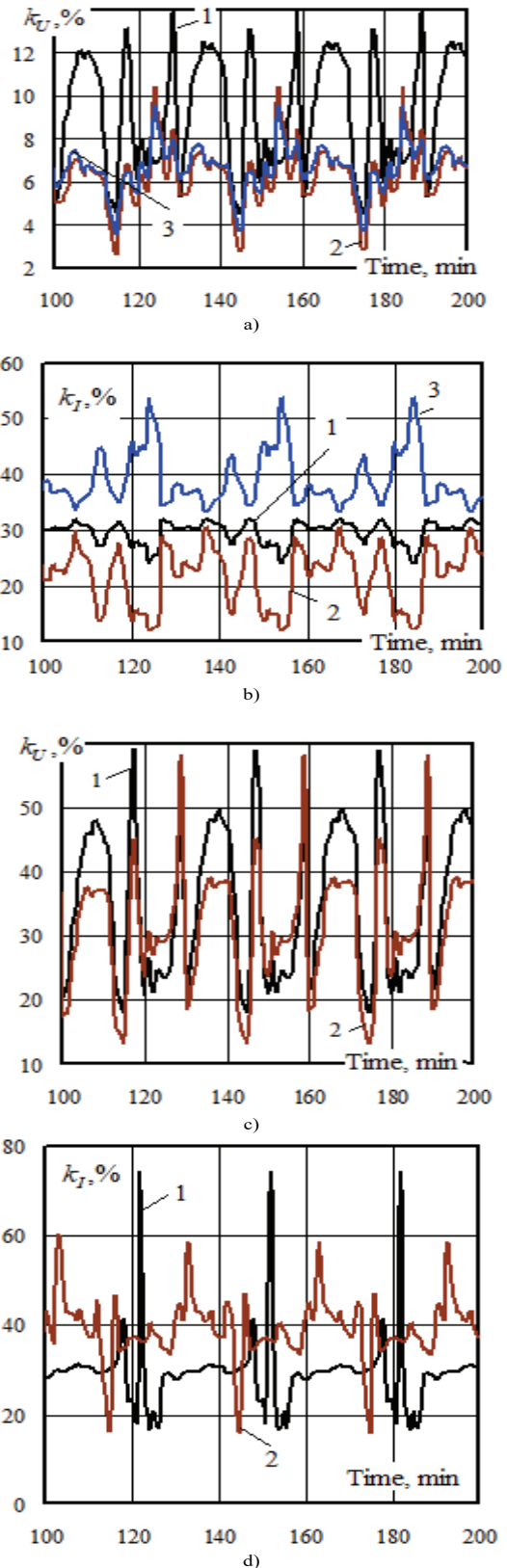
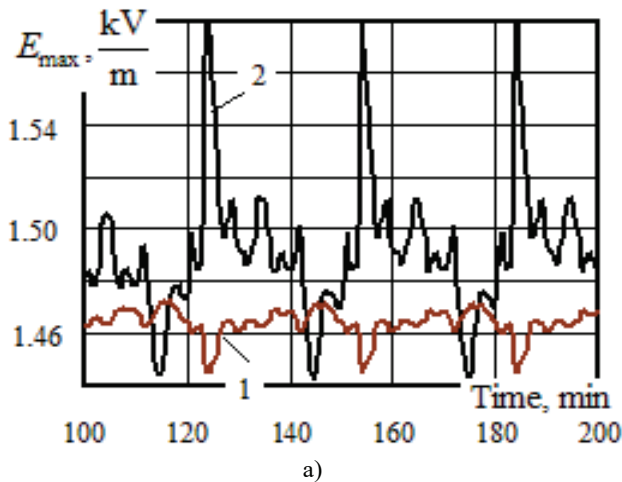
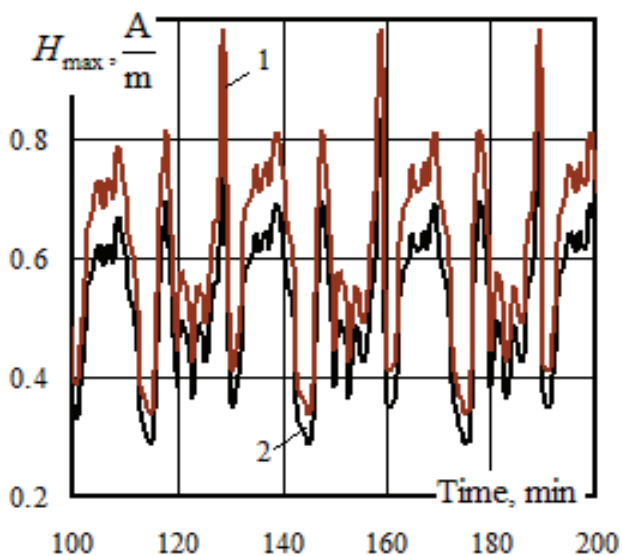


Fig. 22. The total harmonic current and voltage distortion factors versus simulation time: a, b – OPL; c, d – overhead system;  $k_U, k_I$  – total harmonic current and voltage distortion factors; in a, b: 1 – phase A; 2 – phase B; 3 – phase C; in c, d: 1 – overhead catenary of the odd track; 2 – overhead catenary of the even track



a)

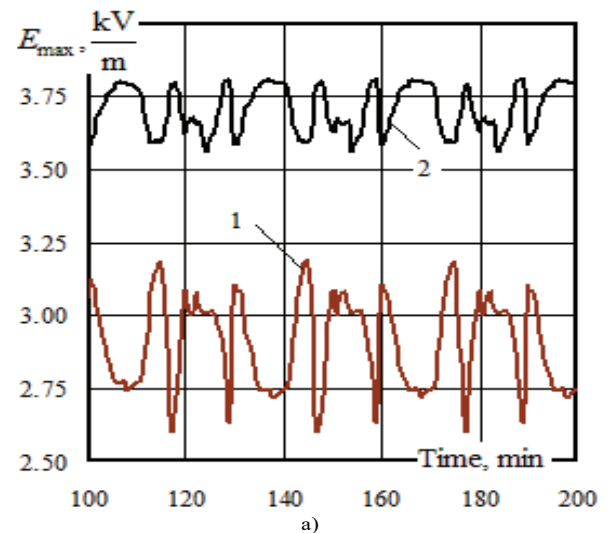


b)

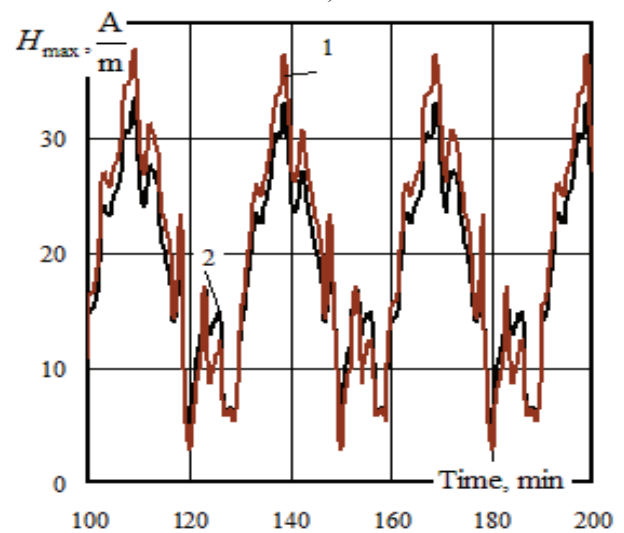
Fig. 23. Maximum intensities of EMF generated by OPL versus simulation time: a – electric field; b – magnetic field; 1 – for fundamental frequency; 2 – for higher harmonics.

harmonics (Fig. 17), which entails significant distortions of current and voltage waveforms. Harmonics of traction networks penetrate into 110-220 kV supply networks and increase harmonics of network voltage. For this reason, electromagnetic fields generated by a 25 kV overhead system and 110-220 kV power lines supplying traction substations contain a significant proportion of higher harmonics [18]. This factor should be kept in mind when assessing the interference immunity of various types of equipment and when determining the electromagnetic safety conditions. Higher harmonics complicate the polarization picture [22–27], and the best way to simulate is to analyze the fields separately for different harmonics, with their subsequent superposition.

Calculation of EMF intensities requires a preliminary computation of operating conditions of single-phase traction network and external three-phase power supply



a)



b)

Fig. 24. Amplitudes of intensities of EMF generated by the traction network versus simulation time: a – electric field; b – magnetic field; 1 – for fundamental frequency; 2 – for higher harmonics.

system. Nonstationarity and changes in the location of traction loads create additional difficulties in calculating the operating conditions, which are almost overcome for fundamental frequency in [18].

The changes in magnitudes and spatial location of traction loads are factored in by computations of a series of operating conditions satisfying the given time instants. The diagrams for such computations are usually built with the discreteness of 1 minute. The electromagnetic field of the traction network is determined by the voltage and current of the catenary wires and rails. Rail currents are calculated as induced currents of grounded conductors located on the ground surface. The electric and magnetic fields of parallel rectilinear wires are linearly polarized, the position of the intensity vectors changes during the period.

Electromagnetic fields of traction network and OPL are plane-parallel and identical in any plane perpendicular

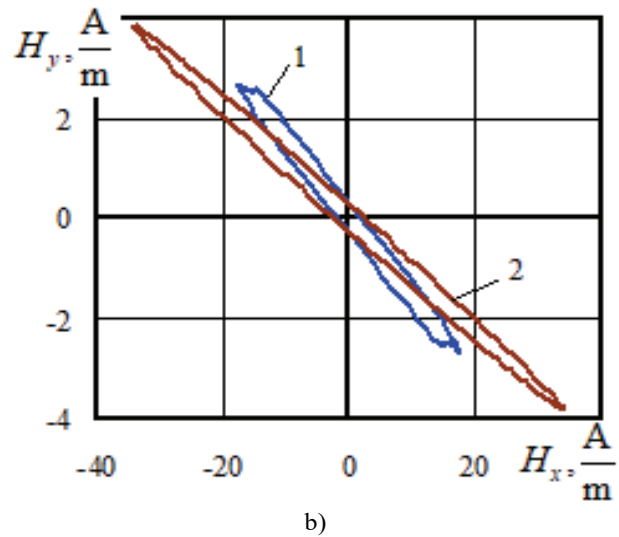
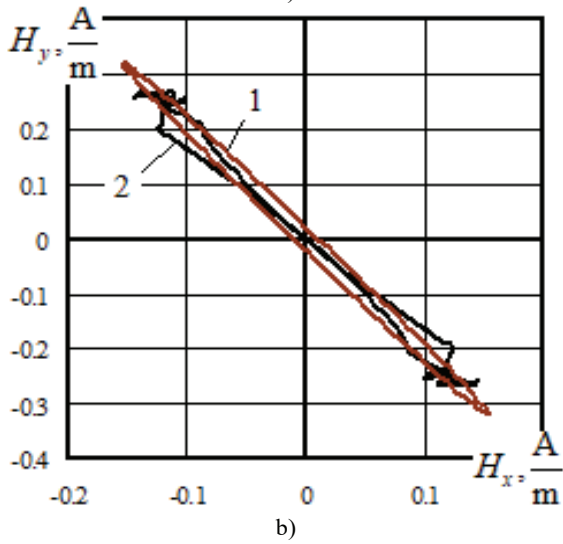
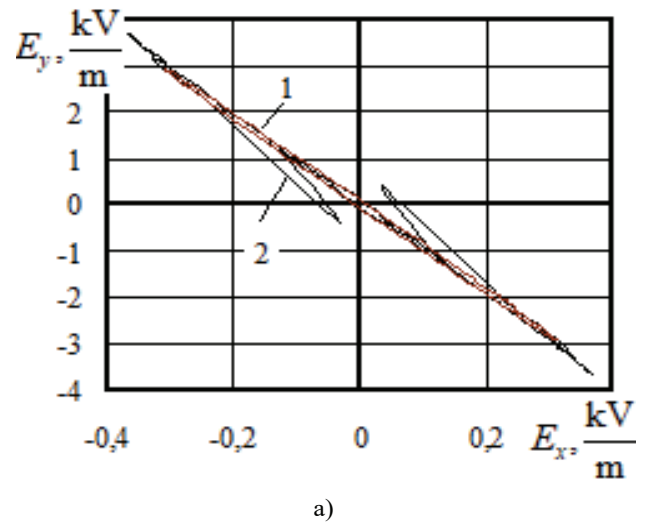
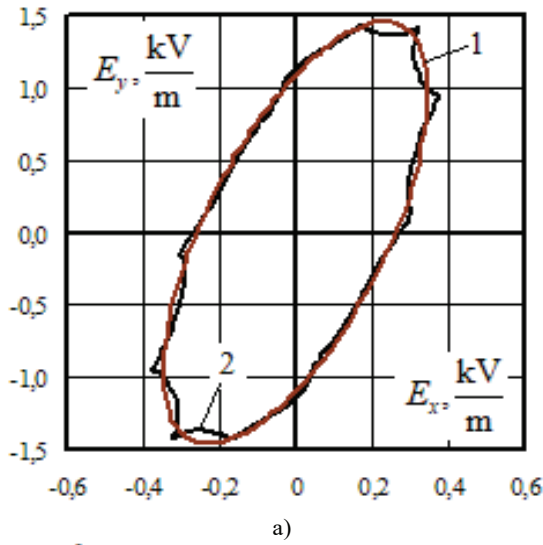


Fig. 25. Loci of the OPL EMF intensity vectors at the 206th simulation minute: a – electric field; b – magnetic field; 1 – for fundamental frequency; 2 – for higher harmonics.

Fig. 26. Loci of the traction network EMF intensity vectors at the 206th simulation minute: 1 – for fundamental frequency; 2 – for higher harmonics; a – electric field; b – magnetic field.

to the wires. As noted before, it is convenient to use the Cartesian coordinate system to describe such fields because the origin of the system lies on the ground surface under the center of the wire system, the  $X$ -axis is perpendicular to the wires along the ground surface, the  $Y$ -axis is directed vertically upward, and the  $Z$ -axis is directed against the positive direction of currents (Fig. 18).

Electric field intensities at a point with coordinates  $x, y$  for each  $k$  harmonic of the line, including  $N$  wires, are calculated using the formulas similar to those provided above:

$$\begin{aligned} \dot{E}_{kx} &= \frac{2}{\pi \epsilon_0} \sum_{i=1}^N \dot{\tau}_{ki} \frac{(x-x_i)y y_i}{\xi_i}; \\ \dot{E}_{ky} &= -\frac{1}{\pi \epsilon_0} \sum_{i=1}^N \dot{\tau}_{ki} \frac{y_i [(x-x_i)^2 - y^2 + y_i^2]}{\xi_i}, \end{aligned}$$

where  $\dot{\tau}_{ki}$  is the charge of wire  $i$  per unit of length for harmonic  $k$ , determined from the first group of Maxwell's formulas

$\dot{\mathbf{T}}_k = \mathbf{A}^{-1} \cdot \dot{\mathbf{U}}_k$ ;  $\dot{\mathbf{U}}_k = [\dot{U}_{k1} \dots \dot{U}_{kN}]^T$  is the vector of wire potentials at harmonic  $k$ ;  $\dot{\mathbf{T}}_k = [\dot{\tau}_{k1} \dots \dot{\tau}_{kN}]^T$  is the vector of linear charges of wires,  $\mathbf{A}$  is the frequency-independent matrix of potential coefficients.

For each electric field harmonic, the time dependences of spatial components are determined by the expression

$$\vec{E}_k(t) = E_{mx} \sin(k\omega t + \psi_{kx}) \vec{e}_x + E_{my} \sin(k\omega t + \psi_{ky}) \vec{e}_y,$$

where  $\vec{e}_x, \vec{e}_y$  are unitary vectors of the Cartesian coordinate system;  $\omega = 314$  rad/s. As shown in [21], the vectors of field extreme values  $\vec{E}_{k\max}$  and  $\vec{E}_{k\min}$  are located in the polarization plane of a given harmonic and the intensity vector rotates in this plane with an ellipse-shaped locus. The time instants satisfying the intensity extreme values are calculated for each harmonic based on

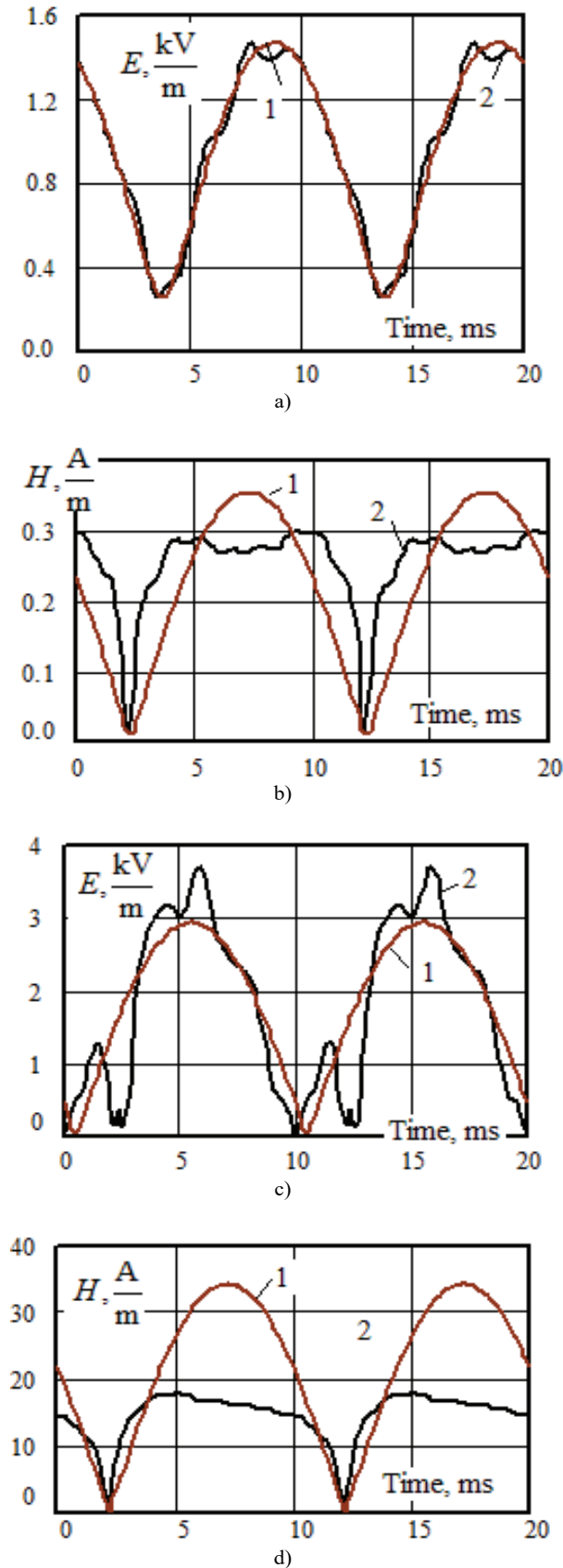


Fig. 27. Shapes of intensity curves at the 206-th simulation minute: a, b – OPL; c, d – traction network; a, c – electrical field; b, d – magnetic field.

the following relationship:

$$k\omega t_{k, \min, \max} = -\frac{1}{2} \arctg((E_{kmx}^2 \sin 2\psi_{kx} + E_{kmy}^2 \sin 2\psi_{ky}) / (E_{kmx}^2 \cos 2\psi_{kx} + E_{kmy}^2 \cos 2\psi_{ky})).$$

The first arctangent value is chosen within  $[-\pi/2, \pi/2]$ , the second one differs by the value of  $\pi$ . The maximum and minimum absolute values of intensity are determined by the signs of the second derivative:

$$\text{sign}(E_{kmx}^2 \cos[2(k\omega t_{k, \max} + \psi_{kx})] + E_{kmy}^2 \cos[2(k\omega t_{k, \max} + \psi_{ky})]).$$

The directions of the vector maxima and minima  $\vec{E}(t)$  vary within the period according to the changes in the direction cosines

$$\cos(\vec{e}_i, \vec{E}_{k, \max}) = \frac{E_{kmi} \sin(k\omega t_{\max} + \psi_{ki})}{E_{k, \max}};$$

$$E_{k, \max} = \sqrt{\sum_{i=1}^2 [E_{kmi} \sin(k\omega t_{\max} + \psi_{ki})]^2};$$

$$\cos(\vec{e}_i, \vec{E}_{k, \min}) = \frac{E_{kmi} \sin(k\omega t_{\min} + \psi_{ki})}{E_{k, \min}};$$

$$E_{k, \min} = \sqrt{\sum_{i=1}^2 [E_{kmi} \sin(k\omega t_{\min} + \psi_{ki})]^2},$$

where  $i = x, y$ .

The horizontal and vertical components of the magnetic field intensity of the multi-wire line at harmonics are calculated using the formulas similar to those given above:

$$\dot{H}_{kx} = \frac{1}{2\pi} \sum_{i=1}^N \dot{I}_{ki} \frac{y - y_i}{(x_i - x)^2 + (y_i - y)^2};$$

$$\dot{H}_{ky} = -\frac{1}{2\pi} \sum_{i=1}^N \dot{I}_{ki} \frac{x - x_i}{(x_i - x)^2 + (y_i - y)^2},$$

with the only difference, the effective value of current  $\dot{I}_{ki}$  of wire  $i$  is taken for harmonic  $k$ .

These formulas are valid for all harmonics of practical importance at distances of no more than 100 m from a system of wires that create the field. Parameters of the magnetic field intensity vector are determined in the same way as for the electric field.

The presented technique is implemented in the Fazonord software. The simulation assumes the following:

- the electric system under study may contain transmission lines, transformers, loads, and AC traction network;
- the earth surface is assumed to be flat and perfectly conductive for the electric field; image charges are used to factor in the earth influence; the magnetic field of the near area is virtually not affected by the earth; however, the Carson formulas [28] are implemented in the software to calculate EMF at distances of more than 100 m from the field source;
- based on the network calculation, the wire potentials and currents are determined; electric field intensities are calculated via the linear charges of wires with the help of potential coefficients;

Table 1. Maximum and average values of EMF intensity amplitudes for OPL and Traction Network.

Network element	Field	Index	Higher harmonics considered	Higher harmonics are not considered	Difference, %
OPL	Electric, kV/m	Average	1.47	1.47	0.0
		Maximum	1.58	1.48	6.8
	Magnetic, A/m	Average	0.32	0.37	-13.5
		Maximum	0.37	0.98	-15.3
Traction network	Electric, kV/m	Average	3.62	3.14	15.3
		Maximum	3.14	3.52	8.2
	Magnetic, A/m	Average	13.8	14.9	-7.4
		Maximum	37.4	43.4	-13.8

- EMF intensities are calculated for each harmonic.

An enlarged algorithm of EMF calculation in terms of harmonics includes the following stages.

1. Generate a calculation diagram, which includes models of multi-wire lines and transformers connected to other elements.
2. Set the coordinates of space points for each line under study. These space points require the intensities to be calculated.
3. Calculate EMF intensities for each instantaneous diagram after determining the operating conditions at the frequency of the current harmonic, including the fundamental one, with the above formulas:
  - Calculate potential coefficients;
  - Determine complexes of linear charge densities of wires;
  - Determine components of electric field intensity complexes at the control points of space;
  - Calculate currents of individual wires of multi-wire systems and magnetic field intensities at the same points.
4. Determine time dependences of total field intensities of harmonics with the maximum values obtained for a time interval equal to the period of the fundamental frequency. Intensity curve shapes are calculated with a 0.2 ms step. Based on these data and the scale selected, the vector loci are plotted.

A typical diagram of traction and external AC power supply system is chosen to illustrate the capabilities of the technique described. It includes four sections of 220 kV OPL with AC-240 wires, three traction substations, and two inter-substation zones (ISZ) with a length of 50 km. The EMF intensities, given harmonics, were calculated in the middle of the left-hand ISZ and on the OPL left-hand end adjacent to the intermediate traction substation. The sources of current harmonics were seven trains of odd direction with a weight of 6 300 tons and seven trains of even direction with a weight of 6 000 tons (Fig. 19). The mountain pass section of the railroad with the pass at the railway milepost 219 km entails considerable current consumption by trains (Fig. 20). The EMF calculations require, as input data, coordinates of the multi-wire system wires that are equivalent in terms of sag. Fig. 21 shows their cross-sectional position.

Simulation modeling of train operation at the interval of simulated time up to the 327th min provided the time dependences of the following parameters:

- total harmonic voltage and current distortion factors in the middle of the left-hand ISZ, and on the left-hand end of OPL of the second substation; Fig. 22 shows the dependences at the interval from the 100th to the 200th minute, when the railroad section is filled with trains;
- maximum values of electric and magnetic field intensities at the height of 1.8 m (Figs. 23, 24); the intensities were calculated for the traction network at the point with coordinates  $x = 2.1$  m;  $y = 1.8$  m; for OPL  $x = 4$  m;  $y = 1.8$  m.

The time dependences of  $k_U$ ,  $k_I$  parameters, shown in Fig. 22, indicate that the operating conditions under consideration are characterized by significant levels of harmonic current and voltage distortions. The maximum values of  $k_U$ ,  $k_I$  for the traction network reach 60 and 75%, respectively, and for the OPL – 14 and 55%, for the whole simulation time. The overhead catenary of the odd track is characterized by higher levels of harmonics, which is associated with high traction loads of the odd track close to the control point.

Figures 22, 23, and 24 demonstrate significant variability of non-sinusoidality and EMF intensity parameters associated with trains operation. The maximum amplitudes of the OPL electric field intensities, calculated for higher harmonics, are higher than similar indicators for the field of fundamental frequency by 7% (Table 1). However, a reverse situation is observed for the magnetic field – the intensities maxima decrease by 15% (with higher harmonics considered), which is associated with the specific features of phase characteristics of current harmonics.

The loci of EMF intensity vectors indicate the ellipse distortions due to the higher harmonic current and voltage effect. The same distortions are observed in the shapes of curves of the field absolute values during the period of fundamental frequency (Fig. 27). The presented results confirm the importance of factoring in harmonic distortions when simulating EMF generated by traction networks and power lines adjacent to traction substations.

The presented technique of calculating the intensities of EMF generated by power lines and traction networks includes preliminary computations of operating conditions

of the integrated system of traction and external power supply at fundamental and harmonic frequencies as an essential stage. The considered example of a three-phase – single-phase electrical network has proved the importance of considering harmonic distortions when determining EMF. This technique can also be employed to factor in higher harmonics to determine EMF generated by multi-wire power lines of any design.

#### VIII. CONCLUSION

The technique developed to determine electromagnetic fields generated by overhead power lines has the following features:

1. systems approach, which manifests itself in the possibility of simulating electromagnetic fields considering the properties and characteristics of a complex TPSS and a supplying EPS;
2. universality ensuring simulation of power transmission lines and traction networks of various designs;
3. appropriateness to the environment, which is achieved via a precise analysis of the underlying surface, underground communications, and artificial railroad structures, such as galleries, bridges, and tunnels;
4. comprehensiveness provided by integrating the network calculation and the EMF intensity determination at the fundamental frequency and higher harmonics frequencies.

In the context of power industry digitalization, this technique, when put into practice, will provide the scientifically grounded approach to the analysis of electromagnetic safety conditions in electric power systems and at railroad transport facilities and the development of measures to improve electromagnetic safety.

#### REFERENCES

- [1] S.M. Apollonsky, A.N. Bogarinova, “EMF intensities of the air environment on the electrified railroad,” *Collection of reports of the ninth Russian research and technology conference on electromagnetic compatibility of technical means and electromagnetic safety*. St.P., Russian, 2006.
- [2] A.I. Sidorov, I.S. Okrainskaya, *Electromagnetic fields near ultrahigh voltage electrical installations*. Chelyabinsk: South Ural State University, 2008, p. 204.
- [3] A.B. Kosarev, B.I. Kosarev, *Basics of electromagnetic safety of railroad transport power supply systems*. Moscow: Intext, 2008, p. 480.
- [4] N.V. Byakova, V.P. Zakaryukin, A.V. Kryukov, *Electromagnetic safety in railroads power supply systems: modeling and control: monograph*, ed. by A.V. Kryukov. Angarsk: Editorial and Publishing Department, Angarsk State Technical University, 2018, p. 382.
- [5] Levitt B. Blake, *Protection against electromagnetic fields. On the effects of household appliances, cell phones, power lines and other electrical devices on the human body*. Moscow: ACT, Astel, 2007, p. 447.
- [6] Lars Abrahamsson, *Railway Power Supply Models and Methods for Long-term Investment Analysis. Licentiate Thesis. Royal Institute of Technology School of Electrical Engineering Electric Power Systems*. Stockholm, Sweden, 2008, p. 166.
- [7] R. Doleček, O. Černý, Z. Němec and J. Pidanič, “The behavior of the traction power supply system of AC 25 kV 50 Hz during operation,” *Rail Transport – Systems Approach, Studies in Systems, Decision and Control 87*. Springer International Publishing AG, 2017, pp. 35–65.
- [8] A. Ogunsola and A. Mariscotti, *Electromagnetic Compatibility in Railways*. Springer-Verlag Berlin Heidelberg 2013, p. 568.
- [9] M. Mandić, I. Uglešić, V. Milardić, “Design and testing of 25 kV AC electric railway power supply systems,” *Tehnički vjesnik 20*, pp. 505-509, March 2013.
- [10] R.J. Hill, “Modelling and simulation of electric railway traction, track signaling and power systems,” *Transactions on the Built Environment*. Vol. 6, pp. 383-390, 1994.
- [11] Luan Xiaotian, Zhu Haijing, Qiu Bo, Han Bochong, “EMC in Rail Transportation,” *CUE2016-Applied Energy Symposium and Forum 2016: Low carbon cities & urban energy systems*. Available at: [www.sciencedirect.com](http://www.sciencedirect.com). (accessed 30.04.2021)
- [12] S. Baranowski, H. Ouaddi, L. Kone and N. Idir, “EMC Analysis of Railway Power Substation Modeling and Measurements Aspects,” *Infrastructure Design, Signalling and Security in Railway*. ISBN: 978-953-51-0448-3, InTech. Available at: [www.intechopen.com](http://www.intechopen.com). (accessed 30.04.2021)
- [13] H. Ouaddi, S. Baranowski, G. Nottet, B. Demoulin, and L. Koné. (2011). Study of HF behaviour of railway power substation in reduced scale. *The European Physical Journal - Applied Physics*, 53(3), 33603. DOI:10.1051/epjap/2010100061
- [14] μPAS. Power Application Software. User manual for dynamic train-drive simulation. PROLEITEC AG, CH-8903 Birmensdorf, February 2013. p. 167.
- [15] Fabel – Enotrac Ag, *Software for the simulation of electric vehicles and power supply networks*. Available at: [www.enotrac.com](http://www.enotrac.com). (accessed 30.04.2021)
- [16] R. Kircher, J. Klühspies, R. Palka, et al. “Electromagnetic Fields Related to High Speed Transportation Systems,” *Transportation Systems and Technology 2018*, vol. 4(2), pp. 152-166. DOI: 10.17816/transsyst201842152-166.
- [17] R. Kircher, R. Palka, E. Fritz, K. Eiler, M. Witt, L. Blow, J. Klühspies, “Electromagnetic Fields of High-Speed Transportation Systems Maglev Technologies in Comparison with Steel-Wheel-Rail,” *The International Maglev Board C/O CERM Institute, Technical University of Deggendorf of Applied Sciences*. Available at: [www.maglevboard.net](http://www.maglevboard.net). (accessed 30.04.2021)

- [18] V.P. Zakaryukin, A.V. Kryukov, *Complex asymmetrical modes of electrical systems*. Irkutsk: Irkutsk State University, 2005. 273 p.
- [19] V.P. Zakaryukin, A.V. Kryukov, A.V. Cherepanov *Intelligent technologies of power quality management*. Irkutsk: ISTU Publishing House, 2015. p. 218.
- [20] O.I. Mitruyev, "Phase coordinate method to compute industrial frequency electromagnetic fields," *Enhancing energy production efficiency and use in the conditions of Siberia*. Irkutsk: ISTU Publishing House. 2006. pp. 301-311.
- [21] R.A. Kats, L.S. Perelman, "Computation of electrical field of a three-phase power line," *Elektrichestvo*, no. 1, pp. 16-19, 1978.
- [22] G.A. Greenberg, B.E. Bonstedt, "Fundamentals of the exact theory of the wave field of power lines," *Journal of Theoretical Physics*, vol. 24, no. 1, pp. 7-95, 1954.
- [23] M.V. Kostenko, D.G. Messerman, "Deformation of lightning overvoltage waves in over and ultra high voltage transmission lines at long run lengths," *Proceedings of the Academy of Sciences of the USSR: Energy and Transport*, no. 3, pp. 158-164. 1987.
- [24] D.G. Messerman, L.S. Perelman, "Parameters of wave propagation along a long wire above the ground," *Proceedings of the Academy of Sciences of the USSR. Energy and Transport*, no. 1, pp. 65-74, 1986.
- [25] D.G. Messerman, L.S. Perelman, "Calculation of modal parameters of multi-wire power transmission lines," *Proceedings of the Academy of Sciences of the USSR. Energy and Transport*, no. 1, pp. 9-17, 1984.
- [26] L.M. Wedepohl, "Application of matrix methods to the solution of travelling-wave phenomena in polyphase systems," *IEEE*, vol. 110, no. 12, 1963.
- [27] L.M. Wedepohl, "Electrical characteristics of polyphase transmission systems with special reference to boundary-value calculations at power-line carrier frequencies," *IEEE*, vol. 112, no. 11, 1965.
- [28] I.R. Carson, "Wave propagation in overhead wires with ground return," *Bell System Technical Journal*, vol. 5, pp. 539-554, 1926.



**Natalya Buyakova** is an Associate Professor in the Department of Power Supply of Industrial Enterprises, Angarsk State Technical University. In 1995, she graduated from Angarsk Technological Institute. Natalya Buyakova received the Ph.D. degree in engineering from Irkutsk State University of Transport in 2012. Her research interests are modeling and management of electric power systems and railroad supply systems; and smart grids.



**Vasili Zakaryukin** is Consultant Professor at LLC "Smart grid" at Irkutsk State Transport University. He graduated from Irkutsk State University in 1971. Vasili Zakaryukin received the degree of Ph.D. in engineering from Tomsk Polytechnic Institute in 1983 and the degree of D.Sc. in engineering from Omsk State Transport University in 2010. His research interests are modeling of electric power systems and railway power supply systems.



**Andrey Kryukov** is a Professor at Transport Power Engineering Department at Irkutsk State Transport University, a Professor at Power Supply and Electrical Equipment Department at Irkutsk National Research Technical University, Russia. He graduated from East Siberian Technological Institute in 1974. Andrey Kryukov received his degree of Ph.D. in engineering from Leningrad Polytechnic Institute in 1982 and the degree of D.Sc. in engineering from Energy Systems Institute of the Russian Academy of Sciences in 1997. His research interests are modeling and control of electric power systems and railway power supply systems; and smart grids.



**Dmitry Seregin** is a postgraduate student at Irkutsk State Transport University. In 2019, he graduated from Irkutsk State Transport University, majoring in Railway Power Supply. His research interests are modeling of electric power systems, electromagnetic safety, and electromagnetic compatibility.